

# THÈSE DE DOCTORAT

Soutenue à AMU — Aix-Marseille Université  
le 13 décembre 2024 par

**Raffael DÜLL**

**A 3D ELECTROMAGNETIC MODEL IN SOLEDGE3X:  
Application to turbulent simulations of tokamak edge plasma**

**Discipline**

Sciences pour l'Ingénieur

**Spécialité**

Fusion magnétique

**École doctorale**

ED 353 Sciences pour l'ingénieur: mécanique, physique, micro et nanoélectronique

**Partenaires de recherche**

Laboratoire de Mécanique, Modélisation & Procédés Propres (M2P2), AMU

Institut de Recherche sur la Fusion par Confinement Magnétique (IRFM), CEA Cadarache

**Composition du jury**

Benjamin DUDSON Senior Researcher, Lawrence Livermore National Laboratory	Rapporteur
Boniface NKONGA Professeur, Université Côte d'Azur	Rapporteur
Daniela GRASSO Assistant Professor, Politecnico di Torino	Examinateuse
Paolo RICCI Professor, EPFL	Examinateur
Eric NARDON Directeur de recherche, CEA Cadarache	Président du jury
Eric SERRE Directeur de recherche, CNRS M2P2	Directeur de thèse
Hugo BUFFERAND Chercheur, CEA Cadarache	Co-encadrant de thèse

# Affidavit

I, undersigned, Raffael Düll, hereby declare that the work presented in this manuscript is my own work, carried out under the scientific supervision of Eric Serre, in accordance with the principles of honesty, integrity and responsibility inherent to the research mission. The research work and the writing of this manuscript have been carried out in compliance with both the french national charter for Research Integrity and AMU charter on the fight against plagiarism.

This work has not been submitted previously either in this country or in another country in the same or in a similar version to any other examination body.

Marseille 24/09/2024



This work is licensed under [Creative Commons Attribution-NonCommercial-NoDerivatives 4.0 International Public License](#)

# List of publications and/or patents and conference participation

## (1) List of publications and/or patents produced as part of the thesis project:

1. **Düll, R.**, Bufferand, H., Serre, E., Ciraolo, G., Quadri, V., Rivals, N. and Tamain, P., 2024. Introducing electromagnetic effects in Soledge3X. *Contributions to Plasma Physics*, p.e202300147.
2. **Düll, R.**, Ciraolo, G. Bufferand, H., Serre, E., Quadri, V., Rivals, N., Tamain, P., Sureshkumar, S. and Varadarajan, N. Implementation of a non-axisymmetric magnetic configuration in SOLEDGE3X to simulate 3D toroidal magnetic ripple effects: Application to WEST. *Nuclear Materials and Energy* [under review]
3. **Düll, R.**, Bufferand, H., Serre, E., Ciraolo, G., Quadri, V., Rivals, N., Schwander, F. and Tamain, P., An electromagnetic model in SOLEDGE3X for edge plasma turbulence simulations in tokamak. *Journal of Computational Physics* [to be submitted]
4. Quadri, V., Tamain, P., Marandet, Y., Bufferand, H., Rivals, N., Ciraolo, G., Falchetto, G., **Düll, R.** and Yang, H., 2024. Self-organization of plasma edge turbulence in interaction with recycling neutrals. *Contributions to Plasma Physics*, p.e202300146.
5. Quadri, V., Tamain, P., Marandet, Y., Bufferand, H., Rivals, N., Ciraolo, G., Falchetto, G.L., **Düll, R.**, Sureshkumar, S., Varadarajan, N. and Yang, H., 2024. Edge plasma turbulence simulations in detached regimes with the SOLEDGE3X code. *Nuclear Materials and Energy*, p.101756.
6. De Gianni, L., Ciraolo, G., Giruzzi, G., Falchetto, G., Rivals, N., Balbinot, L., Varadarajan, N., Sureshkumar, S., Artaud, J.F., Bufferand, H. and **Düll, R.**, Core and edge modeling of JT-60SA H-mode highly radiative scenarios using SOLEDGE3X-EIRENE and METIS codes. *Frontiers in Physics*, 12, p.1422286.

## **(2) Participation in conferences and summer schools during the thesis period:**

1. Summer School PlasmaSurf by Instituto de Plasmas e Fusão Nuclear. July 2022, Lisbon, Portugal
2. Conference EPS - 49th European Conference on Plasma Physics, European Physical Society. July 2023, Bordeaux, France. Poster presentation: "*A new electromagnetic model in SOLEDGE3X*"
3. Conference PET19 - 19th International Workshop on Plasma Edge Theory in Fusion Devices. September 2023, Hefei, China. Contributed talk: "*Introducing electromagnetic effects in Soledge3X*"
4. Conference PSI-26 - 26th International Conference on Plasma Surface Interaction in Controlled Fusion Devices. May 2024, Marseille, France. Poster presentation: "*Electromagnetic effects on turbulent structures in edge plasmas with SOLEDGE3X*"
5. EUROfusion - TSVV3 Annual Workshop. May 2024, Leuven, Belgium [remote participation]. Presentation: "*Simulating electromagnetic effects in SOLEDGE3X*"
6. Conference ECCOMAS - 9th European Congress on Computational Methods in Applied Sciences and Engineering. June 2024, Lisbon, Portugal. Participation at the mini-symposium: Magnetohydrodynamic Numerical Modeling of Magnetised Plasmas. I with the oral presentation: "*An electromagnetic model for SOLEDGE3X*"
7. EUROfusion - TSVV1 Progress Workshop. September 2024, Garching, Germany. Presentation: "*A new electromagnetic model for turbulent simulations in SOLEDGE3X*"

# Résumé et mots clés

Dans le bord du tokamak, les gradients abrupts et la courbure magnétique génèrent des structures turbulentes de grande échelle qui transportent les particules de plasma du cœur chaud, où la fusion se produit à environ 10 keV, vers la couche limite (SOL) beaucoup plus froide, où les lignes de champ magnétique croisent la paroi. La turbulence réduit le confinement du plasma et détermine la zone où de forts flux de chaleur impactent le divertor. Le code fluide SOLEDGE3X, développé par le CEA/IRFM en collaboration avec Aix-Marseille Université, s'est avéré efficace pour simuler la turbulence electrostatique resistive des ondes de dérive dans des géométries de tokamak réalistes. Cependant, des résultats expérimentaux et numériques ont montré que les effets électromagnétiques ont un impact significatif sur la dynamique des ondes de dérive, et donc sur la turbulence de bord.

Cette thèse introduit un modèle électromagnétique dans SOLEDGE3X, avec trois composantes : l'induction magnétique, le flutter électromagnétique et l'inertie des électrons. L'induction magnétique tient compte de la variation temporelle du potentiel vecteur magnétique parallèle  $A_{\parallel}$  dans la définition du champ électrique parallèle, et  $A_{\parallel}$  est relié à la densité de courant parallèle  $j_{\parallel}$  par la loi d'Ampère. Les fluctuations du champ magnétique, appelées flutter, sont ajoutées au premier ordre et supposées faibles par rapport au champ d'équilibre. L'inertie des électrons, apparaissant avec une masse d'électrons non nulle dans la loi d'Ohm, est nécessaire pour contraindre les vitesses des ondes d'Alfvén à des valeurs physiques. Les nouveaux champs  $A_{\parallel}$  et  $j_{\parallel}$  sont intégrés dans le maillage aligné aux surfaces de flux sur une grille décalée poloïdalement et toroïdalement. Le flutter affecte les équations de transport parallèle et les gradients dans la loi d'Ohm. Sa mise en œuvre a requis une attention particulière pour tenir compte de la nouvelle composante radiale de la direction parallèle  $\mathbf{b}$ . Pour permettre des pas de temps plus importants que les temps d'Alfvén, de transit électronique ou de collision électron-ion, les effets inductifs, inertIELS et résistifs sont résolus implicitement dans un système 3D couplé sur les potentiels  $\Phi$  et  $A_{\parallel}$ . Le modèle a été vérifié au moyen de solutions analytiques et validé sur un cas linéaire, montrant la transition d'ondes d'Alfvén à des ondes électroniques thermiques.

Le flutter contribue peu au transport radial, mais influence la réponse non adiabatique du potentiel aux fluctuations de densité. Les premières simulations dans des géométries slab, circulaires (limitées) et à point X (à divertor) montrent de manière consistante que l'inertie des électrons et l'induction magnétique déstabilisent la turbulence des ondes de dérive, tandis que le flutter la stabilise, à la fois dans les phases linéaires et non linéaires. Sur les lignes de champ ouvertes, l'induction ma-

gnétique réduit la sensibilité des structures turbulentes aux effets de gaine, favorisant la propagation de la turbulence dans la SOL. Sur le plan numérique, l'inertie des électrons améliore considérablement le conditionnement de la matrice de vorticité, en particulier dans les plasmas chauds à faible résistivité, accélérant la résolution d'un facteur quatre. Cependant, l'ajout du flutter dégrade la performance du code, car il nécessite la résolution de systèmes 3D implicites pour les problèmes de viscosité et de diffusion thermique, auparavant traités comme des systèmes 2D découplés sur chaque surface de flux. Dans le prolongement de ce travail, des perturbations de l'équilibre magnétique ont été imposées de manière externe dans une simulation en mode transport portant sur le dépôt de chaleur dans une configuration magnétique non axisymétrique avec ripple sur WEST.

Mots clés : tokamak, plasma de bord, simulations turbulentes, électromagnétisme, SOLEDGE3X

# Abstract and keywords

In the tokamak edge, steep gradients and magnetic curvature generate large-scale turbulent structures that transport plasma particles from the hot core, where fusion occurs at around 10 keV, to the much colder Scrape-Off-Layer (SOL), where magnetic field lines intersect the physical wall. Turbulence reduces plasma confinement and defines the region where strong heat fluxes impact the divertor. The drift-reduced fluid code SOLEDGE3X, developed by CEA/IRFM in collaboration with Aix-Marseille University, has proven effective in simulating electrostatic resistive drift-wave turbulence in realistic tokamak geometries. However, both experimental and numerical results have shown that electromagnetic effects significantly impact drift-wave dynamics, and thus, edge plasma turbulence.

This thesis introduces a new electromagnetic model in SOLEDGE3X for the vorticity equation, incorporating magnetic induction, electromagnetic flutter, and electron inertia. Magnetic induction accounts for the time variation of the parallel magnetic vector potential  $A_{\parallel}$  in the definition of the parallel electric field, and  $A_{\parallel}$  is related to the parallel current density  $j_{\parallel}$  via Ampère's law. Fluctuations in the magnetic field, termed flutter, are added at first order and are assumed to be small compared to the equilibrium field. Electron inertia, represented by a finite electron mass in Ohm's law, is necessary to constrain shear Alfvén wave speeds to physical values. The new fields  $A_{\parallel}$  and  $j_{\parallel}$  are integrated into the flux-surface-aligned FVM framework on a poloidally and toroidally staggered grid. Flutter affects the parallel transport equations and gradients in Ohm's law, and its implementation required special care to account for the new radial component of the parallel direction  $\mathbf{b}$ . To handle timesteps larger than Alfvénic, electron thermal, or electron-ion collision times, the corresponding inductive, inertial, and resistive effects are solved implicitly in a coupled 3D system for the potentials  $\Phi$  and  $A_{\parallel}$ . The model was verified with manufactured solutions and validated on a linear slab case, which demonstrated the expected transition from Alfvén to thermal electron waves as the perpendicular wavenumber increased.

Flutter contributes minimally to cross-field transport but affects the non-adiabatic potential response to density fluctuations in Ohm's law. Simulations in slab, circular (limited), and X-point (diverted) geometries consistently show that electron inertia and magnetic induction destabilize drift-wave turbulence, while flutter stabilizes it in both the linear and nonlinear phases. On open field lines, magnetic induction reduces the sensitivity of turbulent structures to sheath effects, promoting further turbulence spreading in the SOL. Numerically, electron inertia significantly improves the condition number of the vorticity system, especially in hot plasmas with low resistivity, providing a factor-four speedup even in electrostatic scenarios. However, adding flutter degrades code performance, as it requires solving implicit 3D systems

for viscosity and heat diffusion problems that were previously treated as uncoupled 2D systems on each flux surface. As an extension to this work, perturbations to the magnetic equilibrium were externally imposed in a transport mode simulation to study heat deposition in a non-axisymmetric magnetic configuration with ripple on WEST.

Keywords: tokamak, edge plasma, turbulent simulations, electromagnetism, SOLEDGE3X

# Acknowledgments

I would like to thank my thesis director Eric Serre and supervisor Hugo Bufferand for their support throughout my PhD thesis. A big shoutout goes to the entire SOLEDGE3X team, and in particular to Patrick Tamain, for their fruitful discussions, continuous feedback and help with the code framework. I also thank Aix Marseille University, CEA and EUROfusion for permitting this thesis at all and the CINES and CINECA super-computing infrastructures to run simulations.

# Contents

<b>Affidavit</b>	<b>2</b>
<b>List of publications and/or patents and conference participation</b>	<b>3</b>
<b>Résumé et mots clés</b>	<b>5</b>
<b>Abstract and keywords</b>	<b>7</b>
<b>Acknowledgments</b>	<b>9</b>
<b>Contents</b>	<b>10</b>
<b>List of Figures</b>	<b>14</b>
<b>List of Tables</b>	<b>17</b>
<b>I. Introduction</b>	<b>18</b>
<b>II. Description of Magnetized Plasmas in a Tokamak</b>	<b>25</b>
<b>1. Tokamak Concept</b>	<b>26</b>
1.1. Particles in a magnetized plasma . . . . .	27
1.1.1. Gyromotion of a single particle . . . . .	27
1.1.2. Plasma drifts . . . . .	28
1.1.3. Tokamak configuration . . . . .	30
1.1.4. Grad-Shafranov equilibrium . . . . .	31
1.1.5. Realisation of magnetic configurations . . . . .	34
1.2. Interaction between particles . . . . .	36
1.2.1. Debye shielding . . . . .	37
1.2.2. Particle collisions . . . . .	37
1.2.3. Macroscopic effects of plasma collisions . . . . .	40
1.3. Scrape-Off-Layer . . . . .	41
1.3.1. Fundamental sheath physics . . . . .	41
1.3.2. Problematic of heat exhaust . . . . .	42

<b>2. Description of Plasmas</b>	<b>43</b>
2.1. A hierarchy of models . . . . .	44
2.1.1. Direct description of plasma particles . . . . .	44
2.1.2. Three fluid moments of the kinetic equation . . . . .	46
2.1.3. MHD description of plasmas . . . . .	48
2.2. Drift-reduced models for plasma turbulence . . . . .	51
2.2.1. Drift-ordering approximation . . . . .	52
2.2.2. Linear plasma instabilities . . . . .	54
2.3. Electromagnetic effects in edge plasma . . . . .	58
2.3.1. Non-adiabatic plasma response in Ohm's law . . . . .	58
2.3.2. Electromagnetic flutter . . . . .	60
2.3.3. Drift-Alfvén waves . . . . .	61
<b>III. An Electromagnetic Model for SOLEDGE3X</b>	<b>64</b>
<b>3. The physical model</b>	<b>65</b>
3.1. Dimensionless fields . . . . .	66
3.2. Conservation equations . . . . .	68
3.2.1. Mass balance . . . . .	69
3.2.2. Momentum balance . . . . .	69
3.2.3. Energy balance . . . . .	70
3.2.4. Charge balance . . . . .	70
3.3. Ingredients for electromagnetism . . . . .	72
3.3.1. Electron inertia . . . . .	73
3.3.2. Electromagnetic induction . . . . .	74
3.3.3. Electromagnetic flutter . . . . .	75
3.3.4. Full electromagnetic vorticity system . . . . .	76
3.4. Boundary conditions . . . . .	78
<b>4. Numerical Implementation</b>	<b>79</b>
4.1. Geometrical consideration . . . . .	80
4.1.1. Coordinate system . . . . .	80
4.1.2. Domain decomposition and mesh design . . . . .	81
4.1.3. Curvilinear coordinates . . . . .	81
4.2. The staggered mesh . . . . .	83
4.2.1. Description and notation . . . . .	83
4.2.2. Boundary cells . . . . .	84
4.2.3. Staggered discrete operators . . . . .	86
4.2.4. Discretization around the X-point . . . . .	89
4.3. Electromagnetic vorticity system . . . . .	90
4.3.1. Matrix formulation of the electromagnetic system . . . . .	90
4.3.2. Evaluation of the condition number . . . . .	93

4.4. Numerical treatment of flutter . . . . .	97
4.4.1. Radial advection . . . . .	98
4.4.2. Parallel diffusion . . . . .	98
4.4.3. Vorticity equation . . . . .	99
<b>5. Verification and Validation</b>	<b>101</b>
5.1. Verification by the method of manufactured solutions . . . . .	102
5.1.1. Test set-up . . . . .	102
5.1.2. Electromagnetic vorticity equation . . . . .	104
5.1.3. Parallel heat diffusion with flutter . . . . .	106
5.2. Validation on linear systems . . . . .	107
5.2.1. Pure advection . . . . .	107
5.2.2. Electrostatic vorticity equation . . . . .	109
5.2.3. Electromagnetic vorticity equation . . . . .	110
5.2.4. Linear transition from Alfvén to thermal electron waves . . . . .	114
<b>IV. Electromagnetic plasma simulations</b>	<b>117</b>
<b>6. Limited Geometry</b>	<b>118</b>
6.1. Electromagnetic modes excitation . . . . .	119
6.2. Slab configurations . . . . .	122
6.2.1. Analysis of a plasma blob . . . . .	123
6.2.2. Generation of drift waves . . . . .	124
6.3. Circular geometry . . . . .	126
6.3.1. Simulation set-up . . . . .	126
6.3.2. Linear instability growth . . . . .	127
6.3.3. Nonlinear turbulence phase . . . . .	129
6.3.4. Mode structures . . . . .	131
<b>7. Diverted Geometry</b>	<b>134</b>
7.1. Electrostatic versus electromagnetic scenarios . . . . .	135
7.1.1. Simulation set-up . . . . .	135
7.1.2. Comparison between the scenarios . . . . .	136
7.1.3. Numerical performances . . . . .	138
7.2. Flutter in higher power . . . . .	140
7.2.1. Parallel heat conduction . . . . .	140
7.2.2. Characteristics of the fluctuating field . . . . .	142
<b>8. Perspectives for Studying Magnetic Ripple</b>	<b>145</b>
8.1. Motivation for simulating magnetic ripple . . . . .	146
8.2. Generation of a non-axisymmetric magnetic configuration . . . . .	147
8.3. Application to a WEST scenario . . . . .	151
8.4. Conclusion . . . . .	152

<b>V. Conclusion</b>	<b>154</b>
<b>Bibliography</b>	<b>159</b>
<b>APPENDICES</b>	<b>168</b>
<b>A. New software modules</b>	<b>169</b>
A.1. New options in SOLEDGE3X . . . . .	169
A.2. Grad-Shafranov solver . . . . .	173
A.3. Poincaré plots . . . . .	173
A.4. Time plots . . . . .	173
<b>B. Operators on the curvilinear metric</b>	<b>176</b>
B.1. Linear algebra . . . . .	176
B.2. Centered differentiation stencils . . . . .	177
B.3. Staggered operators . . . . .	178
B.3.1. Parallel gradient . . . . .	178
B.3.2. Perpendicular Laplacian . . . . .	179
<b>C. Turbulent profiles</b>	<b>180</b>
C.1. Mid-plane plots for density . . . . .	180
C.2. Perpendicular modes on for electron inertia and magnetic induction on the circular scenario . . . . .	182
C.3. Flutter field in the low-power TCV scenario . . . . .	183

# List of Figures

1.	Fusion reaction cross-sections for the most promising pairs of light elements over center-of-mass energy . . . . .	20
2.	Relation of the fusion trapping $n\tau_E$ to the temperature in current and future devices . . . . .	21
1.1.	Trajectory of a positively and a negatively charged particle along a homogeneous magnetic field line. . . . .	28
1.2.	Simplified scheme of the magnetic field components on a flux surface . . . . .	31
1.3.	Solution of the Grad-Shafranov equation on a circular cross-section with minor radius $a = 0.3$ m . . . . .	33
1.4.	Cutaway of the ITER tokamak . . . . .	35
1.5.	Comparison of the limited and diverted configuration on a WEST geometry . . . . .	36
1.6.	Trajectory of the projectile particle (red) colliding with the target particle (green) . . . . .	38
1.7.	Volume for given $db$ and $dx$ in which collisions on the projectile are considered . . . . .	39
4.1.	Example of typical mesh and domain decomposition mapping the real domain to a Cartesian multiple zones domain . . . . .	81
4.2.	General view of the staggered grid points marked as crosses on top of the collocated cells . . . . .	84
4.3.	General view of the staggered grid points in the $\theta - \varphi$ plane . . . . .	85
4.4.	Neighbors involved to calculated staggered parallel gradients . . . . .	87
4.5.	Neighbors involved to calculated the parallel divergence . . . . .	88
4.6.	Depiction of the relevant cell faces to calculate fluxes of a staggered field . . . . .	89
4.7.	Sketches of the mesh around the X-point . . . . .	90
4.8.	Sketches of the mesh around the X-point . . . . .	92
4.9.	Impact of different parameters on the condition number . . . . .	97
4.10.	Sketches showing the calculation of gradients for the parallel diffusion scheme . . . . .	99
4.11.	Neighbors of the parallel Laplacian stencil with flutter for the vorticity equation . . . . .	100
5.1.	Distorted MMS mesh geometry with $N = 20$ cells per dimension on a 3rd of a torus . . . . .	103
5.2.	Relative error between the initial plasma and the solution after one timestep for the electromagnetic vorticity system . . . . .	106

5.3.	Relative error between the initial plasma and the solution after one timestep for the parallel 3D heat diffusion system with flutter . . . . .	107
5.4.	Evolution of the 1D SLAB system with 64 cells in poloidal direction over 10000 timesteps with the RK4 scheme . . . . .	109
5.5.	Evolution of the 2D electrostatic SLAB system with 64 cells in radial and poloidal direction over 10000 timesteps with the implicit Euler scheme . . . . .	110
5.6.	Snapshot of an electromagnetic SLAB simulation on a domain with $N_\psi = 32$ and $N_\theta = 64$ grid points . . . . .	113
5.7.	Relative error for the fits of the frequency $\omega_0$ and the decay rate $\lambda$ on the evolution of $A_{\parallel}$ . . . . .	114
5.8.	Characteristic evolution of the four-field electromagnetic model in a domain with $N_\psi = N_\theta = N_\varphi = 63$ grid points . . . . .	115
5.9.	Fitted wave frequencies as a function of the perpendicular wave numbers	116
6.1.	Dependency on the perpendicular wavenumber $k_\perp$ of the real and imaginary parts of the all solutions $\omega$ to the dispersion relation 6.1 . . . . .	121
6.2.	Relative difference of drift-wave frequency in the electromagnetic scenarios to the reference electrostatic case . . . . .	122
6.3.	3D representation of the slab domain with four poloidal planes . . . . .	123
6.4.	Density profiles after $9.6\mu\text{s}$ simulated plasma time for the electrostatic (ES), magnetic inductive (EM) and full electromagnetic scenarios (EM-flutter) . . . . .	124
6.5.	Density profiles at the toroidal center of the slab, at about 32m from both limiters . . . . .	125
6.6.	Snapshots of the toroidal fluctuations in electron temperature $T_e - \langle T_e \rangle_\varphi$ after 0.1ms simulated plasma time . . . . .	127
6.7.	Evolution of the root mean square deviation for different values of $m_e$ . . . . .	128
6.8.	Evolution of the root mean square deviation for different values of $\beta$ . . . . .	128
6.9.	Evolution of the radial ion temperature profiles and heat fluxes at the outer mid-plane for the electrostatic scenarios . . . . .	130
6.10.	Evolution of the radial ion temperature profiles and heat fluxes at the outer mid-plane for the electromagnetic scenarios . . . . .	131
6.11.	View of the flux surface at $i_\psi = 70$ at the time for the flutter scenario in real and in Fourier space . . . . .	132
6.12.	Evolution of the power spectrum of $\tilde{n}_\perp$ associated to the perpendicular modes $k_\perp$ in the range $[-400,400]\text{m}^{-1}$ over the simulation time. . . . .	133
7.1.	Simulation snapshots of the full electromagnetic scenario with flutter . . . . .	136
7.2.	Evolution of the turbulent energy and heat exhaust over time iterations on the turbulent TCV scenario . . . . .	137
7.3.	Radial profiles at the outer mid-plane after 6 ms simulated plasma time . . . . .	138
7.4.	Averaged profiles at the outer mid plane taken at different simulation times for the TCV scenario with a 1.2MW heat source . . . . .	141

7.5. Contribution of the different terms in the energy conservation equation to the power transfer from the core to the SOL . . . . .	142
7.6. Poincaré plot of the fluctuating magnetic field in the TCV high-power case for a random seed of 2500 points in a TCV poloidal plane . . . . .	143
7.7. Comparison of the magnitude of the flutter field to the poloidal magnetic field strength $B_{pol}$ . . . . .	144
8.1. Infrared camera view of the divertor target, taken from [8] . . . . .	147
8.2. Exemplary SOLEDGE3X mesh for a WEST single-null geometry . . . . .	148
8.3. Top views of the perturbated field $\mathbf{B}_{pert}$ on the WEST tokamak at the mid plane . . . . .	149
8.4. Map of the poloidal field $B_{pol}$ at several poloidal planes within a ripple perdiod around the lower X-point and the divertor targets . . . . .	150
8.5. Poincaré plot at coil-aligned poloidal planes. Seed points are uniformly distributed on the mid-plane along the radial and toroidal directions .	151
8.6. Calculated electron wall heat flux in the divertor region from the SOLEDGE3X simulation . . . . .	152
C.1. Evolution of the radial ion density profiles and particle fluxes at the outer mid-plane for the electrostatic scenarios. The dashed line indicates the position of the separatrix and the plasma in the first poloidal plane is taken . . . . .	180
C.2. Evolution of the radial ion density profiles and particle fluxes at the outer mid-plane for the electromagnetic scenarios. The dashed line indicates the position of the separatrix and the plasma in the first poloidal plane is taken . . . . .	181
C.3. Evolution of the power spectrum associated to the perpendicular modes $k_\perp$ over the simulation time. Complement to Fig. 6.12 . . . . .	182
C.4. Poincaré plot of the fluctuating magnetic field in the TCV low-power case for a random seed of 500 points in a TCV poloidal plane. . . . .	183

# List of Tables

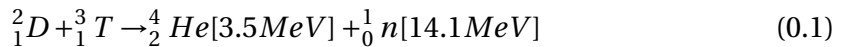
7.1.	Numerical metrics on the four TCV scenarios for one timestep . . . . .	139
8.1.	Technical parameters of the toroidal field coils used to generate the ripple field for the WEST tokamak . . . . .	149
A.1.	New or modified parameters for the SOLEDGE3X parameter file. . . . .	172
A.2.	New parameters for analytic meshes . . . . .	172
A.3.	Global metrics available to plot the time evolution . . . . .	175

# **Part I.**

## **Introduction**

The sun is the primary source of energy for Earth: without its radiation, life would be impossible as it drives photosynthesis in plants, regulates weather and climate systems, and supports ecosystems. Since the beginning of humanity, the sun has been a subject of admiration, occupying a central role in mythological and religious beliefs, where it was often synonym for an infinite and unreachable source of energy. It was not until the early twentieth century that fundamental discoveries in particle and nuclear physics unraveled the secret of solar energy: nuclear fusion. It is the physical process where two light atoms merge to form a heavier atom, releasing significant energy as a result of mass-to-energy conversion. The strong nuclear force is fundamental to confine the positively charged protons with neutrons in an atomic nucleus. Every element is characterized by its total binding energy, that corresponds to the energy needed to break an atom into its constituting protons and neutrons. A higher total binding energy means that the element is more stable. The maximum binding energy is observed for iron ( $^{56}Fe$ ), it means that (roughly) all lighter elements can produce energy by fusion and heavier by fission, as it is done in conventional nuclear power plants.

The dream of achieving nuclear fusion in a laboratory to produce energy emerged shortly thereafter. In today's climate crisis, nuclear fusion is even more appealing because it does not emit carbon emissions, does not present the risk of a catastrophic meltdown and its fuel, hydrogen, is readily available. Since replicating the sun's core conditions on Earth, particularly the gigantic pressure, is not feasible, alternative approaches were searched. A look at Fig. 1 with the reaction cross-section of various pairs of light atoms shows that deuterium-tritium (D-T) fusion has the highest likelihood at the most accessible temperature. These two hydrogen isotopes are hence the most favorable candidates for fusion and the reaction reads:



In the fusion reaction between deuterium and tritium, one alpha-particle (or Helium-4 nucleus) and one neutron are produced. 80% of the released energy is carried by the neutron. Deuterium is a naturally abundant isotope of hydrogen, but tritium, which is radioactive and has a relatively short half-life time of 12 years, must be produced artificially. The most widely used method to obtain tritium is via neutron activation of lithium-6, but this requires either a nuclear power plant or another type of effective neutron source. As each fusion reaction emits one neutron, all future D-T reactor designs rely on a yet-to-be-tested technology to produce tritium inside the reactor, in the so-called "tritium breeding" process. To compensate inevitable particle losses, the neutron flux is first multiplied by hitting a layer of beryllium or lead. The neutrons then react with the lithium in an exothermic reaction, releasing one new tritium and one helium atom. The limiting resource for a large-scale deployment of nuclear fusion for power generation is then lithium, but even then, the required quantities are well below the current extraction for industrial needs.

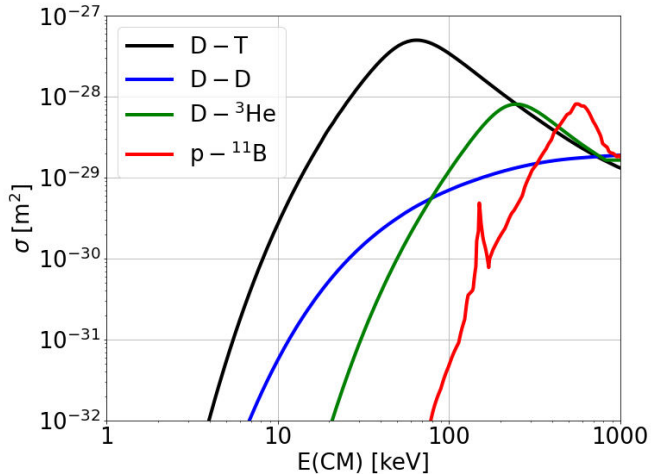


Figure 1.: Fusion reaction cross-sections for the most promising pairs of light elements over center-of-mass energy.

At the very high temperatures needed for nuclear fusion, the electromagnetic force is insufficient to maintain the cohesion of electrons and their atomic nuclei, resulting in the formation of a state of matter known as plasma. Plasma is an ionized gas composed of positively charged nuclei and negatively charged electrons, which interact electromagnetically.

Lawson's criterion [56] estimates the necessary plasma conditions to reach the break-even point, where fusion power exceeds heating and conduction losses. For D-T fusion, the triple product of density  $n$ , temperature  $T$ , and energy confinement time  $\tau_E$  must exceed:

$$nT\tau_E > 10^{-21} \text{ keV} \cdot \text{m}^{-3} \cdot \text{s} \quad (0.2)$$

From a practical point of view, an important metric is the fusion gain  $Q$ , which measures the ratio of power produced in the nuclear fusion reaction to the required heating power to maintain plasma conditions. One major milestone is the break-even point, when the fusion reaction produces enough power to maintain a steady state at  $Q = 1$ . However, the plasma can only capture a fraction of the produced fusion energy, as most fast neutrons rapidly escape the plasma, with, as seen before, 80% of the energy. Therefore, external heating is still required until  $Q > 5$ . Past this point, fusion produces more heat than the total required heating power and sustains itself in a state known as ignition ( $Q = \infty$ ). Commercial operation of fusion power plants requires reliable access to ignition, which still requires decades of research.

The reaction cross-section determines an optimal temperature of approximately 15-40 keV ( 150 million °C) for D-T fusion reactions, leading fusion reactor designs to

maximize either of the two remaining parameters: density or confinement time. There is a large variety of approaches to artificial fusion, but today, two concepts show the most promise. Inertial Confinement Fusion (ICF) seeks to compress dense fuel pellets for an extremely brief duration using high-powered lasers. Conversely, Magnetic Confinement Fusion (MCF) utilizes strong magnetic fields to sustain stable plasmas at relatively low densities. Within MCF, there are two primary designs: tokamaks, which use a toroidal chamber with an axisymmetric magnetic field, and stellarators, which use a twisted magnetic configuration to improve plasma confinement.

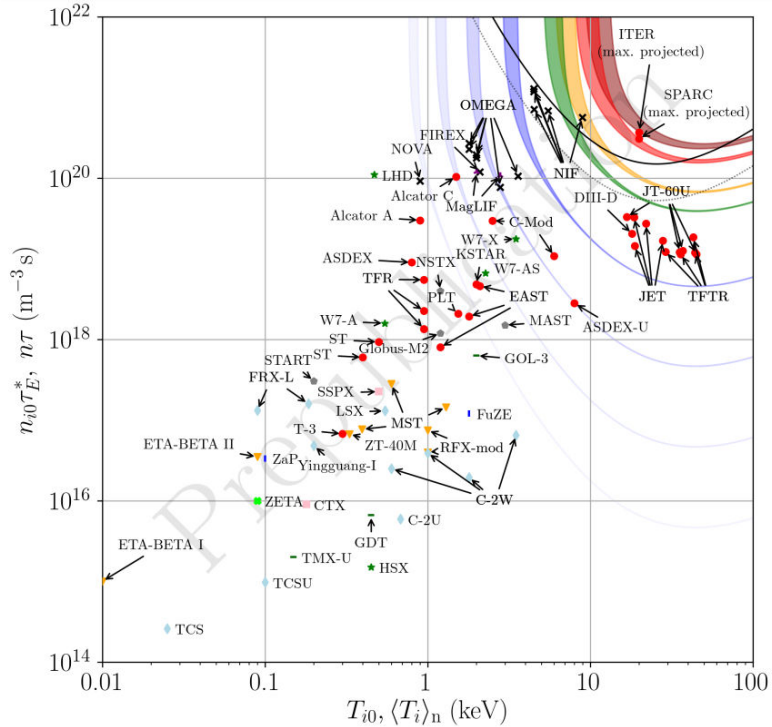


Figure 2.: Relation of the fusion trapping  $n\tau_E$  to the temperature in current and future devices. For MCF The break-even point ( $Q=1$ ) corresponds to the green area and ignition ( $Q=\infty$ ) is brown. Ignition for ICF is reached at the solid black line. Taken from [104]

Figure 2 depicts the current status of fusion experiments with respect to Lawson's criterion. On December 5, 2022, the National Ignition Facility (NIF) reached the break-even point for the first time, achieving a 3.1 MJ fusion yield with 2 MJ of injected laser power[2]. Large MCF devices, such as DIII-D, TFTR, JET, and JT60-SA, are already very close to the break-even point. Next-generation devices, including ITER and SPARC, which are under construction, are expected to achieve  $Q > 1$ .

In this work, we focus on the most promising candidate for MCF, the tokamak. The three Soviet physicists Lavrent'ev, Sakharov, and Tamm had the idea in the early 1950s

[3] to confine the plasma in a strong toroidal magnetic field. Additional coils create a poloidal field to suppress instabilities, such that plasma particles are trapped on helical trajectories. The first experiment was conducted in 1954 at the LIPAN institute in Moscow, the predecessor of the Kurchatov institute. The term "tokamak" or "токамак" was coined in 1957 by Golovin, and is a Russian acronym of "тороидальная камера с магнитными катушками", which translates to "toroidal chamber with magnetic coils," where the "G" from "mag" was transformed to "K" for better sonority [88].

Since then, tokamaks gained popularity in the USSR and abroad. The design was improved with each generation of new devices to operate at ever higher power. In the 1960s, the first devices surpassed the Bohm limit. Technological progress in plasma heating and superconducting coils led to second-generation tokamaks, such as TFTR and JET, which could operate at much higher temperatures and magnetic field strengths. Another breakthrough was the refined shaping of the magnetic equilibrium with the introduction of divertors to carefully direct particle fluxes, which ultimately culminated in the discovery of the high-confinement (H) mode, allowing for much higher core temperatures. The largest fusion experiment, ITER, is currently under construction in southern France by an international collaboration of seven member parties. At full operation, it is expected to achieve ignition, a state where the fusion reaction emits sufficient radiation to maintain plasma conditions. Its scientific goals include maintaining burning plasma for an extended period of time and demonstrating safe operation in the nuclear phase. It will also serve as a test facility for tritium breeding blankets, a much-needed technology to produce tritium in situ. Currently, tritium is only obtained in pressurized water reactors, and the worldwide annual production of about 500 g is far insufficient to meet the required 55.8 kg per GW installed in a fusion power plant[1].

Understanding fundamental physical processes in the plasma still constitutes an important part of today's research on fusion energy. With the harsh conditions inside the tokamak vessel, diagnostics can only measure indirect plasma properties and are limited in spatial resolution. Simulations are then essential to interpret and extend the findings from experimental data and understand the correlations between different observations. They support current tokamak operation with estimates of heat deposition, wall erosion, and by predicting plasma disruptions. For the design of future fusion devices, simulations allow the evaluation of new magnetic configurations and the optimization of these designs. One particular region of interest is the transition from the hot core region, with closed magnetic field lines, to the edge and the scrape-off layer, where particles traveling along the magnetic field collide with the physical wall in the divertor region. Strong temperature gradients lead to large turbulent structures, driven by resistive drift waves. It is crucial to understand the dynamics and interactions with impurities or neutrals, as fluxes crossing the separatrix largely define the quality of plasma confinement. From a material design perspective, edge plasma simulations are essential to characterize the particle and heat fluxes on the physical wall.

The mechanisms at play at the plasma boundary result from the complex interplay of transport processes in the plasma, losses at the wall, and complex atomic and molecular interactions. In this region, particles experience very fast transport along the magnetic field lines and slower, often turbulence-driven, anomalous cross-field transport[61]. The ratio between these phenomena characterizes the decay length of density and temperature profiles, which further determine the confinement quality of the core plasma and the total heat exhaust on the divertor target. Drift-reduced fluid models are particularly suited to simulate tokamak edge plasma, as they focus on low-frequency dynamics dominating the turbulent transport. The simplifications make it numerically feasible to simulate plasma behaviour over relevant time scales with still accurate results. Major simulation frameworks that follow this approach include GRILLIX[93, 94], GBS[33, 74], BOUT++[25, 27] or SOLEDGE3X[10, 97].

In the scope of this thesis, I extended the physical model underlying the SOLEDGE3X code, originally developed at CEA Cadarache in cooperation with Aix Marseille University. In its current version, turbulent simulations are limited to L-modes and small machines due to numerical issues and a limited model for larger machines. A significant limitation arises from the anisotropy between the parallel (resistive) and perpendicular (from the time evolution of the vorticity) Laplacians acting on the electric potential. This becomes problematic when the resistivity is very small. Even in the electrostatic collisional regime found in the plasma edge, electron inertia and electromagnetic effects play a substantial role, especially as electron inertia replaces resistivity as it approaches zero.

As the plasma approaches the L-H transition, electromagnetic effects become increasingly important. The H-mode is characterized by a suppression of cross-field transport due to "ExB" drifts, which are partially replaced by electromagnetic transport. Significant magnetic reconnection processes lead to important transport of plasma particles from the hot core to the cold edge, with radial fluxes still below "ExB" advection, but non-negligible in understanding the overall plasma behavior.

This thesis is dedicated to the implementation of an electromagnetic model within SOLEDGE3X, which includes magnetic induction in the parallel electric field, perturbations of the magnetic equilibrium (flutter), and a finite electron mass in Ohm's law. This development pursues several goals: first, it improves the accuracy of the physical model; second, it enhances numerical robustness by mitigating the poor matrix conditioning associated with low resistivity; and third, it extends the capabilities of SOLEDGE3X to study turbulence and transport in larger machines and for higher-power scenarios.

This thesis is structured in three parts. Chapter 1 of the first part presents the physics of particles in magnetized plasmas and the realization of tokamak configurations. Chapter 2 provides an overview of plasma descriptions, ranging from kinetic

to drift-reduced fluid models, along with a discussion on electromagnetic effects in edge plasma. The second part focuses on the new electromagnetic framework in SOLEDGE3X, covering the physical model in Chapter 3, details of the implementation in Chapter 4, and its verification and validation in Chapter 5. The final part examines electromagnetic effects in simulations of limited geometries in Chapter 6, and of the realistic diverted TCV geometry in Chapter 7. Chapter 8 shows how the new implementation can also be applied to transport simulations in non-axisymmetric magnetic configurations.

## **Part II.**

# **Description of Magnetized Plasmas in a Tokamak**

# 1. Tokamak Concept

## Chapter Summary

With a given initial velocity, charged particles travel along magnetic field lines on a circular trajectory with the Larmor radius  $\rho_L$  and cyclotron frequency  $\omega_B$ .

$$\rho_L = \frac{m\|\mathbf{v}_{\perp,0}\|}{qB} \quad \omega_B = \frac{qB}{m}$$

Any force perpendicular to the magnetic field causes particles to drift with the velocity  $\mathbf{v}_d = \frac{\mathbf{B} \times \mathbf{F}_\perp}{qB^2}$ . To control particle motion, tokamaks employ toroidal and poloidal magnetic fields  $B_\phi$  and  $B_p$  to shape a helical configuration around a torus. To compensate for plasma currents, the magnetohydrodynamic equilibrium causes the so-called Grad-Shafranov shift, which pushes the poloidal field outward. A low ratio between thermodynamic to magnetic pressure,  $\beta = \frac{neT}{B^2/2\mu_0}$ , is important to avoid plasma instabilities.

At scales beyond the Debye length  $\lambda_D = \sqrt{\frac{\epsilon_0 T_e}{n_e e^2}}$ , the plasma organizes itself in a state of quasi-neutrality. Collisions between particles cause momentum, energy and charge exchanges, leading to viscosity, heat diffusion and resistivity according to the Spitzer-Härm model:

$$v_{SH} \propto \frac{T_e^{5/2}}{Z^4 \ln \Lambda} \quad \kappa_{SH} \propto \frac{T_e^{5/2}}{Z \ln \Lambda} \quad \eta_{SH} \propto \frac{Z \ln \Lambda}{T_e^{3/2}}$$

At the sheath, where magnetic field lines intersect the tokamak wall, a net negative charge develops that attracts ions at high speeds. In divertors, the heat exhaust is concentrated on two thin target lines, and the width  $\lambda_q$  is critical for reactor designs.

Fusion reactions require extreme temperatures at about 15keV to happen. At such high temperatures, any matter transforms into an ionized state, called plasma, where electrons are dissociated from their atomic core. Charged particles are particularly responsive to magnetic fields, a property that will be used by tokamaks to confine the hot plasma and protect the physical walls of the device.

A deuterium plasma is an ionized gas comprising positively charged ions ( $D^+$ ) and negatively charged electrons ( $e^-$ ). Initially, both species exhibit independent dynamics. Despite having exactly opposite charges, ions are significantly heavier than electrons, with a mass ratio of  $m_i/m_e \approx 3.7 \cdot 10^3$ . Both ions and electrons can be described by their respective momenta and temperatures. In Sec. 1.1, we first describe their independent behavior in a magnetized environment, then how species interact in Sec. 1.2 and we finish with Sec. 1.3 about the importance of the Scrape-Off-Layer.

## 1.1. Particles in a magnetized plasma

This first section describes the fundamental working principle of plasma confined in a tokamaks. Before all, we must understand how charged particles behave when exposed to strong magnetic fields (in Sec. 1.1.1) and how they experience drifts in perpendicular direction (in Sec. 1.1.2). This knowledge allows us to design a magnetic "cage", in which particles are trapped, or confined (in Sec. 1.1.3). The governing equations of this magnetic configuration are given in Sec. 1.1.4 and Sec. 1.1.5 introduces and compares limited and diverted configurations.

### 1.1.1. Gyromotion of a single particle

To understand how charged plasma particles can be confined on a magnetic field line, we consider the simplest example of a single particle with charge  $q$  in a homogeneous, unidirectional magnetic field  $\mathbf{B}$  with directional unit vector  $\mathbf{b}$ . The amplitude of the magnetic field is then  $B$  such that  $\mathbf{B} = B\mathbf{b}$ . Solely the magnetic component of Lorentz's force acts on a particle with mass  $m$  and charge  $q$ , leading to the following equation for its velocity  $\mathbf{v}$ :

$$m \frac{d\mathbf{v}}{dt} = q\mathbf{v} \times \mathbf{B} \quad (1.1)$$

To solve this differential equation, it is convenient to decompose the velocity vector into a parallel component  $v_{\parallel} = \mathbf{v} \cdot \mathbf{b}$  and a perpendicular component  $\mathbf{v}_{\perp} = \mathbf{v} - v_{\parallel}\mathbf{b}$ . For a given initial velocity  $\mathbf{v}_0$ , the general solution of this system is:

$$\mathbf{v}(t) = v_{\parallel,0}\mathbf{b} + \mathbf{v}_{\perp,0} \cos(\omega_B t) + \mathbf{b} \times \mathbf{v}_{\perp,0} \sin(\omega_B t) \quad (1.2)$$

with  $\omega_B = \frac{qB}{m}$  being the cyclotron frequency. This implies that a charged particle circles around a magnetic field line while following it with its initial velocity. The opposite charges of ions and electrons result in them circling in different directions.

## 1. Tokamak Concept – 1.1. Particles in a magnetized plasma

The trajectory is qualitatively shown in Fig. 1.1. The radius of this gyromotion is called the Larmor radius  $\rho_L$ :

$$\rho_L = \frac{m\|\mathbf{v}_{\perp,0}\|}{qB} \quad (1.3)$$

Because of the high mass ratio, ions have a much larger Larmor radius than electrons. This gyromotion is the fundamental mechanism behind magnetic confinement.

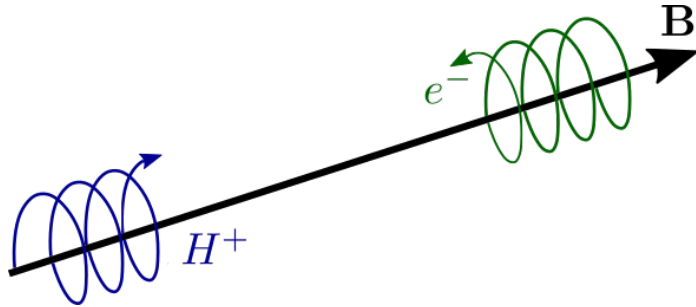


Figure 1.1.: Trajectory of a positively and a negatively charged particle along a homogeneous magnetic field line.

For a non-homogeneous field, Eq. 1.1 does not necessarily have a straightforward solution. To assume gyromotion as the fundamental dynamic for particles, the magnetic field must remain relatively constant along the helical path traced by the field lines. This requirement imposes a criterion on the Larmor radius, known as adiabatic theory:

$$\rho_L \ll \frac{B}{\|\nabla B\|} \quad (1.4)$$

### 1.1.2. Plasma drifts

Plasma drifts refer to the movement of charged particles under the influence of electric and magnetic fields. These drifts do not account for the primary motion along the guiding center, as described in Section 1.1.1. To study drift velocities, it is convenient to decompose every vector quantity into an average parallel component and a fluctuating perpendicular component, such that  $\mathbf{X} = X_{\parallel}\mathbf{b} + \mathbf{X}_{\perp}$ . We then express the Lorentz force equation as:

$$m\partial_t(v_{\parallel}\mathbf{b} + \mathbf{v}_{\perp}) = q [E_{\parallel}\mathbf{b} + \mathbf{E}_{\perp} + (v_{\parallel}\mathbf{b} + \mathbf{v}_{\perp}) \times \mathbf{B}] \quad (1.5)$$

Focusing on the particle's acceleration in the perpendicular direction, we derive the equation of motion:

$$m\partial_t\mathbf{v}_{\perp} = q [\mathbf{E}_{\perp} + (\mathbf{v}_{\perp} \times \mathbf{B})] \quad (1.6)$$

## 1. Tokamak Concept – 1.1. Particles in a magnetized plasma

In steady-state conditions, the electric force compensates the Lorentz force, leading to the electric drift  $\mathbf{v}_E$ , commonly referred to as the "E cross B" or simply "ExB" drift:

$$\mathbf{v}_E = \frac{\mathbf{E}_\perp \times \mathbf{B}}{B^2} \quad (1.7)$$

This velocity applies uniformly to all particles at all times, as it depends only on the electric and magnetic fields in place. Since neither the mass nor the charge contributes to  $\mathbf{v}_E$ , both electrons and ions move in the same direction at the same speed, and under the quasi-neutrality assumption, no current is generated.

Perpendicular pressure gradients also exert a force on particles. They result in the diamagnetic drift:

$$\mathbf{v}_* = \frac{\mathbf{B} \times \nabla_\perp p}{enZB^2} \quad (1.8)$$

For the next drift, we consider the gyromotion of a particle in a non-uniform magnetic field. Under the adiabatic condition from Eq. 1.4, the magnetic moment  $\mu$  of the gyrating particle is conserved along its trajectory:

$$\mu = \frac{m\|\mathbf{v}_\perp\|^2}{2B} \quad (1.9)$$

This moment leads to a potential  $U = -\mu B$ , which exerts a force on the particle:

$$F_{\nabla B} = -\nabla U = \frac{mv_\perp^2}{2B} \nabla B \quad (1.10)$$

This force acts in the direction of the gradient  $\nabla B$ , where the magnetic field strength is lower, allowing the particle to reduce its potential energy. This results in the "grad B" drift:

$$\mathbf{v}_{\nabla B} = \frac{mv_\perp^2}{2q} \frac{\mathbf{B} \times \nabla B}{B^3} \quad (1.11)$$

The helical configuration of a tokamak causes magnetic field lines to bend. To follow the direction of  $\mathbf{B}$ , the particle's trajectory is curved, and a centripetal force is exerted on the particle. With the curvature radius  $\mathbf{R}_c = \mathbf{b} \cdot \nabla \mathbf{b}$ , the force is given by:

$$\mathbf{F}_c = \frac{mv_\parallel^2}{R_c} \mathbf{R}_c = -mv_\parallel^2 \frac{\mathbf{B} \cdot \nabla \mathbf{B}}{B^2} \quad (1.12)$$

This force induces the "curvature" drift  $\mathbf{v}_c$ :

$$\mathbf{v}_c = \frac{mv_\parallel^2}{q} \frac{\mathbf{B} \times (\mathbf{B} \cdot \nabla \mathbf{B})}{B^4} \quad (1.13)$$

The polarization drift occurs if the electric field in the plasma varies with time.

## 1. Tokamak Concept – 1.1. Particles in a magnetized plasma

$$\mathbf{v}_p = \frac{m}{qB^2} \frac{d\mathbf{E}}{dt} \quad (1.14)$$

Note that the directions of "grad B", curvature or polarization drifts depend on the particle's charge, causing electrons and ions to move in opposite directions and generating an effective current. The total perpendicular velocity acting on a confined particle is the sum of all these drifts:

$$\mathbf{v}_d = \mathbf{v}_E + \mathbf{v}_* + \mathbf{v}_{\nabla B} + \mathbf{v}_c + \mathbf{v}_p \quad (1.15)$$

In fact, any force perpendicular to the magnetic field will cause a drift:

$$\mathbf{v}_F = \frac{\mathbf{B} \times \mathbf{F}_\perp}{qB^2} \quad (1.16)$$

All other eventual forces, such as magnetic or gravitational forces, play a subordinate role in the plasma edge and are usually not considered in fluid models. Drift velocities are always orientated in perpendicular direction to then magnetic fields. They do not interfere with (the averaged) parallel fluxes, at a magnitude of  $v_{th}$ , and are primarily responsible for cross-field fluxes.

### 1.1.3. Tokamak configuration

Maxwell's law stipulates that the magnetic field must be divergence-free,  $\nabla \cdot \mathbf{B} = 0$ . Since constructing an infinitely long machine is impractical, particle confinement requires that a given field line be closed, meaning that following its path would return one to the initial position. This necessitates some bending of the magnetic field lines. The fundamental principle of a tokamak lies in its magnetic configuration, which is designed to confine hot plasma within a toroidal chamber. This configuration comprises two primary magnetic field components: the toroidal field  $B_\phi$  and the poloidal field  $B_p$ . Coils encircling the torus generate the toroidal field, which runs parallel to the circular path of the tokamak and serves to confine the plasma. A strong current passing through the plasma itself induces the poloidal field. The combination of these fields creates a twisted, helical magnetic field structure, as shown in Fig. 1.2, that stabilizes the plasma and helps maintain its shape and position within the tokamak.

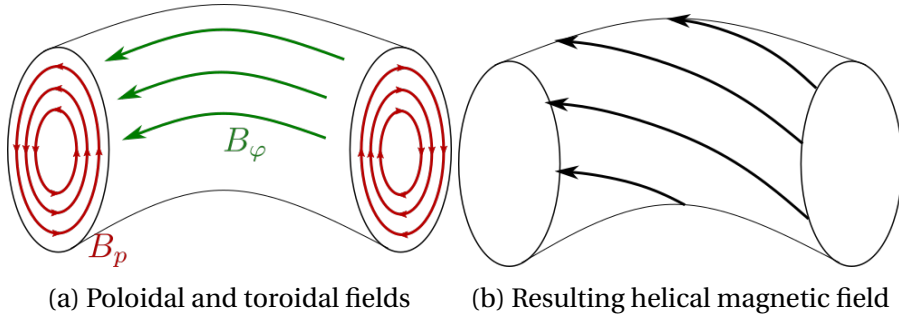


Figure 1.2.: Simplified scheme of the magnetic field components on a flux surface.

The helical configuration of a magnetic field line in a tokamak ensures that tracing its path remains within the same toroidal surface, ultimately returning to the initial point and forming a closed field line. The ensemble of all such field lines constitutes what is termed a "closed magnetic flux surface." These flux surfaces are radially concentric, and the principle of magnetic confinement is to trap plasma particles within these flux surfaces.

At first glance, the toroidal field appears sufficient to close magnetic field lines. However, plasma drifts inevitably add a dynamic perpendicular to the motion parallel to the magnetic field. Internal and external perturbations can cause twisting of the magnetic field lines, potentially leading to disruptions and total loss of plasma confinement. This phenomenon is known as kink instabilities. To suppress them, the poloidal field introduces magnetic shear to the configuration, with field lines circling around the minor radius of the torus. The ratio of toroidal to poloidal rotations of the field lines is known as the safety factor  $q = \frac{aB_\phi}{RB_p}$ . In a cylindrical approximation, the Kruskal-Shafranov limit [55, 86] states that kink instabilities are suppressed for  $q > 1$ . However, the safety factor cannot be too large either, as other instabilities such as tearing [31] or resistive wall [30] modes might appear and deteriorate plasma confinement.

### 1.1.4. Grad-Shafranov equilibrium

How can the magnetic configuration be described in a more mathematical way? The magnetic configuration of a tokamak can be described mathematically in cylindrical coordinates  $(R, Z, \varphi)$  with the corresponding basis vectors  $[\mathbf{e}_R, \mathbf{e}_Z, \mathbf{e}_\varphi]$ . The magnetic field consists of two main components: the poloidal field  $\mathbf{B}_p$ , which lies in the  $(R, Z)$  plane (referred to as the "poloidal plane"), and the toroidal field  $\mathbf{B}_\varphi$ , which is aligned along the  $\varphi$ -direction.

Each magnetic field  $\mathbf{B}$  is associated with a vector potential  $\mathbf{A}$  such that:

$$\nabla \times \mathbf{A} = \mathbf{B} \quad (1.17)$$

Assuming axisymmetry, gradients along the  $\varphi$ -direction vanish. Let  $\mathbf{A} = A_R \mathbf{e}_R +$

## 1. Tokamak Concept – 1.1. Particles in a magnetized plasma

$A_Z \mathbf{e}_Z + A_\varphi \mathbf{e}_\varphi$  represent the three components of the vector potential. The magnetic field can then be expressed as:

$$\mathbf{B} = \left( \frac{1}{R} \frac{\partial(RA_\varphi)}{\partial Z} \right) \mathbf{e}_R - \left( \frac{1}{R} \frac{\partial(RA_\varphi)}{\partial R} \right) \mathbf{e}_Z + \left( \frac{\partial A_Z}{\partial R} - \frac{\partial A_R}{\partial Z} \right) \mathbf{e}_\varphi \quad (1.18)$$

Introducing the poloidal flux function  $\Psi = -RA_\varphi$ , which shapes  $\mathbf{B}_p$ , and the toroidal field function  $F = RB_\varphi$ , the magnetic field components can be written as:

$$\mathbf{B} = \underbrace{\nabla\Psi \times \nabla\varphi}_{\mathbf{B}_p} + \underbrace{F\nabla\varphi}_{\mathbf{B}_\varphi} \quad (1.19)$$

In a tokamak, the plasma is not uniform, leading to a pressure gradient from the colder edge to the hotter core. In a stationary plasma that has reached magnetohydrodynamic (MHD) equilibrium, the magnetic and pressure forces must balance, which is described by the force balance equation:

$$\nabla p = \mathbf{j} \times \mathbf{B} \quad (1.20)$$

Because of the cross-product,  $\nabla p$  is always perpendicular to  $\mathbf{B}$ , implying that  $p$  must be constant along a field line. Under the assumption of axisymmetry,  $\partial_\varphi p = 0$ , meaning that the toroidal component of the magnetic force must be zero. Consequently, only the poloidal field  $\mathbf{B}_p$  responds to a pressure gradient. Since the pressure  $p(\Psi)$  is both axisymmetric and field-aligned, it can only be a function of the poloidal flux  $\Psi$ . The toroidal component of the current density can be expressed as:

$$j_\varphi = R \frac{dp}{d\Psi} + \frac{F}{\mu_0 R} \frac{dF}{d\Psi} \quad (1.21)$$

Ampère's law relates the current density  $\mathbf{j}$  to the magnetic field  $\mathbf{B}$ , with the vacuum permeability  $\mu_0$ :

$$\mu_0 \mathbf{j} = \nabla \times \mathbf{B} \quad (1.22)$$

This gives an alternative expression for the toroidal current:

$$j_\varphi = \frac{1}{\mu_0} \left[ \partial_R \left( \frac{1}{R} \partial_R \Psi \right) + \frac{1}{R} \partial_Z^2 \Psi \right] \quad (1.23)$$

By equating both expressions for  $j_\varphi$ , we arrive at the Grad-Shafranov equation [35, 87] for the poloidal flux:

$$\Delta^* \Psi = R \partial_R \left( \frac{1}{R} \partial_R \Psi \right) + \partial_Z^2 \Psi = -\mu_0 R^2 \frac{dp}{d\Psi} - \mu_0 F \frac{dF}{d\Psi} \quad (1.24)$$

Here we introduced the Shafranov operator  $\Delta^*$ . This equation is a second-order non-linear partial differential equation. The procedure outlined in Appendix A.2 solves Eq. 1.24 iteratively using a Newton-Krylov method. A typical solution for  $\Psi$  is illustrated in Fig. 1.3.

## 1. Tokamak Concept – 1.1. Particles in a magnetized plasma

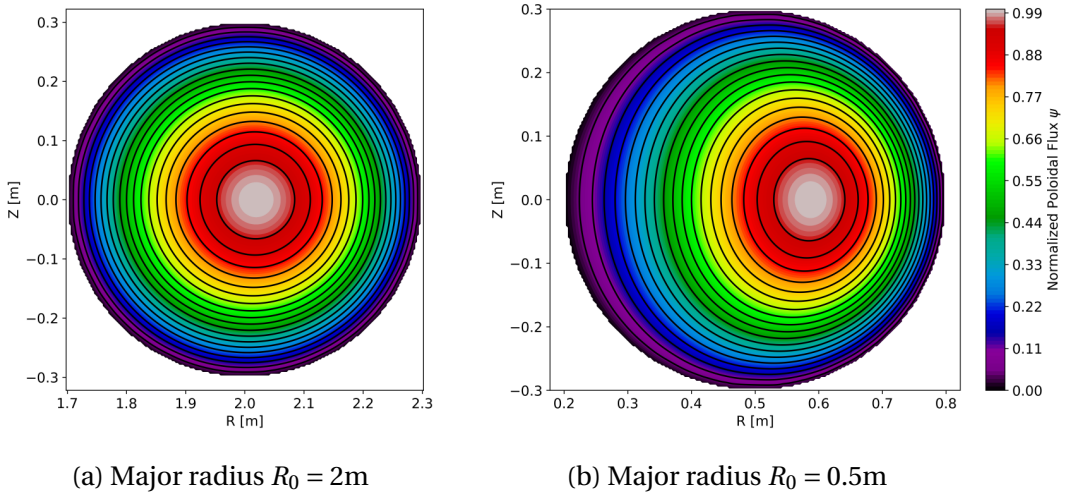


Figure 1.3.: Solution of the Grad-Shafranov equation on a circular cross-section with minor radius  $a = 0.3 \text{ m}$ . A Cartesian mesh with  $N = 200$  equidistant discretization points is used for the  $R$  and  $Z$  coordinates. The flux  $\Psi$  is forced to 0 at the boundary. The toroidal magnetic field is given by  $B_\varphi = B_0 R_0 / R$  with  $B_0 = 1\text{T}$ . The pressure follows an exponential distribution  $p(\Psi) = p_0(e^{-\Psi} - 1)$  with  $p_0 = 1 \text{ MPa}$ .

The plasma pressure causes the magnetic axis to shift outward in a phenomenon known as the Grad-Shafranov shift. The radial displacement from the centerline of the torus can be approximated by:

$$\Delta \approx \frac{2\mu_0 p}{B_p} \frac{a^2}{R_0} \quad (1.25)$$

The two scenarios presented in Fig. 1.3 differ by their major radius. As the Grad-Shafranov shift is inversely proportional to  $R_0$ , we expect that the larger curvature in the case 1.3b  $R_0 = 0.5\text{m}$  induces a larger shift, which is precisely what is observed.

An important metric in this context is the ratio  $\beta$  of plasma pressure over magnetic pressure.

$$\beta = \frac{p}{p_{mag}} = \frac{n e T}{B^2 / 2\mu_0} \quad (1.26)$$

There is a concurrent dynamic between thermodynamic and magnetic pressures: the former exerts an expansive force on the plasma, while the latter seeks to confine the plasma particles within their magnetic flux surfaces. A lower value of  $\beta$  is generally desired for a more effective plasma confinement, but requires strong magnetic fields. However, generating such intense magnetic fields entails considerable costs and technical challenges.  $\beta$  typically takes values between 1% and 5% in present large tokamaks.

## 1. Tokamak Concept – 1.1. Particles in a magnetized plasma

It is possible to distinguish between two operational regimes: L-mode and H-mode. The (L)ow-confinement mode is the standard operational mode. The plasma loses much of its energy to the wall with a consequent short confinement time. In 1982, the (H)igh-confinement mode was first observed on ASDEX in Germany and subsequently thoroughly investigated[99]. Its key feature is a strong reduction of turbulence around the separatrix, which reduces particle transport from the core to the SOL. As a consequence, temperature and density gradients steepen, forming a "pedestal" and creating a transport barrier.

### 1.1.5. Realisation of magnetic configurations

The magnetic tokamak configuration in a tokamak is controlled by a set of coils. An example of the technical realisation in the ITER tokamak is shown in Fig. 1.4. The fundamental configuration discussed before, is created by the toroidal field coils encircling the plasma chamber, appear in orange on the scheme. As it from the name, they drive the toroidal magnetic field  $B_\varphi$ . The poloidal field is driven by a strong toroidal current, itself induced by the central solenoid (central column with yellow ends).

They are completed by poloidal field coils (light purple), placed outside the main plasma chamber and distributed along the height of the tokamak. They generate a poloidal magnetic field that wraps around the plasma with the minor radius, perpendicular to the toroidal field. By adjusting the current, it is possible to control the vertical position, elongation, and triangularity of the plasma. For example, increasing the current in certain poloidal coils can elongate the plasma, giving it an oval cross-section, or induce triangularity by pulling the plasma boundary inward at the top and bottom.

## 1. Tokamak Concept – 1.1. Particles in a magnetized plasma

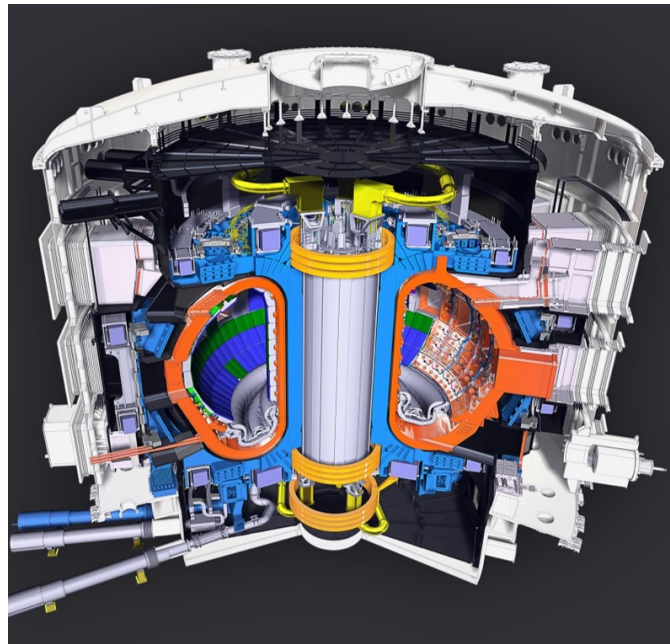


Figure 1.4.: Cutaway of the ITER tokamak (source: ITER Organization)

The limited configuration is one of the simpler magnetic configurations in a tokamak. In this setup, the plasma is in direct contact with material components which act as a limiter (see Fig. 1.5a). It effectively splits the domain in a confined core region with closed field lines and the Scrape-Off-Layer (SOL), that extends to the wall and where field lines are open, e.g. they cross the wall. The confined plasma boundary is given by the last closed flux surface, tangential to the wall in one point. Such a configuration suffers from significant power loads on the limiters, resulting in high erosion rates and potential contamination of the plasma with impurities. The confinement is generally lower in this configuration.

A diverted configuration, as depicted in Fig. 1.5b, improves the situation by a lot. The poloidal field coils shape the magnetic field lines in a fashion that they do not intersect with solid surfaces within the main plasma chamber but are instead directed to a separate region called the divertor. The last closed flux surface is then called "separatrix" and never touches the tokamak wall. The poloidal magnetic field contains now a singularity, the "X-point", and the area where the divertor plate intercepts the continuation of the separatrix is called the "target line". The divertor handles the exhaust of heat and particles from the plasma and this configuration tends to improve overall plasma confinement and reduce impurity levels.

## 1. Tokamak Concept – 1.2. Interaction between particles

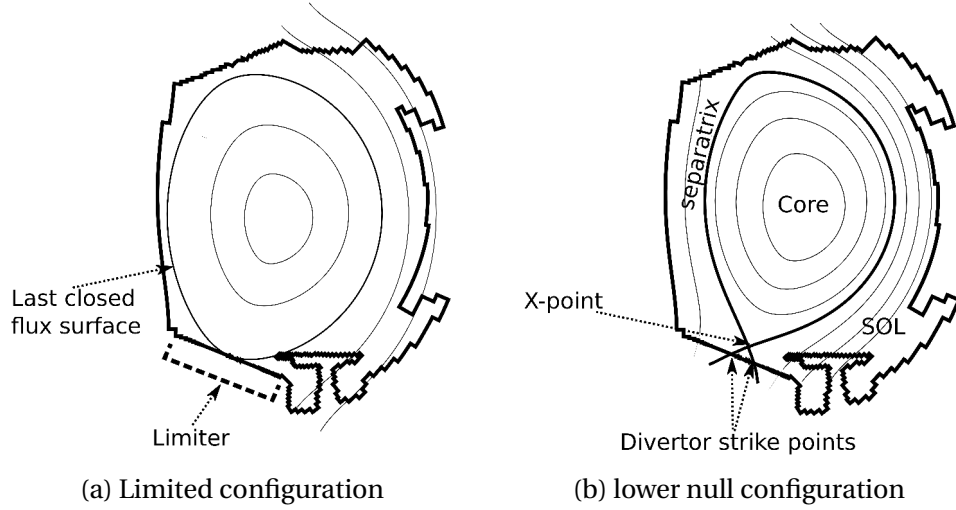


Figure 1.5.: Comparison of the limited and diverted configuration on a WEST geometry.

More exotic configurations are also feasible. In the double-null configuration, there are two divertor regions, typically located above and below the main plasma body. It splits heat loads on both divertor targets and can improve symmetry in power and particle exhaust. This symmetry helps in balancing the plasma dynamics and stabilizing the plasma, particularly with respect to vertical displacement events (VDEs), which are large-scale instabilities that can occur in tokamaks. Similarly, the X-point can be a higher-order singularity and split in more than four branches, spreading the heat load in several branches[81]. Such "snowflake" divertors can be achieved with an additional set of poloidal field coils in proximity to the divertor. Such configurations are still subject to active research in the perspective to optimize the plasma confinement and better control the heat exhaust.

Another important parameter of the magnetic configuration is its triangularity. It refers to the shaping of the plasma cross-section, where the plasma boundary is not circular but has an elongated shape with triangular indentations. The degree of triangularity  $\delta$  measures the extent of the indentation relative to the plasma's minor radius. High triangularity configurations can enhance plasma stability and confinement, in particular in the edge region, by allowing for higher pressure gradients.

## 1.2. Interaction between particles

So far we have seen how particles are confined in magnetic field lines. It gives only a partial picture of the physical processes that occur in a tokamak. A plasma contains positively and negatively charged particles at high energetic levels and they will inevitably interact between themselves. In Sec. 1.2.1 we look at how electrons and ions organize to form a state of quasi-neutrality, in Sec. 1.2.2 we dive into the mechanisms

that drive particle collisions and in Sec. 1.2.3 we conclude how collisions translate into resistive effects.

### 1.2.1. Debye shielding

Debye shielding refers to the macroscopic phenomenon that electric fields naturally dissipate in a plasma at rest. When a charged particle is introduced into a plasma, electrons, being lighter and more responsive than ions, quickly redistribute themselves around the introduced charge. There is then a localized region of increased electron density that counteracts the introduced electric field. The characteristic length over which this electric field is significantly attenuated is known as the Debye length  $\lambda_D$ :

$$\lambda_D = \sqrt{\frac{\epsilon_0 T_e}{n_e e^2}} \quad (1.27)$$

The Coulomb potential around a point charge  $Q$  exponentially decreases for distances beyond the Debye length:

$$\Phi(r) = \frac{Q}{4\pi\epsilon_0 r} e^{-r/\lambda_D} \quad (1.28)$$

It effectively means that at scales larger than  $\lambda_D$ , the plasma can be considered quasi-neutral, where the electron density compensates the charge of all present ions.

$$n_e = \sum_i q_i n_i \quad (1.29)$$

### 1.2.2. Particle collisions

At scales below the Debye length, the Coulomb force

$$\mathbf{F}_C = \frac{q_1 q_2}{4\pi\epsilon_0} \frac{\mathbf{r}}{\|\mathbf{r}\|^3} \quad (1.30)$$

drives collisions between two particles with charges  $q_1$  and  $q_2$  at a distance  $\mathbf{r} = \mathbf{r}_2 - \mathbf{r}_1$ , where  $\epsilon_0$  is the vacuum permittivity. By Newton's first and third laws of motion, this force defines the acceleration of each particle  $m_{1/2} \frac{d^2 \mathbf{r}_{1,2}}{dt^2} = \mathbf{F}_{12/21}$  and acts in opposite directions  $\mathbf{F}_{12} = -\mathbf{F}_{21}$  for the respective particles.

Following the derivation in Chapter 3 of Hutchinson *et al.*[50], we can combine the two equations of motion to express the dynamics of a single particle (projectile) with position  $\mathbf{r}$  and reduced mass  $m_r = \frac{m_1 m_2}{m_1 + m_2}$ , that collides with a stationary second particle (target) at the origin. This description corresponds to a reference frame attached to the common center of mass. For an initial velocity  $\mathbf{v}_r$ , the projectile will be deviated by the collision as represented in Fig. 1.6.

## 1. Tokamak Concept – 1.2. Interaction between particles

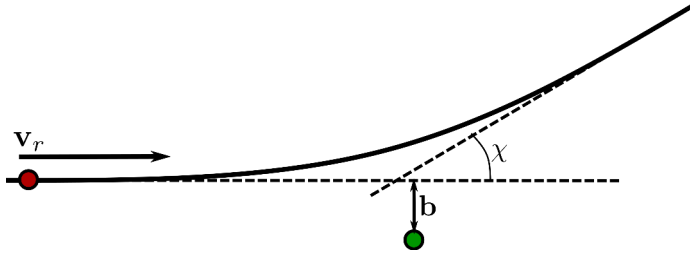


Figure 1.6.: Trajectory of the projectile particle (red) colliding with the target particle (green). The vector  $\mathbf{b}$  denotes the impact factor and  $\chi$  is the deflection angle caused by the collision.

To conserve angular momentum, the deflection of the projectile depends on the impact factor or the distance  $b = \|\mathbf{b}\|$  of the initial trajectory to the target. Let

$$b_{90} = \frac{q_1 q_2}{4\pi\epsilon_0} \frac{1}{m_r \|\mathbf{v}_r\|^2} \quad (1.31)$$

be the impact factor at which the projectile is deflected by a  $90^\circ$  angle. We can then express the deflection angle  $\chi$  at a given  $b$ :

$$\chi = \tan^{-1} \frac{b_{90}}{b} \quad (1.32)$$

This angle represents the deflection of the particle relative to the common center of mass. If we now consider two individual particles with finite mass, where the projectile approaches a stationary target with velocity  $\mathbf{v}_1 = (v_1, 0)^T$ , the deflection observed in an external frame is approximately  $\chi_1 \approx \frac{m_2}{m_1 + m_2} \chi$  (using the small angle approximation). To conserve momentum in the initial direction, the target also starts moving. The projectile exits the collision with:

$$\mathbf{v}'_1 = \left( \frac{\frac{m_1 v_1}{m_1 + m_2} + \frac{m_2 v_1}{m_1 + m_2} \cos \chi}{\frac{m_2 v_1}{m_1 + m_2} \sin \chi} \right) \quad (1.33)$$

At each collision, kinetic energy is transferred, and the projectile loses:

$$\begin{aligned} \Delta K &= K - K' = \frac{1}{2} m_1 \|\mathbf{v}_1\|^2 - \frac{1}{2} m_1 \|\mathbf{v}'_1\|^2 \\ &= \frac{2m_1^2 m_2}{(m_1 + m_2)^2} v_1^2 \sin^2 \frac{\chi}{2} \\ &\approx \frac{2m_1^2 m_2}{(m_1 + m_2)^2} v_1^2 \left( \frac{b_{90}}{b} \right)^2 \end{aligned} \quad (1.34)$$

where the last line uses the small angle approximation  $\chi \ll 1$ .

In practice, we do not want to study every collision but are interested in the total number of collisions a particle experiences over a given length when traversing a medium with density  $n$ . For that, we consider all collisions with particles at an impact

## 1. Tokamak Concept – 1.2. Interaction between particles

factor between  $b$  and  $b + db$  over a distance  $dx$  (see Fig. 1.7). This means we look at the volume  $V = 2\pi bdbdx$  in which we count a total of  $nV$  collisions.

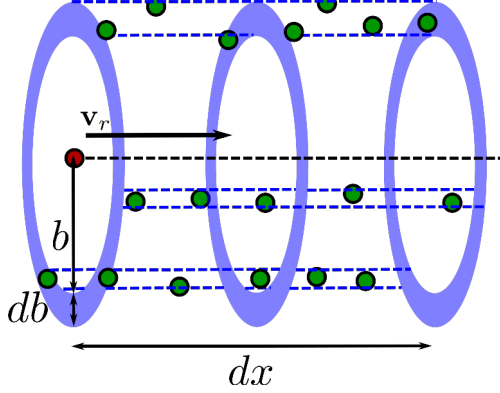


Figure 1.7.: Volume for given  $db$  and  $dx$  in which collisions on the projectile are considered.

Using Eq. 1.34 for the energy loss at each collision, we can estimate the energy our projectile loses after all collisions with the targets in the volume:

$$\Delta_V K = \frac{2m_1^2 m_2}{(m_1 + m_2)^2} v_1^2 \left( \frac{b_{90}}{b} \right)^2 n 2\pi bdbdx \quad (1.35)$$

The stopping power  $\frac{dK}{dx}$  describes the rate of energy loss per unit path length. It requires integrating over all possible impact factors  $b$ :

$$\frac{dK}{dx} = \frac{2m_1^2 m_2}{(m_1 + m_2)^2} v_1^2 n 2\pi b_{90}^2 \int_{b_{min}}^{b_{max}} \frac{1}{b} db \quad (1.36)$$

This integral diverges in both limits  $b_{min} \rightarrow 0$  and  $b_{max} \rightarrow \infty$ . We need to define cut-off values:

- $b_{min} = b_{90}$  because the small angle approximation in Eq. 1.34 implies that  $b > b_{90}$
- $b_{max} = \lambda_D$  because the Coulomb potential from Eq. 1.28 vanishes quickly at distances beyond the Debye length and so does the effective Coulomb force  $\mathbf{F}_C$

With these bounds, we evaluate the integral and define the Coulomb logarithm:

$$\ln \Lambda = \int_{b_{90}}^{\lambda_D} \frac{1}{b} db = \ln \left( \sqrt{\frac{\epsilon_0 T_e}{n_e e^2}} \right) - \ln \left( \frac{q_1 q_2}{4\pi \epsilon_0 m_r \|\mathbf{v}_r\|^2} \right) \quad (1.37)$$

For ion-ion collisions, masses  $m_1 = m_2$  and charges  $q_1 = q_2$  are equal. The collision frequency  $\omega_c$  describes at which rate a particle loses energy through collisions relative

## 1. Tokamak Concept – 1.2. Interaction between particles

to its total energy. The power loss is proportional to the stopping power with the particle velocity  $\frac{dK}{dt} = v \frac{dK}{dx}$ . We can then relate  $\omega_c$  to the stopping power:

$$\omega_c = \frac{v}{K} \frac{dK}{dx} \quad (1.38)$$

If we now inject Eqs. 1.32, 1.36 and 1.37 we obtain following expression for  $\omega_c$ :

$$\omega_c = \frac{q^4 n}{16\pi\epsilon_0^2 \sqrt{2m} K^{3/2}} \ln \Lambda \quad (1.39)$$

Assuming that the kinetic energy follows directly the plasma temperature with the relation  $K = 3/2T$ , we can express the characteristic collision time  $\tau_c$  and mean free path  $\lambda_c$ :

$$\tau_c = \frac{1}{\omega_c} = \frac{52\sqrt{3}\pi\epsilon_0^2\sqrt{m}}{q^4 \ln \Lambda} \frac{T^{3/2}}{n} \quad (1.40)$$

$$\lambda_c = \frac{v}{\omega_c} = \frac{32\sqrt{3/2}\pi\epsilon_0^2}{q^4 \ln \Lambda} \frac{T^2}{n} \quad (1.41)$$

It is worth noting that  $\tau_c$  is proportional to  $T^{3/2}/n$  and  $\lambda_c$  to  $T^2/n$  as all other terms are near-constant for a given ion in a tokamak.

### 1.2.3. Macroscopic effects of plasma collisions

As particles collide, energy is transferred from faster-moving to slower-moving particles, which, at a macroscopic scale, corresponds to heat conduction. Spitzer and Härm developed a model for plasmas in a near-equilibrium state[91], where deviations from the Maxwellian particle distribution due to the temperature gradient is small. The heat flux is then inversely proportional to the temperature gradient:

$$q = -\kappa_{SH} \nabla T \quad (1.42)$$

In a weakly collisional regime, the thermal conductivity  $\kappa_{SH}$  then corresponds to the rate at which energy is transported and is proportional to its speed  $v_{th}$  and the distance transported before the next collision  $\lambda_c$ . From the previous discussion on collisions,  $\kappa_{SH}$  then depends on the electron temperature  $T_e$  taken to the exponent 5/2:

$$\kappa_{SH} \propto \frac{T_e^{5/2}}{Z \ln \Lambda} \quad (1.43)$$

In a similar fashion, weak collisionality results in viscous effects. Alike energy, momentum is transferred from fast to slow particles, whereby velocity gradients are reduced over time. The particle flow is overall smoothed and becomes more uniform. The resultant viscous force

$$F = \nu_{SH} \nabla v \quad (1.44)$$

depends on the velocity gradient. The same reasoning as for the conductivity holds for the viscosity and we can express:

$$\nu_{SH} \propto \frac{T_e^{5/2}}{Z^4 \ln \Lambda} \quad (1.45)$$

Finally, collisions scatter electrons, with the effect to impend the current flow. This translates into electric resistivity  $\eta_{SH}$ , which is directly proportional to the collision frequency  $\omega_c$ . We then have:

$$\eta_{SH} \propto \frac{Z \ln \Lambda}{T_e^{3/2}} \quad (1.46)$$

Plasma resistivity is essential to understand current flow and Ohmic heating. As the plasma heats up, collisions are less frequent, and it becomes a more efficient conductor. Characteristic times for heat conductivity and resistivity are of the order of the electron-ion collision time  $\tau_c$  at around  $10^{-5}$ s while viscosity occur on the the much slower scale of the ion-ion collision time, which reaches up to a few milliseconds.

## 1.3. Scrape-Off-Layer

As presented in Sec. 1.1.5, the magnetic configuration in tokamaks can be split in two main regions: the core with closed magnetic field lines and the the scrape-off-layer (SOL) with open field lines. The properties of the latter are important to describe the plasma and to design a nuclear fusion device. Where magnetic field lines penetrate the material wall, the sheath, described in Sec. 1.3.1, strongly alters the physical properties of the plasma. It is followed by a discussion in Sec. 1.3.2 on the particle and heat fluxes at the wall and an introduction to the impact of SOL physics on plasma confinement.

### 1.3.1. Fundamental sheath physics

The SOL is characterized by open flux surfaces and where magnetic field lines cross the wall, the quasi-neutrality assumption from Sec. 1.2.1 does not hold anymore. The much lighter electrons travel much faster towards the wall (about  $\sqrt{m_i/m_e}$  faster than ions), creating a net negative charge in the direct proximity to the wall. It is not until a few Debye lengths  $\lambda_D$  before shielding restores known plasma conditions forming a region known as "electrostatic sheath". The negative charge attracts ions and repulses electrons, and we can assume that the electron density decreases exponentially approaching the wall. This eventually leads to the Bohm criterion[75], which states that at the sheath entrance the ion speed must be equal or larger than the sound speed of the plasma.

$$v_{se} \geq c_s = \sqrt{\frac{T_i + T_e}{m_i}} \quad (1.47)$$

From there, it is possible to calculate a sheath particle flux:

$$\gamma_{se} = n v_{se} \quad (1.48)$$

and a heat flux:

$$q_{se} = \gamma n T \gamma_{se} \quad (1.49)$$

with the sheath transmission coefficient  $\gamma$ . As the sheath is not collisional, these coefficients have to be determined from kinetic theory[92]. For hydrogen plasma, it is common to take the values  $\gamma_i = 2.5$  for ions and  $\gamma_e = 4.5$  for electrons.

### 1.3.2. Problematic of heat exhaust

An important part of the heat produced in a tokamak, whether it originates from external heating or from the fusion reaction, is evacuated by hot plasma particles. Cross-field transport allows confined particles from the hot core to cross the separatrix. As they enter the SOL, they follow the magnetic field lines until they impact the divertor on the thin target band. This region is extremely critical as large amounts of power are directed on a fairly small area. It is projected for ITER that heat loads at the targets are very close to material limits[39]. The peak heat flux  $q_{peak}$  could reach values over  $10\text{MW/m}^2$ . For a safe tokamak operation, it is essential to well understand and predict heat fluxes on the strike points. An important metric to take into the consideration is the heat flux o power fall-off width  $\lambda_q$ . It describes the spread of the heat flux on the divertor targets, and a larger value allows to spread the power exhaust on a larger area. It allows to describe the heat flux at a distance  $r$  from the target:

$$q(r) = q_{peak} e^{-\frac{r}{\lambda_q}} \quad (1.50)$$

Eich *et al.*[29] developed a scaling law to estimate  $\lambda_q$  for H-mode operation based on machine parameters. It states that the width is inversely proportional to the toroidal magnetic field  $\lambda_q \propto B_\phi^{-0.8}$ , meaning that larger machines with stronger coils will also have a thinner target line.

## 2. Description of Plasmas

### Chapter Summary

The kinetic description of plasmas applies the Lorentz equation to distribution functions  $f$  of particle densities and velocities with appropriate collision operators.

$$\frac{\partial f}{\partial t} + \mathbf{v} \cdot \nabla_{\mathbf{x}} f + \frac{\mathbf{F}}{m} \cdot \nabla_{\mathbf{v}} f = C_{\text{coll}} + C_{\text{other}}$$

From this, conservation equations for mean quantities can be derived for density, momentum, and energy, with fluid closures to avoid higher-order moments. These equations are coupled to Gauss's, Ampère's, and Faraday's laws for magnetism.

$$\begin{aligned} -\partial_t n + \nabla \cdot (n\mathbf{v}) &= S_n & mn(\partial_t \mathbf{v} + \mathbf{v} \cdot \nabla \mathbf{v}) &= -\nabla p + \mathbf{F} \\ \partial_t p + \mathbf{v} \cdot \nabla p + \frac{5}{3} p \nabla \cdot \mathbf{v} &= \frac{2}{3} \nabla \cdot \mathbf{Q} + S_E \\ \nabla \cdot \mathbf{B} &= 0 & \nabla \times \mathbf{B} &= \mu_0 \mathbf{j} & \partial_t \mathbf{B} &= \nabla \times (\mathbf{v} \times \mathbf{B} - \eta \mathbf{j}) + S_{\mathbf{B}} \end{aligned}$$

In drift-reduced fluid models, MHD equations are projected onto the parallel direction, where the drift-ordering assumption allows to incorporate plasma drifts in the advection terms and finite-Larmor radius effects. These models are well-suited to simulate drift-wave and interchange instabilities in the tokamak edge. Turbulence arises from electrostatic potential fluctuations to density fluctuations in the non-adiabatic electron response in Ohm's law. These instabilities are characterized by collisional (resistive), inertial, and inductive effects, with associated parameters:

$$C = \eta \left( \frac{qR}{L_{\perp}} \right)^2 \quad \mu_{eff} = \frac{m_e}{m_i} \left( \frac{qR}{L_{\perp}} \right)^2 \quad \beta_{eff} = \beta \left( \frac{qR}{L_{\perp}} \right)^2$$

The interplay between these parameters determines whether the turbulence is driven by collisional, electron inertial, or electromagnetic effects.

The difficulty in obtaining global experimental measurements in tokamaks requires complementary numerical simulations. Currently, these numerical data are essential to complement experimental measurements and support their interpretation. In the longer term, they will be used to make predictions and support the design of ITER experiments. Self-consistent simulations of the plasma edge are challenged by a complex geometry and the variety of involved scales. The magnetic equilibrium exhibits both open and closed magnetic field lines, breaking the toroidal symmetry. Turbulent fluctuations typically have sizes on the order of the ion gyroradius  $\rho_\alpha$  ( $\geq 0.4 \text{ mm}$ )<sup>[47]</sup> in the perpendicular direction to the magnetic field lines, and compete with phenomena occurring along them on the order of the parallel connection length  $\propto q_s R_0$  (where  $q_s$  is the safety factor, and  $R_0$  the tokamak major radius), which can extend up to 100 meters.

This chapter presents the different approaches to describe plasma self-consistently. In a first section 2.1, we explain the steps how the Lorentz force can be successively rewritten in a kinetic equation and in a conservation equations on mean plasma quantities. We extend the discussion in Sec. 2.2 to drift-reduced fluid models that are commonly used for turbulent plasma simulations of the tokamak edge. Finally, we analyze in Sec. 2.3.3 from a theoretical point of view the impact of electromagnetic effects on drift-wave turbulence in our models.

## 2.1. A hierarchy of models

Plasmas can be modeled using various sets of equations that trade off between accuracy and computational feasibility. Generally, more accurate models are prohibitively expensive and are beyond the capabilities of current high-performance computing (HPC) infrastructure when applied to large systems. Depending on the scientific objective, high-fidelity models will accurately capture physical processes while reduced models complement this with full-scale simulations at relevant time scales. In this chapter, we introduce the major approaches that are used nowadays, with a special care to highlight how they are connected and where they differ. The most comprehensive approach in Sec. 2.1.1 rely on plasma particles themselves or their statistical distribution. From there, the Chapman-Enskog expansion in Sec. 2.1.2 allows to express conservation equations on averaged plasma quantities and lay the foundations for fluid models. Finally, MHD models in Sec. 2.1.3 offer a framework to combine those conservation equations with the evolution of electromagnetic properties of the plasma.

### 2.1.1. Direct description of plasma particles

Particles are the foundation of the first set of models. They can either be solved individually as in Sec. 2.1.1.1 or represented by their distribution functions in the so-called kinetic models (Sec. 2.1.1.2).

### 2.1.1.1. Particle tracking

In the most general description, each particle in a tokamak—whether neutron, ion, atom, or electron—is represented individually with three degrees of freedom for both position  $\mathbf{x}$  and velocity  $\mathbf{v}$ . The system's dynamics are governed by the Lorentz force:

$$\frac{\partial \mathbf{v}}{\partial t} = \mathbf{F} = q\mathbf{E} + q\mathbf{v} \times \mathbf{B} \quad (2.1)$$

$$\frac{\partial \mathbf{x}}{\partial t} = \mathbf{v} \quad (2.2)$$

where  $\mathbf{E}$  is the electric field,  $\mathbf{B}$  the magnetic field, and  $q$  the charge of the particle. Given that a medium-sized tokamak like WEST contains approximately  $N_p \approx 10^{20}$  particles, each with six degrees of freedom, direct numerical simulation is infeasible. Computational effort can be reduced by using macro-particles, which represent many real particles. A prominent approach utilizing this concept is the particle-in-cell (PIC) method[100], where macro-particles evolve in pre-calculated fields on a mesh or interact directly with one another. PIC methods are employed to study phenomena such as collisions with neutral particles[5], plasma-wall interactions[54], or instabilities induced by fusion products[18].

### 2.1.1.2. Kinetic models

As a further abstraction, an ensemble of particles can be described statistically through a distribution function  $f(\mathbf{x}, \mathbf{v}, t)$ . This kinetic description replaces individual particles with a probability distribution, avoiding the need to calculate exact positions and velocities at each moment in time. The behavior of the distribution function is governed by the Boltzmann equation:

$$\frac{\partial f}{\partial t} + \mathbf{v} \cdot \nabla_{\mathbf{x}} f + \frac{\mathbf{F}}{m} \cdot \nabla_{\mathbf{v}} f = C_{\text{coll}} + C_{\text{other}} \quad (2.3)$$

where  $C_{\text{coll}}$  represents the collision operator, handling Coulomb collisions as introduced in Sec. 1.2.2, and  $C_{\text{other}}$  includes additional source terms. Substituting the force vector  $\mathbf{F}$  with the Lorentz force (Eq. 2.1) yields the Vlasov equation.

To achieve sufficient accuracy, approximately  $N_x = 10^9$  spatial discretization points and  $N_\sigma = 10^6$  points for the distribution function are required. Considering that both position and velocity have three components each, this results in  $6 \cdot 10^{15}$  degrees of freedom—significantly fewer than in the particle description.

Further simplification is achieved through the gyrokinetic approach. While particles in a plasma predominantly follow magnetic field lines, their motion forms a helical trajectory characterized by the Larmor frequency and radius:

$$\omega_L = \frac{eZB}{m} \quad l_L = \frac{mv_\perp}{eZB} \quad (2.4)$$

This allows the elimination of one degree of freedom in the distribution function, as the velocity can be described by its parallel component  $v_{\parallel}$  along the magnetic field line and its perpendicular component  $v_{\perp}$ . This simplification is valid only when the Larmor frequency and radius are much smaller than any characteristic frequency or length in the system, which is typically true in the core of the tokamak but not in the scrape-off layer (SOL), where the gyrokinetic approach is less suitable.

Gyrokinetic models are particularly useful to study transport barriers and turbulence driven by ion and electron temperature gradients (ITG/ETG) or trapped electron mode (TEM) instabilities and typically use full- $f$  turbulence models. The code GY-SELA[36, 37] follows a semi-Lagrangian method to study core turbulence, zonal flows and neoclassical transport and is capable of relatively long simulated plasma times. Plasma-wall interactions and kinetic neutrals make XGC[41] particularly well-suited for edge and SOL turbulence. It allowed for comprehensive divertor heat exhaust studies[13] and is capable of complex 3D magnetic configurations found in stellarators[16]. The Eulerian code GENE-X[34, 63] is ideal for full- $f$  electromagnetic simulations of turbulence at multiple scale in the core-edge region.

### 2.1.2. Three fluid moments of the kinetic equation

Deriving transport equations for plasma quantities analogous to the Navier-Stokes equations in classical fluid dynamics is highly desirable. Such an approach would enable the use of established computational fluid dynamics (CFD) methods for turbulence modeling, significantly reducing the number of degrees of freedom. Starting with the distribution function  $f$ , the  $k$ -th moment of the transport equation is obtained by applying the tensor product  $\mathbf{v} \otimes \dots$   $k$  times and then integrating over the velocity:

$$\mathcal{M}^k = \int_{\mathbf{v}} f \mathbf{v}^k d\mathbf{v}^3 \quad (2.5)$$

Substituting the kinetic equation 2.3 into this expression yields the following equation for the  $k$ -th moment:

$$\begin{aligned} \partial_t \int_{\mathbf{v}} f \mathbf{v}^k d\mathbf{v}^3 + \int_{\mathbf{v}} \mathbf{v}^k \mathbf{v} \cdot \nabla_{\mathbf{x}} f d\mathbf{v}^3 + \int_{\mathbf{v}} \mathbf{v}^k \frac{\mathbf{F}}{m} \cdot \nabla_{\mathbf{v}} f d\mathbf{v}^3 &= \int_{\mathbf{v}} \mathbf{v}^k C d\mathbf{v}^3 \\ \partial_t \mathcal{M}^k + \nabla_{\mathbf{x}} \cdot \mathcal{M}^{k+1} - \frac{k}{m} \mathbf{F} \otimes \mathcal{M}^{k-1} &= \int_{\mathbf{v}} \mathbf{v}^k C d\mathbf{v}^3 \end{aligned} \quad (2.6)$$

Expressing the  $k$ -th moment requires knowledge of the  $k-1$ -th and  $k+1$ -th moments. Consequently, a fully consistent plasma description would require infinitely many equations, which is impractical. Therefore, we typically consider only the first three moments, using fluid closures to compensate for the missing higher-order equations. These moments effectively allow us to replace a particle-based description with averaged quantities:

$$\text{Particle density: } \mathcal{M}^0 = n = \int_{\mathbf{v}} f d\mathbf{v}^3 \quad [\text{m}^{-3}] \quad (2.7)$$

$$\text{Momentum density: } \mathcal{M}^1 = \boldsymbol{\gamma} = n\mathbf{u} = \int_{\mathbf{v}} f \mathbf{v} d\mathbf{v}^3 \quad [\text{m}^{-2} \cdot \text{s}^{-1}] \quad (2.8)$$

$$\text{Pressure tensor: } m\mathcal{M}^2 = \boldsymbol{\Pi} = m \int_{\mathbf{v}} f \mathbf{v} \otimes \mathbf{v} d\mathbf{v}^3 \quad [\text{kg} \cdot \text{m}^{-1} \cdot \text{s}^{-2}] \quad (2.9)$$

where  $\mathbf{u}$  is the fluid velocity and  $m$  the particle mass. This framework sets the stage for deriving the three fundamental conservation equations for fluid models of plasmas.

### 2.1.2.1. Mass conservation ( $k = 0$ )

Starting from Eq. 2.3, the mass balance equation for the unknowns  $n$  and  $\mathbf{u}$  is derived as follows:

$$\partial_t n + \nabla \cdot (n\mathbf{u}) = S_n \quad (2.10)$$

This equation provides one relation but involves four unknowns, necessitating additional equations to fully describe the system. The term  $S_n$  accounts for particle sources arising from non-elastic collisions in  $C_{\text{other}}$ , such as ionization or recombination processes.

### 2.1.2.2. Momentum conservation ( $k = 1$ )

For the first moment equation, we multiply the Boltzmann equation 2.3 by  $\mathbf{v}$  and integrate over the velocity space, yielding:

$$\partial_t \left( \int_{\mathbf{v}} \mathbf{v} f d\mathbf{v} \right) + \int_{\mathbf{v}} \mathbf{v} \otimes \mathbf{v} \cdot \nabla_{\mathbf{x}} f d\mathbf{v} + \int_{\mathbf{v}} \mathbf{v} \frac{\mathbf{F}}{m} \cdot \nabla_{\mathbf{v}} f d\mathbf{v} = \int_{\mathbf{v}} C v d\mathbf{v} \quad (2.11)$$

To simplify the tensor product, we decompose the velocity  $\mathbf{v}$  into the fluid velocity  $\mathbf{u}$  and a new quantity  $\mathbf{w}$ , such that  $\mathbf{v} = \mathbf{u} + \mathbf{w}$ . We introduce the static pressure tensor:

$$\mathbf{P} = m \int_{\mathbf{w}} f \mathbf{w} \otimes \mathbf{w} d\mathbf{w} \quad (2.12)$$

The pressure tensor  $\boldsymbol{\Pi}$  can then be expressed as:

$$\boldsymbol{\Pi} = m \int_{\mathbf{w}} f \mathbf{u} \otimes \mathbf{u} d\mathbf{w} + m \int_{\mathbf{w}} f \mathbf{w} \otimes \mathbf{w} d\mathbf{w} = mn\mathbf{u} \otimes \mathbf{u} + \mathbf{P} \quad (2.13)$$

Substituting this into the first moment equation, we obtain the conservation equation for momentum:

$$m\partial_t(n\mathbf{u}) + m\nabla \cdot (n\mathbf{u} \otimes \mathbf{u} + \mathbf{P}) = enZ\mathbf{E} + enZ\mathbf{u} \times \mathbf{B} + S_u + R \quad (2.14)$$

Here,  $S_u$  represents the momentum source term, and  $R$  accounts for friction, both arising from  $C_{\text{coll}}$  and  $C_{\text{other}}$ .

### 2.1.2.3. Energy conservation ( $k = 2$ )

Finally, to solve for the static pressure tensor  $\mathbf{P}$ , we assume isotropic pressure in the plasma, simplifying the pressure tensor to a scalar pressure  $p$  such that  $\mathbf{P} = p\mathbf{I}$ . This reduces the nine unknowns in  $\mathbf{P}$  to a single scalar  $p$ . Given that  $p = nT$ , the second moment can be expressed as an energy conservation equation. The total energy density  $\varepsilon$  is the sum of kinetic and thermal energy in the plasma:

$$\varepsilon = \frac{3}{2}nT + \frac{1}{2}mn\|\mathbf{u}\|^2 \quad (2.15)$$

To derive a conservation equation for  $\varepsilon$ , we multiply Vlasov's equation 2.3 by the kinetic energy per unit mass:

$$\partial_t \left( \int_{\mathbf{v}} \frac{1}{2} u^2 f d\mathbf{v} \right) + \int_{\mathbf{v}} \frac{1}{2} u^2 \mathbf{v} \cdot \nabla_{\mathbf{x}} f d\mathbf{v} + \int_{\mathbf{v}} \frac{1}{2} u^2 \frac{\mathbf{F}}{m} \cdot \nabla_{\mathbf{v}} f d\mathbf{v} = \int_{\mathbf{v}} \frac{1}{2} u^2 C d\mathbf{v} \quad (2.16)$$

This simplifies to:

$$\partial_t \varepsilon + \nabla \cdot (\varepsilon \mathbf{u} + [n\mathbf{u} \otimes \mathbf{u} + \mathbf{P}] \cdot \mathbf{u} + \mathbf{q}) = enZ\mathbf{E} \cdot \mathbf{u} + Q + R_{\varepsilon} \quad (2.17)$$

The collisional heat flux  $\mathbf{q}$  arises from the fluid closure, replacing all higher-order moments. The term  $Q$  represents a collisional heat source, while  $R_{\varepsilon}$  accounts for sources associated with non-Coulombian collisions in  $C_{\text{other}}$ . Notably, the magnetic field term  $\mathbf{u} \times \mathbf{B}$  does not appear in the energy equation, as the torque  $\frac{1}{2}u^2\mathbf{u} \times \mathbf{B} \cdot \nabla_{\mathbf{v}} f$  does not perform work and therefore does not contribute to energy changes.

The three conservation equations for density  $n$ , momentum  $\gamma$ , and energy  $\varepsilon$  form the foundation of the SOLEDGE3X framework. The exact model will be given in Chap. 3.

### 2.1.3. MHD description of plasmas

In the magnetohydrodynamics (MHD) approach, the conservation equations are coupled to Maxwell's and Ohm's laws, introducing electromagnetic behavior into the system. Unlike earlier models, the magnetic equilibrium is not static; the electric and magnetic fields evolve over time. MHD models typically differentiate between ideal MHD and extended models that include resistive and two-fluid effects, which are essential for accurately describing tokamak plasmas. The ideal MHD model and its extension with tokamak-specific terms in Sec. 2.1.3.1 is the most accurate approach to simulate the electromagnetic intrications in plasmas. Fast wave dynamics represent a major restriction and reduced models in Sec. 2.1.3.2 are therefore much more widespread.

### 2.1.3.1. Extended MHD model

Many of the explanations in this section are based on the lecture notes by E. Franck[60]. The complete set of MHD equations is as follows:

$$\partial_t n + \nabla \cdot (n\mathbf{u}) = 0 \quad (2.18)$$

$$mn\partial_t \mathbf{u} + mn\mathbf{u} \cdot \nabla \mathbf{u} + \nabla p = \mathbf{j} \times \mathbf{B} \boxed{-\nabla \cdot \boldsymbol{\Pi}} \quad (2.19)$$

$$\frac{3}{2}\partial_t p_i + \frac{3}{2}\mathbf{u} \cdot \nabla p_i + \frac{5}{2}p_i \nabla \cdot \mathbf{u} = \boxed{-\nabla \cdot \mathbf{q}_i - \nabla \cdot (\boldsymbol{\Pi}_i : \nabla \mathbf{u})} \quad (2.20)$$

$$\frac{3}{2}\partial_t p_e + \frac{3}{2}\mathbf{u} \cdot \nabla p_e + \frac{5}{2}p_e \nabla \cdot \mathbf{u} = \boxed{-\nabla \cdot \mathbf{q}_e - \nabla \cdot (\boldsymbol{\Pi}_e : \nabla \mathbf{u}) + \eta \|\mathbf{j}\|^2 + \frac{3}{2}\mathbf{j} \cdot \mathcal{P}} \quad (2.21)$$

$$\partial_t \mathbf{B} = -\nabla \times \left( -\mathbf{u} \times \mathbf{B} \boxed{+ \eta \mathbf{j} - \mathcal{P} + \mathcal{H}} \right) \quad (2.22)$$

$$\nabla \cdot \mathbf{B} = 0 \quad (2.23)$$

$$\nabla \times \mathbf{B} = \mu_0 \mathbf{j} \quad (2.24)$$

Equations 2.18 through 2.24 are derived directly from the fluid moments described in Sec. 2.1.2, where the pressure replaces the energy and is solved for both ions and electrons. These equations are coupled with Ohm's law (Eq. 2.22) under the magnetostatic assumption, Gauss's law for magnetism (Eq. 2.23), and Ampère's law (Eq. 2.24). In ideal steady-state, we see that the momentum balance is dominated by the equilibrium between thermodynamic and magnetic forces  $\nabla p = \mathbf{j} \times \mathbf{B}$ . In combination with Ampère's law, all components are available to derive the Grad-Shafranov equation 1.24 as it has been done in Sec. 1.1.4.

The terms enclosed in boxes represent the additional terms required for extending the model from ideal MHD. These include viscous-resistive effects, as well as a pressure term  $\mathcal{P}$  and a Hall term  $\mathcal{H}$ . Without these boxed terms, the system describes the ideal MHD model. Linearizing the ideal MHD equations results in three types of waves:

- **Alfvén waves:** These incompressible waves cause the magnetic field lines to bend and propagate only in the parallel direction. In the low-beta limit, their propagation speed,  $v_A^2 = \frac{B^2}{mn\mu_0}$ , is much greater than the speed of sound in the plasma,  $c_s^2 = \frac{eT}{m}$ .
- **Slow magnetoacoustic waves:** These waves propagate only in the parallel direction, causing compression in the plasma without perturbing the magnetic field lines. Their propagation speed  $v_s$  is similar to the speed of sound.
- **Fast magnetoacoustic waves:** These waves can propagate in any direction and compress magnetic field lines. They have a propagation speed approximately given by  $v_f^2 = v_A^2 + c_s^2$ .

Fast waves, in particular, pose challenges for numerical modeling as they require very small timesteps and implicit methods to be accurately resolved. The full MHD model introduces two additional dispersive waves into the system.

### 2.1.3.2. Reduced MHD model

To eliminate the fast magnetoacoustic waves and to reduce the size of the system, physicists often resort to reduced MHD models. Instead of solving for all components of  $\mathbf{B}$ , we decompose the magnetic field into the poloidal flux  $\Psi$  and the toroidal field function  $F$  as in Eq. 1.19. The toroidal field  $B_\varphi$  and  $F$  are imposed, so we only remain with the unknown scalar  $\Psi$  to replace the three unknowns of  $\mathbf{B}$ . As a reminder from Sec. 1.1.4,  $\Psi$  is equivalent to the toroidal component  $A_\varphi$  of the magnetic vector potential and uniquely defines the poloidal field  $B_p$ . Consequently, Ampère's law 2.24 reduces to:

$$\mu_0 j_\varphi = \Delta^* \Psi = R^2 \nabla \cdot \left( \frac{1}{R^2} \nabla_p \Psi \right) \quad (2.25)$$

with the poloidal gradient  $\nabla_p$ .

In the second simplification for the reduced MHD model, the velocity vector is decomposed into a parallel and a perpendicular component. The projected fields are:

$$u_\perp = \mathbf{e}_\varphi \cdot \nabla \times (R^2 \mathbf{u}) \quad (2.26)$$

$$u_\parallel = \mathbf{B} \cdot \mathbf{u} \quad (2.27)$$

$$(2.28)$$

This projection is consequently applied to all terms in the momentum conservation equation 2.19, that can then be solved independently for both velocities. In addition to reducing the number of equations from three to two, it permits to split the slow magnetoacoustic waves, that propagate at sound speed in the parallel directions, from the much slower dynamics in the poloidal plane that consist of electric and diamagnetic drifts.

The JOREK code[48, 51] for example is a fully implicit simulation framework that includes several levels of MHD reduction. It works on diverted magnetic configuration and considers advanced SOL physics. It is mainly used to study the dynamics, cycles and control of edge-localized modes (ELMs), as well as disruptions in form of thermal and current quenches.

### 2.1.3.3. Fluid closures

We only considered MHD models up to the second moment. To maintain the validity of the model, we need additional closure terms in the momentum and energy equations. Braginskii[6] proposed a set of forces and heat fluxes that apply to the momentum and energy conservation equations. They originate the assumption of a weakly collisional plasma in line with the Spitzer-Härm model presented in Sec. 1.2.3. Because of the strong magnetic fields in a tokamak, collisional phenomena experience a strong

## 2. Description of Plasmas – 2.2. Drift-reduced models for plasma turbulence

anisotropy and it is appealing to split them in a parallel and perpendicular direction to the magnetic equilibrium. We can then define the pressure tensor and the viscous stress tensor:

$$\mathbf{P} = p_{\perp} \mathbf{I} + (p_{\parallel} - p_{\perp}) \mathbf{b} \mathbf{b} \quad (2.29)$$

$$\boldsymbol{\Pi} = \boldsymbol{\Pi}_{\parallel} + \boldsymbol{\Pi}_{\perp} = \eta_{\parallel} \nabla_{\parallel} \mathbf{v}_{\parallel} + \eta_{\perp} \nabla_{\perp} \mathbf{v}_{\perp} \quad (2.30)$$

The unit vector  $\mathbf{b}$  defines the direction of the magnetic field. Similarly, the heat flux is decomposed in its parallel and perpendicular components:

$$\mathbf{q} = q_{\parallel} \mathbf{b} + \mathbf{q}_{\perp} = -\kappa_{\parallel} \nabla_{\parallel} T - \kappa_{\perp} \nabla_{\perp} T \quad (2.31)$$

Braginskii only considered electrons and one type of ions, The work was extended by Zhdanov[109] to handle multi-species plasmas. Particle collisions between different species lead to a friction force, proportional to the velocity difference, and a thermal force along the temperature gradient. For a species  $\alpha$ , the contribution of all other species  $\beta$  to these forces is:

$$\mathbf{F}_{\alpha} = \underbrace{\sum_{\beta} -\omega_{\alpha\beta} m_{\alpha} n_{\alpha} (\mathbf{v}_{\alpha} - \mathbf{v}_{\beta})}_{\text{Friction}} - \underbrace{\frac{m_{\alpha} n_{\alpha}}{e Z_{\alpha}} \delta_{\alpha} \nabla T_{\alpha}}_{\text{Thermal}} \quad (2.32)$$

The coefficient  $\delta_{\alpha}$  describes the thermal diffusion of particles driven by the temperature gradient. For electron-ion collisions, the friction force corresponds to the electric to the current resistive. The force  $\mathbf{F}_{\alpha}$  needs to be included in the conservation equations in the closure. An instantaneous force balance on electrons, projected on the parallel direction, gives a first expression for the generalized Ohm's law in plasmas:

$$\eta_{\parallel} j_{\parallel} = E_{\parallel} + \frac{1}{n_e} \nabla p_e + 0.71 \nabla T_e \quad (2.33)$$

## 2.2. Drift-reduced models for plasma turbulence

Kinetic models based on the particle distribution function[23, 53] are still limited to fundamental studies because of their very high numerical cost in a (5) 6-dimensional phase space. Thus, when realistic configurations are considered, reduced-dimension (2D/3D) fluid models remain the only feasible option for studying transport and turbulence at the edge of the plasma, although they are only rigorously valid in collisional regimes. A wide range of models have been derived in the literature and implemented in state-of-the-art codes[27, 33, 93] (see also an exhaustive presentation in the recent review by Schwander *et al.*[82]). The basic assumption they share is that the turbulence is characteristically low frequency and long wavelength in nature, leading to a strong scale separation between the parallel and perpendicular directions to the magnetic field. Therefore, the plasma fluid motion perpendicular to the magnetic field can be described explicitly by the so-called velocity drifts given by the quasi-static

balance between Lorentz force, pressure gradient, and electromotive force due to magnetic and electric field inhomogeneities.

We first explain in Sec. 2.2.1 how drifts allow to formulate the drift-ordering assumption, which is at the root of fluid models. The section is concluded in 2.2.2 with an overview over the instabilities caught by the model.

### 2.2.1. Drift-ordering approximation

The separation of scales allows for fluid-drift models, where the parallel and perpendicular momentum equations are treated independently. Mikhailovskii and Tsypin[65] first described slow drift dynamics from a theoretical viewpoint in 1971 with  $\rho_L = 0$ . Hazeltine *et al.*[45] extended the framework to include a finite ion Larmor radius. We focus on low- $\beta$  collisional plasmas, typically found in the edge region of a tokamak. In such plasmas, we can define a characteristic length scale  $L_{\parallel}$  for parallel phenomena, which is on the order of the machine size (e.g., the major radius  $R$ ), where gradients in plasma fields such as density, temperature, or magnetic field strength are established. The perpendicular scale  $L_{\perp}$  is characteristic of cross-field structures. These scales define the parallel and perpendicular wave numbers  $k_{\parallel}$  and  $k_{\perp}$ . In the drift ordering, the following relationships hold[89]:

$$\beta = \frac{2\mu_0(p_e + p_i)}{B^2} \ll 1 \quad \frac{\rho_L}{L_{\perp}} \sim \frac{\lambda_c}{L_{\parallel}} \ll 1 \quad (2.34)$$

where  $\rho_L$  is the ion Larmor radius, and  $\lambda_c$  is the mean free path between collisions. The electric force is much weaker than the magnetic force. Similarly, characteristic plasma frequencies should be much lower than the ion cyclotron frequency, giving rise to the following ordering parameters:

$$\epsilon_E = \frac{mE}{eZB^2} \ll 1 \quad \epsilon_l = \frac{L_{\perp}}{L_{\parallel}} \ll 1 \quad \epsilon_t = \frac{\omega_{\perp}}{\omega_L} \ll 1 \quad (2.35)$$

The averaged gyromotion of particles is parallel to the magnetic field lines, with parallel velocities  $v_{\parallel} \approx \sqrt{2T/m}$  consistent with the kinetic energy in the plasma. Drift velocities, on the other hand, are typically much slower. Since  $\nabla B$  and the curvature radius  $R_c$  occur at machine scales  $L_{\parallel}$ , we can provide orders of magnitude for the drift velocities introduced in Sec. 1.1.2:

$$v_E \sim \epsilon_E v_{\parallel} \quad v_{\nabla B} \sim \epsilon_l v_{\parallel} \quad v_c \sim \epsilon_l v_{\parallel} \quad v_p \sim \epsilon_t v_{\parallel} \quad (2.36)$$

This leads to the assumption in the Lorentz equation 1.5 that the perpendicular acceleration is negligible compared to parallel dynamics, such that  $m\partial_t v_{\perp} \approx 0$ . For

## 2. Description of Plasmas – 2.2. Drift-reduced models for plasma turbulence

the perpendicular velocity, we project the momentum conservation equation onto the perpendicular direction:

$$\begin{aligned} \mathbf{b} \times [\partial_t(mn\mathbf{v}) + \nabla \cdot (mn\mathbf{v} \otimes \mathbf{v})] &= -\mathbf{b} \times \nabla p_\perp - \mathbf{b} \times \nabla \cdot \tilde{\Pi} + nq\mathbf{b} \times \mathbf{E} \\ &\quad + nq(\mathbf{b} \times \mathbf{v} \times \mathbf{B}) + \mathbf{b} \times \mathbf{R} + \mathbf{b} \times \mathbf{S}_u \\ \Leftrightarrow \mathbf{v}_\perp &= \frac{\mathbf{b} \times \nabla p}{enZB} + \frac{\mathbf{b} \times \nabla \cdot \tilde{\Pi}}{enZB} + \frac{\mathbf{E} \times \mathbf{b}}{B} + \frac{(\mathbf{R} + \mathbf{S}) \times \mathbf{b}}{enZB} \\ &\quad + \frac{\mathbf{b}}{enZB} \times (\partial_t(mn\mathbf{v}) + \nabla \cdot (mn\mathbf{v} \otimes \mathbf{v})) \end{aligned} \quad (2.37)$$

In addition to the diamagnetic, electric and polarization drifts  $\mathbf{v}^*$ ,  $\mathbf{v}_E$  and  $\mathbf{v}_p$  known from Sec. 1.1.2, we introduce here the parallel viscous stress and friction force drifts  $\mathbf{v}_{\perp,\Pi}$  and  $\mathbf{v}_{\perp,S}$ . The expression for the perpendicular velocity  $\mathbf{v}_\perp$  is not explicit as the right-hand side depends on the full velocity vector. However, we can fairly well approximate it with two calculation steps. All terms that do not depend on  $\mathbf{v}$  are first evaluated to get  $\mathbf{v}_\perp^{(0)}$  (and with equation 3.11 we can also calculate  $\mathbf{v}^{(0)}$ ), and then  $\mathbf{v}_\perp^{(1)}$  is calculated by replacing every occurrence of  $\mathbf{v}$  by  $\mathbf{v}^{(0)}$ .

$$\mathbf{v}_\perp^{(0)} = \frac{\mathbf{b} \times \nabla p}{enZB} + \frac{\mathbf{E} \times \mathbf{b}}{B} = \mathbf{v}_* + \mathbf{v}_E \quad (2.38)$$

$$\begin{aligned} \mathbf{v}_\perp^{(1)} &= \frac{\mathbf{b} \times \nabla \cdot \tilde{\Pi}(\mathbf{v}^{(0)})}{enZB} - \frac{\mathbf{b} \times (R(\mathbf{v}^{(0)}) + S(\mathbf{v}^{(0)}))}{enZB} \\ &\quad + \frac{\mathbf{b}}{n\omega_c} \times (\partial_t(n\mathbf{v}^{(0)}) + \nabla \cdot (n\mathbf{v}^{(0)} \otimes \mathbf{v}^{(0)})) \\ &= \mathbf{v}_{\perp,\Pi} + \mathbf{v}_{\perp,S} + \mathbf{v}_p \end{aligned} \quad (2.39)$$

$$\mathbf{v}_\perp \approx \mathbf{v}_\perp^{(0)} + \mathbf{v}_\perp^{(1)} \quad (2.40)$$

This simplification holds because the contribution of  $\mathbf{v}_\perp^{(1)}$  is small, of the order of  $\epsilon_t$ . Next, let us extract the divergence free contribution from the diamagnetic flux  $n\mathbf{v}^*$ .

$$\begin{aligned} n\mathbf{v}^* &= -\nabla \times \frac{p\mathbf{B}}{eZB^2} + n\tilde{\mathbf{v}}^* \\ \text{with: } \tilde{\mathbf{v}}^* &= \frac{2T\mathbf{B} \times \nabla B}{eZB^3} + \frac{T}{eZB^2} \nabla \times \mathbf{B} \end{aligned} \quad (2.41)$$

The second term in  $\tilde{\mathbf{v}}^*$  accounts for the "gradB" and curvature drifts. The polarization drift  $v_p$  in Eq. 2.39 can be found through algebraic manipulations and neglecting some small curvature terms:

$$n\mathbf{v}_p = \partial_t \boldsymbol{\omega} - \nabla \cdot (\mathbf{v}^{(0)} \otimes \boldsymbol{\omega})$$

with:  $\boldsymbol{\omega} = \frac{m}{eZB^2} \left( n\nabla_{\perp}\Phi + \nabla_{\perp} \left( p - \frac{\pi_{\parallel}}{3} \right) \right) - \frac{m}{q^2B^2} S_{\mathbf{v}_{\perp}}$

(2.42)

Let us introduce the vorticity  $\boldsymbol{\Omega} = \nabla \times \mathbf{v}$ , which measures the local rotation of a fluid element. It is a vector quantity, where the direction indicates the axis of rotation and its magnitude indicates the strength of the rotational motion. As perpendicular phenomena are essentially described by the parallel component of  $\boldsymbol{\Omega}$ , we only solve for the conservation of  $\Omega_{\parallel}$ .

$$\Omega_{\parallel} = \mathbf{b} \cdot \nabla \times \mathbf{v}_p = \nabla \cdot \boldsymbol{\omega}$$
(2.43)

With the expression of the polarization drift, we obtain a conservation equation for the ion vorticity:

$$\frac{n_i m_i}{q_i B^2} (\partial_t \Omega_{\parallel} + (v_{i,\parallel} \mathbf{b} + \mathbf{v}_{i,\perp}) \cdot \nabla \Omega_{\parallel}) = \nabla \cdot (j_{\parallel} \mathbf{b} + \mathbf{j}_{\perp} - e n \mathbf{v}_E)$$
(2.44)

where the perpendicular current arises from drifts in opposite directions for electrons and ions,  $\mathbf{j}_{\perp} = q_i n_i \mathbf{v}_{i,\perp} - q_e n_e \mathbf{v}_{e,\perp}$ . There is a "grad B," curvature, and polarization current, but no "ExB" current, as the electric drift is independent of the species' mass and charge. The parallel current density is given by Ohm's law:

$$\eta_{\parallel} j_{\parallel} + \frac{m_e}{e} \frac{d j_{\parallel}}{dt} = E_{\parallel} + \frac{\nabla_{\parallel} p_e}{n_e} + 0.71 \nabla_{\parallel} T_e$$
(2.45)

In the first order, the evolution of the perpendicular electric field derives from the evolution of the potential gradient  $d\mathbf{E}_{\perp}/dt = -d\nabla_{\perp}\Phi/dt$ . The full electric field is given by:

$$\mathbf{E}_{\perp} = -\nabla_{\perp}\Phi \quad E_{\parallel} = -\nabla_{\parallel}\Phi - \partial_t A_{\parallel}$$
(2.46)

where the time variation  $\partial_t A_{\parallel}$  accounts for magnetic induction effects.

A full derivation of the drift-reduced equations, including all possible terms, was provided by Simakov and Catto[89]. Notably, they derived a self-consistent expression for the ion parallel and gyroviscous stress tensors, ensuring full energy conservation in the fluid model.

### 2.2.2. Linear plasma instabilities

To understand how turbulent structures appear and travel in the plasma, it is essential to understand the physical mechanisms covered by the drift-reduced equations. In this section, we delve into the different linear phenomena that appear plasma in the

SOL.

### 2.2.2.1. Non-adiabatic drift waves

One key mechanism within this framework is the non-adiabatic density response to potential perturbations. In this context, resistivity induces a phase shift between density and potential perturbations, which can either amplify or dampen these perturbations. The Hasegawa-Wakatani model[42] provides a foundational understanding of this process. This model considers an isothermal plasma with an unsheared magnetic field, where particles are advected solely by the electric drift, and parallel ion motion is neglected. We assume that the magnetic field is purely toroidal, and radial density gradients are imposed by the pressure gradient. We then remain with two degrees of freedom on which to perform the linear analysis: a perpendicular, poloidal direction and a parallel, toroidal direction. Perturbations on any quantity are expressed as  $X = X_0(\psi) + \tilde{X}(\theta, \varphi)$ , with  $\tilde{X}(\theta, \varphi) = e e^{i(-\omega t + k_\perp \theta + k_\parallel \varphi)}$  and the equilibrium fields  $X_0$  varies across flux surfaces. Radial density gradients are imposed from the pressure gradient and can be approximated  $\partial_\psi n_0 = \bar{n}_0 / \lambda_p$  where  $\lambda_p$  is a characteristic length for the pressure gradient. In a slab equations, the perpendicular direction is hence perpendicular to both the magnetic field and the density gradient. The governing equations are:

$$\partial_t n + \mathbf{v}_E \cdot \nabla n = \frac{1}{e} \nabla \cdot (j_\parallel \mathbf{b}) \quad (2.47)$$

$$\eta_\parallel j_\parallel = T_0 \nabla_\parallel \log(n) - \nabla_\parallel \Phi \quad (2.48)$$

$$\nabla \cdot \frac{nm_i}{B^2} (\partial_t \nabla_\perp \Phi + \mathbf{v}_E \cdot \nabla \nabla_\perp \Phi) = \nabla \cdot (j_\parallel \mathbf{b}) \quad (2.49)$$

The advection term by the electric drift can be expressed using Poisson brackets:

$$\begin{aligned} \mathbf{v}_E \cdot \nabla n &= -\frac{1}{B} (\nabla \Phi \times \mathbf{b}) \cdot \nabla n = -\frac{1}{B} (\partial_\theta \Phi \partial_\psi n - \partial_\psi \Phi \partial_\theta n) \\ &= -\frac{1}{B} [\Phi, n]_{\psi, \theta} \end{aligned} \quad (2.50)$$

The wavenumber vector  $\mathbf{k}$  contains both parallel and perpendicular components, such that in the Fourier space  $k_\parallel^2 \sim \nabla_\parallel^2$  and  $k_\perp^2 \sim \nabla_\perp^2$ . Using the ion Larmor radius  $\rho_L^2 = T_0 m_i / (eB^2)$ , the dispersion relation for the system is:

$$\omega^2 + i \frac{1 + \rho_L^2 k_\perp^2}{\rho_L^2 k_\perp^2} \frac{T_0 k_\parallel^2}{e n_0 \eta_\parallel} \omega - i \frac{1}{\rho_L^2 k_\perp^2} \frac{T_0^2 k_\perp k_\parallel^2}{e n_0 B \lambda_p \eta_\parallel} = 0 \quad (2.51)$$

The solution to this system can be decomposed into a real component  $\omega_*$  that corresponds to the natural frequency of the system and an imaginary component  $\gamma$  that describes the growth or damping rate. From the drift-ordering parameters, we know that  $k_\perp^2 \rho_L^2$  must be small, simplifying the system. If we assume the resistivity

small, we can estimate the solutions:

$$\omega_* = \frac{T_e k_\perp}{B \lambda_p} \quad \gamma = \frac{\rho_L^2 k_\perp^2 e n_0 \eta_\parallel}{T_0 k_\parallel^2} \omega_*^2 \quad (2.52)$$

The system frequency  $\omega_*$  is called the diamagnetic frequency and is driven by the density gradient. We observe that the growth rate  $\gamma$  is positive, indicating that under certain conditions, perturbations may grow indefinitely. The more resistive a plasma is, the faster perturbations grow and in an ideal plasma with zero resistivity, the system remains stable with the single real solution  $\omega_*$ . In this case, the interaction is adiabatic, and density and potential oscillate in phase at the diamagnetic frequency.

### 2.2.2.2. Sound waves

Parallel ion motion produces sound waves. If we consider only the parallel velocity, the conservation equation can be expressed in a reduced form:

$$\partial_t n + \nabla \cdot (v_\parallel n \mathbf{b}) = 0 \quad (2.53)$$

$$m_i n \left( \partial_t v_\parallel + \nabla \cdot (v_\parallel^2 \mathbf{b}) \right) = -\nabla_\parallel (p_i + p_e) \quad (2.54)$$

Density and velocity perturbations then travel in the parallel direction at the sound speed  $c_s = \sqrt{e(T_e + T_i)/m_i}$ . Sound waves do not lead to instabilities nor do they grow or damp, but they naturally arise with perturbations and interact with other wave dynamics. The associated frequency is  $\omega_s = c_s k_\parallel$ .

### 2.2.2.3. Shear Alfvén waves

They appear as one introduces electromagnetic induction to the parallel electric field  $E_\parallel = -\nabla_\parallel \Phi - \partial_t A_\parallel$ . The parallel magnetic vector potential in turn is known from the parallel current via Ampère's law.

$$\nabla \cdot \left[ \frac{m_i n_i}{B^2} \partial_t \nabla_\perp \Phi \right] = \nabla \cdot (j_\parallel \mathbf{b}) \quad (2.55)$$

$$\nabla_\perp^2 A_\parallel = -\mu_0 j_\parallel \quad (2.56)$$

$$\eta_\parallel j_\parallel = (-\nabla_\parallel \Phi - \partial_t A_\parallel + T_e \nabla_\parallel \log(n_e)) \quad (2.57)$$

$$\partial_t n_e = \frac{1}{e} \nabla \cdot (j_\parallel \mathbf{b}), \quad (2.58)$$

It will modify the parallel current, and introduce a new wave dynamics that travel at the Alfvén velocity  $v_A = \frac{B}{\sqrt{m_i n_i \mu_0}}$ . The dispersion relation for the system above is:

$$\omega_A^2 = \left( v_A^2 + \frac{T_0 k_\perp^2}{n_e \mu_0} \right) k_\parallel^2 - \frac{\eta_\parallel^2}{4\mu_0^2} \quad (2.59)$$

In the zero-resistivity limit, the dispersion relation has a single real solution. It describes shear Alfvén, travelling in parallel direction along magnetic field lines at the Alfvén velocity  $v_A$ .

#### 2.2.2.4. Resistive ballooning modes

Magnetic curvature also plays an important role in the formation of drift waves. The effective gravity force opposes the pressure gradient, leading to inherent plasma instability and the development of resistive ballooning modes[44]. In the vorticity conservation equation, as given in Eq. 2.44, the term  $\nabla \cdot \mathbf{v}_\perp$  appears. Both the electric and diamagnetic drifts take the form  $(\mathbf{B} \times \nabla X)/B^2$ . In a homogeneous magnetic field, as assumed above, the divergence of the drifts vanishes. However, in a curved magnetic field, this term introduces additional coupling between the vorticity and the density and potential gradients. It is particularly pronounced at the low-field side, and plasmas blobs traveling outwards typically take a jelly shape.

In a realistic tokamak configuration with both poloidal and toroidal field components and a high aspect ratio  $R/a$ , poloidal perturbations can be expressed as  $\tilde{X} = \sum_m \tilde{X}_m e^{im\theta}$ . A perturbation mode  $m$  in the density or potential is then coupled to the modes  $m-1$  and  $m+1$  of the other field. The common phenomenon is the appearance of geodesic acoustic modes that have been well-observed and described in real and numerical experiments[17]. They occur, for a major radius  $R_0$  and local safety factor  $q$ , at the frequency:

$$\omega_{GAM}^2 = \frac{2c_s^2}{R_0^2} \left( 1 + \frac{1}{2q^2} \right) \quad (2.60)$$

So far we have considered several wave dynamics in the plasma individually, with each their own characteristic frequency. In reality, all these modes impact the plasma simultaneously and the actual linear behavior is far more complex and combines all frequencies. In a mid-sized tokamaks such as TCV, edge plasma is found with the typical conditions:  $n = 10^{19} \text{ m}^{-3}$ ,  $T_e = T_i = 50 \text{ eV}$ ,  $\lambda_p = 0.01 \text{ m}$  and  $B = 1 \text{ T}$ . For a pure deuterium plasma, we the characteristic times for drift waves, GAM modes, shear Alfvén waves, ion and electron transit are then of the order of:

$$\tau_* = 10^{-6} \text{ s} \quad \tau_{GAM} = 10^{-5} \text{ s} \quad \tau_A = 5 \cdot 10^{-7} \text{ s} \quad \tau_i = 10^{-4} \text{ s} \quad \tau_e = 10^{-6} \text{ s} \quad (2.61)$$

Leddy *et al.*[57] compared the linear behavior of drift-reduced and full-velocity

descriptions of plasmas. They found that while the drift reduction suppresses fast wave dynamics, easing timestep constraints and motivating the use of reduced MHD models as introduced in Sec. 2.1.3.2, the linear behavior of the two approaches only agrees within a limited parameter space, generally including tokamak conditions. However, the agreement is only robust in the edge region, with significant discrepancies appearing in the core, limiting the validity of drift-reduced models in simulation that consider both sides of the separatrix.

## 2.3. Electromagnetic effects in edge plasma

Numerous studies have demonstrated the electromagnetic effects on edge dynamics, both on blob dynamics in simple geometries[58, 95], and on turbulence and transport properties in real tokamak geometries[110, 111]. Their impact increases with  $\beta$  and can become crucial, particularly when approaching the L-H transition or in large machines like ITER operating in the high confinement mode (H-mode)[110]. In these electromagnetic models, magnetic fluctuations are explicitly determined by Ampère's and Ohm's laws[25, 27, 33, 74, 93, 108]. Thus, electron inertia is retained, and magnetic effects occur both through magnetic induction and flutter.

Magnetic induction is captured by the time derivative of the parallel vector potential  $A_{\parallel}$ , which is principally a linear phenomenon, with the Coulomb gauge  $E_{\parallel} = -\nabla_{\parallel}\Phi - \partial_t A_{\parallel}$ , such that fluctuations in the electrostatic potential induce magnetic fluctuations. Magnetic flutter[12], on the other hand, refers to additional transport by magnetic fluctuations appearing through the perturbed parallel gradient such as  $A_{\parallel} = (\mathbf{b} + \tilde{\mathbf{B}}/B) \cdot \nabla$  (where  $\mathbf{b}$  is the equilibrium magnetic field unit vector and  $\tilde{\mathbf{B}} = \nabla \times (\tilde{A}_{\parallel} \mathbf{b})$ ), involving purely nonlinear phenomena. However, up to very recently, most studies did not discuss these effects, as pure electrostatic simulations are very difficult to achieve with their explicit time solvers[33, 93] and the consequent high constraints on the timestep size.

One particular interaction we want to study is the impact of electromagnetic effects on edge plasma turbulence. Shear Alfvén waves have already been introduced above, however they travel at much higher speeds than drift waves. In this section, we focus more on drift-Alfvén waves, which appear with the presence of a magnetic induction term in the non-adiabatic response. We then discuss the nonlinear impact of fluctuations of the magnetic equilibrium on the plasma.

### 2.3.1. Non-adiabatic plasma response in Ohm's law

As early as 1997, Scott[84] questioned the importance of magnetic induction for the evolution of drift waves. The parallel current density in Ohm's law balances the plasma pressure with electric forces and resistive friction. As soon as we consider a finite  $\beta$ , the variation of the electromagnetic vector potential  $\mathbf{A}$  adds to the electric potential gradient in the definition of the electric field  $\mathbf{E} = -\partial_t \mathbf{A} - \nabla \Phi$ . At drift scales,  $k_{\parallel} \ll k_{\perp}$

## 2. Description of Plasmas – 2.3. Electromagnetic effects in edge plasma

and only the parallel component  $A_{\parallel} = \mathbf{A} \cdot \mathbf{b}$  of the electromagnetic potential effectively impacts electric forces. It is directly linked to the current density via Ampère's law:

$$\nabla \cdot \nabla A_{\parallel} = -\mu_0 j_{\parallel} \quad (2.62)$$

If we then include  $A_{\parallel}$  in the parallel electric field, magnetic induction leads to an extended, electromagnetic Ohm's law:

$$E_{\parallel} = -\nabla_{\parallel}\Phi - \partial_t A_{\parallel} \quad (2.63)$$

$$\eta_{\parallel} j_{\parallel} = -\nabla\Phi - \partial_t A_{\parallel} + \frac{1}{n_e} \nabla_{\parallel} p_e + 0.71 \nabla_{\parallel} T_e \quad (2.64)$$

Magnetic induction introduces drift Alfvén waves to the system with a velocity  $v_A^2 = B^2/(m_i \mu_0 n_i)$ . Because of the interplay between Ampère's (2.62) and Ohm's (2.64) laws, the magnetic induction term quickly dominates over the parallel resistivity. This occurs as soon as the perpendicular scale exceeds the collisionless skin depth, or if  $\beta > (k_{\perp} \rho_s)^2 (m_e/m_u)$ [64]. In drift-wave turbulence the characteristic scales may be much larger than the Larmor radius, in which case electromagnetic effects are dominant even at plasmas with low  $\beta$  values of  $10^{-6}$ [84]. It is apparent that magnetic induction strongly impacts the response of the parallel current to the force balance and as such wave speeds in the plasma. For higher  $\beta$ , it essentially replaces the electric resistivity as the driver of the current response. Furthermore, magnetic curvature adds a layer of instability to the system and reinforces the phase shift of  $\tilde{p}$  ahead of  $\tilde{\Phi}$ . Ballooning does, however, not modify the mode structure and thus the general shape and scale of the turbulence[83].

Dudson *et al.*[26] further pointed out that a uniquely resistive current response does not prevent the Alfvén velocity to exceed the speed of light. It occurs particularly in the upper  $k_{\perp}$  limit. With electron inertia the parallel transport is limited by the thermal electron speed and hence within physical realistic values. Electron inertia effects are then needed to complete the resistive dissipation in Ohm's law. Incidentally, studies on HSX have shown that electron inertia effect may, in fact, dominate over resistivity for the generation of resistive ballooning modes[73]. In our model, we introduce a transport term on the parallel current to Ohm's law:

$$\eta_{\parallel} j_{\parallel} + \frac{m_e}{e} (\partial_t + v_j \cdot \nabla) j_{\parallel} = -\nabla\Phi - \partial_t A_{\parallel} + \frac{1}{n_e} \nabla_{\parallel} p_e + 0.71 \nabla_{\parallel} T_e \quad (2.65)$$

In his later paper[85], Scott identified three effective parameters that will determine whether the non-adiabatic plasma response is rather dominated by resistive effects, electron inertia or magnetic induction. They are scaled versions of the parallel resistivity  $\eta_{\parallel}$ , the electron-to-ion mass ratio and the pressure ratio  $\beta$ .

$$C = \eta \left( \frac{qR}{L_{\perp}} \right)^2 \quad \mu_{eff} = \frac{m_e}{m_i} \left( \frac{qR}{L_{\perp}} \right)^2 \quad \beta_{eff} = \beta \left( \frac{qR}{L_{\perp}} \right)^2 \quad (2.66)$$

### 2.3.2. Electromagnetic flutter

So far, we only discussed magnetic induction in Ohm's law. The magnetic potential  $\mathbf{A}$ , in its primary definition, drives the magnetic field itself. The magnetic field can be decomposed in equilibrium and fluctuation components:

$$\mathbf{B} = \mathbf{B}_{eq} + \tilde{\mathbf{B}} \quad (2.67)$$

The fundamental definition 1.17 of the magnetic field through its vector potential will be used. In the drift-reduced framework, we only consider the parallel projection of the magnetic vector potential  $\mathbf{A} \approx A_{\parallel} \mathbf{b}$ . It is then possible to calculate the fluctuating field  $\tilde{\mathbf{B}}$ :

$$\tilde{\mathbf{B}} = \nabla A_{\parallel} \times \mathbf{b}_{eq} + A_{\parallel} \nabla \times \mathbf{b}_{eq} \quad (2.68)$$

The second term contains the plain  $A_{\parallel}$  without its derivative, which might seem counterintuitive from the the definition of the magnetic field and contradicts any gauge theory. The contribution of this second term to the flutter field is however negligible compared to the first. Notwithstanding the smallness of the flutter field, it is important to maintain the total magnetic field divergence-free. Let us verify this property with the definition of the flutter field:

$$\begin{aligned} \nabla \cdot \mathbf{B} &= \nabla \cdot B \mathbf{b}_{eq} + \nabla \cdot B \tilde{\mathbf{b}} \\ &= -\beta_0 \mathbf{b}_{eq} \times \nabla \tilde{A}_{\parallel} + \beta_0 \tilde{A}_{\parallel} \nabla \times \mathbf{b}_{eq} \\ &= \beta_0 [ -(\nabla \times \mathbf{b}_{eq}) \cdot \nabla A_{\parallel} + \mathbf{b}_{eq} \cdot (\nabla \times \nabla A_{\parallel}) + A_{\parallel} \nabla \cdot (\nabla \times \mathbf{b}_{eq}) + \nabla A_{\parallel} \cdot (\nabla \times \mathbf{b}_{eq}) ] \\ &= 0 \end{aligned} \quad (2.69)$$

The equilibrium field is externally provided such that it is divergence free, so  $\nabla \cdot B \mathbf{b}_{eq} = 0$ . We further used the vector calculus identities on second-order derivatives  $\nabla \times \nabla X = 0$  and  $\nabla \cdot (\nabla \times \mathbf{X})$ . It further proves the importance of the second (small) term in the definition of  $\tilde{\mathbf{b}}$  (with  $\nabla \times \mathbf{b}_{eq}$ ), as without it, the flutter field would not be divergence-free. On the other hand, this term is problematic with respect to gauge-fixing. The field  $A_{\parallel}$  appears directly in the equation without derivative. This is in contradiction with gauge theory, which says that the electromagnetic vector potential is defined up to a constant. This problem appears at all because we do not take the entire vector potential  $\mathbf{A}$ , but only its projection on the parallel equilibrium direction.

With respect to the equilibrium field, flutter can be viewed as an additional drift acting on the plasma. In reality it is not an actual drift as flutter transport is in fact a

deformation of the magnetic field lines and a redirection of the parallel advection.

Introducing electromagnetic effects, and specifically flutter, to the drift-reduced equations reduces the gap to MHD descriptions of plasma presented in Sec. 2.1.3.2. There are however some considerable difference: Instead of the parallel current and magnetic vector potential, the MHD model retains only their toroidal component. The magnetic vector potential there is then self-similar to the poloidal flux function  $A_\varphi = \Psi$ . With the knowledge of  $\Psi$ , the exact poloidal field is reconstructed for example in JOREK[48]. Magnetic reconnection and island formation is fundamental for tearing modes, and it remains uncertain if the fluctuating approach pursued here is sufficient to capture electromagnetic dynamics at the machine scale.

A major difference remains in the targeted physics: drift-reduced codes are suited for a precise description of edge turbulence driven by drift-wave and interchange instabilities, while MHD codes focus on large-scale MHD instabilities such as ELMs[69] or disruptions[67]. Even if the necessary physics was available in SOLEDGE3X or other fluid codes, their specialization on drift waves requires low timestep sizes for dynamics at the microsecond scale (see Eq. 2.61), making it extremely expensive to simulate a type-I ELM cycle that can last up to 100ms.

### 2.3.3. Drift-Alfvén waves

In this section, we take a more formal approach to the interaction between the three new terms (magnetic induction, electron inertia and flutter) and the well-known resistive drift-wave instabilities. As they all terms appear in Ohm's law, this is the place where they will all compete and modify the non-adiabatic response of the plasma.

#### 2.3.3.1. Dispersion relation

Let us consider the same system as in Sec. 2.2.2.1 and combine it with the shear Alfvén dynamics from Sec. 2.2.2.3. We then have the system:

$$\partial_t n + \mathbf{v}_E \cdot \nabla n = \frac{1}{e} \nabla \cdot (j_{\parallel} \mathbf{b}) \quad (2.70)$$

$$\frac{n m_i}{B^2} \partial_t \nabla_{\perp}^2 \Phi = \nabla \cdot (j_{\parallel} \mathbf{b}) \quad (2.71)$$

$$\left( \eta_{\parallel} + \frac{m_e}{n_e e^2} \partial_t \right) j_{\parallel} = \frac{T_e}{n} \nabla_{\parallel} n - \nabla_{\parallel} \Phi - \partial_t A_{\parallel} \quad (2.72)$$

$$\nabla_{\perp}^2 A_{\parallel} = -\mu_0 j_{\parallel} \quad (2.73)$$

Here parallel gradients and divergence use the total magnetic field  $\mathbf{b}$ . As in the previous setting the equilibrium field is purely toroidal and  $\mathbf{b}_{eq} = (0, 0, 1)^T$ . Again, only consider poloidal and toroidal perturbations with respective wavenumbers  $k_{\perp}$  and  $k_{\parallel}$ . If we only consider the dominating term of  $\tilde{\mathbf{b}}$ , any gradient  $\nabla_{\parallel} f$  can be expressed as:

## 2. Description of Plasmas – 2.3. Electromagnetic effects in edge plasma

$$\begin{aligned}
\mathbf{b} \cdot \nabla f &= \mathbf{b}_{eq} \cdot \nabla f + \tilde{\mathbf{b}} \cdot \nabla f \\
&= \mathbf{b}_{eq} \cdot \nabla f + \frac{1}{B} (\nabla A_{\parallel} \times \mathbf{b}) \cdot \nabla f \\
&= \partial_{\varphi} f + \frac{1}{B} [A_{\parallel}, f]_{\psi, \theta}
\end{aligned} \tag{2.74}$$

One can see from this expression the similarity between the flutter contribution to the advection and the "ExB" advection in Eq. 2.50, reassuring us in the idea to consider flutter as a new drift. Parallel divergences can be written in the exact same way, as on a slab geometry the terms  $f\partial_{\psi}\partial_{\theta}A_{\parallel}$  and  $f\partial_{\theta}\partial_{\psi}A_{\parallel}$  cancel out.

$$\nabla \cdot (f\mathbf{b}) = \partial_{\varphi} f + \frac{1}{B} [A_{\parallel}, f]_{\psi, \theta} \tag{2.75}$$

From the thermodynamic force, radial density gradients are prescribed to  $n_0/\lambda_p$ , but  $\partial_{\psi}\Phi$ ,  $\partial_{\psi}j_{\parallel}$  or  $\partial_{\psi}A_{\parallel}$  are assumed to zero in the linear analysis. The system of study can then be rewritten as:

$$\partial_t n - \frac{n_0}{B\lambda_p} \partial_{\theta}\Phi - \frac{1}{e} \partial_{\varphi} j_{\parallel} = 0 \tag{2.76}$$

$$\frac{nm_i}{B^2} \partial_t \nabla_{\perp}^2 \Phi - \partial_{\varphi} j_{\parallel} = 0 \tag{2.77}$$

$$\left( \eta_{\parallel} + \frac{m_e}{n_e e^2} \partial_t \right) j_{\parallel} - \frac{T_e}{n_0} \partial_{\varphi} n + \partial_{\varphi} \Phi + \left( \frac{T_e}{\partial_t - B\lambda_p} \partial_{\theta} \right) A_{\parallel} = 0 \tag{2.78}$$

$$\partial_{\theta}^2 A_{\parallel} + \mu_0 j_{\parallel} = 0 \tag{2.79}$$

This system can now be transformed to the Fourier space:

$$\begin{pmatrix}
-i\omega & i\frac{n_0}{T_0}\omega_* & -i\frac{1}{e}k_{\parallel} & 0 \\
0 & i\frac{en_0}{T_0}\rho_L^2 k_{\perp}^2 \omega & -ik_{\parallel} & 0 \\
-i\frac{T_0}{n_0}k_{\parallel} & ik_{\parallel} & \eta_{\parallel} - i\frac{m_e}{(n_e e^2)}\omega & i\omega_* - i\omega \\
0 & 0 & \mu_0 & -k_{\perp}^2
\end{pmatrix}
\begin{pmatrix}
\hat{n} \\
\hat{\Phi} \\
\hat{j}_{\parallel} \\
\hat{A}_{\parallel}
\end{pmatrix} = \begin{pmatrix}
0 \\
0 \\
0 \\
0
\end{pmatrix} \tag{2.80}$$

To get the complex system frequencies, we need to solve the determinant of the matrix for  $\omega$ . We can express the dispersion relation as a third order polynomial equation on  $\omega$ :

$$i \left( \underbrace{\rho_{L,e}^2 k_{\perp}^2}_{\text{finite } m_e} + \underbrace{\beta_0}_{\text{induct.}} \right) \omega^3 + \left( -i \underbrace{\beta_0 \omega_*}_{\text{flutter}} - \underbrace{\frac{\eta_{\parallel} en_0 T_0 k_{\perp}^2}{B^2}}_{\text{resistivity}} \right) \omega^2 - i\omega_s^2 (\omega_* - (1 + \rho_L^2 k_{\perp}^2) \omega) = 0 \tag{2.81}$$

with the electron Larmor radius  $\rho_{L,e}^2 = m_e T_0 / (eB^2)$  and the pressure ratio  $\beta_0 = en_0 T_0 \mu_0 / B^2$ . The terms arising from the different components of the electromagnetic

model are clearly labeled.

### 2.3.3.2. Perturbative solution

The solution to the dispersion relation takes the form  $\omega_{DAW} = \omega_0 + i\gamma$ . To obtain a neat expression for the wave phase frequency  $\omega_0$  and the growth rate  $\gamma$ , let us assume that the drift-Alfvén frequency  $\omega_{DAW}$  is close to the diamagnetic frequency, with  $\delta = \omega_{DAW} - \omega_*$  such that higher orders  $\delta^n$  can be ignored. To improve the readability, let us refer to the resistive term as  $R = \eta_{\parallel} e n_0 T_0 / B^2$ . We can then express  $\delta$ :

$$\delta = \frac{R k_{\perp} \omega_*^2 - i \rho_{L,e}^2 k_{\perp}^2 \omega_*^3}{i (\beta_0 - 3 \rho_{L,e}^2 k_{\perp}^2) \omega_*^2 - 2 R k_{\perp} \omega_* - i \omega_s^2} \quad (2.82)$$

If we further assume a small but still finite resistivity  $R$  (dropping higher-order terms), we can concisely express the real and imaginary parts of  $\delta$ .

$$\delta \approx \frac{\rho_{L,e}^2 k_{\perp}^2 \omega_*^3}{(\beta_0 - 3 \rho_{L,e}^2 k_{\perp}^2) \omega_*^2 + \omega_s^2} + i \frac{R k_{\perp} \omega_*^2}{(\beta_0 - 3 \rho_{L,e}^2 k_{\perp}^2) \omega_*^2 + \omega_s^2} \quad (2.83)$$

At this point, a single term remains for electromagnetic induction and flutter. This is because the flutter has a stabilizing effect on the inductive term. It already appears in the dispersion relation 2.81 that the flutter term largely compensates the electromagnetic induction in the difference  $i \beta_0 (\omega - \omega_*) \omega^2$ .

It is interesting to discuss how the electromagnetic terms modify the characteristic drift-wave frequency  $\omega_*$  known from the electrostatic setting. Since we estimated the drift-Alfvén wave by  $\omega_{DAW} = \omega_* + \delta$ , it is also essential to justify the assumptions made above. For that, let us compare of  $\delta$  to the diamagnetic frequency.

$$\frac{\text{Re}\{\delta\}}{\omega_*} = \frac{\rho_{L,e}^2 k_{\perp}^2 \omega_*^2}{(\beta_0 - 3 \rho_{L,e}^2 k_{\perp}^2) \omega_*^2 + \omega_s^2} \quad (2.84)$$

The resistive terms do not contribute to a change of frequency.

This discussion is only valid in cases where  $\rho_{L,e}^2 k_{\perp}^2$  is small and hence  $\omega_{DAW}$  is close to the diamagnetic frequency  $\omega_*$ .

## **Part III.**

# **A New Electromagnetic Model for SOLEDGE3X**

### 3. The physical model

#### Chapter Summary

In the new electromagnetic model for SOLEDGE3X, conservation equations for mass, momentum, energy, and charge are extended to include magnetic induction and electron inertia effects. Additionally, it requires solving for the parallel magnetic vector potential  $A_{\parallel}$  in Ampère's law. The dimensionless model equations are:

$$\begin{aligned} \partial_t n_i + \nabla \cdot (n_i \mathbf{u}) &= S_{n,i} - \mathfrak{D}_n^i \\ m_i \partial_t \gamma_i + m_i \nabla \cdot (\gamma_{\parallel,i} \mathbf{u}) + \nabla_{\parallel} p_i &= Z_i n_i E_{\parallel} - \mathbf{b} \cdot \nabla \cdot \boldsymbol{\Pi}_i + S_{\gamma,i} + R_{\parallel,i} - \mathfrak{D}_{\gamma}^i \\ \partial_t \varepsilon_{\alpha} + \nabla \cdot ((\varepsilon_{\alpha} + p_{\alpha}) \mathbf{u}_{\alpha} + \boldsymbol{\Pi}_i \cdot \mathbf{u}_{\alpha} + q_{\alpha}) &= \mathbf{u}_{\alpha} \cdot (Z_{\alpha} n_{\alpha} \mathbf{E}_{\alpha} + \mathbf{R}_{\alpha}) + Q_{\alpha} + S_{\varepsilon,\alpha} - \mathfrak{D}_{\varepsilon}^{\alpha} \\ \nabla \cdot \left[ \frac{m_i n_i}{B^2} \partial_t \nabla_{\perp} \Phi \right] - \nabla (j_{\parallel} \mathbf{b}) &= \nabla \cdot (\mathbf{j}_{VB} + \mathbf{j}_{\Pi} + \mathbf{j}_{\pi}) - \partial_t \Omega_{p_i} - \mathfrak{D}_{\Omega} \\ \eta_{\parallel} j_{\parallel} + \frac{m_e}{n_e} (\partial_t j_{\parallel} + \mathfrak{D}_j + \nabla \cdot [\mathbf{u}_j j_{\parallel}]) &= -\nabla_{\parallel} \Phi - \beta_0 (\partial_t A_{\parallel} + \mathfrak{D}_A) \\ &\quad + T_e \nabla_{\parallel} \log(n_e) + 1.71 \nabla_{\parallel} T_e \\ \nabla \cdot \nabla_{\perp} A_{\parallel} &= -j_{\parallel} \end{aligned}$$

The magnetic potential drives perturbations in the magnetic field, commonly referred to as flutter. To avoid double-counting currents already included for the poloidal equilibrium field, only toroidal fluctuations  $\tilde{A}_{\parallel} = A_{\parallel} - \langle A_{\parallel} \rangle_{\varphi}$  contribute. Flutter is calculated as:

$$\tilde{\mathbf{b}} = \beta_0 \left( -\frac{\mathbf{b}_{eq} \times \nabla \tilde{A}_{\parallel}}{\|\mathbf{B}\|} + \frac{\tilde{A}_{\parallel} \nabla \times \mathbf{b}_{eq}}{\|\mathbf{B}\|} \right)$$

The flutter field is assumed to be small compared to the equilibrium field and is added as a first-order correction,  $\mathbf{b} = \mathbf{b}_{eq} + \tilde{\mathbf{b}}$ . It affects transport in the parallel direction as well as parallel gradients in Ohm's law, parallel viscous forces, and parallel heat conduction.

In the previous chapter, we laid the foundations of drift-reduced models for edge plasma. The project SOLEDGE3X was born with the merge of the 3D turbulence code TOKAM3X[97] and the 2D transport code SolEdge2D[11]. It stands as a comprehensive multi-species 2D/3D fluid solver to investigate transport and turbulence at the plasma edge up to the first wall, with a particular focus on modeling plasma-wall interactions. This has allowed successful investigations of numerous facets of edge plasma dynamics, such as turbulence[10] impurity transport[14] or ITER first-wall fluxes[76]. Until now, however, the model has been limited to electrostatic turbulence, with only fluctuations in the electric potential, determined by the non-adiabatic response to density fluctuations, being taken into account.

By the end of this chapter, we will have formulated a set of self-consistent transport equations that include electromagnetic effects. The existing SOLEDGE3X framework is extended to accomodate a finite electron mass in Ohm's law, an inductive term in the parallel electric field and flutter perturbations of the magnetic equilibrium. This requires the addition of two new fields: the parallel current density  $j_{\parallel}$  and the parallel magnetic vector potential  $A_{\parallel}$ .

In the first section 3.1, we introduce reference values for all quantities against which all variables are normalized, including the new electromagnetic fields. Then, section 3.2 recaps the density, momentum, energy and charge conservation equations and their exact formulation in SOLEDGE3X. The entire section 3.3 is dedicated to the electromagnetic model and its formulation within the charge balance equation. Finally, section 3.4 describes boundary conditions imposed at the sheath, the core and the first wall.

## 3.1. Dimensionless fields

To simplify the equations and improve the numerical stability, the code solves the equation for dimensionless physical quantities. It means that each variable  $X$  is scaled by a factor  $X_0$  to obtain a dimensionless  $\hat{X} = X / X_0$ , where  $X_0$  is representative for the range of values of  $X$ . Therefore, all quantities  $\hat{X}$  have similar values and we can prevent some numerical issues that might occur in equations containing variables with strongly different orders of magnitude.

The reference density  $n_0$ , temperature  $T_0$  and magnetic field  $B_0$  are free parameters that must be specified by the user to best match the conditions of the simulated scenario. Masses are expressed as factors of the atomic unit mass  $m_u$  and the Coulomb logarithm for particle collisions is set to  $\Lambda = 15$ . In the sheath-dominated SOL, the electric potential  $\Phi$  is proportional to the temperature with  $\Phi_{se} = \ln(\sqrt{m_i/(2\pi m_e)}) T \approx 3T$ . The potential is hence of the same order of magnitude as the temperature and it is convenient to set  $\Phi_0 = T_0$ . In this context, it is important to remember that temperatures are always expressed as energies in units of electronvolts [eV]. From the

### 3. The physical model – 3.1. Dimensionless fields

set of free parameters, we can derive spatial and temporal reference values to match the cyclotronic time  $\tau_0$  and the Larmor radius  $\rho_0$ :

$$\tau_0 = \frac{m_u}{eB_0} \quad (3.1)$$

$$\rho_0^2 = \frac{T_0 m_u}{eB_0^2} \quad (3.2)$$

$$\rho_0 = c_0 \tau_0 \quad \text{with the reference thermal ion speed } c_0 = \sqrt{\frac{eT_0}{m_u}} \quad (3.3)$$

In addition, dimensionless versions of the Spitzer-Härm viscosity  $\nu_{\parallel,\alpha}$ , conductivity  $\kappa_{\parallel,\alpha}$  and resistivity  $\eta_{\parallel}$  may be defined:

$$\nu_{\parallel,\alpha}^0 = \frac{\tau_0}{n_0 \rho_0^2 m_u} T_0^{2.5} \quad \kappa_{\parallel,\alpha}^0 = \frac{\tau_0}{en_0 \rho_0^2} T_0^{2.5} \quad \eta_{\parallel}^0 = \frac{en_0}{B_0} T_0^{-1.5} \quad (3.4)$$

As for all other physical quantities, the newly introduced fields  $A_{\parallel}$  and  $j_{\parallel}$  are replaced by dimensionless quantities in the code. First of all we need to define two constants  $A_{\parallel}^0$  and  $j_{\parallel}^0$  so that the dimensionless quantities  $\hat{A}_{\parallel}$  and  $\hat{j}_{\parallel}$  have about the same magnitude as the existing fields:

$$\hat{j}_{\parallel} = j_{\parallel} / j_{\parallel}^0 \quad \hat{A}_{\parallel} = A_{\parallel} / A_{\parallel}^0 \quad (3.5)$$

As the main occurrence of  $j_{\parallel}$  is in the vorticity conservation equation 2.44, it is wise to normalize  $j_{\parallel}$  to it. An expression for  $j_{\parallel}^0$  can be derived:

$$\begin{aligned} & \hat{\nabla} \cdot \left[ \frac{m_u n_0 \Phi_0}{\tau_0 B_0^2 \rho_0^2} \frac{\hat{m}_\alpha \hat{n}_\alpha}{\hat{B}^2} \hat{\partial}_t \hat{\nabla}_\perp \hat{\Phi} \right] \sim \hat{\nabla} \cdot \left[ \frac{j_{\parallel}^0}{\rho_0} \hat{j}_{\parallel} \mathbf{b} \right] \\ \Rightarrow & j_{\parallel}^0 = \frac{m_u n_0 \Phi_0}{\tau_0 B_0^2 \rho_0} = en_0 c_0 \end{aligned} \quad (3.6)$$

This reference value is coherent with the definition of the parallel current density as the difference of electron and ion momentum balances.

To define  $A_{\parallel}^0$ , there are essentially two different possible choices: the first option originates in Ampère's law 2.62 and compels  $A_{\parallel}^{0(1)}$  to depend on the magnetic permeability  $\mu_0$  and the reference parallel current  $j_{\parallel}^0$ .

$$\frac{A_{\parallel}^{0(1)}}{\rho_0^2} = \mu_0 j_{\parallel}^0 \quad \Leftrightarrow \quad A_{\parallel}^{0(1)} = \mu_0 en_0 c_0 \rho_0^2 \quad (3.7)$$

The second option relies on the revised definition of the parallel electric field in Eq.

### 3. The physical model – 3.2. Conservation equations

[2.63](#) and states that  $\partial_t A_{\parallel}$  is homogeneous to  $\nabla\Phi$ . This yields:

$$\frac{A_{\parallel}^{0(2)}}{\tau_0} = \frac{\Phi_0}{\rho_0} \quad \Leftrightarrow \quad A_{\parallel}^{0(2)} = \frac{\Phi_0 \tau_0}{\rho_0} \quad (3.8)$$

Both variants are valid, and they differ by a factor:

$$\frac{A_{\parallel}^{0(1)}}{A_{\parallel}^{0(2)}} = \beta_0 \quad (3.9)$$

where the reference plasma parameter  $\beta_0$  is the ratio between reference plasma and magnetic pressures:

$$\beta_0 = \frac{en_0 T_0}{B_0^2 / \mu_0} \quad (3.10)$$

$A_{\parallel}^{0(1)}$  and  $A_{\parallel}^{0(2)}$  are about four orders of magnitude away in the edge. From a numerical point of view, we need both relations, so an occurrence of the parameter  $\beta_0$  is inevitable in the dimensionless formulation of the system. The first option, based on Ampère's law, is chosen for the implementation. In the continuation of this chapter, all relations are expressed with the dimensionless fields.

## 3.2. Conservation equations

For simulations of the SOL in SOLEDGE3X, the three fluid moments in Eqs. [2.10](#), [2.14](#) and [2.17](#) are used for the ion density and momentum conservation, electron and ion energy conservation, and vorticity conservation equations. In the drift-reduced formulation, to compute the different drifts that compose the velocity  $\mathbf{u}$ , it is convenient to decompose it into a parallel component  $u_{\parallel}$  along the magnetic field lines  $\mathbf{b}$  and orthogonal  $\mathbf{u}_{\perp}$  components. This relationship is given by:

$$\mathbf{u} = u_{\parallel} \mathbf{b} + \mathbf{u}_{\perp} \quad \text{with} \quad u_{\parallel} = \mathbf{u} \cdot \mathbf{b} \quad \text{and} \quad \mathbf{u}_{\perp} = \mathbf{b} \times \mathbf{u} \quad (3.11)$$

This decomposition also applies to any other vector field. The perpendicular velocity is calculated with the plasma drifts in Eq. [1.15](#). Similarly, we define parallel and perpendicular gradient operators as follows:

$$\nabla_{\parallel} = \mathbf{b} \cdot \nabla \quad \nabla_{\perp} = \nabla - \nabla_{\parallel} \quad (3.12)$$

Anomalous perpendicular diffusion is included in all conservation equations via a term  $\mathfrak{D}_X^{\alpha}$ :

$$\mathfrak{D}_X^\alpha = \nabla \cdot (D \nabla_\perp X_\alpha) \quad (3.13)$$

Its usage is twofold: for transport simulations, it accounts for the total cross-field transport with a correspondingly larger diffusion coefficient  $D$ , such that perpendicular drift velocities are not required. In turbulent simulations with self-consistent drifts,  $D$  is much smaller but remains finite to capture phenomena at scales below the mesh resolution and to improve numerical stability. A typical value for the diffusion coefficient is  $D = 10^{-2} \text{ m}^2/\text{s}$ .

In general, the code is capable of handling multiple species, with the index  $i$  referring to any of the ion species. Further, the index  $e$  denotes electrons, and  $\alpha$  variables that apply to both electrons and ions. We can now formulate the balance equations that constitute the SOLEDGE3X model.

### 3.2.1. Mass balance

The mass conservation equation for ions is straight-forward:

$$\partial_t n_i + \nabla \cdot (n_i \mathbf{u}) = S_{n,i} - \mathfrak{D}_n^i \quad (3.14)$$

The ion source term  $S_{n,i}$  in the mass balance comes from imposed external sources or from recombination and ionization processes after particle collisions with neutrals.

It is sufficient to solve the mass balance for ions, as the fluid density of electrons can be easily retrieved with the quasi-neutrality assumption:

$$n_e = \sum_i Z_i n_i \quad (3.15)$$

### 3.2.2. Momentum balance

In the drift-reduced approach, the momentum conservation equation is primarily solved in parallel direction on  $\gamma_i = n_i u_{\parallel,i}$ .

$$m_i \partial_t \gamma_i + m_i \nabla \cdot (\gamma_{\parallel,i} \mathbf{u}) = +Z_i n_i E_\parallel - \nabla_\parallel p_i - \mathbf{b} \cdot \nabla \cdot \boldsymbol{\Pi}_i + S_{\gamma,i} + R_{\parallel,i} - \mathfrak{D}_\gamma^i \quad (3.16)$$

The source term  $S_{\gamma,i}$  is again due to ionization, recombination and radiation processes. Collisions between particles lead to the parallel friction term  $R_{\parallel,i}$ , which is known from Braginskii's and Zhdanov's closures. The parallel projection of the stress tensor  $\boldsymbol{\Pi}_i$  can be expressed as [6, 46, 107]:

$$\mathbf{b} \cdot \nabla \cdot \boldsymbol{\Pi}_i = \frac{2}{3} \nabla_\parallel \cdot \pi_\parallel + \pi_\parallel \nabla \cdot \mathbf{b} \quad \text{with: } \pi_\parallel = 3\nu_\parallel \left( \nabla_\parallel u_{\parallel,i} - \boldsymbol{\kappa} \cdot \mathbf{u}_{\perp,i} - \frac{1}{3} \nabla \cdot \mathbf{u} \right) \quad (3.17)$$

### 3. The physical model – 3.2. Conservation equations

including the curvature of the magnetic field  $\kappa = \mathbf{b} \cdot \nabla \mathbf{b}$ . In the most simple model, the electron velocity is calculated under full ambipolarity assumption:

$$\gamma_{\parallel,e} = \sum_i Z_i \gamma_i \quad (3.18)$$

with more accurate models currently under development.

#### 3.2.3. Energy balance

The energy conservation equation is solved for both electrons and ions. As already described in Sec. 2.1.2.3, the total energy is the sum of thermal and kinetic energy:

$$\varepsilon_\alpha = \frac{3}{2} n_\alpha T_\alpha + \frac{1}{2} m_\alpha n_\alpha u_\alpha^2 \quad (3.19)$$

where the kinetic contribution is negligible for electrons. The transport equation for energy is then:

$$\partial_t \varepsilon_\alpha + \nabla \cdot ((\varepsilon_\alpha + p_\alpha) \mathbf{u}_\alpha + \boldsymbol{\Pi}_i \cdot \mathbf{u}_\alpha + q_\alpha) = \mathbf{u}_\alpha \cdot (Z_\alpha n_\alpha \mathbf{E}_\alpha + \mathbf{R}_\alpha) + Q_\alpha + S_{\varepsilon,\alpha} - \mathfrak{D}_\varepsilon^\alpha \quad (3.20)$$

For  $q_\alpha$ , we currently only consider the parallel heat flux  $q_{\parallel,\alpha} = \kappa_{\parallel,\alpha} \nabla T_\alpha$  from the Spiter-Härm model. Additional heat fluxes  $Q_\alpha$  and sources  $S_{\varepsilon,\alpha}$  arise from the fluid closure.

#### 3.2.4. Charge balance

To complete the system, a last equation on the charge balance is needed. This approach is equivalent to the vorticity conservation equation from Eq. 2.44. Because of the quasineutrality assumption the volume charge  $\rho$  is assumed to be 0 and charge conservation is ensured if the total current divergence is 0.

$$\nabla \cdot \mathbf{j} = 0 \quad (3.21)$$

The total current is due to charge transport by plasma species. It is hence calculated as:

$$\mathbf{j} = \sum_\alpha Z_\alpha n_\alpha \mathbf{u}_\alpha \quad (3.22)$$

As the current is directly linked to the plasma species transport, it is decomposed into the same terms as the velocities in equations 2.38 and 2.39. The "E cross B" drift is the same for all species therefore its contribution to the current vanishes with the quasineutrality assumption. The "grad B", parallel pressure and the polarization current from the Reynold's stress tensor are directly calculated from the corresponding drift velocities:

$$\mathbf{j}_{\nabla B} = \sum_{\alpha} Z_{\alpha} n_{\alpha} \mathbf{u}_{\nabla B, \alpha} \quad \mathbf{j}_{\pi} = -\frac{1}{3} \sum_i Z_i \frac{\pi_{\parallel, i}}{T_i} \mathbf{u}_{\nabla B, i} \quad \mathbf{j}_{\Pi} = \sum_{\alpha} Z_{\alpha} n_{\alpha} \mathbf{u}_{\Pi, \alpha} \quad (3.23)$$

Neglecting curvature terms, we can derive an expression for the perpendicular polarization current from Eq. 2.42.

$$\mathbf{j}_p = -\partial_t \boldsymbol{\omega}_s - \sum_i Z_i \nabla \cdot (\mathbf{u}_i^{(0)} \otimes \boldsymbol{\omega}_i) \quad (3.24)$$

with:  $\boldsymbol{\omega}_s = \sum_i Z_i \boldsymbol{\omega}_i$

Only the zero-th order drift velocities from Eq. 2.38 contribute to the polarization current. The problem is not solved on  $\mathbf{j}$  itself but on the vorticity defined as  $\Omega = \nabla \cdot \boldsymbol{\omega}_s$  which gives the expression on  $\mathbf{j}_p$ :

$$\nabla \cdot \mathbf{j}_p = -\partial_t \Omega + \nabla \cdot \sum_i Z_i \nabla \cdot (\mathbf{u}_i^{(0)} \otimes \boldsymbol{\omega}_i) = -\partial_t \Omega \quad (3.25)$$

The divergence of the total current can then be transformed into a transport equation on the vorticity:

$$\begin{aligned} & \nabla \cdot \mathbf{j} = 0 \\ \Leftrightarrow & -\nabla \cdot \mathbf{j}_p = \nabla \cdot (j_{\parallel} \mathbf{b} + \mathbf{j}_{\nabla B} + \mathbf{j}_{\perp, \Pi} + \mathbf{j}_{\pi}) \\ \Leftrightarrow & \partial_t \Omega = \nabla \cdot \sum_i Z_i \nabla \cdot (\mathbf{u}_i^{(0)} \otimes \boldsymbol{\omega}_i) + \nabla \cdot (j_{\parallel} \mathbf{b} + \mathbf{j}_{\nabla B} + \mathbf{j}_{\perp, \Pi} + \mathbf{j}_{\pi}) \end{aligned} \quad (3.26)$$

If this equation is combined with Eq. 2.42 we get :

$$\begin{aligned} \boldsymbol{\omega}_i &= \frac{m_i}{Z_i B^2} \left( n_i \nabla_{\perp} \Phi + \frac{1}{Z_i} \nabla_{\perp} \left( p_i - \frac{\pi_{\parallel, i}}{3} \right) \right) - \frac{m_i}{Z_i^2 B^2} \mathbf{s}_{u_{\perp, i}} \\ \Leftrightarrow & \sum_i Z_i \boldsymbol{\omega}_i = \sum_i Z_i \left[ \frac{m_i}{Z_i B^2} \left( n_i \nabla_{\perp} \Phi + \frac{1}{Z_i} \nabla_{\perp} \left( p_i - \frac{\pi_{\parallel, i}}{3} \right) \right) - \frac{m_i}{Z_i^2 B^2} \mathbf{s}_{u_{\perp, i}} \right] \\ \Leftrightarrow & \Omega = \nabla \cdot \sum_i \left[ \frac{m_i}{B^2} \left( n_i \nabla_{\perp} \Phi + \nabla_{\perp} \left( p_i - \frac{\pi_{\parallel, i}}{3} \right) \right) - \frac{m_i}{Z_i B^2} \mathbf{s}_{u_{\perp, i}} \right] \\ \Leftrightarrow & \partial_t \Omega = \nabla \cdot \left[ \frac{m_i n_i}{B^2} \partial_t \nabla_{\perp} \Phi \right] + \partial_t \Omega_{p_i} - \mathfrak{D}_{\Omega} \\ \Leftrightarrow & \nabla \cdot \left[ \frac{m_i n_i}{B^2} \partial_t \nabla_{\perp} \Phi \right] = \nabla \cdot (j_{\parallel} \mathbf{b} + \mathbf{j}_{\nabla B} + \mathbf{j}_{\perp, \Pi} + \mathbf{j}_{\pi}) - \partial_t \Omega_{p_i} - \mathfrak{D}_{\Omega} \end{aligned} \quad (3.27)$$

In this calculation we used the Boussinesq approximation and the Einstein summation over the ion index  $i$  allows for a more compact expression. Since we express a conservation on the vorticity  $\Omega$ , we also introduced an anomalous diffusion term  $\mathfrak{D}_{\Omega}$ . All pressure terms are regrouped in  $\Omega_{p_i}$ :

$$\Omega_{p_i} = \nabla \cdot \sum_i \left( \frac{m_i}{Z_i B^2} \nabla_{\perp} [n_i T_i] \right) \quad (3.28)$$

The parallel current density is calculated from the generalized Ohm's law neglecting the electron mass (for now) and using Spitzer-Härm resistivity  $\eta_{\parallel}$ :

$$j_{\parallel} = \sigma_{\parallel} \left( E_{\parallel} + \frac{\nabla_{\parallel} p_e}{n_e} + 0.71 \nabla_{\parallel} T_e \right) \quad \text{with:} \quad \sigma_{\parallel} = 1/\eta_{\parallel} \quad (3.29)$$

For now, we assume a static magnetic field and define the parallel electric field as the negative gradient of the electrostatic potential in parallel direction  $E_{\parallel} = -\nabla_{\parallel} \Phi$ . With the electron pressure  $p_e = n_e T_e$ , we get:

$$\frac{1}{n_e} \nabla_{\parallel} p_e = T_e \nabla_{\parallel} \log(n_e) + \nabla_{\parallel} T_e$$

If we now inject Eq. 3.29 into the vorticity equation Eq. 3.27, we obtain:

$$\nabla \cdot \left[ \frac{m_i n_i}{B^2} \partial_t \nabla_{\perp} \Phi \right] = \nabla \cdot \sigma_{\parallel} \left[ -\nabla_{\parallel} \Phi + T_e \nabla_{\parallel} \log(n_e) + 1.71 \nabla_{\parallel} T_e \right] \mathbf{b} + F_{\Omega} \quad (3.30)$$

where  $F_{\Omega} = \nabla \cdot (\mathbf{j}_{\nabla B} + \mathbf{j}_{\Pi} + \mathbf{j}_{\pi}) - \partial_t \Omega_{p_i} - \mathcal{D}_{\Omega}$  regroups the remaining terms. The vorticity equation gives a relation for the electric potential  $\Phi$ , required to calculate "ExB" drifts and therefore essential to simulate plasma turbulence. Because of the low resistivity  $\eta_{\parallel}$ , this problem is actually numerically hard to solve. Explicit approaches are then strongly constrained by a timestep size of the order of the collision time. Implicit approaches have to handle a numerically difficult problem, with two Laplacian operators, one perpendicular and one parallel, with a high anisotropy because of the unfavorable ratio  $\sigma_{\parallel} B^2 / m_i n_i$  between the respective diffusion coefficients. The hardness to solve the system is a major obstacle for turbulent simulations on larger tokamaks because of prohibitive solve times of iterative solvers. Hotter scenarios, as they would occur in fusion-relevant devices, pose an additional problem as  $\eta_{\parallel} \propto T_e^{-1.5}$ , resulting in an even poorer numerical condition of the problem.

### 3.3. Ingredients for electromagnetism

Until now we have expressed the SOLEDGE3X transport equations as they are used in the existing electrostatic version of the code. It lays the framework on which we are now going to build the electromagnetic model. As demonstrated in the previous Sec. 2.3, it consists of three key elements: electron inertia, magnetic induction and flutter. In this section, each of the ingredients will be introduced separately, to clearly identify the impact of each on the vorticity equation.

### 3.3.1. Electron inertia

The first element to the electromagnetic model is the electron inertia term in the generalized Ohm's law. To properly derive this term, we start with the parallel momentum conservation equations for electrons 3.31 and ions 3.32.

$$m_e \partial_t \gamma_e + m_e \nabla \cdot (\gamma_{\parallel,e} \mathbf{u}_e) = -n_e E_{\parallel} - \nabla_{\parallel} p_e - \mathbf{b} \cdot \nabla \cdot \boldsymbol{\Pi}_e + S_{\gamma,e} + R_{\parallel,e} - m_e \mathfrak{D}_{\gamma}^e \quad (3.31)$$

$$m_i \partial_t \gamma_i + m_i \nabla \cdot (\gamma_{\parallel,i} \mathbf{u}_i) = +Z_i n_i E_{\parallel} - \nabla_{\parallel} p_i - \mathbf{b} \cdot \nabla \cdot \boldsymbol{\Pi}_i + S_{\gamma,i} + R_{\parallel,i} - m_i \mathfrak{D}_{\gamma}^i \quad (3.32)$$

Next we multiply the equation for the electrons by  $-1/m_e$  and the equation for ions  $Z_i/m_i$ . If we then take the sum over all species (electrons and all ions), we get a conservation equation for the parallel current density  $j_{\parallel} = \sum_{\alpha} Z_{\alpha} \gamma_{\parallel,\alpha}$  (defining  $Z_e = -1$ ).

$$\begin{aligned} \frac{m_e}{n_e} \partial_t j_{\parallel} + \frac{m_e}{n_e} \nabla \cdot (Z_i \gamma_{\parallel,i} \mathbf{u}_i - \gamma_{\parallel,e} \mathbf{u}_e) &= \left(1 + \frac{m_e}{m_i} \frac{Z_i^2 n_i}{n_e}\right) E_{\parallel} + \frac{1}{n_e} \nabla_{\parallel} p_e - \frac{m_e}{m_i} \frac{Z_i}{n_e} \nabla_{\parallel} p_i \\ &\quad + \frac{1}{n_e} \mathbf{b} \cdot \nabla \cdot \boldsymbol{\Pi}_e - \frac{m_e}{m_i} \frac{Z_i}{n_e} \mathbf{b} \cdot \nabla \cdot \boldsymbol{\Pi}_i - \frac{1}{n_e} S_{\gamma,e} + \frac{m_e}{m_i} \frac{Z_i}{n_e} S_{\gamma,i} \\ &\quad + \frac{1}{n_e} R_{\parallel,e} + \frac{m_e}{m_i} \frac{Z_i}{n_e} R_{\parallel,i} + \frac{m_e}{n_e} \mathfrak{D}_{\gamma}^e - \frac{m_e Z_i}{n_e} \mathfrak{D}_{\gamma}^i \end{aligned} \quad (3.33)$$

Here the sum over ion species is not written explicitly, but every term involving the index  $i$  should be seen as a sum over all ions. Braginskii's closure provides a neat expression for the electron friction terms  $R_{\parallel,\alpha}$ . It involves an Ohmic term, caused by collisions between charged particles that dissipate the current, and a thermoelectric force, where a temperature gradient can create currents.

$$R_{\parallel,e} = n_e [0.71 \nabla_{\parallel} T_e - \eta_{\parallel} j_{\parallel}] \quad (3.34)$$

If we neglect all terms involving the electron mass, we exactly recover the electrostatic Ohm law from Eq. 3.29. The aim of this section is to consider a finite  $m_e$ , so we keep all terms. To truly obtain a transport equation on the current, we need to reformulate the advection term. There is no effective advection velocity for  $j_{\parallel}$  readily available and the poor ambipolar definition of  $\gamma_{\parallel,e}$  is of little help here. We can instead develop this term to obtain a formulation where  $j_{\parallel}$  is advected by the electron velocity:

$$\nabla \cdot \left( \sum_i Z_i \gamma_{\parallel,i} \mathbf{u}_i - \gamma_{\parallel,e} \mathbf{u}_e \right) = \nabla \cdot \left( \sum_i Z_i \gamma_{\parallel,i} (\mathbf{u}_i - \mathbf{u}_e) - j_{\parallel} \mathbf{u}_e \right) \quad (3.35)$$

If we now rewrite Eq. 3.33 with the considerations above, we get:

$$\frac{m_e}{n_e} \partial_t j_{\parallel} + \frac{m_e}{n_e} \nabla \cdot (j_{\parallel} \mathbf{u}_e) - \frac{m_e}{n_e} \nabla \cdot \left( \sum_i Z_i \gamma_i \mathbf{u}_e \right) = E_{\parallel} + \frac{\nabla_{\parallel} p_e}{n_e} + 0.71 \nabla_{\parallel} T_e - \eta_{\parallel} j_{\parallel} + \sum_i Z_i \partial_t \gamma_i - \frac{m_e}{n_e} \mathfrak{D}_j^e \quad (3.36)$$

With this transport equation on the parallel current, the anomalous diffusion is also calculated with  $j_{\parallel}$ . The term  $\sum_i Z_i \partial_t \gamma_i$  contains all other terms in Eq. 3.33, but they do not need to be explicated in the implementation as they are already known from the ion momentum conservation equations. Numerical experiments have proven the necessity to carefully treat all the terms, especially the advection of  $j_{\parallel}$ , to avoid numerical instabilities.

If we now combine Ohm's with electron inertia with the electrostatic vorticity equation 3.30, we obtain following system:

$$\begin{cases} \nabla \cdot \left[ \frac{m_i n_i}{B^2} \partial_t \nabla_{\perp} \Phi \right] - \nabla \cdot [j_{\parallel} \mathbf{b}] = F_{\Omega} \\ j_{\parallel} + \frac{\sigma_{\parallel} m_e}{n_e} [\partial_t j_{\parallel} + \nabla \cdot (j_{\parallel} \mathbf{u}_e)] = \sigma_{\parallel} (-\nabla_{\parallel} \Phi + T_e \nabla_{\parallel} \log n_e + 1.71 \nabla_{\parallel} T_e) \\ \qquad \qquad \qquad + \frac{\sigma_{\parallel} m_e}{n_e} \left[ \sum_i Z_i [\nabla \cdot (\gamma_i \mathbf{u}_e) + \partial_t \gamma_i] - \mathfrak{D}_j^e \right] \end{cases} \quad (3.37)$$

For better readability let us express the system in matrix form, where  $\circ$  shall be replaced by the corresponding field within operators and all advection terms in  $j_{\parallel}$  and  $\gamma_i$  are regrouped in the term  $\mathcal{A}_j$ .

$$\begin{pmatrix} \nabla \cdot \left[ \frac{m_i n_i}{B^2} \partial_t \nabla_{\perp} \circ \right] & -\nabla \cdot [\circ \mathbf{b}] \\ \sigma_{\parallel} \nabla_{\parallel} \circ & 1 + \frac{\sigma_{\parallel} m_e}{n_e} \partial_t \circ \end{pmatrix} \begin{pmatrix} \Phi \\ j_{\parallel} \end{pmatrix} = \begin{pmatrix} F_{\Omega} \\ \sigma_{\parallel} \left( T_e \nabla_{\parallel} \log n_e + 1.71 \nabla_{\parallel} T_e - \frac{m_e}{n_e} \mathfrak{D}_j^e \right) + \mathcal{A}_j \end{pmatrix} \quad (3.38)$$

### 3.3.2. Electromagnetic induction

Magnetic induction is added to the system with the term  $\partial_t A_{\parallel}$  to the definition of the parallel electric field. It appears in the generalized Ohm's law for the parallel current 3.29, which in turn is member of the vorticity equation 3.26.

$$E_{\parallel} = -\nabla_{\parallel} \Phi - \beta_0 (\partial_t A_{\parallel} + \mathfrak{D}_A) \quad (3.39)$$

The parallel magnetic vector potential  $A_{\parallel}$  was never calculated before and needs to be introduced to the system. In Ampère's law under the Coulomb gauge,  $j_{\parallel}$  is equal to the perpendicular diffusion of  $A_{\parallel}$ :

$$\nabla \cdot \nabla_{\perp} A_{\parallel} = -j_{\parallel} \quad (3.40)$$

As we evolve the magnetic potential together with the electric potential gradient, we also introduce an anomalous diffusion on  $A_{\parallel}$  by the term  $\mathfrak{D}_A$ . It does not have any physical meaning and primarily serves to numerically stabilize the system from sub-mesh instabilities. The electric potential  $\Phi$  is thus implicitly linked to  $j_{\parallel}$  and  $A_{\parallel}$  and all three unknowns need to be solved in one common system. To summarize, the new set of equations reads:

$$\left\{ \begin{array}{l} \nabla \cdot \left[ \frac{m_i n_i}{B^2} \partial_t \nabla_{\perp} \Phi \right] - \nabla \cdot [j_{\parallel} \mathbf{b}] = F_{\Omega} \\ j_{\parallel} = \sigma_{\parallel} (-\nabla_{\parallel} \Phi - \beta_0 \partial_t A_{\parallel} - \beta_0 \mathfrak{D}_A + T_e \nabla_{\parallel} \log n_e + 1.71 \nabla_{\parallel} T_e) \\ \nabla \cdot \nabla_{\perp} A_{\parallel} = -j_{\parallel} \end{array} \right. \quad (3.41)$$

It can also be compactly expressed in matrix form:

$$\begin{aligned} & \begin{pmatrix} \nabla \cdot \left[ \frac{m_i n_i}{B^2} \partial_t \nabla_{\perp} \circ \right] & -\nabla \cdot [\circ \mathbf{b}] & 0 \\ \sigma_{\parallel} \nabla_{\parallel} \circ & 1 \circ & \sigma_{\parallel} \beta_0 \partial_t \circ \\ 0 & 1 & \nabla \cdot [\nabla_{\perp} \circ] \end{pmatrix} \begin{pmatrix} \Phi \\ j_{\parallel} \\ A_{\parallel} \end{pmatrix} \\ &= \begin{pmatrix} F_{\Omega} \\ \sigma_{\parallel} (T_e \nabla_{\parallel} \log n_e + 1.71 \nabla_{\parallel} T_e - \beta_0 \mathfrak{D}_A) \\ 0 \end{pmatrix} \end{aligned} \quad (3.42)$$

These equations use Ohm's law without the electron inertia term previously introduced in ssec:ModelElectronInertia. It is obviously possible (and even necessary) to include the temporal  $j_{\parallel}$  in the electromagnetic equations and it is recommended to do so. To allow for maximal flexibility, any combination of  $\Phi$  with  $A_{\parallel}$  and/or  $j_{\parallel}$  can be used and we will discuss each of these combinations in later chapters.

### 3.3.3. Electromagnetic flutter

Due to the strong anisotropy in tokamaks, most edge turbulence codes rely on alignment to the magnetic equilibrium (see discussion in Ref.[82]). However, in the electromagnetic model, small perturbations of  $\mathbf{B}_{eq}$  can exist and are driven by fluctuations of  $A_{\parallel}$  such as  $\tilde{\mathbf{B}} = \nabla \times (\tilde{A}_{\parallel} \mathbf{b})$ . Therefore, these fluctuations of  $A_{\parallel}$  have to be estimated and  $A_{\parallel}$  cannot be used directly. Indeed, the diamagnetic current induced by the evolution of the full plasma pressure is balanced by a stationary background parallel current, the Pfirsch-Schlüter current, which induces a stationary part of significant amplitude in  $A_{\parallel}$  through Ampere's law (Eq. 3.40). This latter is denoted  $A_{\parallel,0}$ , and corresponds to the Grad-Shafranov shift due to Pfirsch-Schlüter currents that are accounted for in the parallel current. This shift  $A_{\parallel,0}$  is obviously accounted for in  $B_{eq}$ , and therefore it has

### 3. The physical model – 3.3. Ingredients for electromagnetism

to be subtracted from  $A_{\parallel}$  in nonlinear parallel operators. This is done in this work by simply removing the toroidal average as proposed by Ref.[33] in the GBS code:

$$\tilde{A}_{\parallel} = A_{\parallel} - \langle A_{\parallel} \rangle_{\varphi} \quad (3.43)$$

Therefore, the flutter is computed as follows:

$$\nabla \times (\mathbf{A}_{\parallel,0} + \tilde{A}_{\parallel} \mathbf{b}_{eq}) = \mathbf{B}_{eq} + \tilde{\mathbf{B}} \quad (3.44)$$

This leads to:

$$\tilde{\mathbf{b}} = \beta_0 \left( -\frac{\mathbf{b}_{eq} \times \nabla \tilde{A}_{\parallel}}{\|\mathbf{B}\|} + \frac{\tilde{A}_{\parallel} \nabla \times \mathbf{b}_{eq}}{\|\mathbf{B}\|} \right) \quad (3.45)$$

The gradient  $\nabla \tilde{A}_{\parallel}$  scales with the characteristic turbulent length  $1/L_{\perp}$  and the curl  $\nabla \times \mathbf{b}$  with the machine dimension  $1/a$ . Therefore,  $\frac{\mathbf{b}_{eq} \times \nabla \tilde{A}_{\parallel}}{\|\mathbf{B}\|}$  is the main contributor to the flutter field.

Note that Hager *et al.*[41] have suggested an additional time-averaged  $\langle A_{\parallel} \rangle_{\varphi,t}$  to evaluate fluctuations in the parallel electromagnetic potential, arguing that turbulent structures might appear at the same position on all poloidal planes and should therefore not be removed in the flutter calculation. This approach has been used in recent work in the GRILLIX code [108], but was not adopted in the present work, as it was estimated that the gain in accuracy did not compensate for the additional computation and memory costs.

The perturbed magnetic unit field  $\tilde{\mathbf{b}}$  is calculated at the beginning of each timestep and added to the equilibrium unit vector  $\mathbf{b}_{eq}$ . The complete vector  $\mathbf{b} = \mathbf{b}_{eq} + \tilde{\mathbf{b}}$  is then used in all parallel advection, gradient, and diffusion terms. Since we base our calculations on plasma fields from the previous timestep, this perturbation can be seen as an additional first-order drift in the equations. The expression in the framework of the conservation equations does not change with flutter, but the underlying definition of parallel gradients and divergence surely increases in complexity.

#### 3.3.4. Full electromagnetic vorticity system

Let us now consider the electromagnetic system with electron inertia, magnetic induction and flutter. The full vorticity system is then given by, where flutter is included in the direction of the magnetic field  $\mathbf{b}$ :

$$\left\{ \begin{array}{l} \nabla \cdot \left[ \frac{m_i n_i}{B^2} \partial_t \nabla_{\perp} \Phi \right] - \nabla \cdot [j_{\parallel} \mathbf{b}] = F_{\Omega} \\ j_{\parallel} + \frac{\sigma_{\parallel} m_e}{n_e} [\partial_t j_{\parallel} + \nabla \cdot (j_{\parallel} \mathbf{u}_e)] = \sigma_{\parallel} (-\nabla_{\parallel} \Phi + T_e \nabla_{\parallel} \log n_e + 1.71 \nabla_{\parallel} T_e) \\ \quad - \sigma_{\parallel} \beta_0 (\partial_t A_{\parallel} + \mathcal{D}_A) \\ \quad + \frac{\sigma_{\parallel} m_e}{n_e} \left[ \sum_i Z_i [\nabla \cdot (\gamma_i \mathbf{u}_e) + \partial_t \gamma_i] - \mathcal{D}_j^e \right] \\ \nabla \cdot \nabla_{\perp} A_{\parallel} = - j_{\parallel} \end{array} \right. \quad (3.46)$$

We then have a system over the parallel current  $j_{\parallel}$  and the potential fields  $\Phi$  and  $A_{\parallel}$ . In matrix form, this final system reads:

$$\begin{aligned} & \begin{pmatrix} \nabla \cdot \left[ \frac{m_i n_i}{B^2} \partial_t \nabla_{\perp} \circ \right] & -\nabla \cdot [\circ \mathbf{b}] & 0 \\ \sigma_{\parallel} \nabla_{\parallel} \circ & 1 + \frac{\sigma_{\parallel} m_e}{n_e} \partial_t \circ & \sigma_{\parallel} \beta_0 \partial_t \circ \\ 0 & 1 & \nabla \cdot [\nabla_{\perp} \circ] \end{pmatrix} \begin{pmatrix} \Phi \\ j_{\parallel} \\ A_{\parallel} \end{pmatrix} \\ &= \begin{pmatrix} F_{\Omega} \\ \sigma_{\parallel} \left( T_e \nabla_{\parallel} \log n_e + 1.71 \nabla_{\parallel} T_e - \frac{m_e}{n_e} \mathcal{D}_j^e - \beta_0 \mathcal{D}_A \right) + \mathcal{A}_j \\ 0 \end{pmatrix} \end{aligned} \quad (3.47)$$

This system is a differential-algebraic equation (DAE), where the vorticity equation and Ohm's law are differential equations and Ampère's law forms an algebraic constraint on  $A_{\parallel}$  and  $j_{\parallel}$ .

$$\left\{ \begin{array}{l} 0 = f(\partial_{\perp}^2 \partial_t \Phi, \partial_{\parallel} j_{\parallel}, \psi, \theta, \varphi, t) \\ 0 = g(\partial_t j_{\parallel}, \partial_t A_{\parallel}, \partial_{\parallel} \Phi, j_{\parallel}, \psi, \theta, \varphi) \\ 0 = h(\partial_{\perp}^2 A_{\parallel}, j_{\parallel}) \end{array} \right. \quad (3.48)$$

Since the function  $h$  needs to be differentiated once to obtain the terms  $\partial_t j_{\parallel}$  and  $\partial_t A_{\parallel}$  from function  $g$ , the system is a Hessenberg index-1 DAE. Such systems are generally stiff and usually require appropriate implicit solvers that work best if an analytic expression of the Jacobian matrix is provided, which is a non-trivial task for our system. Consistent initial conditions on  $A_{\parallel}$  and  $j_{\parallel}$  are also essential to avoid bad numerical behavior or even divergence. One common solution is to reformulate the system into a standard PDE by eliminating the algebraic constraint. The obvious path here is to solve  $h$  for  $j_{\parallel}$  and replace all occurrences of  $j_{\parallel}$  by  $\partial_{\perp}^2 A_{\parallel}$ . However, a triple spatial derivative  $\partial_{\parallel} \partial_{\perp}^2 A_{\parallel}$  then appears in the vorticity equation, which adds stiffness, leads to non-physical oscillations, imposes a higher regularity in the solution (at least  $C^3$ ), and requires complex boundary conditions to avoid boundary layers and singularities. Instead, we can solve for  $j_{\parallel}$  and substitute the solution into the functions  $f$  and  $h$ . Their expressions then involve a large number of terms, but none of them exceeds 2nd order spatial derivatives, and the system remains well-defined. It will

### 3. The physical model – 3.4. Boundary conditions

also introduce the differential terms  $\partial_t j_{\parallel}$  and  $\partial_t A_{\parallel}$  to Ampère's law, such that the new system is effectively a coupled, first-order in time PDE. The abstract form of this new formulation is then:

$$\begin{cases} 0 = \hat{f}(\partial_{\perp}^2 \partial_t \Phi, \partial_{\parallel} \partial_t A_{\parallel}, \partial_{\parallel} \partial_t j_{\parallel}, \partial_{\parallel}^2 \Phi, \psi, \theta, \varphi, t) \\ 0 = \hat{h}(\partial_t A_{\parallel}, \partial_t j_{\parallel}, \partial_{\perp}^2 A_{\parallel}, \partial_{\parallel} \Phi, j_{\parallel}, \psi, \theta, \varphi) \end{cases} \quad (3.49)$$

We still need to solve  $g$  for  $j_{\parallel}$  to have an expression for  $\partial_t j_{\parallel}$ , which can be done implicitly in a separate step. Details about the exact implementation are given in Sec. 4.3 of the next chapter.

## 3.4. Boundary conditions

Boundary conditions are required at the tokamak wall and at the core edge boundary. They need to be defined in both parallel and perpendicular directions to the magnetic field lines.

- In the perpendicular direction, zero Neumann boundary conditions for all plasma variables, i.e.,  $\partial_{\perp}(.) = 0$ , are imposed both at the wall and the core edge boundary except for the electromagnetic potential, which is fixed to  $A_{\parallel} = 0$  at the two radial boundaries.
- In the parallel direction, boundary conditions are derived from the generalized Bohm-Chodura sheath boundary conditions [92]. They model the physics of the sheath located next to the limiter wall, where many assumptions used to derive the fluid models (quasi-neutrality, drift-ordering) are no longer valid. They can be expressed as:

- $|\mathbf{v} \cdot \mathbf{n}_{\text{wall}}| \geq |c_s \mathbf{b} \cdot \mathbf{n}_{\text{wall}}|$  with  $\mathbf{n}_{\text{wall}}$  being the outward normal to the wall, meaning that the outgoing velocity normal to the wall is larger than the parallel sound speed normal to the wall. This property guarantees that the total plasma velocity is oriented outward.
- $\phi_{\mathcal{E},se} = \gamma T \phi_{n,se}$ . For each species,  $\phi_{\mathcal{E},se}$  is the total energy flux at the sheath entrance,  $\phi_{n,se}$  is the particle flux at the sheath entrance, and  $\gamma$  is the sheath transmission factor equal to 2.5 for ions and 4.5 for electrons.
- $j_{\text{wall}} = \left[ 1 - \exp\left(\Lambda - \frac{\phi}{T_e}\right) \right] \phi_{n,se}$  is the total plasma current on the wall. The ion saturation current is computed from ion particle fluxes  $\phi_{n,se}$ , and  $\Lambda$  denotes the normalized potential drop in the sheath with  $\Lambda \sim 3$ .
- $A_{\parallel} = 0$  at the magnetic pre-sheath entrance.

## 4. Numerical Implementation

### Chapter Summary

The SOLEDGE3X mesh is aligned with magnetic flux surfaces and uses a multi-domain decomposition to handle singularities at X-points. In the FVM approach, time integration is performed with an implicit-explicit scheme, where all collisional processes and the new Alfvénic and electron inertial dynamics are solved implicitly. To benefit from first-order spatial derivatives, the new fields  $A_{\parallel}$  and  $j_{\parallel}$  are defined on a poloidally and toroidally staggered grid. This setup requires new discrete operators to accommodate the divergence  $|\nabla \cdot X^{stg} \mathbf{b}|_{col}$  of a staggered field onto a collocated grid and parallel gradients  $|\mathbf{b} \cdot \nabla X^{col}|_{stg}$  of collocated fields onto the staggered grid for the electromagnetic vorticity equation, as well as a staggered-to-staggered perpendicular Laplacian operator  $|\nabla \cdot \nabla_{\perp} X^{stg}|_{stg}$  for Ampère's law. With four staggered radial cell faces facing the X-point at once, Neumann boundary conditions are applied there.

The new Ampère's law is solved along with the vorticity equation in a coupled 3D system for  $\Phi$  and  $A_{\parallel}$ :

$$\begin{pmatrix} \nabla \cdot [D_{\perp} \nabla_{\perp} \circ] + \nabla \cdot [D_{\parallel} \nabla_{\parallel} \circ \mathbf{b}] & \frac{\beta_0}{\delta_t} \nabla \cdot [D_{\parallel} \circ \mathbf{b}] \\ -D_{\parallel} \nabla_{\parallel} \circ & \frac{\beta_0}{\delta_t} D_{\parallel} \circ -\nabla \cdot [\nabla_{\perp} \circ] \end{pmatrix} \begin{pmatrix} \Phi^{n+1} \\ A_{\parallel}^{n+1} \end{pmatrix} = \begin{pmatrix} \nabla \cdot [D_t j_{\parallel}^n \mathbf{b}] + \text{RHS}^{\Phi} \\ D_t j_{\parallel}^n + \text{RHS}^{A_{\parallel}} \end{pmatrix}$$

with:  $D_{\perp} = \frac{m_i n_i}{B^2 \delta_t}, D_{\parallel} = \frac{1}{\eta_{\parallel} + \mu}, D_t = \frac{\mu}{\eta_{\parallel} + \mu}$ , and  $\mu = \frac{m_e}{(n_e \delta_t)}$

Electron inertia mitigates the anisotropy between perpendicular and parallel Laplacian operators, acting as a lower bound for resistivity  $\eta_{\parallel}$ , and significantly improves the condition number in high-temperature plasmas. However, coupling with  $A_{\parallel}$  worsens the matrix condition.

Flutter adds a radial component to the magnetic field, requiring adjustments to all parallel operators in the flux-aligned geometry. For advection, flutter is treated as an additional drift velocity. The off-diagonal terms in the vorticity system increase coupling between  $\Phi$  and  $A_{\parallel}$ , raising computational costs. To ensure consistency, the discrete parallel Laplacian on  $\Phi$  must match the combination of divergence with gradient operators. For parallel viscous forces and heat conductivity, a new discrete operator was developed to limit radial numerical diffusion, but solving these problems now requires a full-domain 3D solver, increasing the computational cost.

The SOLEDGE3X framework uses a finite-volume method (FVM) with an implicit-explicit time integration scheme and variable stepsize (VSIMEX)[103]. The second-order conservative FVM scheme associated with a 3rd-order WENO reconstruction and Donat, Marquina fluxes for a modified Riemann solver for the advection terms to handle both shocks and complicated smooth solution structures [9, 97]. In turbulence simulations, we focus on timescales slower than the cyclotronic frequency  $\omega_C$ , allowing explicit time-stepping for advection, friction, pressure, and energy source terms. This multi-step method is implemented for orders 1 to 3, with the timestep updated to match a targeted CFL value.

Ionization/recombination processes, resistive and viscous effects from the Spitzer-Härm model, electron inertia, and Alfvén dynamics involve faster dynamics than the ion cyclotronic time, and would strongly restrict the timestep size. These terms are therefore solved implicitly. To reduce complexity, they can be decoupled and solved sequentially for density, parallel velocity, temperature, and the vorticity equation.

This chapter details the implementation of the new electromagnetic model in this implicit-explicit framework. Sec. 4.1 gives an overview of the field-aligned meshing and curvilinear coordinate system. Sec. 4.2 introduces the poloidally and toroidally staggered mesh for the new fields  $A_{\parallel}$  and  $j_{\parallel}$ , with the necessary discrete operators. Sec. 4.3 discusses the new electromagnetic vorticity equation, solved implicitly on  $\Phi$  and  $A_{\parallel}$ . Finally, Sec. 4.4 addresses the impact of the radial magnetic field component from flutter on all parallel operators.

## 4.1. Geometrical consideration

### 4.1.1. Coordinate system

Let  $R_0$  be the major radius on the magnetic axis and  $(R, Z, \varphi)$  a fixed cylindrical coordinate system. The magnetic equilibrium is assumed to be toroidally symmetric and to encompass both closed and open flux surfaces with singularities at one or more X-points. The 2D equilibrium magnetic field  $\mathbf{B}_{eq} = B_{eq}\mathbf{b}_{eq}$  is a combination of a toroidal field,  $\mathbf{B}_{eq,\varphi}$ , and a poloidal field,  $\mathbf{B}_{eq,p}$ , as described in Sec. 1.1.3:

$$\mathbf{B}_{eq} = \mathbf{B}_{eq,\varphi} + \mathbf{B}_{eq,p} = F\nabla\varphi + \nabla\Psi \times \nabla\varphi \quad (4.1)$$

where  $\varphi$  is the toroidal angle,  $F$  a toroidal flux function, and  $\Psi(R, Z)$  a poloidal flux function from which  $\mathbf{B}_{eq,\varphi}$  and  $\mathbf{B}_{eq,p}$  are respectively derived (see Sec. 1.1.4). The iso- $\Psi$  surfaces are tangent to the magnetic field and  $\Psi$  labels flux surfaces (one value for each flux surface). It is thus natural to define a curvilinear system of coordinates denoted  $(\psi, \theta, \varphi)$ .  $\psi$  defines a radial coordinate based on the poloidal magnetic flux  $\Psi$ , which is by construction always perpendicular to a magnetic flux surface.  $\theta$  denotes a curvilinear abscissa along the poloidal direction in the  $(R, Z)$  plane that defines the poloidal plane, i.e., along iso- $\Psi$  surfaces and orthogonal to  $\nabla\varphi$ .

#### 4. Numerical Implementation – 4.1. Geometrical consideration

In the base  $(\mathbf{e}_\psi, \mathbf{e}_\theta, \mathbf{e}_\varphi)$  associated with  $(\psi, \theta, \varphi)$ , the magnetic equilibrium field is written as:

$$\mathbf{B}_{eq} = B_{eq,p} \frac{\mathbf{e}_\theta}{|\mathbf{e}_\theta|} + B_{eq,\varphi} \frac{\mathbf{e}_\varphi}{|\mathbf{e}_\varphi|} \quad (4.2)$$

#### 4.1.2. Domain decomposition and mesh design

In order to keep a structured flux-surfaces aligned mesh for any magnetic equilibrium, the real domain is mapped into a Cartesian domain decomposed into multiple connected zones [97]. Each point of the domain is distinctly identified by the set of curvilinear coordinates  $[\psi, \theta, \varphi]$  defined in Sec. 4.1.1. The domain is segmented along the toroidal coordinate  $\varphi$ , into  $N_\varphi$  poloidal planes. Tables of data fields are provided for each subdomain. Ghost cells store the information on the neighborhood within a matrix that defines how these subdomains are connected to each other. Depending on the domain, these ghost cells contain either the values of the neighboring subdomains' fields or the values imposed by the boundary conditions. An example of the mesh and its zone decomposition is shown in Fig. 4.1, where the X-point requires six zones.

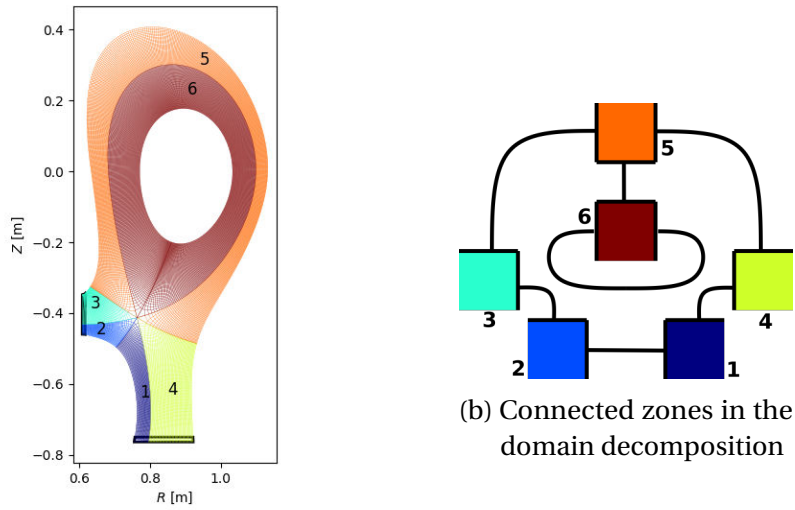


Figure 4.1.: Example of typical mesh and domain decomposition mapping the real domain (a) to a Cartesian multiple zones domain (b). Each colored zone is isomorphic to a cube, the lines connecting the edges indicate the neighbours mapping.

#### 4.1.3. Curvilinear coordinates

The flux-surface-aligned discretization involves a curved grid in poloidal  $\theta$  and toroidal  $\varphi$  directions. To map the real geometry to the orthonormal grid on each subdomain,

#### 4. Numerical Implementation – 4.1. Geometrical consideration

we require a metric transformation. The second chapter of the book by D'haeseleer *et al.*[19] describes well the numerical implications of curvilinear grids and serves as the basis of the present implementation.

Let  $U = [u^\psi, u^\theta, u^\varphi]^T$  be the three parameters that describe every point in the domain  $\Omega$  with respect to the curvilinear system of coordinates. On a torus, we can find an invertible transformation  $R$  that maps each possible  $U \in \Omega$  to a unique point in cartesian coordinates, thus:

$$\begin{bmatrix} x \\ y \\ z \end{bmatrix} = \mathbf{R}(u^\psi, u^\theta, u^\varphi) \quad (4.3)$$

If we fix one parameter and allow the two remaining to vary freely, we obtain the so-called coordinate surface. Analogously if we fix two parameters, we obtain the coordinate curve associated to the free parameter and an accommodating choice for the scalar values  $u^i$  is the curve length from an arbitrary reference point. At any point  $P \in \Omega$ , a local basis  $\mathbf{e}_\psi, \mathbf{e}_\theta, \mathbf{e}_\varphi$  can be defined by the tangents to the respective coordinate curves crossing this point. Consequently, the basis vectors are easily expressed as:

$$\mathbf{e}_\psi = \frac{\partial \mathbf{R}}{\partial u^\psi} \quad \mathbf{e}_\theta = \frac{\partial \mathbf{R}}{\partial u^\theta} \quad \mathbf{e}_\varphi = \frac{\partial \mathbf{R}}{\partial u^\varphi} \quad (4.4)$$

The parameter choice of  $u^i$  can be seen as the curve length and it might or might not be a unit length. The dimension index appears in subscript  $e_i$  to indicate that the basis vectors originate from a  $u^i$  located below the fraction line.

An alternative basis can be defined from the gradients of the parameters  $u^i$  which hence uses a superscript notation:

$$\mathbf{e}^\psi = \nabla u^\psi \quad \mathbf{e}^\theta = \nabla u^\theta \quad \mathbf{e}^\varphi = \nabla u^\varphi \quad (4.5)$$

These basis vectors are orthogonal to the respective coordinate surfaces at the point  $P$ . It can be shown that both basis are reciprocal, thus:

$$e^i \cdot e_j = \delta_j^i$$

where  $\delta_j^i$  is the Kronecker delta.

This leads to the introduction of the covariant (linked to subscripts) and contravariant (linked to the superscripts) components of a vector. As it is known from linear algebra, any vector  $\mathbf{v}$  can be expressed with respect to an arbitrary basis  $\tilde{\mathbf{e}}_i$  as  $\mathbf{v} = \tilde{v}_i \tilde{\mathbf{e}}_i$ . For the two previously introduced basis, the respective components of  $\mathbf{v}$  are given by:

$$\text{Covariant components: } v_i = \mathbf{v} \cdot \mathbf{e}_i \Rightarrow \mathbf{v} = v_i \mathbf{e}^i \quad (4.6)$$

$$\text{Contravariant components: } v^i = \mathbf{v} \cdot \mathbf{e}^i \Rightarrow \mathbf{v} = v^i \mathbf{e}_i \quad (4.7)$$

(4.8)

It is common practice to call the representation of  $\mathbf{v}$  using the co-/contravariant components the co-/contravariant vector of  $\mathbf{v}$  albeit the co- and contravariant vectors both naturally describe the same vector  $\mathbf{v}$ .

Next, we introduce the metric coefficients  $g_{ij} = \mathbf{e}_i \cdot \mathbf{e}_j$  and their reciprocal metric coefficients  $g^{ij} = \mathbf{e}^i \cdot \mathbf{e}^j$ . If available, they allow for an easy both-way conversion of contravariant to covariant vectors and consequently an easy change of basis.

$$v_i = g_{ij} v^j \quad \mathbf{e}_i = g_{ij} \mathbf{e}^j \quad (4.9)$$

$$v^i = g^{ij} v_j \quad \mathbf{e}^i = g^{ij} \mathbf{e}_j \quad (4.10)$$

It may be noted that the matrices formed by the indices  $i, j \in \{\theta, \psi, \varphi\}$  are each other's inverse matrix. Further details on the curvilinear metric applied to the magnetic configuration are given in App. ??.

## 4.2. The staggered mesh

In order to benefit from the first-order parallel derivative that separates the  $A_{\parallel}$  and  $j_{\parallel}$  from the other plasma fields  $\Phi$ ,  $n_e$ , and  $T_e$  (Eq. 3.46), these two variables are defined on a toroidally  $\varphi$  and poloidally  $\theta$  staggered grid. They are calculated at cell edges in the parallel direction and can be directly matched to the fluxes entering and leaving the collocated cells. One of the major benefits is to minimize numerical diffusion and preserve turbulent structures, following findings in FVM simulations for fluid mechanics [62]. In the radial  $\psi$  direction, we keep the collocated position as the only parallel gradient in  $\psi$  comes from the flutter term, which in nature is much smaller than the equilibrium field. If the mesh were also staggered in  $\psi$ , we would face strong numerical radial diffusion of parallel fluxes, defying the motivation of a staggered grid for  $A_{\parallel}$  and  $j_{\parallel}$ .

### 4.2.1. Description and notation

The scalar variable  $A_{\parallel}$  is the magnitude of the parallel magnetic vector potential that is a factor of the unit vector  $\mathbf{b}$  in direction of the externally induced magnetic field lines. By construction of the domain,  $\mathbf{b}$  has only components in  $\varphi$  and  $\theta$  directions. So far, all physical quantities are calculated on the collocated grid points at the domain

cell centers. In the newly introduced equation on  $A_{\parallel}$ , the magnetic vector potential appears homogeneous to the potential, pressure and temperature gradients and the additional  $A_{\parallel}$  term in the original equation states that the divergence of  $A_{\parallel}$  accounts for the change in vorticity. Thus,  $A_{\parallel}$  is always one spatial derivative away from the original quantities. As it is common in classical CFD simulation the velocity,  $A_{\parallel}$  is not defined on cell centers but on a staggered grid on the cell edges in  $\psi$ -direction. Because the magnetic field lines do not evolve in radial direction and only parallel gradients contribute to  $A_{\parallel}$ , its grid is only staggered in poloidal and toroidal directions. To distinguish quantities on both grids, the indexes  $[i_{\psi}, i_{\theta} - \frac{1}{2}, i_{\varphi} - \frac{1}{2}]$  describe discrete positions on the staggered grid.

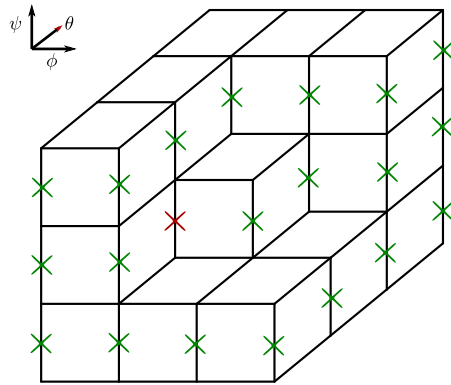


Figure 4.2.: General view of the staggered grid points marked as crosses on top of the collocated cells. The red cross at the position  $[i_{\psi}, i_{\theta} - \frac{1}{2}, i_{\varphi} - \frac{1}{2}]$  corresponds to the central cell with index  $[i_{\psi}, i_{\theta}, i_{\varphi}]$

In the following work, quantities evaluated at staggered grid points are indicated either by the superscript  $stg$  or by a  $-\frac{1}{2}$  shift in the index. This means that following notations are equivalent:

$$X_{[i_{\psi}, i_{\theta}, i_{\varphi}]}^{stg} = X_{[i_{\psi}, i_{\theta} - \frac{1}{2}, i_{\varphi} - \frac{1}{2}]} \quad \text{or} \quad X_{[i_{\psi}, i_{\theta} + 1, i_{\varphi}]}^{stg} = X_{[i_{\psi}, i_{\theta} + \frac{1}{2}, i_{\varphi} - \frac{1}{2}]}$$

### 4.2.2. Boundary cells

Staggered quantities require a different treatment at the domain boundary. On the collocated mesh, cells are located either entirely in the plasma or in the physical wall. Staggered quantities in the boundary layer are thus always half a cell width away from the wall and boundary conditions are enforced accordingly. For the magnetic vector potential this holds for walls in  $\psi$  direction but in  $\varphi$  and  $\theta$  directions, the staggered grid points are on the tokamak wall for the boundary cells with lowest index and one cell width away at the highest index. For consistency, accuracy and symmetry purposes, the staggered solvable domain shall be either extended by one row of cells at the upper index to include the wall in the solution or reduced by one row at the lower end. In both cases, the number of collocated and staggered grid points do not match anymore

#### 4. Numerical Implementation – 4.2. The staggered mesh

and inhibit all eventual symmetry properties of the matrix in the dual-grid system.  $A_{\parallel}$  requires Dirichlet boundary conditions with the value 0 everywhere, thus the solution on the wall is already known and is not needed in the system. The parallel current  $j_{\parallel}$  is fixed by the sheath current perpendicular to the wall, but is still needed for the parallel component tangential to the sheath. In Fig. 4.3, the position of the staggered fields  $A_{\parallel}$  and  $j_{\parallel}$  along the wall is shown.

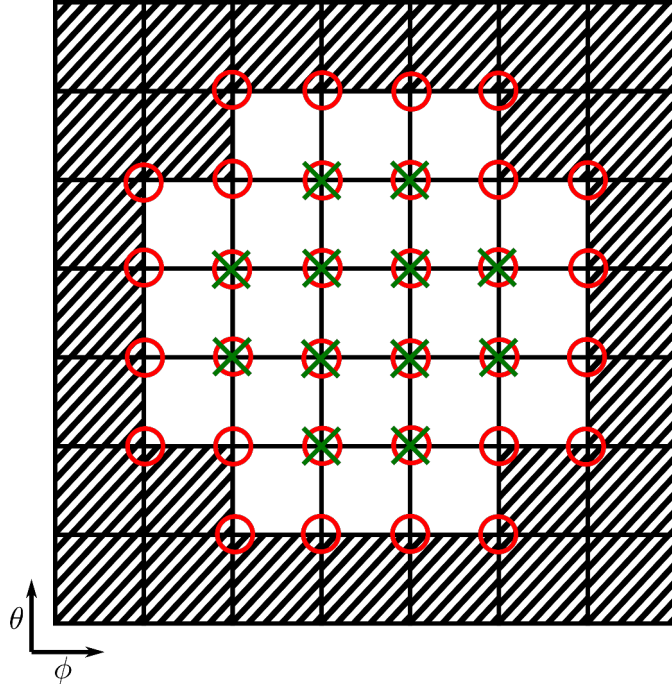


Figure 4.3.: General view of the staggered grid points in the  $\theta - \phi$  plane. The field  $A_{\parallel}$  is defined at the green crosses and  $j_{\parallel}$  at the red circles. Crossed cells are boundary cells where the mask is  $\chi = 1$ .

To ensure a correct implementation of the system and the stencils that appear in it, a new mask describes which cells contain staggered grid points in the solvable domain. It is defined from the original collocated wall mask  $\chi$  as:

$$\chi_{[i_{\psi}, i_{\theta}, i_{\varphi}]}^{A_{\parallel}} = 1 - (1 - \chi_{[i_{\psi}, i_{\theta}, i_{\varphi}]}) (1 - \chi_{[i_{\psi}, i_{\theta}-1, i_{\varphi}]}) (1 - \chi_{[i_{\psi}, i_{\theta}, i_{\varphi}-1]}) (1 - \chi_{[i_{\psi}, i_{\theta}-1, i_{\varphi}-1]}) \quad (4.11)$$

$$\chi_{[i_{\psi}, i_{\theta}, i_{\varphi}]}^{j_{\parallel}} = \chi_{[i_{\psi}, i_{\theta}, i_{\varphi}]} \chi_{[i_{\psi}, i_{\theta}-1, i_{\varphi}]} \chi_{[i_{\psi}, i_{\theta}, i_{\varphi}-1]} \chi_{[i_{\psi}, i_{\theta}-1, i_{\varphi}-1]} \quad (4.12)$$

The value of  $\chi^{A_{\parallel}}$  is therefore 1 if the staggered cell with index  $[i_{\psi}, i_{\varphi}, i_{\theta}]$  overlaps with the wall and is 0 inside the solvable domain. Conversely, the mask  $\chi^{j_{\parallel}}$  is 0 unless the entire cell lies in the wall.

Let us discuss a bit further sheath boundary conditions for staggered fields, where  $A_{\parallel}$  and  $j_{\parallel}$  lie on the domain boundary. For collocated fields, we impose sheath fluxes from the Bohm-Chodura model (see Sec. 3.4) on the first cell in the simulation domain.

#### 4. Numerical Implementation – 4.2. The staggered mesh

For the magnetic potential  $A_{\parallel}$ , the 0-Dirichlet condition is imposed in the concerned cell. For the parallel current  $j_{\parallel}$ , we add the sheath current  $j_{\text{wall}}$  to any parallel currents tangential to the wall. Indeed, if the sheath boundary is in the  $\theta$  direction, the  $\varphi$  component of the parallel current remains unaffected and needs to be solved.

### 4.2.3. Staggered discrete operators

As the parallel current  $j_{\parallel}$  and the magnetic vector potential  $A_{\parallel}$  are defined on a staggered grid, new stencil operators are needed to be compatible with the electric potential  $\Phi$  defined on the collocated grid at the cell centers.

#### 4.2.3.1. Parallel gradient

To calculate the parallel current in Ohm's law, we require the parallel gradients of potential, density and electron temperature. The three fields are defined on the collocated grid, and the result of the operator shall lie on the staggered grid.

$$[\nabla_{\parallel} X]_{[i_{\psi}, i_{\theta}, i_{\varphi}]}^{stg} \quad (4.13)$$

Wave structure travel along the parallel direction, dominated by the equilibrium field  $\mathbf{b}_{eq}$  in  $\theta$  and  $\varphi$ -directions. Because of the high anisotropy given  $B_{eq,p} \ll B_{eq,\varphi}$ , this operator is prone to numerical dissipation if not properly implemented. Both directions are calculated in a common step

$$\begin{aligned} [\mathbf{b}_{eq} \cdot \nabla X]_{[i_{\psi}, i_{\theta}, i_{\varphi}]}^{stg} = & \frac{1}{2} \left( (+b_{stg}^{\theta} + b_{stg}^{\varphi}) X_{[i_{\psi}, i_{\theta}, i_{\varphi}]} + (-b_{stg}^{\theta} + b_{stg}^{\varphi}) X_{[i_{\psi}, i_{\theta}-1, i_{\varphi}]} \right. \\ & \left. + (+b_{stg}^{\theta} - b_{stg}^{\varphi}) X_{[i_{\psi}, i_{\theta}, i_{\varphi}-1]} + (-b_{stg}^{\theta} - b_{stg}^{\varphi}) X_{[i_{\psi}, i_{\theta}-1, i_{\varphi}-1]} \right) \end{aligned} \quad (4.14)$$

This discrete operator involves four neighbors, as shown in Fig. 4.4a. It is appreciated in the finite elements community for anisotropic wave propagation[43, 80, 106] for its good numerical properties and is used in the anisotropic heat diffusion problem in magnetized plasmas by Günter et al[40].

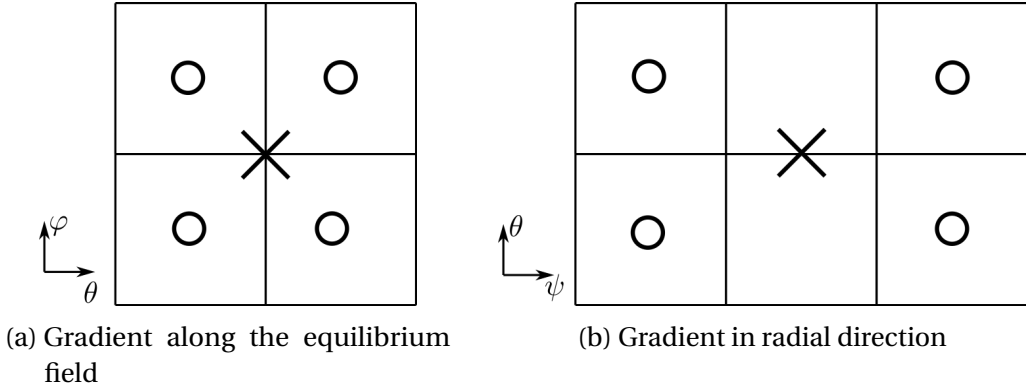


Figure 4.4.: Neighbors involved to calculated staggered parallel gradients.

The gradient in radial direction, that comes from the magnetic flutter, is treated in a separate step. Because of the staggered grid configuration, that does not apply to the radial direction, the gradient requires 8 neighbors, of which four are shown in Fig. 4.4b, the other four being out of plane in the next poloidal plane.

$$[\tilde{\mathbf{b}} \cdot \nabla X]_{[i_\psi, i_\theta, i_\varphi]}^{stg} = \frac{1}{4} b_{stg}^\psi \left( X_{[i_\psi+1, i_\theta, i_\varphi]} - X_{[i_\psi-1, i_\theta, i_\varphi]} + X_{[i_\psi+1, i_\theta, i_\varphi-1]} - X_{[i_\psi-1, i_\theta, i_\varphi-1]} \right. \\ \left. + X_{[i_\psi+1, i_\theta-1, i_\varphi]} - X_{[i_\psi-1, i_\theta-1, i_\varphi]} + X_{[i_\psi+1, i_\theta-1, i_\varphi-1]} - X_{[i_\psi-1, i_\theta-1, i_\varphi-1]} \right) \quad (4.15)$$

The poloidal and toroidal components of the magnetic fluctuations are solved together with the equilibrium part in Eq. 4.14.

#### 4.2.3.2. Parallel divergence

The divergence of  $j_{\parallel}$  needs to be calculated at the collocated grid in the vorticity equation. It is the counterpart to the gradient operator above, and calculates the divergence on the collocated grid based on staggered fields.

$$[\nabla \cdot X^{stg} \mathbf{b}]_{[i_\psi, i_\theta, i_\varphi]} \quad (4.16)$$

In Eq. B.11, the divergence of a parallel vector field has been introduced. We consider a collocated cell as in Fig. 4.2. The divergence is then the sum of all in- and outgoing fluxes  $\frac{\partial(JXb^i)}{\partial u^i}$  across the six cell faces.

$$[\nabla \cdot X^{stg} \mathbf{b}]_{[i_\psi, i_\theta, i_\varphi]} = \frac{1}{J_{[i_\psi, i_\theta, i_\varphi]}} \left( F_{[i_\psi, i_\theta, i_\varphi]}^{X, \psi} - F_{[i_\psi+1, i_\theta, i_\varphi]}^{X, \psi} + F_{[i_\psi, i_\theta, i_\varphi]}^{X, \theta} - F_{[i_\psi, i_\theta+1, i_\varphi]}^{X, \theta} + F_{[i_\psi, i_\theta, i_\varphi]}^{X, \varphi} - F_{[i_\psi, i_\theta, i_\varphi+1]}^{X, \varphi} \right) \quad (4.17)$$

We want calculate these fluxes from the flux  $F^{X, i} = JXb^i$  of the staggered field  $X^{stg}$ . As centered cell faces do not overlap with the staggered grid, we need to take the

#### 4. Numerical Implementation – 4.2. The staggered mesh

interpolate the fluxes calculated at the staggered mesh onto the cell face. For the equilibrium direction it involves two neighbors per flux (see Fig. 4.5a). As an example, here are the fluxes written out for the incoming poloidal flux:

$$F_{[i_\psi, i_\theta, i_\varphi]}^{X, \theta} = \frac{1}{2} \left( F_{[i_\psi, i_\theta - \frac{1}{2}, i_\varphi - \frac{1}{2}]}^{X, \theta} + F_{[i_\psi, i_\theta - \frac{1}{2}, i_\varphi + \frac{1}{2}]}^{X, \theta} \right)$$

In the radial direction, we need, again, the fluxes at eight neighboring staggered locations (see Fig. 4.5b) to calculate a flux on a single cell face.

$$\begin{aligned} F_{[i_\psi, i_\theta, i_\varphi]}^{X, \psi} = & \frac{1}{8} \left( F_{[i_\psi, i_\theta - \frac{1}{2}, i_\varphi - \frac{1}{2}]}^{X, \psi} + F_{[i_\psi, i_\theta - \frac{1}{2}, i_\varphi + \frac{1}{2}]}^{X, \psi} + F_{[i_\psi, i_\theta + \frac{1}{2}, i_\varphi - \frac{1}{2}]}^{X, \psi} + F_{[i_\psi, i_\theta + \frac{1}{2}, i_\varphi + \frac{1}{2}]}^{X, \psi} \right. \\ & \left. + F_{[i_\psi - 1, i_\theta - \frac{1}{2}, i_\varphi - \frac{1}{2}]}^{X, \psi} + F_{[i_\psi - 1, i_\theta - \frac{1}{2}, i_\varphi + \frac{1}{2}]}^{X, \psi} + F_{[i_\psi - 1, i_\theta + \frac{1}{2}, i_\varphi - \frac{1}{2}]}^{X, \psi} + F_{[i_\psi - 1, i_\theta + \frac{1}{2}, i_\varphi + \frac{1}{2}]}^{X, \psi} \right) \end{aligned}$$

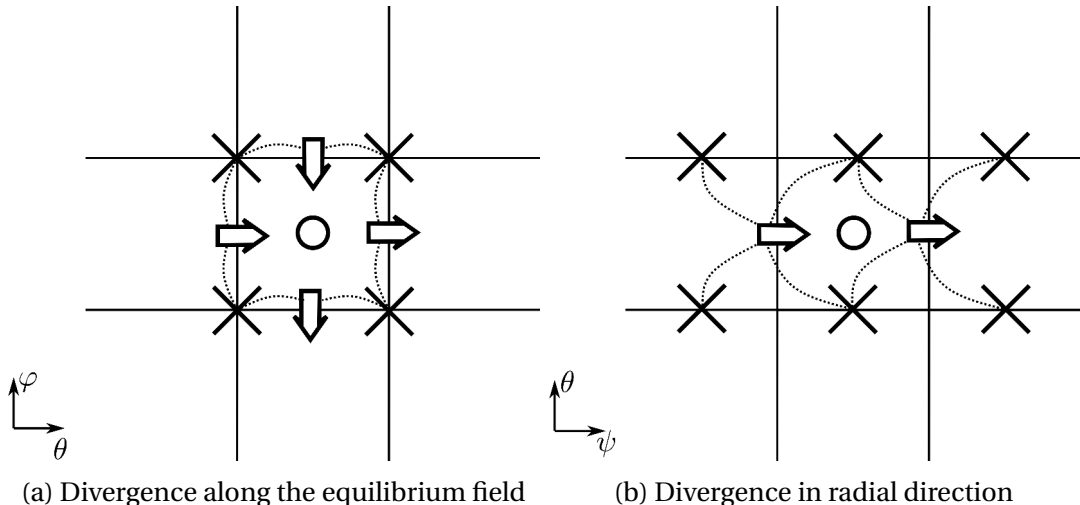


Figure 4.5.: Neighbors involved to calculate the parallel divergence. The arrows indicate the in- and outgoing fluxes that need to be calculated, and the dashed lines connect the arrows to the staggered points they require.

##### 4.2.3.3. Perpendicular Laplacian

Ampère's law requires the perpendicular Laplacian on the staggered grid to link  $j_{\parallel}$  and  $A_{\parallel}$ , two staggered fields.

$$[\nabla \cdot \nabla_{\perp} X^{stg}]_{[i_\psi, i_\theta, i_\varphi]}^{stg} \quad (4.18)$$

Let us consider a staggered cell over the regular mesh, depicted in red in Fig. 4.6a. Since the Laplacian operator can be treated as a divergence of a gradient, the task . Each flux  $F^{Y,i}$  is defined as the perpendicular gradient at the corresponding cell

#### 4. Numerical Implementation – 4.2. The staggered mesh

face, approximated with finite differences. The metric and diffusion coefficients  $JD(g^{ij} - b^i b^j)$  are also required at the faces and we obtain them by taking their average on the closest collocated points. In poloidal and toroidal directions two collocated points shown in green in Fig. 4.6c and Fig. 4.6d are sufficient but in radial direction we need to consider eight points around the face to calculate the correct coefficients.

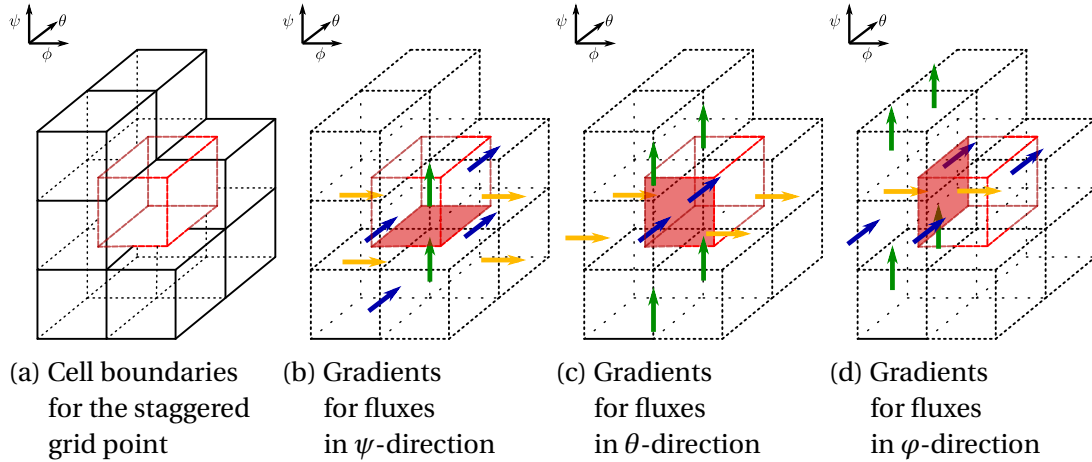


Figure 4.6.: Depiction of the relevant cell faces to calculate fluxes of a staggered field at coordinate index  $[i_\psi, i_\theta - \frac{1}{2}, i_\varphi - \frac{1}{2}]$ .

#### 4.2.4. Discretization around the X-point

The staggered grid has direct implications on the estimation of fluxes around mesh singularities: while for regular fields, every cell around the X-point has well-defined neighbors (see Fig. 4.7a), radial fluxes in and out of staggered cells directly cross the X-point (see Fig. 4.7b). They affect the perpendicular Laplacian operator on  $A_{\parallel}$  in Ampere's law (Eq. 3.40), advection on  $j_{\parallel}$  in Eq. 3.35, and the anomalous perpendicular diffusion  $\mathfrak{D}_{A,j}$ . To cope with the ill-defined cell faces, fluxes across the X-point are forced to 0 by Neumann-like boundary conditions. Neighbors of the involved cells must be defined separately from the regular cells with the same index.

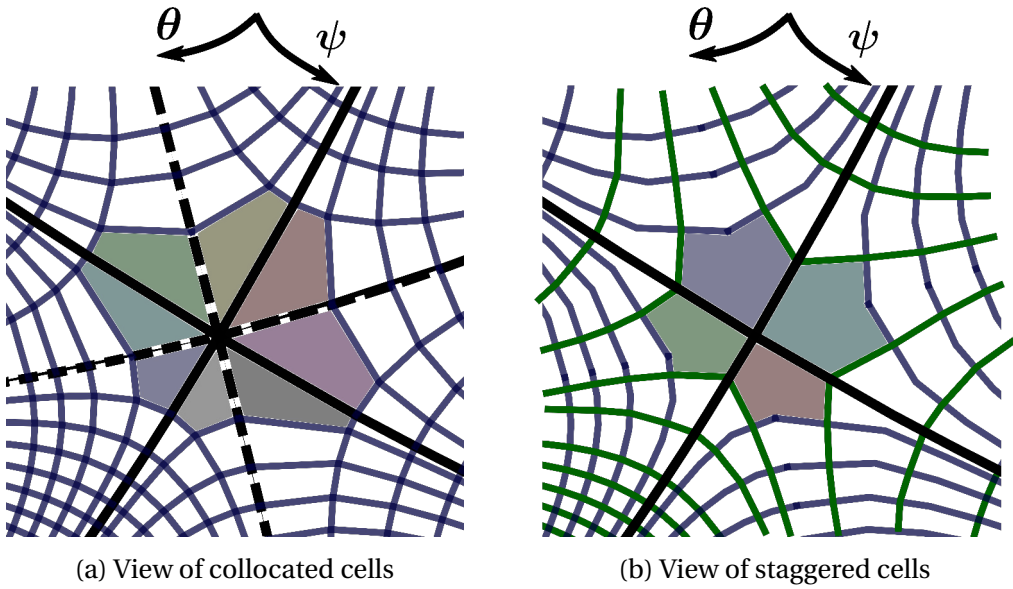


Figure 4.7.: Sketches of the mesh around the X-point. For collocated cells (a), 8 cells touch the X-point at a corner. For staggered cells (b), the X-point is located at the radial face of 4 cells, effectively modifying the shape of the cells to pentagons. Fluxes across the involved faces are hence ill-defined.

## 4.3. Electromagnetic vorticity system

The newly introduced fields  $j_{\parallel}$  and  $A_{\parallel}$  are solved implicitly along with the electric potential  $\Phi$ . As we face a coupled system that connects all points in the domain, direct solvers such as PASTIX are not suitable, especially for fine 3D meshes. We instead prefer to use iterative solvers available in the PETSc or HYPRE libraries. For the original vorticity system, the Stabilized version of the Biconjugate Gradient method (BiCGStab) along with the Geometric Algebraic Multigrid (GAMG) preconditioner proved to be very efficient and it is desirable to use them on the new systems. This section describes some special numerical features in the construction of the system to facilitate the convergence of the above iterative scheme. Sec. 4.3.1.1 introduces specific row and column scaling to equilibrate the blocks in the new system and Sec. 4.3.1.2 describes how to handle staggered fields to be compatible with the iterative scheme.

### 4.3.1. Matrix formulation of the electromagnetic system

With the values for  $n_e$  and  $T_e$  known at time-step  $n + 1$ , the vorticity equation (Eq. 3.46) corresponds to a 3D costly system involving  $\Phi$ ,  $j_{\parallel}$ , and  $A_{\parallel}$ . To solve it efficiently, the advection of  $j_{\parallel}$  and the anomalous perpendicular diffusion are treated explicitly. Following the discussion in Sec. 3.3.4, we integrate Ohm's law into the vorticity equation and Ampère's law. Then, at time-step  $n + 1$ , the following dimensionless system

coupling the two potentials  $\Phi$  and  $A_{\parallel}$  must be solved:

$$\begin{pmatrix} \nabla \cdot [D_{\perp} \nabla_{\perp} \circ] + \nabla \cdot [D_{\parallel} \nabla_{\parallel} \circ \mathbf{b}] & \frac{\beta_0}{\delta_t} \nabla \cdot [D_{\parallel} \circ \mathbf{b}] \\ D_{\parallel} \nabla_{\parallel} \circ & \frac{\beta_0}{\delta_t} D_{\parallel} \circ - \nabla \cdot [\nabla_{\perp} \circ] \end{pmatrix} \begin{pmatrix} \Phi^{n+1} \\ A_{\parallel}^{n+1} \end{pmatrix} = \begin{pmatrix} \nabla \cdot [D_t j_{\parallel}^n \mathbf{b}] + \text{RHS}^{\Phi} \\ D_t j_{\parallel}^n + \text{RHS}^{A_{\parallel}} \end{pmatrix} \quad (4.19)$$

with  $D_{\perp} = \frac{m_i n_i}{B^2 \delta_t}$ ,  $D_{\parallel} = \frac{1}{\eta_{\parallel} + \mu}$ ,  $D_t = \frac{\mu}{\eta_{\parallel} + \mu}$ , and  $\mu = m_e / (n_e \delta_t)$  accounting for electron inertia effects. The parameter  $\delta_t$  derives from the integration scheme and is equal to the time-step in the case of a first-order implicit Euler scheme.

Since  $\eta_{\parallel} \propto T_e^{-1.5}$ , the parallel resistivity  $\eta_{\parallel}$  is often a small parameter that leads to strong anisotropy between the perpendicular and parallel Laplacian operators. However, the electron inertia term, being implemented in the current solver, acts as an upper limit for the parallel diffusion coefficient, which is expected to improve the matrix conditioning as  $\eta_{\parallel}$  approaches zero. This is in contrast to the original electrostatic model from [9].

#### 4.3.1.1. Equilibration of the Matrix Blocks

Apart of the use of dimensionless quantities, no effort was made so far to ensure that the blocks in the electromagnetic matrix (Eq. 4.19) are roughly of the same order of the magnitude, which is important for the condition number of the matrix, nor that the matrix is diagonally dominant, which is generally a desirable feature for fast convergence of iterative schemes.

In the following bits, we introduce some column  $c_X$  and row  $r_X$  scaling factors that are specific to the blocks  $X$  of the matrix such that the above conditions are fulfilled as well as possible. To ensure a correct solution, the row scaling factor  $r_X$  must be applied to the corresponding entry in the RHS vector. As a matter of fact, in the original vorticity matrix, we already have  $r_{\Phi} = J$  the metrical Jacobian from Sec. 4.1.3 to remove the effect of different mesh sizes in the domain on the discrete Laplacian operators. The column scaling factors  $c_X$  must be taken care of when retrieving the fields from the numerical solution and it is strongly recommended to apply them to the initial guess for the iterative scheme.

Some strategies exist to optimize the scaling task[70, 90]. However, they all require an expensive matrix analysis phase that must be repeated regularly since the system changes with the progress of the simulation. Therefore, we use the knowledge about the construction of the matrix blocks to define sufficiently good scaling factors. An

educated row and column scaling can considerably improve the condition number of a matrix[101]. In fact, we do not want the perfect scaling to minimize the condition number (which would be as expensive as a direct solver), but give the matrix the best possible shape for the subsequent use of the GAMG pre-conditioner. It was designed for positive-definite (almost) symmetric matrices[7] as they occur in elliptic PDEs and performs reasonably for diffusion-dominated parabolic problems. Note that the two diagonal blocks already have a convenient shape, and the anti-diagonal blocks contain parallel divergence and gradient operators, whose discrete stencils are almost equal and somewhat similar to the off-diagonal elements of a discrete Laplacian operator. Therefore, by scaling the second column with  $c_A = \sqrt{\delta_t/\beta_0}$  and the second row with  $r_A = -J\sqrt{\delta_t/\beta_0}$  the resulting matrix becomes almost symmetric and well-suited for GAMG. The minus sign is important to have the same sign for the Laplacians on  $\Phi$  and  $A_{\parallel}$ , ensuring global positive definiteness, and to make the off-diagonal truly symmetric. The scalings  $r_{\Phi} = J$  and  $c_{\Phi} = 1$  remain unchanged from the original vorticity implementation.

#### 4.3.1.2. Staggered Fields in the Matrix

The GAMG multigrid solves the system on different coarser levels by restricting the matrix and the RHS vector and then interpolates the solution back to the finer levels. In the new system, two consecutive entries belong to different fields, which makes the whole restriction-interpolation task obsolete from the very first level since neither the solution nor the matrix entries are similar between neighbours. PETSc takes care of multiple fields in a coupled system if one defines a block size that indicates GAMG how to match corresponding entries. However, as seen in Fig. 4.8, the fields  $A_{\parallel}$  is defined on a staggered grid in parallel direction as opposed to the collocated field  $\Phi$ . For the system it means that at each wall in negative directions, a line and column for  $\Phi^1$  exists but not for the corresponding  $A_{\parallel}^1$ . This in turn is problematic for GAMG as the blocks are globally defined and two different fields would again end up together and the total system size might even not be a multiple of the blocksize, which at all prevents the initialization of the preconditioner. As a solution, a dummy line is added to the matrix for  $A_{\parallel}^1$  with a 1 on the diagonal that is not coupled to any other line.

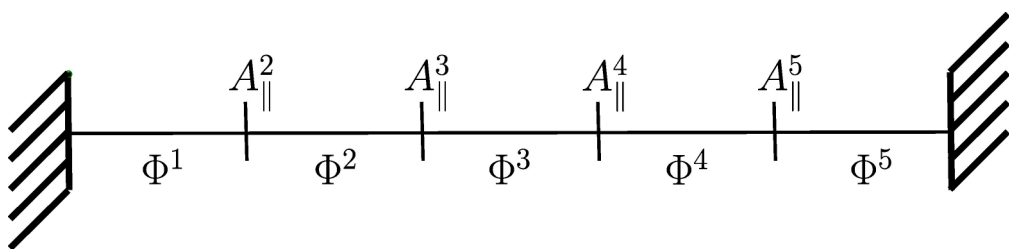


Figure 4.8.: Ordering of the fields in the vorticity equation along the  $\theta$  direction

It is important for GAMG to alternate entries for  $A_{\parallel}$  and  $\Phi$  in the matrix and not have one big block for each field as it reduces the distance of the non-zeros from

#### 4. Numerical Implementation – 4.3. Electromagnetic vorticity system

the diagonal. It was also found that the pre-conditioner performs much better if each block is ordered  $[A_{\parallel}^{i_\theta}, \Phi^{i_\theta}]$  as the staggered grid point lies between  $\Phi^{i_\theta-1}$  and  $\Phi^{i_\theta}$  and the matrix ordering hence better reflects the geometrical configuration. For the geometry in Fig. 4.8, the matrix entries for the off-diagonal blocks would resemble:

$$\begin{pmatrix} 0 & \partial_\theta \\ -\partial_\theta & 0 \end{pmatrix} \begin{pmatrix} \Phi \\ A_{\parallel} \end{pmatrix} = \begin{pmatrix} 1 & & & & & \\ & 1 & & & & \\ & & 1 & -1 & & \\ & & & -1 & 1 & \\ & & & & \ddots & \ddots \\ & & & & & 1 & -1 & \\ & & & & & & -1 & 1 \end{pmatrix} \begin{pmatrix} A_{\parallel}^1 \\ \Phi_{\parallel}^1 \\ A_{\parallel}^2 \\ \Phi_{\parallel}^2 \\ \vdots \\ A_{\parallel}^5 \\ \Phi_{\parallel}^5 \end{pmatrix} \quad (4.20)$$

### 4.3.2. Evaluation of the condition number

The electromagnetic vorticity system needs to be solved implicitly, and the condition number of the matrix is an important property that essentially defines the speed of convergence of iterative solvers. Extensive research over the past decade[24, 38, 71, 96], particularly on GMRES and conjugate gradient methods as they are used in SOLEDGE3X, has shown that a high condition number results in an increased number of iterations to reach convergence. The condition number of a matrix  $\mathbf{M}$  is defined as the ratio between its largest and smallest eigenvalues:

$$\kappa(\mathbf{M}) = \frac{|\lambda_{\max}(\mathbf{M})|}{|\lambda_{\min}(\mathbf{M})|} \quad (4.21)$$

It is therefore of particular interest to investigate how the electromagnetic extension of the system affects the conditioning of the vorticity system. While there are efficient algorithms to estimate the largest eigenvalue of a matrix, the smallest is much more expensive to compute. For the large 3D vorticity system, directly calculating the condition number is not feasible. Instead, we approach this question analytically.

Consider a 2D orthonormal system, with perpendicular gradients exclusively in the  $x$  direction and parallel gradients in the  $y$  direction, with  $N_x \times N_y$  discretization points. All fields are assumed to take some constant reference value, the timestep size is fixed to  $\delta_t$ , and time advancement is performed using the first-order implicit Euler method. Without a curvilinear grid, the gradient and divergence stencils are identical, and with the row/column scaling from Sec. 4.3.1.1, the vorticity system can then be expressed as:

$$\mathbf{M} = \begin{pmatrix} \alpha \mathbf{L}_{\perp} + \sigma \mathbf{L}_{\parallel} & \gamma \mathbf{G}_{\parallel} \\ -\gamma \mathbf{G}_{\parallel}^T & \gamma^2 \mathbf{L}_{\perp} - \sigma \mathbf{I} \end{pmatrix} \quad (4.22)$$

where  $\alpha = \frac{m_i n_i}{B^2 \delta_t}$ ,  $\sigma = \frac{1}{\eta_{\parallel} + \frac{m_e}{n_e \delta_t}}$ , and  $\gamma = \sqrt{\frac{\delta_t}{\beta_0}}$ . The stencil matrices  $\mathbf{L}_{\perp}$  and  $\mathbf{L}_{\parallel}$  describe

#### 4. Numerical Implementation – 4.3. Electromagnetic vorticity system

the Laplacians between the  $x$  and  $y$  neighbors, respectively, while  $\mathbf{G}_{\parallel}$  represents the gradient over  $y$ . Their matrices take the following forms:

$$\begin{aligned} \mathbf{L}_{\perp} &= \begin{pmatrix} -2 & 1 & 0 & \cdots & 0 \\ 1 & -2 & 1 & \cdots & 0 \\ 0 & 1 & -2 & \cdots & 0 \\ \vdots & \vdots & \vdots & \ddots & \vdots \\ 0 & 0 & 0 & \cdots & -2 \end{pmatrix}_{N_x \times N_x} & \mathbf{L}_{\parallel} &= \begin{pmatrix} -2 & 1 & 0 & \cdots & 1 \\ 1 & -2 & 1 & \cdots & 0 \\ 0 & 1 & -2 & \cdots & 0 \\ \vdots & \vdots & \vdots & \ddots & \vdots \\ 1 & 0 & 0 & \cdots & -2 \end{pmatrix}_{N_y \times N_y} \\ \mathbf{G}_{\parallel} &= \begin{pmatrix} -1 & 1 & 0 & \cdots & 0 \\ 0 & -1 & 1 & \cdots & 0 \\ \vdots & \vdots & \vdots & \ddots & \vdots \\ 1 & 0 & 0 & \cdots & -1 \end{pmatrix}_{N_y \times N_y} \end{aligned} \quad (4.23)$$

In order to make the system invertible and avoid an infinite condition number, we assume Dirichlet-0 boundary conditions in the perpendicular direction and periodic boundary conditions in the parallel direction. This can be viewed as a region of closed flux surfaces connected to a region with a very crude sheath-dominated plasma. We can compute the eigenvalues of the two Laplacians and the gradient coupling matrix exactly.

$$\lambda_{k_x}(\mathbf{L}_{\perp}) = 4 \sin^2\left(\frac{(k_x + 1)\pi}{2N_x}\right) \quad \lambda_{k_y}(\mathbf{L}_{\parallel}) = 4 \sin^2\left(\frac{k_y\pi}{N_y}\right) \quad \lambda_{k_y}(\mathbf{G}_{\parallel}) = i \sin\left(\frac{k_y\pi}{N_y}\right) \quad (4.24)$$

where  $k_x \in [0, N_x - 1]$  and  $k_y \in [0, N_y - 1]$  are indices for all eigenvalues. We observe that both parallel systems have a zero eigenvalue that corresponds to a constant mode, due to the periodic boundary conditions along the closed flux surfaces, indicating that the solution can be determined up to a constant. The perpendicular operators, with fixed boundaries, make the system invertible with a unique solution.

Let us now evaluate the extremal eigenvalues of the diagonal blocks of  $\mathbf{M}$ . For the upper-left block, which contains the sum of Laplacians, the eigenvalues correspond to the combinations of  $(k_x, k_y)$  such that  $|\lambda_{k_x}| + |\lambda_{k_y}|$  is minimized or maximized:

$$\lambda_{min}(\alpha\mathbf{L}_{\perp} + \sigma\mathbf{L}_{\parallel}) = \alpha \cdot \frac{\pi^2}{N_x^2} \quad \lambda_{max}(\alpha\mathbf{L}_{\perp} + \sigma\mathbf{L}_{\parallel}) = 4(\alpha + \sigma) \quad (4.25)$$

For the lower-right block matrix, the identity matrix will shift the eigenvalues of the perpendicular Laplacian by  $\sigma$ :

$$\lambda_{min}(\sigma\mathbf{I} - \gamma^2\mathbf{L}_{\perp}) = \sigma - 4\gamma^2 \quad \lambda_{max}(\gamma^2\sigma\mathbf{I} - \mathbf{L}_{\perp}) = \sigma - \gamma^2 \frac{\pi^2}{N_x^2} \quad (4.26)$$

#### 4. Numerical Implementation – 4.3. Electromagnetic vorticity system

For sufficiently large systems, the largest eigenvalue will be on the order of  $\sigma$ . If  $\sigma \gg \gamma^2$ , all eigenvalues will be close to  $\sigma$ , resulting in an excellent matrix condition. However, if  $\sigma < 4\gamma^2$ , some eigenvalues may become negative, causing the system to lose its positive-definiteness. This can lead to strong instabilities, and standard iterative solvers (e.g., GMRES or BiCGStab) may fail or produce unreliable results, as these methods are generally designed for positive-definite matrices. To ensure that the problem remains well-posed, we must enforce the constraint:

$$\frac{1}{4}\beta_0 > \delta_t \eta_{\parallel} + \frac{m_e}{n_e} \quad (4.27)$$

This condition states that  $\beta_0$  cannot be too small for the system to remain solvable. Assuming this lower condition on  $\beta_0$  holds with a sufficient margin, the minimum and maximum eigenvalues in Eq. 4.26 are simply  $\lambda_{min} = \lambda_{max} = \sigma$ .

We now have all extremal eigenvalues along the block diagonal. For the combined matrix  $\mathbf{M}$ , the gradient coupling plays a crucial role. If the coupling is small, the eigenvalues of  $\mathbf{M}$  are given by the union of the eigenvalues of the diagonal blocks. The condition number of  $\mathbf{M}$  is then the ratio of the overall maximum and minimum eigenvalues of the block matrices. Since  $\gamma$  is certainly smaller than  $\sigma$ , we should investigate the impact of the coupling in more detail. The matrix  $\mathbf{M}$  can be transformed into a block diagonal form by applying the Schur complement  $\mathbf{S}$  on the lower-left block.

$$\mathbf{M} = \begin{pmatrix} \mathbf{A} & \mathbf{B} \\ -\mathbf{B}^T & \mathbf{C} \end{pmatrix} = \begin{pmatrix} \mathbf{I} & 0 \\ -\mathbf{B}^T \mathbf{A}^{-1} & \mathbf{I} \end{pmatrix} \begin{pmatrix} \mathbf{A} & 0 \\ 0 & \mathbf{S} \end{pmatrix} \begin{pmatrix} \mathbf{I} & \mathbf{A}^{-1} \mathbf{B} \\ 0 & \mathbf{I} \end{pmatrix} \quad \text{with: } \mathbf{S} = \mathbf{D} + \mathbf{B}^T \mathbf{A}^{-1} \mathbf{B} \quad (4.28)$$

The block diagonal matrix is multiplied by both a lower and an upper diagonal matrix. Since they are invertible and all diagonal elements are equal to 1, the block diagonal matrix is quasi-similar to  $\mathbf{M}$ [32], thereby preserving its eigenvalues. Calculating the eigenvalues of the block diagonal matrix gives us then a good approximation for the actual eigenvalues of  $\mathbf{M}$ . We now need to estimate the eigenvalues of the Schur complement. Given that  $\mathbf{A}$  is Laplacian-based, the eigenvalues of  $\mathbf{A}^{-1}$  are the reciprocals of the eigenvalues of  $\mathbf{A}$ , as shown in Eq. 4.25. The matrix is sandwiched between the gradient operator and its transpose, and together they behave like a parallel Laplacian with the scaling factor  $\gamma^2$ . We can first estimate:

$$\lambda_{min}(\mathbf{B}^T \mathbf{A}^{-1} \mathbf{B}) = \frac{\gamma^2 \lambda_{min}(L_{\parallel})}{\lambda_{max}(\alpha \mathbf{L}_{\perp} + \sigma \mathbf{L}_{\parallel})} = 0 \quad (4.29)$$

$$\lambda_{max}(\mathbf{B}^T \mathbf{A}^{-1} \mathbf{B}) = \frac{\gamma^2 \lambda_{max}(L_{\parallel})}{\lambda_{min}(\alpha \mathbf{L}_{\perp} + \sigma \mathbf{L}_{\parallel})} = \frac{4\gamma^2 N_x^2}{\alpha \pi^2} \quad (4.30)$$

By combining this result with the eigenvalues of  $\sigma \mathbf{I} - \gamma^2 \mathbf{L}_{\perp}$  from Eq. 4.26, we can estimate the extremal eigenvalues of the Schur complement:

$$\lambda_{min}(\mathbf{S}) = \sigma \quad \lambda_{max}(\mathbf{S}) = \sigma + \frac{4\gamma^2 N_x^2}{\alpha\pi^2} \quad (4.31)$$

Everything is now in place to address the eigenvalues of  $\mathbf{M}$  with the two block diagonals  $\mathbf{A}$  and  $\mathbf{S}$ . Recall the assumption  $\sigma \gg \gamma^2$  from Eq. 4.27, thus the double-Laplacian system in Eq. 4.25 defines the minimum eigenvalue of  $\mathbf{M}$ . Considering that  $\alpha \sim 1/\delta_t$  in the dimensionless equations and  $\gamma^2 \sim \delta_t/\beta_0$  is large, we can reasonably expect  $\gamma^2 \gg \alpha$ . The maximum eigenvalue of  $\mathbf{M}$  arises from the Schur complement in Eq. 4.31. Therefore, the condition number of  $\mathbf{M}$  can be estimated as:

$$\kappa(\mathbf{M}) \approx \frac{\sigma N_x^2}{\alpha\pi^2} + \frac{4\gamma^2 N_x^4}{\alpha^2\pi^4} \quad (4.32)$$

or in terms of dimensionless reference values:

$$\boxed{\kappa(\mathbf{M}) \approx \frac{B^2 \delta_t N_\perp^2}{m_i n_i \pi^2} \cdot \frac{1}{\eta_\parallel + \frac{m_e}{n_e \delta_t}} + \frac{4 \delta_t^3 B^4 N_\perp^4}{\beta_0 m_i^2 n_i^2 \pi^4}} \quad (4.33)$$

In the case of the system with electron inertia, but without electromagnetic induction, the analysis becomes much simpler as only the double Laplacian block matrix constitutes the system. Its condition number is given by the eigenvalues in Eq. 4.25:

$$\kappa(\mathbf{A}) = \frac{4\sigma N_x^2}{\alpha\pi^2} + \frac{4N_x^2}{\pi^2} \quad (4.34)$$

and is primarily determined by the first term. It can be written as:

$$\boxed{\kappa(\mathbf{A}) \approx \frac{B^2 \delta_t N_\perp^2}{m_i n_i \pi^2} \cdot \frac{1}{\eta_\parallel + \frac{m_e}{n_e \delta_t}}} \quad (4.35)$$

From these expressions for the condition number, we observe a degradation as the electric resistivity approaches zero, aligning with the difficulties faced by the original electrostatic implementation in higher-power scenarios. The finite electron mass acts as a lower bound for  $\eta_\parallel$ , which is expected to significantly aid iterative solvers in such scenarios. Magnetic induction introduces the second term in Eq. 4.33, and will always deteriorate the matrix conditioning. However, it is inversely proportional to  $\beta_0$ , such that the deterioration is limited as the pressure ratio increases. Numerically, electromagnetic effects should only be considered in simulation scenarios where  $\beta_0$  is sufficiently large. This point is further emphasized by the condition in Eq. 4.27, which imposes a lower limit on  $\beta_0$  to ensure a positive-definite matrix—an essential property for most iterative solvers. In Fig. 4.9, we illustrate how the condition number changes with  $\eta_\parallel$ ,  $\delta_t$ , and  $N_\perp$  for both electrostatic and electromagnetic systems, with and without electron inertia.

#### 4. Numerical Implementation – 4.4. Numerical treatment of flutter

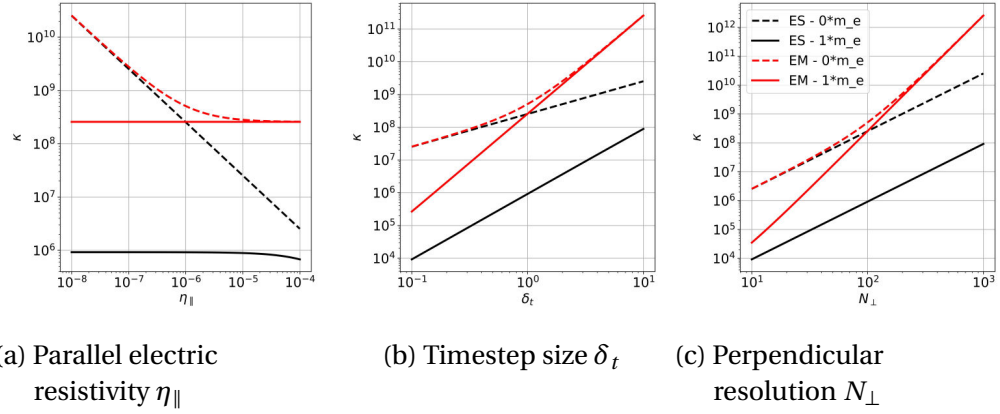


Figure 4.9.: Impact of different parameters on the condition number. Plasma parameters are taken as constant:  $B = 1$ ,  $m_i = 2$ ,  $n_e = n_i = 2$ ,  $m_e = 5.5 \cdot 10^{-4}$ ,  $\beta_0 = 10^{-3}$ ,  $\eta_{\parallel} = 10^{-6}$ ,  $\delta_t = 1$  and  $N_{\perp} = 100$ . The parameters  $\beta_0$  and  $n_e$  are deliberately chosen large to ensure the validity of the positive-definiteness condition 4.27. Black curves correspond to the electrostatic system, and red curves to the electromagnetic matrices, with full lines indicating electron inertia and dashed lines representing  $m_e = 0$ .

Overall, electromagnetic models exhibit a higher condition number. In particular, at larger timestep sizes or higher perpendicular resolutions,  $\kappa$  increases significantly due to the third and fourth exponents in the second term of Eq. 4.33. However, electron inertia positively affects the condition number. This is especially evident as  $\eta_{\parallel}$  approaches zero in Fig. 4.9a, where neglecting the electron mass results in a sharp increase in  $\kappa$ , while electron inertia allows for a stable, low  $\kappa$ . Similarly, for low timestep sizes and resolutions,  $m_e$  improves the system, such that for lower ranges, the electromagnetic system with inertia performs better than the electrostatic system without inertia.

## 4.4. Numerical treatment of flutter

In our perturbative approach, flutter introduces a radial component to the magnetic field. As the meshing remains aligned to the equilibrium field, the unit magnetic field has now an additional non-zero contravariant component  $b^{\psi}$  in the curvilinear metric. We must hence extend all parallel operators in the code to consider it. Flutter also has a poloidal and a (small) toroidal component, but these are much less problematic to treat as they can be added to the equilibrium components:

$$b^{\theta} = b_{eq}^{\theta} + \tilde{b}^{\theta} \quad b^{\varphi} = b_{eq}^{\varphi} + \tilde{b}^{\varphi} \quad (4.36)$$

and the code proceeds as usual.

In this section, we describe how the radial magnetic field has been included in all parallel operators, namely in the advection scheme, the implicit diffusion problems on viscosity and heat and, crucially, the electromagnetic vorticity system.

### 4.4.1. Radial advection

All conserved fields are advected by the total velocity. In the drift-reduced approach, it decomposes into a parallel advection along the magnetic field lines with velocity  $v_{\parallel} = \gamma_{\parallel}/n$  and a perpendicular advection with the plasma drifts. Flutter then corresponds to an additional transport term at  $v_{\parallel}$  in radial direction. For any quantity  $X$ , the advection term can be expressed to:

$$\nabla \cdot [X(v_{\parallel}\mathbf{b}_{eq} + v_{\parallel}\tilde{\mathbf{b}} + \mathbf{u}_{\perp})] \quad (4.37)$$

In the WENO scheme, fluxes in and out a cell are treated independently for each direction. The only novelty with flutter appears for radial fluxes, where the contravariant  $v_{\parallel}\tilde{b}^{\psi}$  adds to the existing advection by  $u_{\perp}^{\psi}$ . Effectively, flutter acts a new drift velocity and required relatively little adaptation of the code.

### 4.4.2. Parallel diffusion

In the magnetostatic setting, the parallel diffusion operator on  $v_i$  and  $T_{\alpha}$  can be solved independently on each flux surface in a 2D system on the  $\theta - \varphi$  plane. The scheme developed by Günter et al. [40] has proven well-suited to solve the 2D parallel Laplacian equations with minimized numerical spread for highly anisotropic problems. For an operator of the type  $\nabla \cdot (\kappa \nabla_{\parallel} \circ \mathbf{b})$ , parallel gradients are first calculated in cell corners with finite differences and then used in the fluxes across each cell face to get the divergence. The corners where gradients are calculated are shown in Figure 4.10a.

However, with flutter (Sec. 3.3.3), magnetic flux surfaces are no longer aligned to the  $\theta - \varphi$  plane because of the new radial component  $b^{\psi}$ . As a consequence, all independent 2D problems across flux surfaces are now coupled into a single 3D problem. For the parallel diffusion solver, a first approach would be to extend the above scheme by calculating gradients in the 3D corners of our cells. However, the new component  $b^{\psi}$  is a pure fluctuation, which is therefore expected to be much smaller than  $b^{\theta}$  or  $b^{\varphi}$  and can even vanish locally. This results in significant spurious numerical diffusion in the radial direction of equilibrium gradients. To prevent this diffusion, and still properly capture radial flutter gradients, only crossed derivatives  $b^{\theta}b^{\psi}$  and  $b^{\varphi}b^{\psi}$  as well as the principal radial diffusion  $b^{\psi}b^{\psi}$  use gradients evaluated at 3D corners, while the equilibrium diffusion remains aligned to the  $\theta - \varphi$  plane. Examples of the gradients used in this new scheme are shown in Figs. 4.10b and 4.10c. The new discretization stencil then corresponds exactly to the equilibrium 2D stencil in the limit  $b^{\psi} = 0$ .

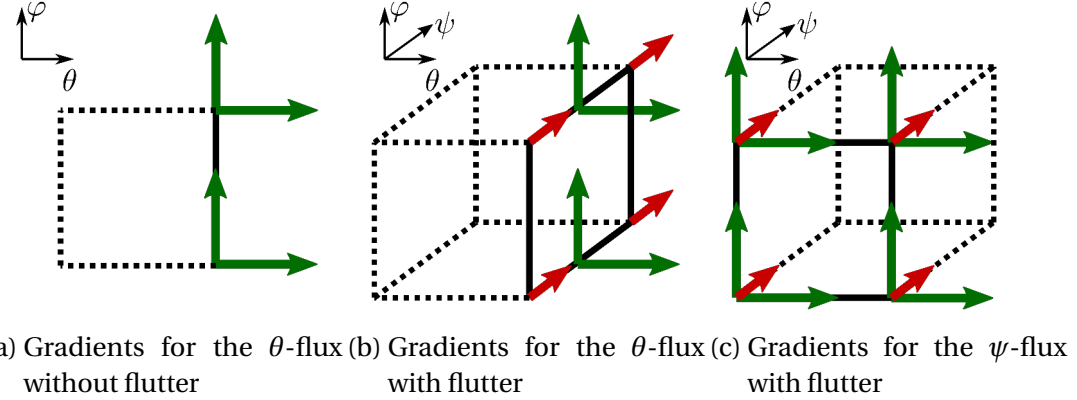


Figure 4.10.: Sketches showing the calculation of gradients for the parallel diffusion scheme. It shows the position where the different gradients are calculated that are relevant for a flux across the cell face with a solid line. Green and red arrows symbolize gradients in the equilibrium and in the radial direction, respectively.

### 4.4.3. Vorticity equation

For the parallel diffusion on the electric potential  $\nabla \cdot [D_{\parallel} \nabla_{\parallel} \Phi \mathbf{b}]$  with flutter, we do not use the stencil introduced in Sec. 4.4.2. To avoid numerical difficulties and the appearance of unphysical modes, the discretization of this term needs to be consistent with the parallel gradient and divergence operators in the same system. Since the grid for  $A_{\parallel}$  and  $j_{\parallel}$  is only staggered in the  $\theta$  and  $\varphi$  directions, we do not know them in the radial corners from Figs. 4.10b and 4.10c. Instead, the discrete diffusion operator is defined as the combination of the operators for the gradient and the divergence. It involves two neighbors on both radial sides, so the resulting stencil is less compact but consistent with the remaining system. Note that in cases without flutter ( $b^{\psi} = 0$ ), the diffusion operator exactly corresponds to Günter's scheme [40] because the staggered fields are known at the corners of the gradients in Fig. 4.10.

Generally spoken, Combining a divergence with a gradient stencil to form a discrete Laplacian is a bad idea. The information for the finite differences scheme stems from two cells away, skipping the intermediate cell. The decoupling between even and odd grid points is prone to high-frequency oscillations and formation of a checkerboard pattern. This behavior is evident if one looks at the stencil neighbors for the Laplacian on a Cartesian grid in Fig. 4.11, where all mixed derivatives vanish.

4. Numerical Implementation – 4.4. Numerical treatment of flutter

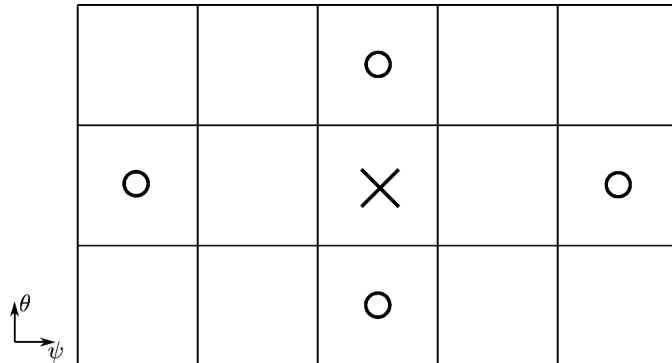


Figure 4.11.: Neighbors of the parallel Laplacian stencil with flutter for the vorticity equation

For the specific application in the vorticity equation, checkerboards are not at risk to appear, because the radial component in the parallel stencil is superseded with the perpendicular Laplacian on  $\Phi$  from the polarization current that considers direct neighbors, which smoothens any high-frequency modes at the resolution. Conversely, it is impossible to run stable simulations with the "better" parallel diffusion stencil with flutter from Sec. 4.4.2, as it does not preserve consistency between the diffused  $\Phi^n$  and  $\Phi^{n-1}$ . The potential  $\Phi^{n-1}$  from the previous timestep enters the system through the divergence of  $\partial_t j_{\parallel}$ , whose time discretization relies on  $j_{\parallel}^{n-1}$ , and as such on  $\nabla_{\parallel} \Phi^{n-1}$ . Note that this reasoning also applies for the parallel Laplacians on  $\log n_e$  and  $T_e$  that appear in the right-hand side of the vorticity equation and are important for the non-adiabatic plasma response.

# 5. Verification and Validation

## Chapter Summary

The implementation of the electromagnetic model is verified using the method of manufactured solutions on a three-dimensional, curved geometry with non-uniform meshing. Physical quantities are initialized as sinusoidal functions, and analytic source terms are computed to compensate for all time-independent terms in the equations, such that the simulation maintains a steady state. The root mean square difference between the initial state and the plasma state after one timestep is appropriate to estimate the discretization error introduced by the implementation. First, the electromagnetic vorticity system with magnetic induction and electron inertia is verified. The complex geometry provides an advanced test for the correct implementation of fields on a staggered grid. The discrete parallel Laplacian operator developed for diffusion problems with flutter is tested separately on the parallel heat conduction term in the energy conservation equation. A resolution scan demonstrates that the error decreases with the square of the mesh size, consistent with the second-order schemes used for the tested stencils.

The physical accuracy is validated on true 2D and 3D slabs with a uniform magnetic field against the linear behavior expected from the dispersion relation. The test setup is first checked on trivial advection and the electrostatic vorticity equation. Next, Alfvén waves are observed on a 2D slab with pure magnetic induction in the vorticity equation. The most comprehensive test is performed on a 3D slab with a (uniform) poloidal and toroidal magnetic field in a four-field model, where  $A_{\parallel}$  and  $j_{\parallel}$  evolve with a  $\pi/2$  phase shift relative to  $\Phi$  and  $n_e$ . A scan over the perpendicular wave motion exhibits the transition from Alfvén dynamics to thermal electron waves. The observed speeds are:

$$v_A = \frac{B}{\sqrt{m_i n_i \mu_0}} \quad v_{th,e} = \sqrt{\frac{T_e}{m_e}}$$

where waves propagate at  $v_A$  in the low  $k_{\perp}$  limit and at  $v_{th,e}$  in the upper  $k_{\perp}$  limit.

## 5. Verification and Validation – 5.1. Verification by the method of manufactured solutions

The electromagnetic extension of the SOLEDGE3X framework required considerable modifications of the code. Before investigating new physics, it is wise to verify the correctness of the implementation and validate electromagnetic plasma behavior with it. In a first series of tests in Sec. 5.1, the implementation of the electromagnetic vorticity equation and the parallel diffusion with flutter are checked against analytic source term. The physical behavior is validated in Sec. 5.2, where test cases on 2D and 3D slabs with increasing model complexity are confronted to the expected linear behavior.

### 5.1. Verification by the method of manufactured solutions

To ensure the correctness of the newly implemented system with the magnetic vector potential  $A_{\parallel}$ , a test model has been set up with the method of manufactured solutions (MMS) [79]. This allows to directly compare the numerical and analytic solutions and therefore validate the implementation and verify the order of convergence of the numerical operators.

#### 5.1.1. Test set-up

The MMS test model is a fraction of a torus with a circular cross-section with an inner radius of 0.48m, an outer radius of 2.72m and a simulated plasma edge width of 0.64m. An example of the 3D mesh geometry is shown in Fig. 5.1. To test the information exchange between zones in the model topology from Sec. 4.1.2, each coordinate direction is split in two zones totaling to 8 zones.

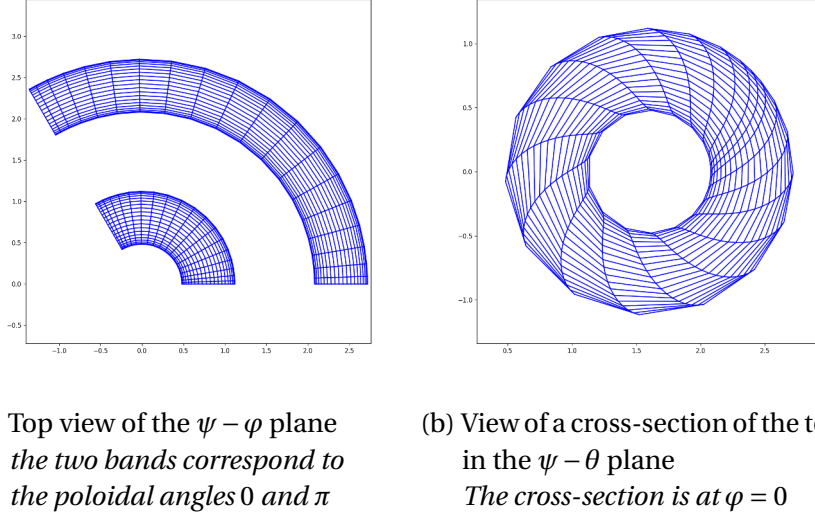


Figure 5.1.: Distorted MMS mesh geometry with  $N = 20$  cells per dimension on a 3rd of a torus

In the MMS geometry,  $\psi$  denotes the radius of the tube and  $R$  the radius of the entire torus. If  $aR_0 = 1.6$  is the distance of the tube center to the torus center, we have:

$$R = aR_0 + \psi \cdot \cos(\theta)$$

Together with the poloidal coordinate  $\theta \in [0, 2\pi]$  and the toroidal coordinate  $\varphi \in [0, 2\pi/N_{div}]$  where  $1/N_{div}$  is the considered fraction of the torus, each point in the domain is uniquely described by the curvilinear coordinates  $[\psi, \theta, \varphi]$ . We can define some  $\mathbf{P} = [X, Y, Z]^T$  in a cartesian basis of the 3D domain:

$$X = R \cos(\varphi) \quad Y = \psi \cdot \sin(\theta) \quad Z = R \sin(\varphi)$$

In this setting, the basis vectors of the curvilinear coordinates from Sec. 4.1.3 can be calculated analytically. The covariant basis vectors are:

$$\mathbf{e}_\psi = \frac{\partial \mathbf{P}}{\partial \psi} = \begin{bmatrix} \cos(\theta) \cos(\varphi) \\ \sin(\theta) \\ \cos(\theta) \sin(\varphi) \end{bmatrix} \quad \mathbf{e}_\theta = \frac{\partial \mathbf{P}}{\partial \theta} = \begin{bmatrix} -\psi \sin(\theta) \cos(\varphi) \\ \psi \cos(\theta) \\ -\psi \sin(\theta) \sin(\varphi) \end{bmatrix} \quad \mathbf{e}_\varphi = \frac{\partial \mathbf{P}}{\partial \varphi} = \begin{bmatrix} -Z \\ 0 \\ X \end{bmatrix}$$

We can further calculate the metric coefficients:

$$g_{ij} = \mathbf{e}_i \cdot \mathbf{e}_j = \begin{bmatrix} 1 & 0 & 0 \\ 0 & \psi^2 & 0 \\ 0 & 0 & R^2 \end{bmatrix} \quad \text{and} \quad J = \sqrt{\det[g_{ij}]} = \psi R$$

As generally required in SOLEDGE3X, the magnetic field is axisymmetric and thus

5. Verification and Validation – 5.1. Verification by the method of manufactured solutions

does not depend on the toroidal coordinate  $\varphi$ . By construction, it only has a poloidal and a toroidal component but no radial component, which are given in Eq. 5.1.

$$\begin{cases} B_\theta = \frac{1}{aR}\Psi_0 & \text{poloidal magnetic field} \\ B_\varphi = \frac{R_0}{R}B_0 & \text{toroidal magnetic field} \end{cases} \quad (5.1)$$

The magnetic field parameters are chosen such that the ratio of toroidal over poloidal magnetic field strength is  $aR_0B_0/\Psi_0 = 12$ . The conserved fields  $n$ ,  $\gamma$  and  $T$  are pre-defined to sinusoidal functions on the grid for electrons and one ion species.

$$n_\alpha = 1 + 0.1 \cos(\theta) \cos\left(\frac{\varphi}{N_{div}}\right) \sin\left(2\pi \frac{\psi - \psi_{min}}{\psi_{max} - \psi_{min}}\right) \quad (5.2)$$

$$\gamma_\alpha = 0.1 \cos(\theta) \cos\left(\frac{\varphi}{N_{div}}\right) \sin\left(2\pi \frac{\psi - \psi_{min}}{\psi_{max} - \psi_{min}}\right) \quad (5.3)$$

$$T_\alpha = 1 + 0.1 \cos(\theta) \cos\left(\frac{\varphi}{N_{div}}\right) \sin\left(2\pi \frac{\psi - \psi_{min}}{\psi_{max} - \psi_{min}}\right) \quad (5.4)$$

Tests have been performed on various mesh geometries in the scope of SOLEDGE3X from a perfectly regular grid with equally spaced cells in all coordinate directions to the distorted mesh depicted above. As the program can be either executed in a 2D or 3D mode with adapted stencils and geometry calculations, MMS tests have been developed for both scenarios.

### 5.1.2. Electromagnetic vorticity equation

We are interested in the vorticity system on the electric potential  $\Phi$  and the parallel magnetic vector potential  $A_\parallel$ . As free variables, they are set to a similar expression as the conserved fields:

$$\Phi = 1 + 0.1 \cos(\theta) \cos\left(\frac{\varphi}{N_{div}}\right) \sin\left(2\pi \frac{\psi - \psi_{min}}{\psi_{max} - \psi_{min}}\right) \quad (5.5)$$

$$A_\parallel = 1 + 0.1 \cos(\theta) \cos\left(\frac{\varphi}{N_{div}}\right) \sin\left(2\pi \frac{\psi - \psi_{min}}{\psi_{max} - \psi_{min}}\right) \quad (5.6)$$

The vorticity  $\Omega$  and the parallel current  $j_\parallel$  depend on the free fields and are initialized according to their definitions, where the derivatives on curvilinear coordinates can be calculated analytically with the metric theory discussed in Sec. 4.1.3 using Maple.

$$\Omega = \nabla \cdot \left( \frac{m_i}{Z_i B^2} \nabla_\perp [n T] + \frac{m_i n_i}{B^2} \nabla_\perp \Phi \right) \quad (5.7)$$

$$j_\parallel = \sigma_\parallel (-\nabla_\parallel \Phi + T_e \nabla_\parallel \log n_e + 1.71 \nabla_\parallel T_e) \quad (5.8)$$

Let us consider a slightly simplified version of the electromagnetic system in Eq.

[3.46](#) without additional currents from the charge balance, advection terms of  $j_{\parallel}$  or anomalous parallel diffusion. As the domain is fully periodic in parallel direction and no sheath boundaries are present to fix the potential, Dirichlet boundary conditions force the fields  $\Phi$  and  $A_{\parallel}$  to their initial values at the two radial boundaries and the system becomes uniquely solvable.

$$\begin{cases} \partial_t \Omega + \nabla \cdot \sigma_{\parallel} \left( \nabla_{\parallel} \Phi + \beta_0 \partial_t A_{\parallel} + \frac{m_e}{n_e} \partial_t j_{\parallel} \right) \mathbf{b} & = \nabla \cdot \sigma_{\parallel} (T_e \nabla_{\parallel} \log n_e + 1.71 \nabla_{\parallel} T_e) \mathbf{b} + S_{\Phi}^{MMS} \\ \nabla \cdot (\nabla_{\perp} A_{\parallel} \mathbf{b}) - \sigma_{\parallel} \left( \nabla_{\parallel} \Phi + \beta_0 \partial_t A_{\parallel} + \frac{m_e}{n_e} \partial_t j_{\parallel} \right) & = -\sigma_{\parallel} (T_e \nabla_{\parallel} \log n_e + 1.71 \nabla_{\parallel} T_e) + S_{A_{\parallel}}^{MMS} \end{cases} \quad (5.9)$$

The MMS source terms  $S_{\Phi}^{MMS}$  and  $S_{A_{\parallel}}^{MMS}$  contain the analytic value of all time-independent terms in the respective line of the equation. The vorticity equation is then solved for one timestep, and if the implementation is correct, the system should maintain a steady state. One drawback of a steady state system is that time derivatives are always assumed to vanish and terms such as the perpendicular Laplacian of  $\Phi$ ,  $j_{\parallel}$  or the divergence of  $A_{\parallel}$  are not confronted to their analytic form in the source term  $S^{MMS}$ . To catch these terms, it is important to consider the full expression of the vorticity  $\Omega$  as its initial value contains the analytic terms.

The system is run for exactly one timestep where only the discretization error modifies the values of the fields. This allows to compare a numerical and an analytic form of the vorticity and confront all terms in Eq. 5.9 to their expected values. To measure the error, we calculate the root mean square error  $\epsilon_d$  of the solution  $X$  to the initial, analytic field  $X_{ana}$ :

$$\epsilon_d = \sqrt{\frac{1}{N} \sum (X - X_{ana})^2} \quad (5.10)$$

where we sum the residual for each point in the domain excluding the imposed Dirichlet boundaries. To quantify the discretization error, we run the same simulation on increasingly high spatial resolutions and compare the error to the coarsest case. Second order stencils were used in the implementation, so we expect that the error reduces by a factor 4 when the resolution is doubled in a direction. The errors for the 2D and 3D implementations of the vorticity system are shown in Fig. 5.2. The dashed line indicates the ideal slope of second order convergence, and we observe that the errors decrease with a close match to the expected convergence as the resolution increases. This verifies the correct implementation of the vorticity equation in the SOLEDGE3X framework.

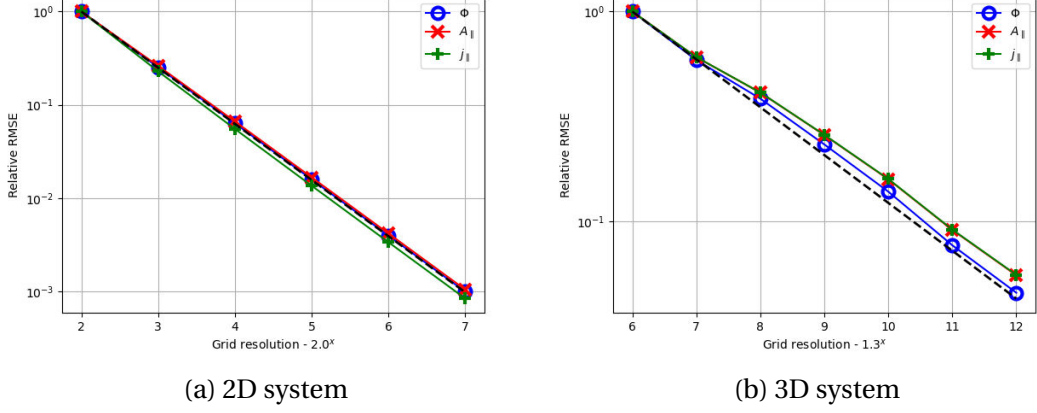


Figure 5.2.: Relative error between the initial plasma and the solution after one timestep for the electromagnetic vorticity system. The  $x$ -axis indicates the number of points per zone in each direction, the total number of points is thus  $N_{tot}^{3D} = 8 \cdot X^3$  (resp.  $N_{tot}^{2D} = 4 \cdot X^2$ ). The dashed lines indicate the slope of the ideal 2nd order convergence

### 5.1.3. Parallel heat diffusion with flutter

A second row of tests affects is dedicated to the correct implementation of the radial magnetic field that originates from flutter. The most critical new code component in that regard are the implicit parallel diffusion equations for heat and viscosity. For that purpose, we consider a very reduced energy conservation equation for electrons and ions, that effectively only remains with the parallel heat conduction from the Spitzer-Härm model.

$$\partial_t \left( \frac{3}{2} n_e T_e \right) = \vec{\nabla} \cdot \left( \kappa_0 T_e^{5/2} \nabla_{\parallel} T_e \vec{b} \right) + S_{T_e}^{MMS} \quad (5.11)$$

$$\partial_t \left( \frac{3}{2} n_i T_i + \frac{1}{2} \frac{m_i}{n_i} \gamma_i^2 \right) = \vec{\nabla} \cdot \left( \kappa_0 T_i^{5/2} \nabla_{\parallel} T_i \vec{b} \right) + S_{T_i}^{MMS} \quad (5.12)$$

The simulation set-up follows the same model as for the test on the vorticity equation as the sources are calculated analytically to maintain a steady-state and radial Dirichlet boundaries are imposed. The main novelty here is the addition of a radial component in the magnetic field, whose contravariant form is given by:

$$b^{\psi} = \frac{0.01}{B_{eq}} \cos(\theta) \cos\left(\frac{\varphi}{N_{div}}\right) \sin\left(2\pi \frac{\psi - \psi_{min}}{\psi_{max} - \psi_{min}}\right) \quad (5.13)$$

To be as realistic as possible with the real flutter, it is scaled by the magnitude of the equilibrium field (and not the total field) and takes both positive and negative values to adequately address the fluctuating nature of flutter. It allows to test the new 3D parallel diffusion operator from Sec. 4.4.2 and challenges it to the crucial case

where  $b^\psi$  tends to zero. The simulation was only run on the 3D MMS mesh, as it is the only effectively relevant use case. The root mean square error is shown in Fig. 5.3 for both temperatures, and we can still observe a satisfying agreement with the expected second order convergence.

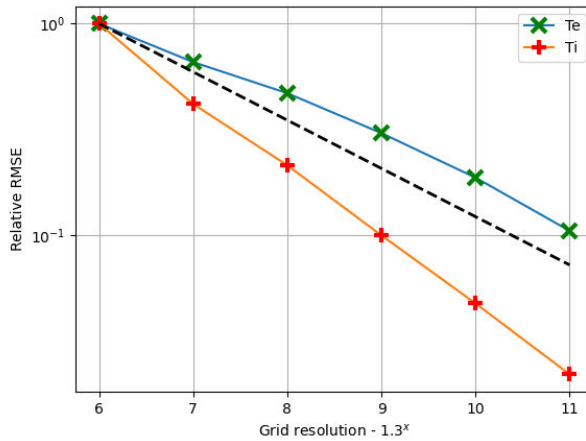


Figure 5.3.: Relative error between the initial plasma and the solution after one timestep for the parallel 3D heat diffusion system with flutter. The  $x$ -axis indicates the number of points per zone in each direction, the total number of points is thus  $N_{tot}^{3D} = 8 \cdot X^3$ . The dashed lines indicate the slope of the ideal 2nd order convergence

## 5.2. Validation on linear systems

The MMS verification confirmed the correctness of the implementation. A more integrative, physics-based validation of the electromagnetic model is proposed here to recover the linear behavior in ideal slab configurations. We first verify the general test framework on the transport term and the electrostatic vorticity equation before investigating Alfvén dynamics and the interaction with electron inertia effects.

### 5.2.1. Pure advection

A first step to validate the correct physical behaviour of the simulation and to test the general validation framework would be to investigate the plasma advection equations. We can hence define parallel and perpendicular wavenumbers  $k_{\parallel}$  and  $k_{\perp}$  that For this objective we set up a simplistic plasma model on a rectangular 2D SLAB topology, where magnetic field is uniform in poloidal Z direction. Periodic boundary conditions in all directions allow to properly observe wave propagation without any inference at the domain boundaries. In an isothermal hydrogen plasma without source terms and drifts, the governing equations then simplify to:

$$\partial_t n_i + \nabla \cdot (n_i \mathbf{u}_i) = 0 \quad (5.14)$$

$$\partial_t (m_i n_i u_{\parallel}) + \nabla \cdot (m_i n_i u_{\parallel} u_i) = -2 T_e \nabla_{\parallel} n_e \quad (5.15)$$

In this simple plasma, only the density and the velocity evolve over time and depend on each other. The electric potential  $\Phi$  can also be computed and observed, but it does not interfere with the system because the parallel electric field in the momentum balance Eq. 5.15 is calculated from the electron pressure gradient  $E_{\parallel} = (\nabla_{\parallel} p_e + R_e)/n_e$ .

To perform the linear analysis of the system, we assume that field variables such as the velocity or density respect some Fourier solution as sum of several wave modes with respective amplitudes  $\tilde{X}_{\omega, k_{\perp}, k_{\parallel}}$ :

$$X = \bar{X} + \hat{X} = X_0 + \sum \tilde{X}_{\omega, k_{\perp}, k_{\parallel}} e^{i(-\omega t + k_{\perp} \psi + k_{\parallel} \theta)} \quad (5.16)$$

Since we do not consider any drifts the radial component  $u_{\psi}$  of the velocity vector vanishes. Further, the mean density is  $\bar{n} = n_0$  while the mean velocity  $\bar{u}_{\theta}$  is zero. Because we are only interested in a first order approximation of the solution, we neglect all higher-order mixed fluctuating terms. Thus, Eq. 5.14 and Eq. 5.15 transform to:

$$\begin{aligned} -i\omega \hat{n} + i\bar{n} k_{\parallel} \hat{u}_{\theta} + i\bar{u}_{\theta} k_{\parallel} \hat{n} &= 0 & \Leftrightarrow \hat{u}_{\theta} &= \frac{\omega}{n_0 k_{\parallel}} \hat{n} \\ -i\omega m_i (\bar{n} \hat{u}_{\theta} + \bar{u}_{\theta} \hat{n}) + i m_i k_{\parallel} (2\bar{n} \bar{u}_{\theta} \hat{u}_{\theta} + \bar{u}_{\theta}^2 \hat{n}) &= -2i T k_{\parallel} \hat{n} & \Leftrightarrow \hat{u}_{\theta} &= \frac{2T k_{\parallel}}{m_i n_0 \omega} \hat{n} \end{aligned}$$

Both are combined to obtain a dispersion relation for the frequency  $\omega$ :

$$\frac{\omega}{n_0 k_{\parallel}} = \frac{2T k_{\parallel}}{m_i n_0 \omega} \quad \Leftrightarrow \quad \omega = \pm \sqrt{\frac{2T}{m}} k_{\parallel} \quad (5.17)$$

It is apparent that both solutions for  $\omega$  are real therefore non-decaying waves travelling with the speed of sound  $c_s = \sqrt{2T/m}$  appear. The perpendicular wave mode does not contribute to the equation so a 1D system along the poloidal axis is sufficient to simulate the behaviour. Both the electron and the ion density are initialized with one sinusoidal perturbation and Fig. 5.4a shows their evolution. The electron velocity in Fig. 5.4b responds to this initial excitation with a shifted standing wave with same frequency.

## 5. Verification and Validation – 5.2. Validation on linear systems

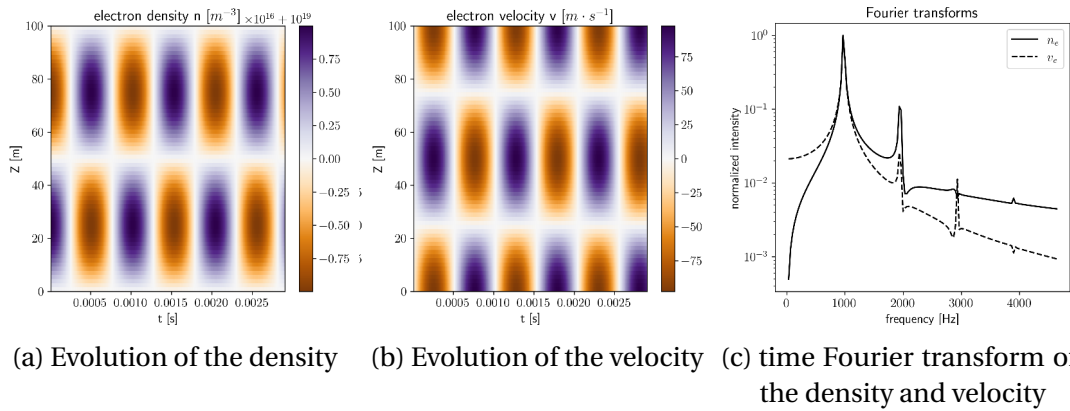


Figure 5.4.: Evolution of the 1D SLAB system with 64 cells in poloidal direction over 10000 timesteps with the RK4 scheme. For a better readability only parts of the graphs are represented

The system is initialized with one wavemode along the "poloidal" length of  $L = 100\text{m}$  so the wavenumber here is  $k_{\parallel} = 2\pi/L \approx 0.0628$ . The plasma temperature is kept constant at  $T = 100\text{eV}$  and the mass of a deuterium atom equals to  $m_i \approx 3.34 \cdot 10^{-27}\text{kg}$ , so we can expect a system frequency of  $\omega \approx 978\text{Hz}$  from the dispersion relation in Eq. 5.17. This corresponds precisely to the main frequency peak in Fig. 5.4c and thus acoustic waves appear in the system as expected. The smaller peaks at higher frequency modes are however not physical and are likely due to numerical noise as their appearance highly depends on the spatial and temporal resolution and their intensity increases for longer simulations.

### 5.2.2. Electrostatic vorticity equation

Before plunging into the vorticity equation with  $A_{\parallel}$  it may be interesting to discuss whether the correct behaviour is actually observed in the original electrostatic implementation. For that we reduce the system to the bare minimum set of equations that involve the electric potential  $\Phi$ . Neglecting all kind of transport equations and source phenomena remains the following simple equation on  $\Phi$ :

$$\partial_t \nabla \cdot \left[ \frac{m_i n_i}{B^2} \nabla_{\perp} \Phi \right] = -\nabla \cdot \sigma_{\parallel} \nabla_{\parallel} \Phi \quad (5.18)$$

whose simple dispersion relation reads, assuming that  $k_{\perp} \neq 0$ :

$$\omega = -\frac{B^2 \sigma_{\parallel}}{m_i n_i} \frac{k_{\parallel}^2}{k_{\perp}^2} i \quad \Rightarrow \quad \lambda = \frac{B^2 \sigma_{\parallel}}{m_i n_i} \frac{k_{\parallel}^2}{k_{\perp}^2} \quad (5.19)$$

As  $\omega$  is a pure negative complex number, we do not expect any oscillations but an exponential decay of the solution. All points in the domain decay with

$$\Phi(t) = \Phi_0 e^{-\lambda t} + C \quad (5.20)$$

where the decay rate  $\lambda$  is the negative imaginary part of  $\omega$  and  $\Phi_0$  relates to the initial distribution of the electric potential.

The time integration of this system can only be performed by solving the implicit system because there is no direct expression for the time derivative of  $\Phi$ . Further, the electric potential  $\Phi$  appears only in perpendicular and parallel Laplacian operators. Together with the periodic boundary conditions in all directions, one degree of freedom remains and the solution of  $\Phi$  can only be calculated up to a constant  $C$ . To make the system invertible, it is thus necessary to add some term to the system. One simple approach is to fix (or ground)  $\Phi$  to a set value  $\Phi^G$  at one point  $[i_\psi^G, i_\theta^G]$  in the domain. This defines the free parameter  $C$  and  $\Phi(t)$  at all points converges to  $\Phi^G$ .

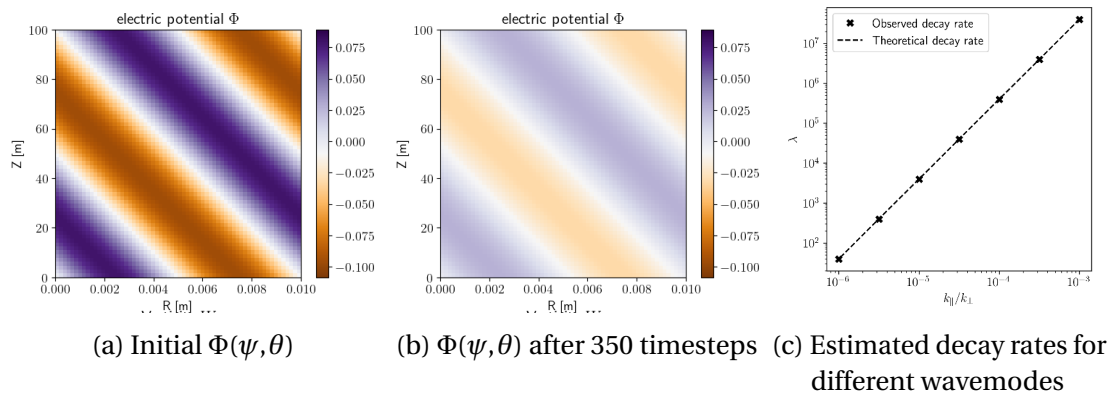


Figure 5.5.: Evolution of the 2D electrostatic SLAB system with 64 cells in radial and poloidal direction over 10000 timesteps with the implicit Euler scheme. The system is grounded at the center of the domain to  $\Phi^G = 0V$ .

The uniform decay can be clearly seen between Fig. 5.5a and Fig. 5.5b. It remains to investigate whether the observed attenuation matches the expected decay rate  $\lambda$ . A Fourier transformation as to determine oscillatory modes for the standing acoustic waves in the previous section is not of great help here, instead we use a non-linear least squares to fit the time evolution of  $\Phi(t)$  at an arbitrary point in the domain except the grounded point. We fit the parameters  $\Phi_0$ ,  $\lambda$  and  $C$  from Eq. 5.20 to the simulation data and compare the hence estimated  $\lambda$  to the theoretical decay rate for the given initial wave. Fig. 5.5c shows that there is a strong agreement between the theoretical and fitted decay rates for a large array of domain configurations. The wavenumbers  $k_{\parallel}$  and  $k_{\perp}$  were modified by changing the poloidal respectively the radial size of the domain with always the first wave mode spanning the entire domain. We can safely claim that the original electrostatic implementation produces the expected physical behaviour.

### 5.2.3. Electromagnetic vorticity equation

While acoustic waves are characteristic for a physical medium, Alfvén waves dominate oscillations of ions within a magnetic field. The motion occurs in direction of the

magnetic field lines where the ion mass accounts for the inertia and the magnetic field tension for the restoring wave force. The Alfvén wave group velocity for a species  $i$  is given by:

$$v_A = \frac{B}{\sqrt{m_i n_i \mu_0}} \quad (5.21)$$

With the new parallel magnetic vector potential  $A_{\parallel}$  into the vorticity Eq. ?? Alfvén waves should appear in the simulation and the aim of this section is to prove their existence. We follow the same approach as in the previous section for the electrostatic case and reduce the system to the strict necessary minimum and keep following equations:

$$\partial_t \nabla \cdot \left[ \frac{m_i n_i}{B^2} \nabla_{\perp} \Phi \right] = \nabla \cdot \sigma_{\parallel} (-\nabla_{\parallel} \Phi - \partial_t A_{\parallel}) \quad (5.22)$$

$$\Delta_{\perp} A_{\parallel} = -\mu_0 \sigma_{\parallel} (-\nabla_{\parallel} \Phi - \partial_t A_{\parallel}) \quad (5.23)$$

We ignore any kind of advection phenomena thus all densities  $n_{i/e}$  and temperatures  $T_{i/e}$  keep their initial uniform distributions their gradients vanish. If we perform the linear analysis of the remaining system we get following relation for Eq. 5.22:

$$\begin{aligned} i \frac{m_i n_i}{B^2} k_{\perp}^2 \omega \hat{\Phi} &= \sigma_{\parallel} k_{\parallel}^2 \hat{\Phi} - \sigma_{\parallel} k_{\parallel} \omega \hat{A}_{\parallel} \\ \Leftrightarrow \qquad \qquad \qquad \hat{A}_{\parallel} &= \left( \frac{k_{\parallel}}{\omega} - i \frac{m_i n_i k_{\perp}^2}{\sigma_{\parallel} B^2 k_{\parallel}} \right) \hat{\Phi} \end{aligned}$$

and for Eq. 5.23:

$$\begin{aligned} -k_{\perp}^2 \hat{A}_{\parallel} &= i \mu_0 \sigma_{\parallel} k_{\parallel} \hat{\Phi} - i \mu_0 \sigma_{\parallel} \omega \hat{A}_{\parallel} \\ \Leftrightarrow \qquad \qquad \qquad \hat{A}_{\parallel} &= \frac{\mu_0 \sigma_{\parallel} k_{\parallel}}{\mu_0 \sigma_{\parallel} \omega + i k_{\perp}^2} \hat{\Phi} \end{aligned}$$

If we combine both expressions we can relate the frequency to the parallel and perpendicular wave modes:

$$\begin{aligned} \frac{k_{\parallel}}{\omega} - i \frac{m_i n_i k_{\perp}^2}{\sigma_{\parallel} B^2 k_{\parallel}} &= \frac{\mu_0 \sigma_{\parallel} k_{\parallel}}{\mu_0 \sigma_{\parallel} \omega + i k_{\perp}^2} \\ \Leftrightarrow \qquad \qquad \qquad i \frac{m_i n_i k_{\perp}^2 \omega}{\sigma_{\parallel} B^2 k_{\parallel}^2} &= 1 - \frac{\mu_0 \sigma_{\parallel} \omega}{\mu_0 \sigma_{\parallel} \omega + i k_{\perp}^2} \\ \Leftrightarrow \qquad \qquad \qquad \omega^2 + i \frac{k_{\perp}^2 \omega}{\mu_0 \sigma_{\parallel}} &= \frac{B^2}{m_i n_i \mu_0} k_{\parallel}^2 \end{aligned}$$

We find the square of the Alfvén group velocity 5.21 as a factor before the parallel wave number. There is an additional imaginary term in the dispersion relation which

depends on the perpendicular wave number and adds some damping to the system. Let us call  $\gamma = 1/(\mu_0\sigma_{\parallel})$  the associated damping coefficient. The dispersion relation can then be rewritten to:

$$\omega^2 + i\gamma k_{\perp}^2 \omega - v_A^2 k_{\parallel}^2 = 0 \quad (5.24)$$

If we transform the system back to the time domain, we expect a damped solution for the potentials  $\Phi$  and  $A_{\parallel}$  of the form [15]:

$$X = X_0 + \hat{X} e^{-\lambda t} e^{i(-\omega_0 t + k_{\perp} \psi + k_{\parallel} \theta)} \quad (5.25)$$

where the decay rate  $\lambda$  contains the imaginary part and the oscillation frequency  $\omega_0$  the real part of  $\omega$ .

In the case that  $\gamma k_{\perp}^2 > 2v_A k_{\parallel}$ , the frequency  $\omega$  is purely imaginary and the system decays to the mean value  $X_0$  with the rate:

$$\lambda = \frac{\gamma}{2} k_{\perp}^2 \pm \sqrt{\frac{\gamma^2}{4} k_{\perp}^4 - v_A^2 k_{\parallel}^2} \quad (5.26)$$

If on the other hand  $\gamma k_{\perp}^2 < 2v_A k_{\parallel}$ , the frequency  $\omega$  has both a real and an imaginary part. The decay rate is then:

$$\lambda = \frac{\gamma}{2} k_{\perp}^2 \quad (5.27)$$

and the system frequency:

$$\omega_0 = \pm \sqrt{v_A^2 k_{\parallel}^2 - \frac{\gamma^2}{4} k_{\perp}^4} \quad (5.28)$$

In the case that the damping term is much smaller than the oscillatory term (if for instance the parallel wave mode dominates over the perpendicular one),  $\omega$  is a real number and the system frequency only depends on the Alfvén group velocity and we should be able to observe pure Alfvén waves.

$$\omega_0 = v_A k_{\parallel}$$

In Eq. 5.26 and Eq. 5.28 we see that there are two possible solution for the decay rate respectively the oscillation frequency. This does not conflict with our assumed wave solution which has been defined in Eq. 5.16 as the sum of several Fourier modes and each solution here contributes to one mode.

As in the electrostatic case from the previous section, the just described system is not invertible and  $\Phi$  is defined up to a constant. Grounding the potential in one single point is however not a suitable solution here because it deteriorates the condition number of the vorticity matrix past solvability. To solve this issue, I set the potential not in one but in several points to a fixed value. The potential in the remaining domain then distributes according to this value and the whole system becomes solvable. Numerically, this is achieved by replacing the row of the matrix corresponding to the

grounded point by a single 1 on the diagonal and the matching term in the RHS vector by the desired value for  $\Phi$ . This operation is equal to enforcing Dirichlet boundary conditions in radial direction if  $\Phi$  is grounded at all points with index  $i_\psi^G = 16$ .

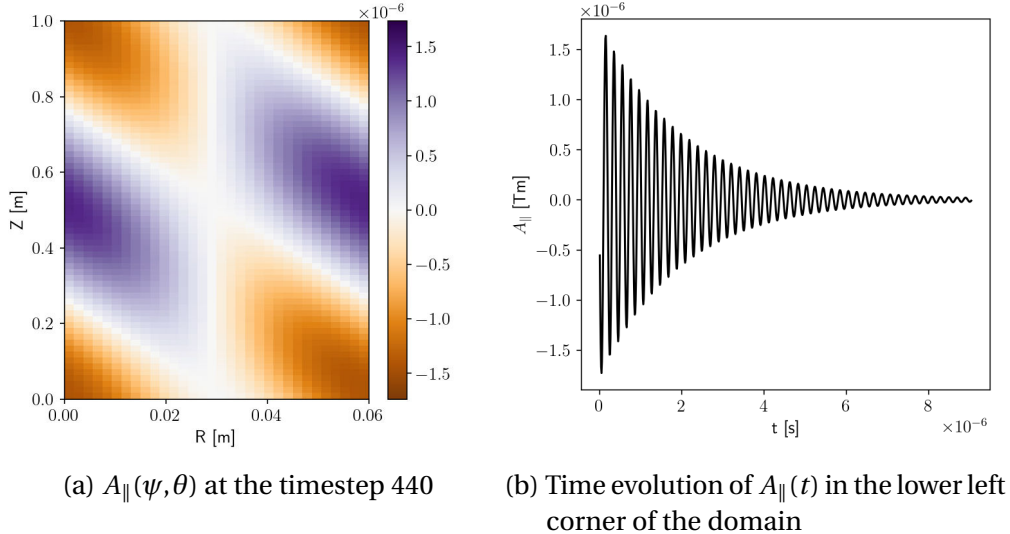


Figure 5.6.: Snapshot of an electromagnetic SLAB simulation on a domain with  $N_\psi = 32$  and  $N_\theta = 64$  grid points. All point at the radial center with  $i_\psi^G$  are grounded.

In the simulations with a grounded line, the initial wave solution has been applied to the vorticity field  $\Omega$  to prevent steep gradients and instabilities if it was done on  $\Phi$  directly. Very soon, the two potentials  $\Phi$  and  $A_{\parallel}$  respond to this initial excitation and a wave profile appears as depicted in Fig. 5.6a. The line of grounded points in the middle of the domain however breaks the wave which then smoothly lines up with the equilibrium point  $\Phi_0 = 0V$  and  $A_{\parallel,0} = 0Tm$  around the grounded line. At this point it may be emphasized that only the electric potential  $\Phi$  is grounded, but as both potential fields are strongly coupled the grounded line affects  $A_{\parallel}$  equally. We thus have a wave that is guided between two poloidal grounded lines (remember that the domain is periodic in radial direction) so by construction the system cannot account for radial dynamics. If we consider a point that is furthest away from the grounded line (e.g. any point on the domain boundary in the example above) we might still be able to observe some expected physical behaviour. At first glance, if we track  $A_{\parallel}$  in one point over time as in Fig. 5.6b, a decaying oscillation appears which is in line with the here dominant underdamped regime.

We investigate the underdamped scenario by opposing simulation results to the expected damping rates  $\lambda$  and frequencies  $\omega_0$ . As for the previous electromagnetic we fit the four free parameters in Eq. 5.25 to simulation data with a nonlinear least squares method. With 1000 sample points we get a high fitting fidelity with a relative standard deviation of the order of  $10^{-9}$  and the difference if the fit is performed on  $\Phi$

or  $A_{\parallel}$  has about the same magnitude.

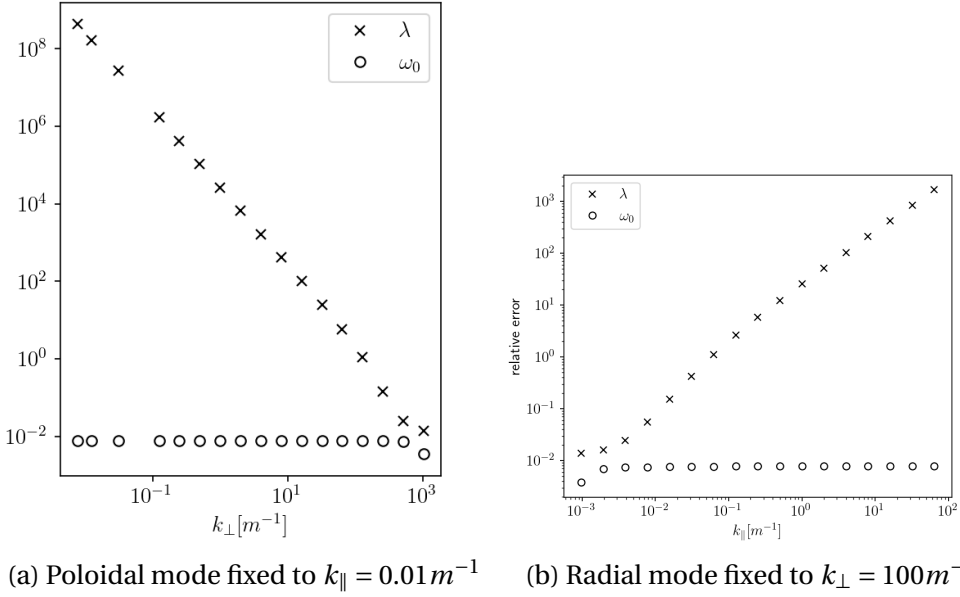


Figure 5.7.: Relative error for the fits of the frequency  $\omega_0$  and the decay rate  $\lambda$  on the evolution of  $A_{\parallel}$  with respect to the expected values in a grounded electromagnetic SLAB simulation on a domain with  $N_y = 32$  and  $N_{\theta} = 64$  grid points.

While the frequency behaves well with respect to the analytic predictions, we see a strong mismatch for the damping, especially for low  $k_{\perp}$  and high  $k_{\parallel}$  values. This is likely due to the grounded points aligned to a same radial, perpendicular coordinate that skews the propagation of the wave. Better results are expected if the grounded points would correspond to the wave dynamics, as will be applied in the subsequent test.

### 5.2.4. Linear transition from Alfvén to thermal electron waves

For the last, most integrative test, we switch to a 3D slab domain. In Sec. 2.3.3, we introduced drift-Alfvén waves. With the electromagnetic extensions, drift-waves are coupled to higher-frequency modes that transition from the Alfvén to the thermal electron speed and travel along magnetic field lines. These modes are associated with negative growth rate and usually dampen out quite fast. They can however be used to validate the electromagnetic implementation. The thought behind it is that if we reduce the system to suppress drift-waves, and run simulations with a sufficiently temporal resolution, the transition should appear in the SOLEDGE3X simulations.

## 5. Verification and Validation – 5.2. Validation on linear systems

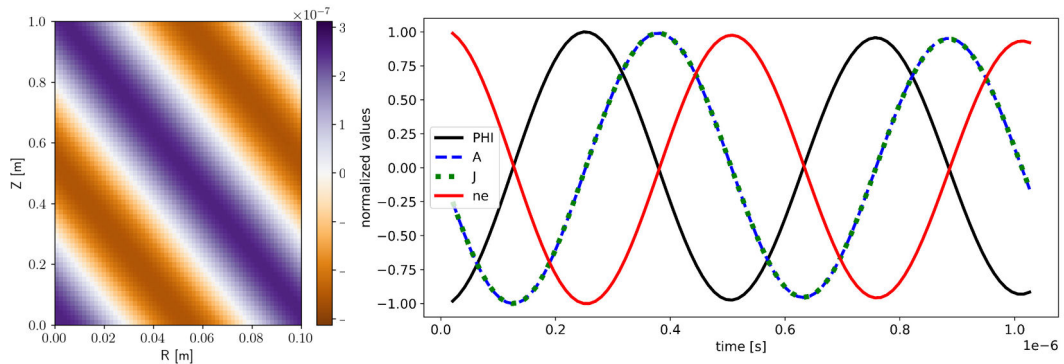
The computational domain is a 3D slab domain with periodic boundary conditions in all directions. The magnetic field is assumed to be constant in the  $\theta - \varphi$  plane, and is therefore somewhat similar to the topology in production cases. It allows to validate the implementation of parallel operators in a realistic setting with respect to the linear behavior. The wavenumbers  $k_\psi$ ,  $k_\theta$ , and  $k_\varphi$  are defined by the respective dimensions of the slab. Parallel and perpendicular wavenumbers express as:

$$k_{\parallel} = b_\theta k_\theta + b_\varphi k_\varphi \quad k_{\perp}^2 = k_\psi^2 + k_\theta^2 + k_\varphi^2 - k_{\parallel}^2 \quad (5.29)$$

The following simplified model (Eq. 5.30) is considered on the electron density  $n_e$ , parallel current  $j_{\parallel}$ , and the potentials  $\Phi$  and  $A_{\parallel}$ :

$$\left\{ \begin{array}{l} \nabla \cdot \left[ \frac{m_i n_i}{B^2} \partial_t \nabla_{\perp}^2 \Phi \right] = \nabla \cdot (j_{\parallel} \mathbf{b}) \\ \nabla_{\perp}^2 A_{\parallel} = -\mu_0 j_{\parallel} \\ \eta_{\parallel} j_{\parallel} + \frac{m_e}{n_e e^2} \partial_t j_{\parallel} = (-\nabla_{\parallel} \Phi - \partial_t A_{\parallel} + T_e \nabla_{\parallel} \log(n_e)) \\ \partial_t n_e = \frac{1}{e} \nabla \cdot (j_{\parallel} \mathbf{b}) \end{array} \right. \quad (5.30)$$

Again we need to ground the potential somewhere to make the system invertible. For the 3D system, I grounded all points on a diagonal plane that cuts the slab in two opposite corners and is orthogonal to the vector  $[1, 1, 1]^T$ . With an initial wave profile on the density, a standing wave appears then for all four fields. A typical snapshot is shown in Fig. 5.8a. The magnetic vector potential  $A_{\parallel}$  and  $j_{\parallel}$  oscillate in phase, while density and potential are shifted by a quarter of a phase in positive and negative direction respectively.



(a) Snapshot of  $A_{\parallel}$  [Tm]      (b) Evolution of the four fields in one point of the domain

Figure 5.8.: Characteristic evolution of the four-field electromagnetic model in a domain with  $N_\psi = N_\theta = N_\varphi = 63$  grid points.

The complex dispersion relation of the four-field model has a real and an imaginary part indicating the appearance of a decaying wave:

$$\omega_A^2 = \left( \frac{v_A^2}{1 + \frac{m_e}{e^2 \mu_0 n_e} k_\perp^2} + \frac{1}{T_0 k_\perp^2 + \frac{1}{v_{th,e}^2}} \right) k_\parallel^2 - \frac{\eta_\parallel^2 k_\perp^4}{4 \left( \mu_0 + \frac{m_e}{e^2 n_i} k_\perp^2 \right)^2} \quad (5.31)$$

The dispersion relation describes "shear Alfvén waves", according to which perturbations travel along magnetic field lines. In cases with high parallel conductivity, the first term dominates the dispersion relation. We then observe that the relation describes a wave in parallel direction whose velocity is bound by the Alfvén wave speed  $v_A = \frac{B}{\sqrt{m_i n_i \mu_0}}$  for small  $k_\perp$  and by the thermal electron wave speed  $v_{th,e} = \sqrt{\frac{T_e}{m_e}}$  for large  $k_\perp$ . This is in line with the findings by Dudson *et al.*[26] and reflects the need for electron inertia to avoid unphysically large speeds in the upper  $k_\perp$  limit.

From Eq. 5.31, we expect a wave in the parallel direction traveling at the Alfvén velocity for small  $k_\perp$  and at the thermal electron velocity at high  $k_\perp$ . In the slab domain,  $k_\perp$  is changed by changing the radial dimension of the domain. The results of our numerical simulations perfectly match the predictions by Dudson [26] and the numerical results obtained by Stegmeir *et al.*[93] and show the expected transition when  $k_\perp$  is varied, Fig. 5.9.

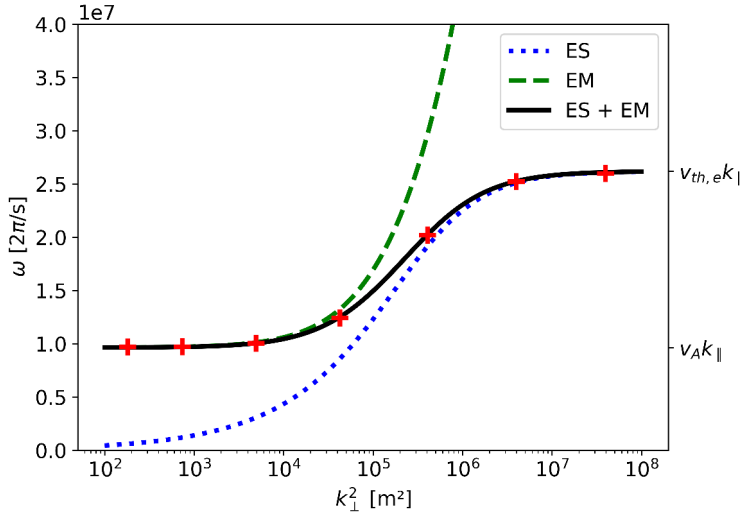


Figure 5.9.: Fitted wave frequencies as a function of the perpendicular wave numbers. The lines indicate the theoretical wave frequencies in the electrostatic case with finite electron mass (ES), the electromagnetic case with  $m_e = 0$  (EM), and the complete electromagnetic case with electron inertia (ES + EM).

## **Part IV.**

# **Electromagnetic Turbulent Plasma Simulations**

# 6. Limited Geometry

## Chapter Summary

The impact of electromagnetic effects on drift-wave turbulence is studied in non-singular magnetic configurations in the presence of a sheath. Simulations are conducted on a 3D curved attached slab configuration and a 3D circular geometry with open and closed flux surfaces. The reference electrostatic model is successively extended by including electron inertia, magnetic induction, and electromagnetic flutter.

The analysis of a plasma blob in the slab configuration shows that the sheath impedes its propagation along the entire toroidal domain length, while the electromagnetic scenarios reduce the sheath's impact and lead to a much stronger bending of the blob. In the circular geometry, this corresponds to a wider spread of turbulent filaments into the SOL.

The drift-Alfvén dispersion relation for the four scenarios is solved analytically, where the characteristic drift-wave frequency is accompanied by two damped modes that arise around the Alfvén and electron transit frequencies. Magnetic induction and, to a lesser extent, electron inertia increase the growth rate of drift-wave instabilities, while flutter stabilizes them. This behavior has been verified during the initial instability growth phase in the circular geometry with  $m_e$  and  $\beta$  scans.

The nonlinear turbulence phase begins when initial perturbations saturate. A slab test case with a radial pressure step shows that magnetic induction widens the turbulent transition zone, while the stabilizing effect of flutter preserves sharp gradients. The evolution of the perpendicular mode structure has been compared on a closed flux surface in the circular case. Starting from a base diamagnetic mode, it appears that with the full electromagnetic model, higher harmonics are regularly excited from the onset of the nonlinear phase. In contrast, in the reference electrostatic scenario, harmonics are less clearly separated but only gradually propagate from low to high wavenumbers.

The linear analysis from the previous section is only of very limited use, as characteristic shear Alfvén and thermal electron times are much shorter than the ion cyclotronic time, which underlies the resolution of typical turbulent SOLEDGE3X simulations. Drift Alfvén waves in turn correspond to the impact of inductive electromagnetic effect on the formation of drift waves, where the term  $\partial_t A_\parallel$  in Ohm's law modifies the non-adiabatic response of the potential  $\Phi$  to parallel fluctuations of the electron pressure  $p_e$ . This chapter seeks to investigate these effects on a few analytic geometries. In the first Sec. 6.1, we take a closer look at the theoretic linear dynamics of drift-Alfvén waves with electromagnetic effects. We then consider a toroidal slab geometry in Sec. 6.2 on which we study the propagation of a plasma blob and the excitation of drift-wave turbulence. Finally in Sec. 6.3, we consider the linear and nonlinear turbulence phases on a limited circular geometry with open and closed field lines.

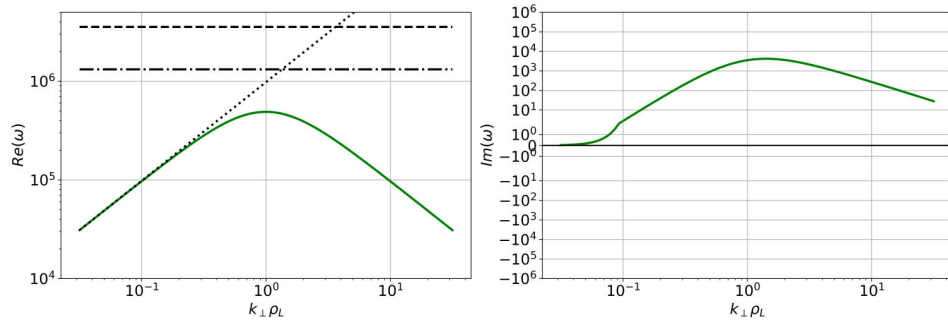
## 6.1. Electromagnetic modes excitation

As an introduction to simulations with SOLEDGE3X, let us consider the linear behavior of drift-Alfvén waves again. To put later simulation results in perspective, we analyze the impact of electromagnetic terms on drift-wave turbulence within a linearized system. Specifically, we compare the effects of a finite electron mass (EI-inert), electromagnetic induction with electron mass (EM), and electromagnetic induction with both flutter and electron mass (EM-flutter) in comparison to the baseline electrostatic case. The dispersion relation from Eq. 2.81 is adjusted to each of the four scenarios and solved exactly using the Python library SymPy for symbolic computation. Notably, we use the full dispersion relation without applying the simplifications used when we introduced the linear behavior of the drift-Alfvén system in Sec. 2.3.3.1. To recall, the dispersion relation is given by:

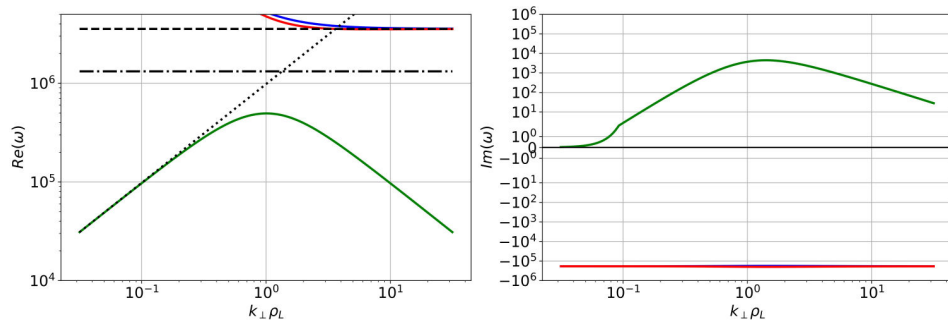
$$i(\rho_{L,e}^2 k_\perp^2 + \beta_0) \omega^3 + \left( -i\beta_0 \omega_* - \frac{\eta_\parallel e n_0 T_0 k_\perp^2}{B^2} \right) \omega^2 - i\omega_s^2 (\omega_* - (1 + \rho_L^2 k_\perp^2) \omega) = 0 \quad (6.1)$$

Given the coupled nature system, there are several complex solutions for  $\omega$  for each scenario, where each corresponds to a different mode. In Fig. 6.1, the real and imaginary components of all modes are plotted as functions of the perpendicular wave number  $k_\perp$ , with typical parameters for a mid-sized tokamak. The real component  $\omega_R$  represents the wave phase frequency, while the imaginary component  $\gamma$  describes the growth or damping rate of each mode. A positive  $\gamma$  indicates an unstable mode with exponential growth, whereas a negative  $\gamma$  corresponds to a stable mode that is damped over time.

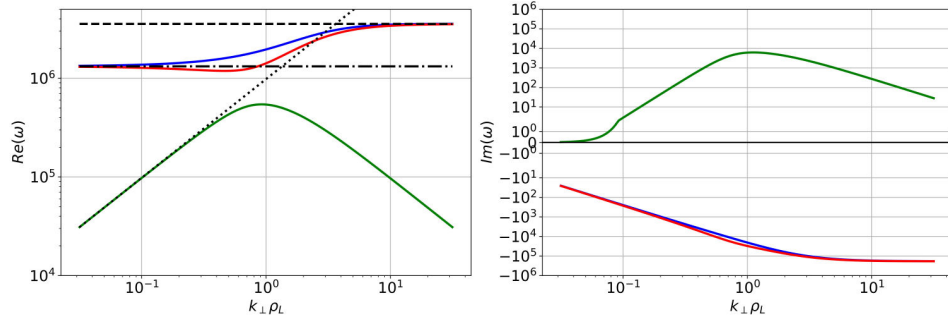
## 6. Limited Geometry – 6.1. Electromagnetic modes excitation



(a) Electrostatic system



(b) Electrostatic system with electron inertia



(c) Electromagnetic system

## 6. Limited Geometry – 6.1. Electromagnetic modes excitation

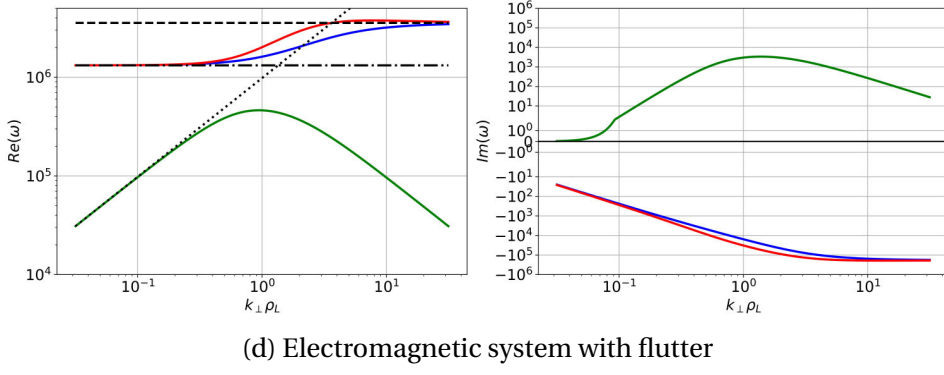


Figure 6.1.: Dependency on the perpendicular wavenumber  $k_{\perp}$  of the real and imaginary parts of the all solutions  $\omega$  to the dispersion relation 6.1. Except for  $k_{\perp}$ , all other values derive from:  $B = 1\text{T}$ ,  $n = 5 \cdot 10^{19}\text{m}^{-3}$ ,  $T = 200\text{eV}$ ,  $\lambda_p = 0.1\text{m}$  and  $k_{\parallel} = 0.6\text{m}^{-1}$ . On a pair of graphs, a given color represents the same mode. In the left plots for  $\text{Re}\{\omega\}$ , characteristic frequencies of the system are shown for reference ("—" diamagnetic  $\omega_*$ , "..." electron sound  $\omega_{s,e}$ , "---" Alfvén  $\omega_A$ ).

In the green curve, we observe the characteristic drift-wave frequency, which initially follows the diamagnetic frequency  $\omega_*$  in the lower  $k_{\perp}$  limit and reaches its maximum at  $k_{\perp}\rho_L = 1$ , before declining again. When the electron inertia term is introduced, a new mode emerges, starting at a significantly higher frequency before stabilizing at the electron sound frequency  $\omega_{s,e} = v_{th,e}k_{\parallel}$ . The introduction of electromagnetic terms governs the behavior of the new modes in the lower  $k_{\perp}$  limit, which are then bounded by the shear Alfvén phase velocity. Qualitatively, the phase frequencies exhibit similar characteristics with or without flutter, with the primary difference being a more pronounced separation between the two modes as they transition from  $\omega_A$  to  $\omega_{s,e}$  in the pure induction. Overall, the characteristic frequencies of the electromagnetic modes are several orders of magnitude higher than the drift-wave frequency.

Looking at the growth rates associated with the modes, we first observe that drift waves are unstable with strong positive growth rates where the frequency is maximal, consistent with the earlier discussion about drift-wave instabilities. On the other hand, electromagnetic (and electron inertial) modes are very stable, showing strong negative  $\gamma$ . If one intends to study the growth and propagation of turbulent structures and their global impact, Alfvénic modes will only marginally contribute. It is hence possible to avoid the numerical costs involved with the high-frequency modes without much loss of accuracy.

It is more important to consider the effects of electromagnetic contributions on the drift-wave mode. For this purpose, Fig. 6.2 compares the real and imaginary parts of the drift-wave modes in the three electromagnetic scenarios with those in the electrostatic scenario.

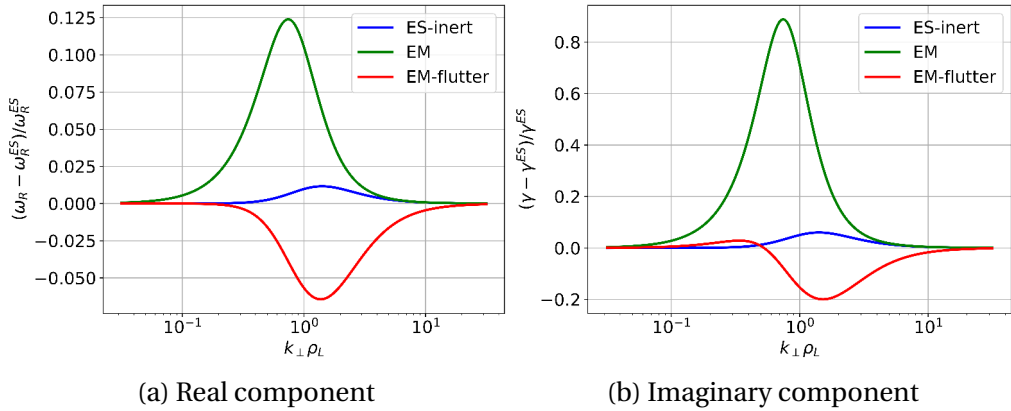


Figure 6.2.: Relative difference of drift-wave frequency in the electromagnetic scenarios to the reference electrostatic case.

The real part is altered by the electromagnetic additions, but the change of phase frequency will only have a minor impact on production cases. On the other hand, the growth rate increases with electron inertia and even more with electromagnetic induction. Electromagnetic flutter on the other hand largely mitigates the instabilities, and even reduces the growth rate observed in electrostatic drift waves.

## 6.2. Slab configurations

We place ourselves in a plasma environment similar to the separatrix region in the diverted TCV simulations from the next Chapter 7. The magnetic field is aligned to the toroidal coordinate with  $B_{eq,t} = 1.3\text{T}$  with a curvature of 1.1m from the tokamak center, similar to the position of the separatrix at the outer mid-plane in TCV. Limiters are placed at both toroidal ends such that that connection length  $L_{\varphi} = 45\text{m}$ . A cartesian grid with coordinates  $r$  and  $z$  discretizes each poloidal plane, allowing radial fluxes out and with periodic boundary conditions in the vertical  $z$ -direction. To simplify the study and prevent numerical difficulties at the sheath, we apply Neumann-0 boundary  $\partial_{\parallel} n^{BC} = 0$  on the density and the potential  $\Phi$  is fixed to  $\Phi^{BC} = \Lambda T_e^{BC}$ . This is a major simplification to the typical SOLEDGE3X sheath conditions described in Sec. 3.4. A 3D representation of the domain is given in Fig. 6.3

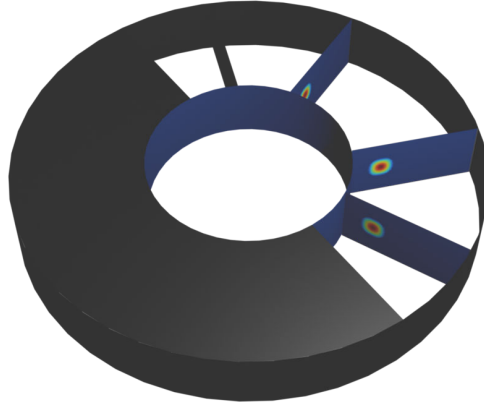


Figure 6.3.: 3D representation of the slab domain with four poloidal planes. The toroidal length of the domain is artificially increased to 45m while keeping the radius at 1.1m

### 6.2.1. Analysis of a plasma blob

In the first series of test, we study the propagation of a plasma blob in the slab domain. The electron temperature is kept constant at  $T_e = 60\text{eV}$ , ions are cold and the background density is set to  $n_0 = 10^{19}\text{part/m}^3$ . The axisymmetric blob initially takes a Gaussian profile

$$n = n_0 \left(1 + \alpha e^{-[(r-r_b)^2 + (z-z_b)^2]/\delta_b^2}\right) \quad (6.2)$$

with a blob overdensity  $\alpha = 2$  and radius  $\delta_b = 1\text{cm}$ . The blob evolves with curvature and electric drifts, neglecting anomalous perpendicular diffusion and viscous effects. Further, electron inertia effect are neglected with  $m_e = 0$ . We compare the reference electrostatic case with magnetic induction in the parallel electric field and the full electromagnetic setting including flutter. The simulation results are collected in Fig. 6.4.

## 6. Limited Geometry – 6.2. Slab configurations

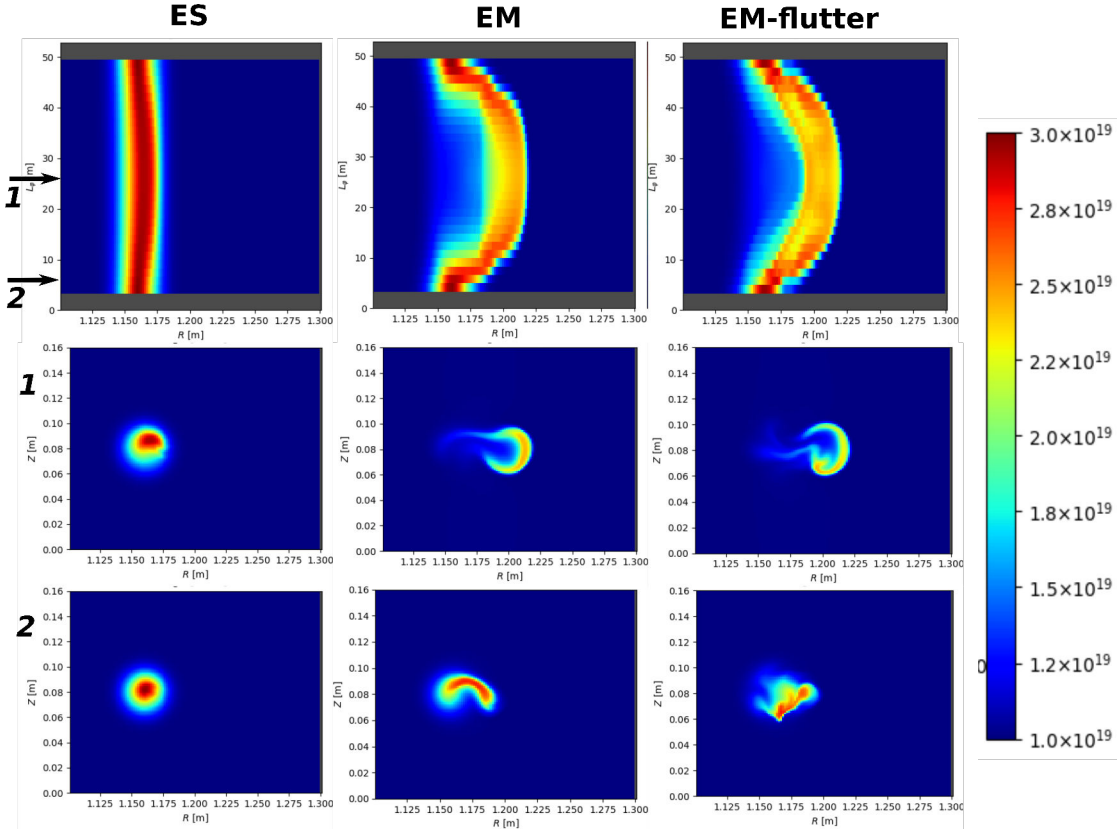


Figure 6.4.: Density profiles [ $\text{part}/\text{m}^3$ ] after  $9.6\mu\text{s}$  simulated plasma time for the electrostatic (ES), magnetic inductive (EM) and full electromagnetic scenarios (EM-flutter). The first row shows a view of the  $R - \varphi$  plane with the maximum density taken along the  $Z$  coordinate. The second and third rows show the density on poloidal planes ( $R - Z$ ) at the center of the field lines (1) and in proximity to the sheath (2).

In the center of the domain, drift waves determine the potential  $\Phi$  but it is dominated by the sheath in proximity to the limiters. Hence a parallel gradient appears on  $\Phi$ , which in turn induces a parallel current responsive to inductive electromagnetic effects. As a result, the blob filaments bends along the toroidal direction, with higher advection velocities in the center of the domain than at the sheath. The bending is much more pronounced for the two electromagnetic scenarios, in line with the findings of previous blob studies[58, 59, 95]. On closed field lines, the blob would conserve its axisymmetry and both  $j_{||}$  and  $A_{||}$  would remain 0 throughout the simulation.

### 6.2.2. Generation of drift waves

In the previous section, we examined how a single plasma blob propagates across open field lines. However, this does not account for how the blob appears in the first place. In this second part of the slab study, we investigate the onset of drift waves.

## 6. Limited Geometry – 6.2. Slab configurations

We consider the same setting as before but with a background density of  $n_0 = 2 \cdot 10^{19}$  part/m<sup>3</sup> and isothermal electrons and ions at  $T_e = T_i = 50$  eV. Instead of an initial overdensity, we apply a constant particle source of  $5 \cdot 10^{22}$  part/s on the core side, at all  $R < 1.12$  m. The emergence of drift-wave instabilities for the three scenarios is shown in Fig. 6.5.

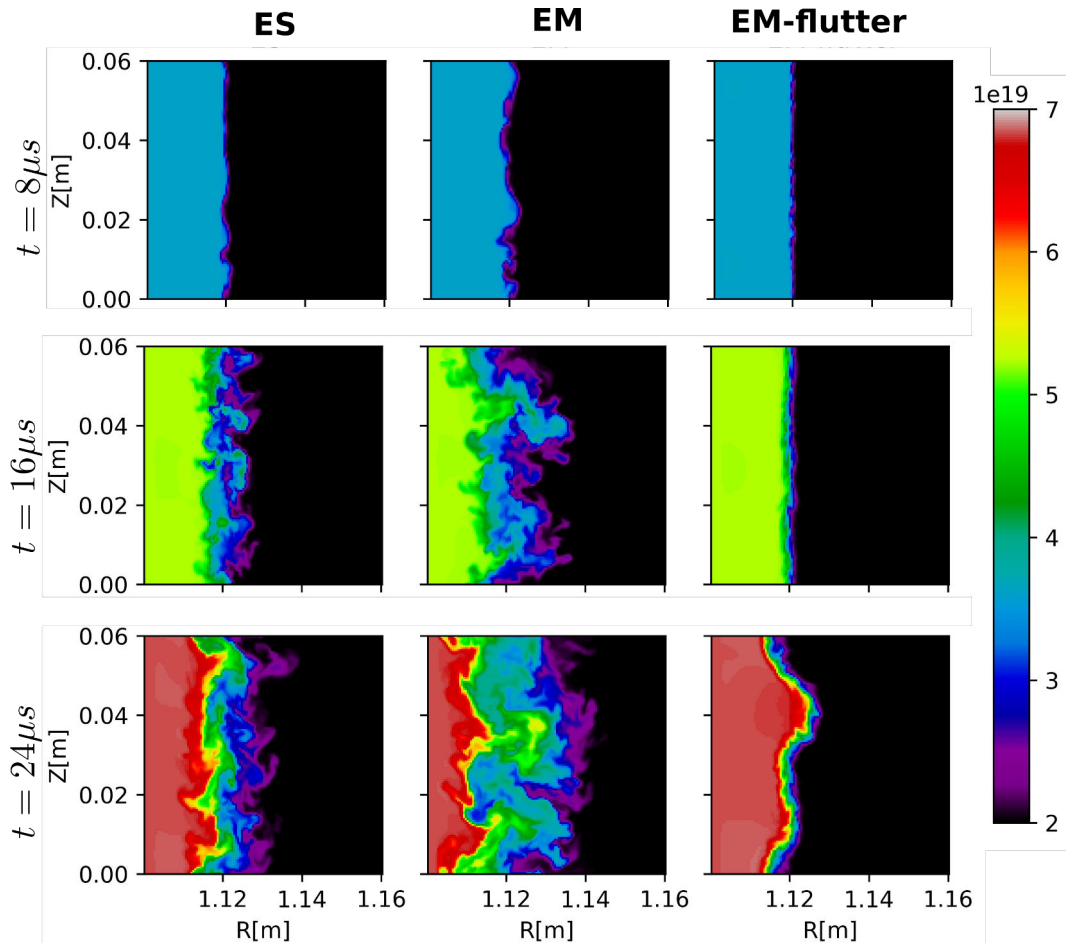


Figure 6.5.: Density profiles [part/m<sup>3</sup>] at the toroidal center of the slab, at about 32m from both limiters. The snapshots compare the electrostatic (ES), magnetic inductive (EM) and full electromagnetic scenarios (EM-flutter) scenarios after 8, 16 and 24 $\mu$ s simulated plasma time.

Initially, the particle source causes the density to build up on the core side of the slab. The radial gradient becomes stronger and soon collapses into drift waves. These waves are particularly pronounced in the electrostatic and electromagnetic inductive models. The term  $\partial_t A_{\parallel}$  in Ohm's law intensifies the turbulent interchange, with plasma filaments reaching much further outward. On the other hand, the electromagnetic model with flutter has a stabilizing effect, producing only a thin turbulent layer at the exit of the source and maintaining a strong gradient at the transition from high-

to low-density regions. As more particles are introduced at the source, the pressure differential causes this transition line to bend at scales of the simulation box, while the local gradient remains very steep.

## 6.3. Circular geometry

In a more integrative scenario, we place ourselves in a circular geometry with a flat limiter on the low-field side. The configuration has now both closed and open flux surfaces with a separatrix at the interface, which allows to study the propagation of turbulent structures from the core to the SOL. We compare the original electrostatic model with electron inertia, electron inertia and magnetic induction, and the full model with electron inertia, induction and flutter.

### 6.3.1. Simulation set-up

The circular geometry corresponds to a tokamak with major and minor radii  $R_0 = 0.9\text{m}$  and  $a = 0.2\text{m}$ . The toroidal magnetic field is  $B_\phi = 1.3\text{T}$  and the poloidal field maintains a safety factor  $q_s = 3$ , such that the pitch angle is constant at  $\alpha = \arctan 1/q_s \approx 18.4^\circ$ . The simulation domain spans the radial coordinates  $[0.8, 1.15]r_{sep}$  and to save simulation time, we only consider a quarter of the torus and assume a periodic extension to the remaining three-quarters. The domain is discretized in  $N_\psi \times N_\theta \times N_\varphi = 128 \times 512 \times 64$  points per direction, or about a total of 4.2 million cells. A constant heat source of 1MW is applied to both electrons and ions and a particle source of  $10^{22} \text{ part/s}$  is applied in a Gaussian-shaped region between 0.81 and  $0.87r_{sep}$ . Initial profiles have been obtained by running the code in transport mode with anomalous perpendicular diffusion coefficients  $1. \text{ m}^2/\text{s}$  and  $0.3 \text{ m}^2/\text{s}$  for density respectively temperature until stable profiles established. Typical simulation snapshots for the four scenarios are given in Fig. 6.6.

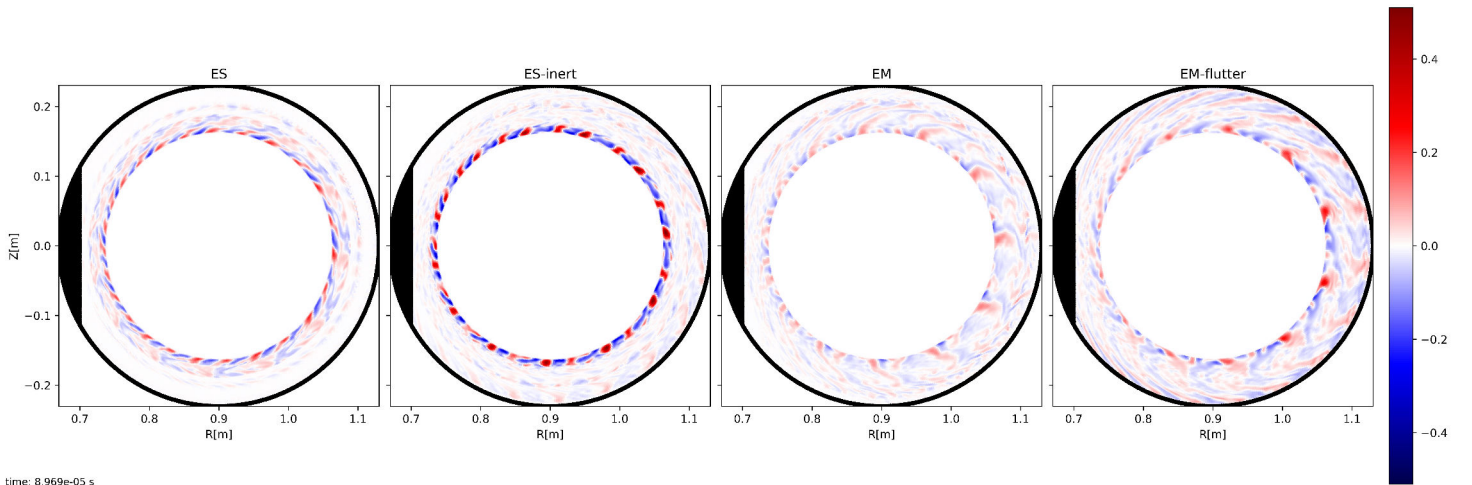


Figure 6.6.: Snapshots of the toroidal fluctuations in electron temperature  $T_e - \langle T_e \rangle_\varphi$  after 0.1ms simulated plasma time.

### 6.3.2. Linear instability growth

As we restart the simulations from a smooth profile, we can observe the growth of instabilities in the beginning of the simulation. Initially, instabilities will grow linearly until they reach a saturation point, when nonlinear effects kick in. In this first (short) phase, we will be able to verify the tendencies from the analysis of the dispersion relation in Sec. 6.1, thus electron inertia has a slight and magnetic induction a strong destabilizing while flutter stabilizes the system. To evaluate the perturbations, we calculate the root mean square (RMS) deviation from the toroidal average in every cell. The global metric is then obtained by averaging the local values over the volume  $V$  of the entire domain.

$$RMS_X = \frac{1}{V} \int_V \sqrt{\frac{X^2 - \langle X \rangle_\varphi^2}{\langle X \rangle_\varphi^2}} dV \quad (6.3)$$

We compare the RMS for both the ion density and temperature at each timestep where a plasma save is available.

#### 6.3.2.1. Electron inertia

First, we study the impact of electron inertia. For that, we artificially modify the value of the electron mass from its physical value. The results for the RMS of ion density and temperature are collected in Fig. 6.7. We observe that perturbations grow faster as the electron mass increases, reaching the saturation level earlier. The saturation itself is comparable in both cases. The biggest difference already appears between the cases  $0m_e$  and  $0.5m_e$ , hence adding a finite electron mass has an immediate effect to the original implementation where electrons react instantaneously to the system, even for a small mass.

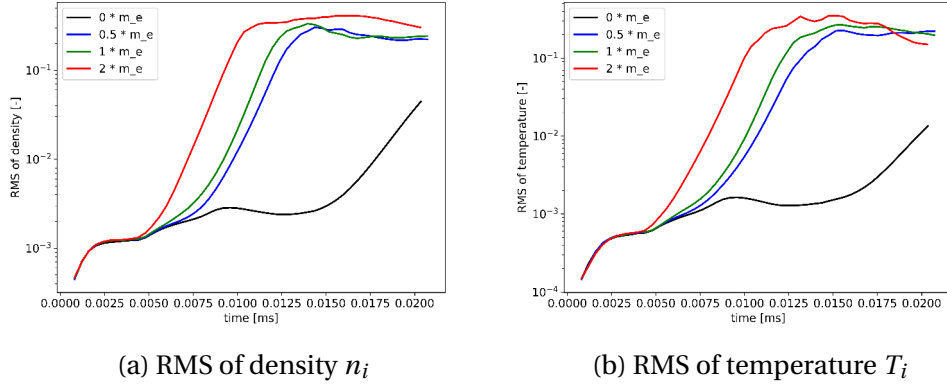


Figure 6.7.: Evolution of the the root mean square deviation for different values of  $m_e$ . The electron mass is artificially increased and the 0 factor corresponds effectively to the electrostatic reference

### 6.3.2.2. Magnetic induction

Second, we modify the value of the reference  $\beta_0$  that appears in the dimensionless equations for the term  $\partial_t A_{\parallel}$  in the parallel electric field. From a physical standpoint, we actually change the vacuum permeability  $\mu_0$  as the reference pressure  $n_0 T_0$  and magnetic field strength  $B_0$  remain unchanged for the rest of the model. All simulations are run with the true value of the electron mass, so the base case  $0\beta_0$  is equivalent to the green line in the  $m_e$  scan above. In Fig. 6.8, we observe that perturbations grow faster the stronger  $\beta_0$  is. For the case  $1\beta_0$ , we also included flutter as a dashed line, and we see there that the growth rate is reduced again to levels below the electron inertial case.

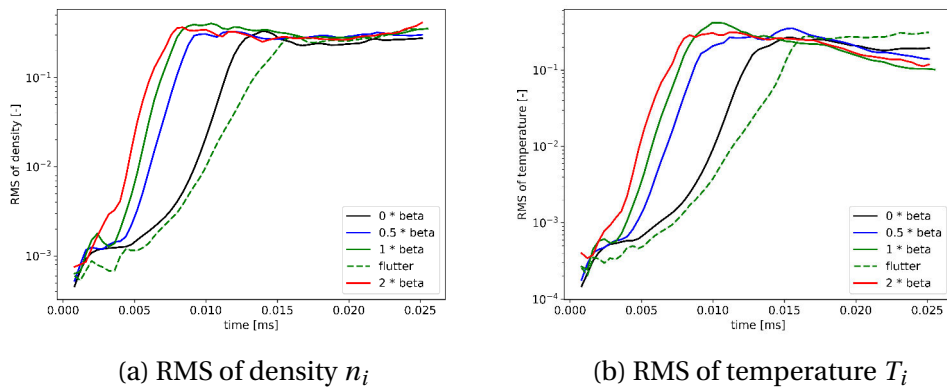


Figure 6.8.: Evolution of the root mean square deviation for different values of  $\beta$ . The is artificially increased and the 0 factor corresponds effectively to the electrostatic with electron inerita. The electron mass for all scenarios is physical (factor 1 in Fig. 6.7).

For both the  $m_e$  and  $\beta_0$  scan, we could see that the linear growth corresponds to the expectations from the linear analysis. As the effects of electron inertia and magnetic induction get stronger, plasma perturbations grow faster and reach their saturation point faster. Note that the saturation levels are similar for all scenarios, so the used RMS metric is not very adapted to analyze the subsequent nonlinear phase of the simulation.

The results here can however not be correlated one-to-one to the dispersion relation. In the SOLEDGE3X model, interchange instabilities also contribute to the rise of perturbation, and the simulation was run with the energy conservation equation and hence ion and electron temperature gradients add an additional source of instability. The dispersion relation was calculated without curvature effects and using an isothermal assumption, but the general expected trend is still observed.

### 6.3.3. Nonlinear turbulence phase

The linear phase only concerns the very beginning of the simulation. During the vast majority of the density and energy ramp-up phase, fluctuations have saturated and nonlinear effects dominate turbulent structures. For this phase, we drop the  $m_e$  and  $\beta$  scans and only consider the scenarios with their true physical values.

#### 6.3.3.1. Evolution of mid-plane profiles

At first, let us compare temperature profiles at the outer mid-plane for the electrostatic scenarios with and without electron inertia. The evolution of the profiles, as well as the associated particle fluxes, are given in Fig. 6.9. The corresponding plots for the density are found in App. C.

One can recognize the linear growth phase in the beginning of the simulation, during which temperature builds up in direct vicinity to the core. After about 0.04ms plasma time, the hot plasma collapses into energy bursts that start traveling towards the separatrix. With a finite electron mass, bursts travel at twice the speed and hence propagate into the SOL much further. As the bursts dissipate, a stable background temperature around 80eV establishes almost immediately at the beginning of the nonlinear turbulence phase throughout the SOL. In the reference electrostatic case, this process is diffusive and the temperature spreads at a much lower pace towards the wall.

## 6. Limited Geometry – 6.3. Circular geometry

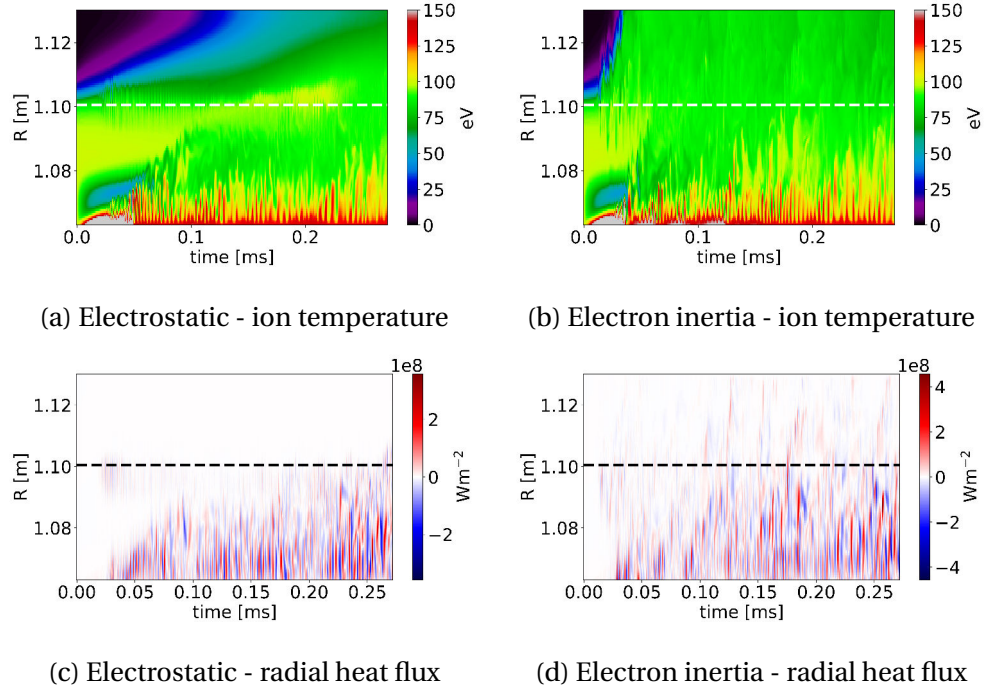


Figure 6.9.: Evolution of the radial ion temperature profiles and heat fluxes at the outer mid-plane for the electrostatic scenarios. The dashed line indicates the position of the separatrix and the plasma in the first poloidal plane is taken

In Fig. 6.10, the same graph is shown for the electromagnetic cases without and with flutter. As with electron inertia only, the background temperature reaches the wall quickly at even higher fluxes. Bursts appear at a lower frequency, but are more powerful and cannot maintain high temperatures even at the core boundary, where the heat source is located. As bursts also penetrate deeper into the SOL with a higher energy, temperatures there reach values around 100eV. In this scenario, flutter does not have a strong effect on the turbulence structure.

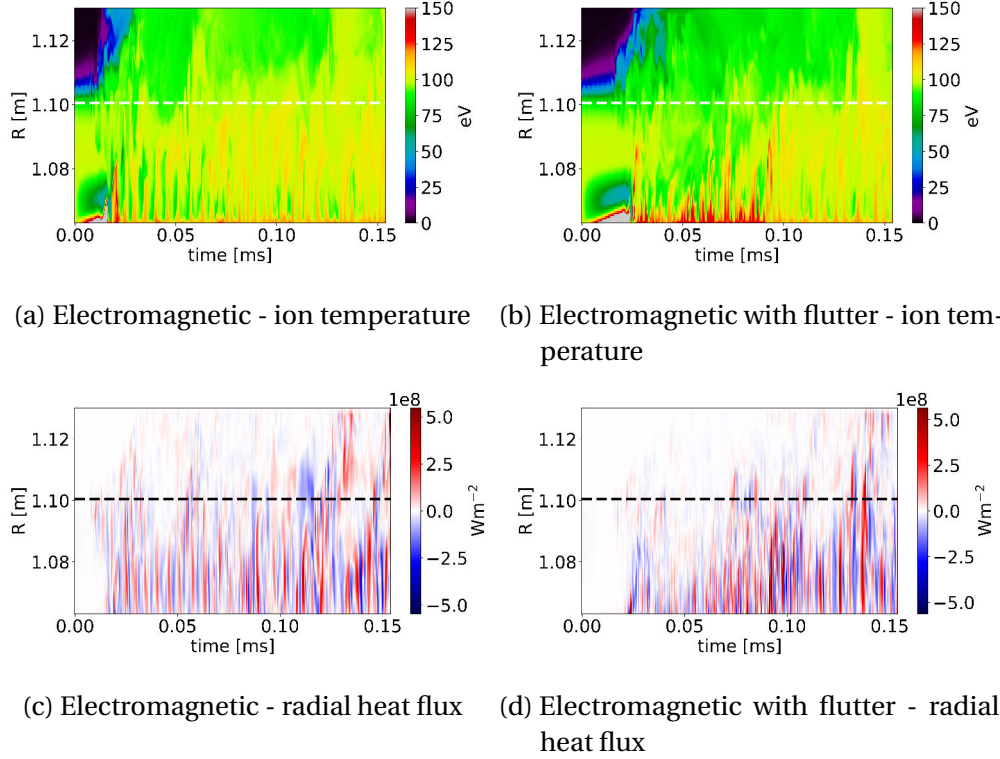


Figure 6.10.: Evolution of the radial ion temperature profiles and heat fluxes at the outer mid-plane for the electromagnetic scenarios. The dashed line indicates the position of the separatrix and the plasma in the first poloidal plane is taken

### 6.3.4. Mode structures

In the simulation snapshots in Fig. 6.6, we observe turbulent blobs on all four graphs. To assess the turbulence, it could be interesting to compare their structures and detect any differences between the scenarios. For this purpose, we rather consider a flux surface instead of a poloidal plane. Specifically, we choose the surface at  $i_\psi = 70$  as it is just short of the separatrix on the core side. The advantage of a closed surface is its periodicity in both directions, such that we can easily perform a modal analysis there. To remove any constant mode, we first remove the toroidal average of the density field  $n'_i = n_i - \langle n_i \rangle_\varphi$ . A view of the field is in Fig. 6.11a. We observe long, seemingly toroidally attached filaments that appear regularly in the perpendicular direction.

On this field, we now perform a two-dimensional Fourier transform, and extract its power spectrum:

$$P_{\tilde{n}}(k_\theta, k_\varphi) = |\tilde{n}(k_\theta, k_\varphi)|^2 \quad \text{with: } \tilde{n}(k_\theta, k_\varphi) = \mathcal{F}\{n'_i(\theta, \varphi)\} \quad (6.4)$$

To remove noise from the discretization scale, we first apply a Gaussian filter with

a small  $\sigma$  on the data. The next step is to transform the poloidal and toroidal wave representation to the parallel and perpendicular space. For this purpose, we simply rotate the wave vectors by the pitch angle  $\alpha$

$$\mathbf{k}_{\parallel} = +\mathbf{k}_{\varphi} \cos \alpha + \mathbf{k}_{\theta} \sin \alpha \quad \mathbf{k}_{\perp} = -\mathbf{k}_{\varphi} \sin \alpha + \mathbf{k}_{\theta} \cos \alpha \quad (6.5)$$

The rotated power spectrum for the flutter scenario can be seen in 6.11b. We observe a dominant mode at  $k_{\parallel} = 0$  that matches the long filaments. The black diagonal line effectively corresponds to the toroidal mode  $k_{\varphi} = 0$ , which is exactly 0 because the toroidal average of  $n$  was removed. The modes at high  $k_{\perp}$  also vanished thanks to the Gaussian filter.

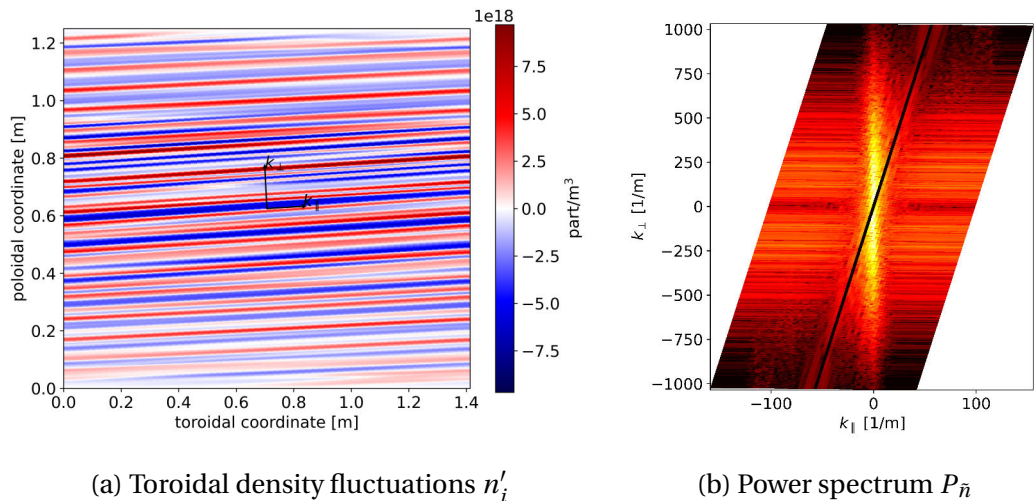


Figure 6.11.: View of the flux surface at  $i_{\psi} = 70$  at the time for the flutter scenario in real and in Fourier space. The arrows indicate the direction of the parallel and perpendicular wave vectors  $\mathbf{k}_{\parallel}$  and  $\mathbf{k}_{\perp}$ . The spectrum is rotated to the  $[\mathbf{k}_{\parallel}, \mathbf{k}_{\perp}]$  coordinate system.

In the perpendicular direction, we can distinguish some bands that characterize the filamentary structure of the turbulence. To isolate them, we take the sum over all  $k_{\parallel}$  while excluding all modes that are too close to the constant mode  $\pm 30 \text{ m}^{-1}$ :

$$\tilde{n}_{\perp}(k_{\perp}) = \int_{\mathbb{R} \setminus (-30, 30)} \tilde{n} dk_{\parallel} \quad (6.6)$$

We can then plot the evolution of the power spectrum  $\tilde{n}_{\perp}$  over the simulated plasma time. For the electrostatic and flutter scenarios, they are in Fig. 6.12. The size of the largest eddies (with the lowest  $k_{\perp}$ ) are similar at around 2cm, of the order of a few ion Larmor radii as one expects in drift-wave turbulence. A difference appears for the higher harmonics: in the electrostatic case, initial small structures collapse into large eddies and progressively excite higher modes again. With the full electromagnetic model, the base mode and its harmonics are excited simultaneously in regular

## 6. Limited Geometry – 6.3. Circular geometry

intervals. Especially higher harmonics are clearly separated and multiples of the base mode, which is not the case for the electrostatic case. A look at the eddies in the electron inertia and induction scenarios (see App. C.2) reveals that this regular mode structure already appears with a finite electron mass.

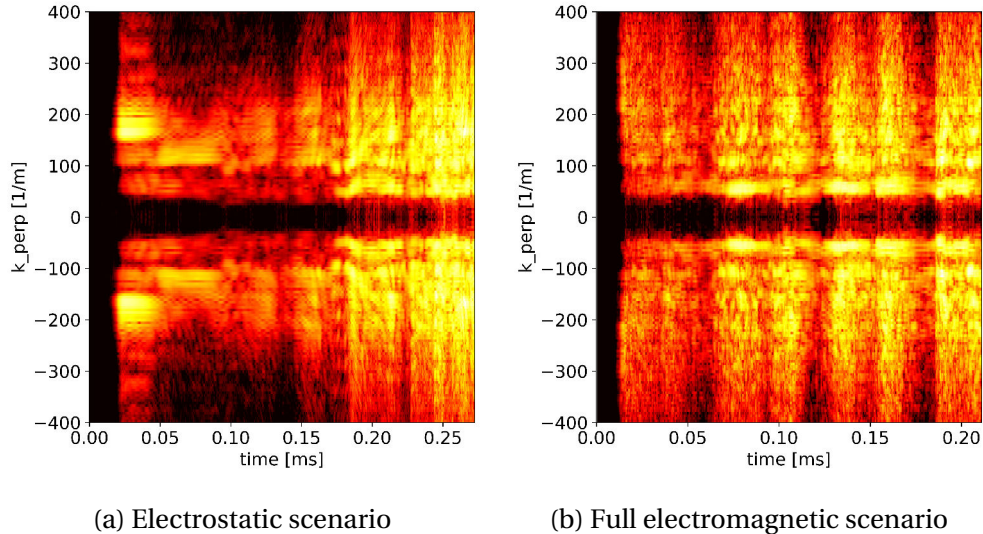


Figure 6.12.: Evolution of the power spectrum of  $\tilde{n}_\perp$  associated to the perpendicular modes  $k_\perp$  in the range  $[-400,400]\text{m}^{-1}$  over the simulation time.

# 7. Diverted Geometry

## Chapter Summary

The electromagnetic model is tested on a realistic X-point configuration based on the TCV-X21 benchmark case. In a flux-driven simulation with an injected power of 150kW, representative of an L-mode plasma, we compare the same four scenarios (electrostatic, electrostatic with electron inertia, magnetic induction, and magnetic induction with flutter). Overall, the plasma behavior is consistent with the findings in the limited geometries. Electron inertia does not significantly impact turbulence levels or mid-plane profiles. However, magnetic induction considerably increases cross-field particle and heat transport, leading to a strong flattening of density and temperature profiles, such that an energetic quasi-steady state is reached within 3ms of simulated plasma time. Flutter counteracts the inductive destabilization and restores steep profiles at a lower turbulence level than in the electrostatic cases.

Numerically, electron inertia accelerates the simulation by improving the condition number of the vorticity equation. The increase in system size due to magnetic induction slightly deteriorates CPU time, even though the number of iterations required for convergence remains below the level of the electrostatic case. With flutter, code performance worsens considerably, mainly due to the radial connection between flux surfaces in the geometry, which adds coupling in the implicit viscosity, parallel heat conduction, and vorticity problems.

In a preliminary study, the injected power was increased to 1.2MW with the full electromagnetic model and additional fluid neutrals. Under these conditions, flutter-induced radial heat transport in the parallel heat conduction starts to compete with energy transport by ExB drifts and eventually dominates the total electron power across the separatrix. Simultaneously, the fluctuating magnetic field shapes island-like patterns along the separatrix.

To demonstrate the abilities of SOLEDGE3X to perform electromagnetic turbulence simulations of a realistic tokamak geometry, the configuration of the test cases has been inspired by the TCV-X21 benchmark[68]. This latter addresses L-mode discharges in TCV with a single lower X-point.

## 7.1. Electrostatic versus electromagnetic scenarios

The semi-implicit time discretization implemented in this model allows comparisons to be made between the electrostatic and electromagnetic models using the same code. Four cases have therefore been considered here: electrostatic (ES), electrostatic with electron inertia (ES-inert), electromagnetic (EM), and electromagnetic with flutter (EM-flutter).

### 7.1.1. Simulation set-up

The plasma is pure deuterium, and only a quarter-torus with a relatively low resolution of approximately 1.9 million cells has been considered to speed up computations (see the mesh in a poloidal plane in Fig. 4.1a). A constant heat source of 25 kW is applied to both electrons and ions, equating to a full-torus equivalent total Ohmic heating of 200 kW. The external toroidal magnetic field is  $B_t = 0.95$  T, and the density at the separatrix is targeted to  $7 \cdot 10^{18}$  part/m<sup>3</sup>.

Since the aim of these preliminary computations was to focus on electromagnetic effects, neutrals have been omitted to speed up the convergence of the solutions. Simulations with a more complete physical model will be performed in a further work, including in particular the latest fluid neutral model [72] developed for regimes dominated by charge exchanges [49].

In all cases, the initial condition is the corresponding 2D transport solution obtained by increased perpendicular diffusion coefficients.

In Fig. 7.1, typical poloidal cuts of important plasma fields are shown. The local value of  $\beta$  varies between  $10^{-3}$  at the hot core boundary,  $10^{-4}$  around the separatrix and divertor region, and  $10^{-5}$  or lower in the far SOL. Consequently, the flutter perturbation  $\tilde{B}$  of the magnetic field remains small compared to the equilibrium field, barely exceeding 0.1% of  $B_t$  on the hot core side of the domain. The advection velocity associated with the flutter is also minimal, contributing to less than 0.1% of the cross-field transport, dominated by the electric "ExB" drift.

## 7. Diverted Geometry – 7.1. Electrostatic versus electromagnetic scenarios

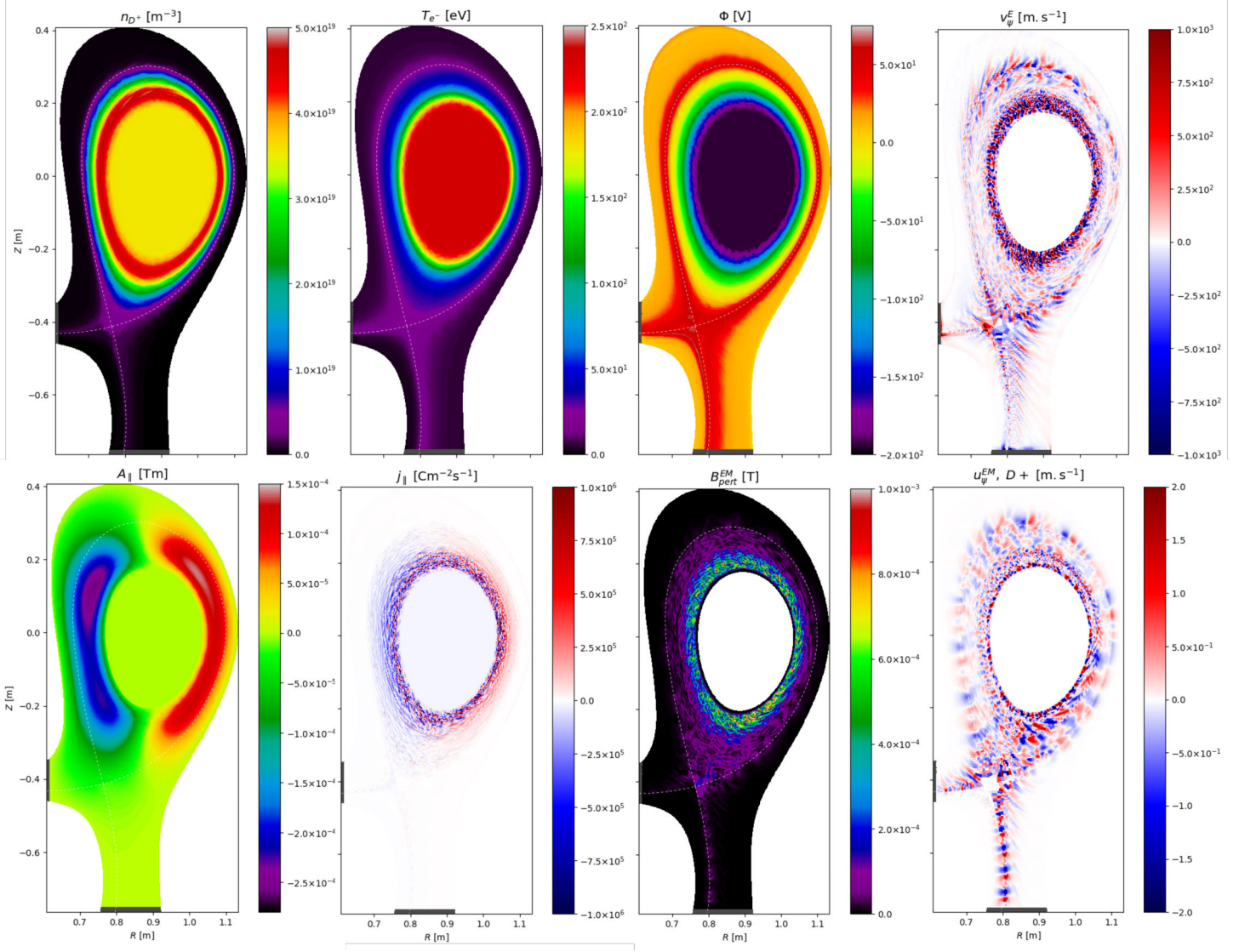


Figure 7.1.: Simulation snapshots of the full electromagnetic scenario with flutter. The first poloidal plane is shown after 6 ms simulated plasma time on the TCV case. From left to right, the first row shows the ion density  $n_i$ , the electron temperature  $T_e$ , the electric potential  $\Phi$ , and the radial "ExB" drift velocity  $v_E^\psi$ . The second row shows the parallel magnetic potential  $A_\parallel$ , the parallel current density  $j_\parallel$ , the amplitude of the flutter field  $\|\tilde{\mathbf{B}}\|$ , and the radial flutter advection velocity  $v_{\tilde{\psi}}$ .

### 7.1.2. Comparison between the scenarios

We now compare the impact of the different levels of new physics on the TCV scenario. Since turbulent structures are essentially driven by the electric "ExB" drift, we consider the associated total kinetic energy  $E_{ExB} = \frac{1}{2} m_i \int_V n_i \|v_E\|^2 dV$  to estimate the turbulence level. As shown in Fig. 7.2a, a finite electron mass does not change the energy

## 7. Diverted Geometry – 7.1. Electrostatic versus electromagnetic scenarios

level with respect to the reference electrostatic scenario. Next, adding magnetic induction with  $A_{\parallel}$  further amplifies the turbulent interchange. This enhancement arises from the increased coupling between the magnetic and electric fields, leading to more instabilities and modified turbulent dynamics. Consequently, turbulent filaments give way to smaller, rounder blobs. Finally, the inclusion of flutter has a stabilizing effect on the turbulence, where fluctuations fall again to the level in the electrostatic case. Nonlinear effects in the parallel current equation, namely from the parallel pressure gradient  $\nabla_{\parallel} p_e$ , substantially impact the profiles of  $j_{\parallel}$  and hence the response of the potential  $\Phi$ . The direct consequence is a modification of the radial electric field and a modified evolution of "ExB" drifts. This does not contradict our previous observation that magnetic advection is negligible with respect to the electric drift.

With a different turbulence level, the heat exhaust is also affected, as shown in Fig. 7.2b. Without radiative effects, the quasi-totality of the heat leaves the tokamak at two divertor targets. The supplementary radial turbulent transport in the magnetic inductive scenario allows more hot particles to cross the separatrix from the core, which will then eventually reach the divertor. Overall, the heat flux is multiplied by a factor of 10. Electron inertia alone leads to an increase by a factor of 2, despite very similar turbulence levels. This phenomenon needs further investigation. Flutter does not reduce further the heat exhaust as one might expect because it is already very low in the electrostatic case.

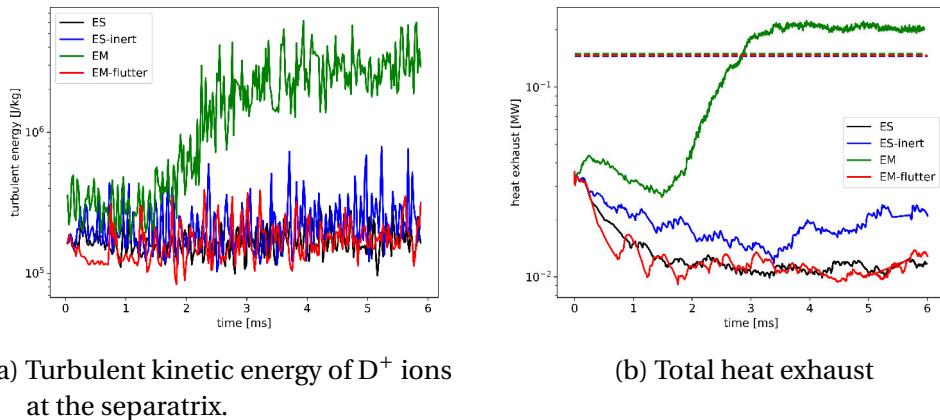


Figure 7.2.: Evolution of the turbulent energy and heat exhaust over time iterations on the turbulent TCV scenario. It indicates the turbulence level and its consequence on the total heat transport.

The change in turbulence intensity naturally impacts the mean profiles in Fig. 7.3. The most noticeable change affects the electromagnetic inductive scenario, where density and temperature gradients are considerably reduced by the additional radial turbulent transport. Again, the finite electron mass has no significant impact, and the

## 7. Diverted Geometry – 7.1. Electrostatic versus electromagnetic scenarios

reduced turbulence levels by flutter lead to steeper gradients. At this point, we stress the similarity to the simplified drift wave simulations on slab in Sec. 6.2.2, where the gradients from the dense core follow the same pattern.

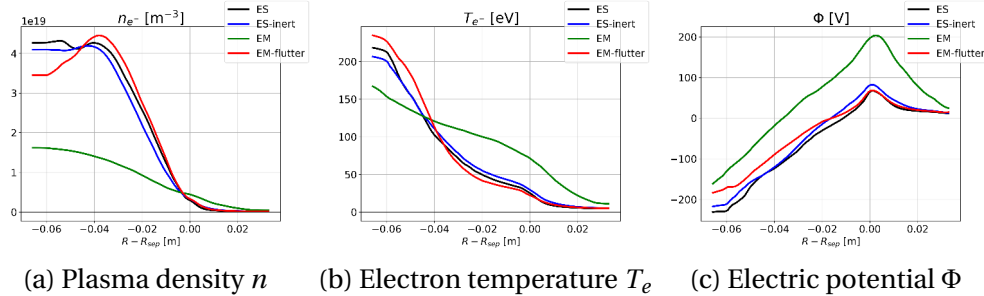


Figure 7.3.: Radial profiles at the outer mid-plane after 6 ms simulated plasma time. These profiles were obtained by averaging simulation data across all 32 toroidal planes and over the last 20 available plasma saves.

### 7.1.3. Numerical performances

In previous works about the electrostatic model[9, 97], it was pointed out that solving the implicit 3D vorticity operator is the most expensive and tricky operation in the algorithm. Adding new variables inevitably modifies the code's performance. With the rather coarse mesh used in the present work, simulations have been run on 16 nodes with 48 CPUs each on the MARCONI supercomputer operated by CINECA [52]. Implicit systems, such as the 3D vorticity operator, have been inverted using the stabilized biconjugate gradient method (BCGS) [102] with the generalized algebraic multigrid preconditioner (GAMG) by PETSc [4].

The overall performance of the code largely depends on how quickly a certain plasma timespan can be calculated. Table 7.1 presents the average simulation time for one timestep, broken down by the cost of each implicit solver. For the vorticity system, we also provide the number of iterations the BCGS needed to match the imposed tolerance ( $10^{-8}$ ), as it relates to the condition number of the matrix. This system has always accounted for a considerable share of the total execution time and was heavily modified with the new electromagnetic model. Finally, the timestep size is provided, as a higher timestep size can compensate a costlier problem because the desired simulation time is reached in fewer iterations. As described earlier in Chap. 4, SOLEDGE3X uses a variable timestep scheme to maximize the CFL condition with the calculated fluxes.

The introduction of a finite electron mass to the vorticity system significantly reduces the number of solver iterations and allows to reach a solution much faster. This improvement occurs because electron inertia effects dominate Ohm's law, thereby

## 7. Diverted Geometry – 7.1. Electrostatic versus electromagnetic scenarios

	Total execution time per timestep [ms]	Execution time for the viscosity [ms]	Execution time for the heat diffusion [ms]	Execution time for the vorticity [ms]	N° of vorticity solver iterations	Timestep size [ns]
<b>ES</b>	664	61	76	339	80	15.6
<b>ES-inert</b>	523	61	77	193	32	16.4
<b>EM</b>	895	63	82	552	60	15.9
<b>EM-flutter</b>	2019	225	390	1147	55	16.6

Table 7.1.: Numerical metrics on the four TCV scenarios for one timestep. All quantities are averaged over the last 20000 timesteps of the simulation. The execution time refers to the wall-clock time and must be multiplied by the number of used processors (768) to get the actual used CPU time.

reducing the anisotropy between the perpendicular and parallel Laplacians on  $\Phi$  in the electrostatic scenario. This reduction in anisotropy is due to the parallel diffusion coefficient being the conductivity  $\sigma_{\parallel}$  in the electrostatic case, but a finite electron mass  $m_e$  imposes an upper limit on it. Adding  $A_{\parallel}$  doubles the size of the matrix and introduces a more complex structure, challenging the solvers and requiring more iterations. Despite the higher complexity, a finite electron mass allows the solver to converge in fewer iterations than in the reference electrostatic case. However, the effective solve time is still worse due to the doubling in system size. Finally, including flutter slightly improves the matrix condition compared to the scenario with only magnetic induction, but the execution time is significantly increased. At first glance, one would expect the solve time to correlate with the number of BCGS iterations as both electromagnetic scenarios solve a coupled 3D system on  $\Phi$  and  $A_{\parallel}$ . Since flutter introduces the radial direction to parallel gradients, and the coupling terms between the two unknowns are exactly a parallel gradient and a divergence (see Eq. 4.19), the matrix exhibits a decreased sparsity ratio. This circumstance is further aggravated by the fact that  $A_{\parallel}$  is not staggered in the radial direction, so the radial discrete gradient/divergence operator has a larger stencil width than its poloidal and toroidal counterparts.

The viscosity and heat diffusion solvers are not directly affected by the electromagnetic model, and their solve times are similar for the first three scenarios. Electromagnetic flutter, however, with its radial gradient (again), heavily modifies the parallel diffusion operators and requires solving one global 3D system instead of separate 2D systems on each flux surface (see Sec. 4.4.2). This is immediately reflected in the code performance, as both solvers take up to 5 times longer to solve.

In total, electron inertia decreases the computing time with an excellent improvement of the vorticity matrix condition. The magnetic inductive model means slightly

higher computational costs, because the implicit vorticity problem doubles in size. Including electromagnetic flutter in the system almost quadruples the execution time compared to the original implementation because the radial parallel gradient complicates both the implicit vorticity and the parallel diffusion problem. The timestep size does not vary considerably between the scenarios and hence has only a limited impact on the overall performance.

## 7.2. Flutter in higher power

In the previous section, we compared the new electromagnetic model in an L-mode scenario inspired by the TCV-X21 benchmark. Electromagnetic effects scale with the pressure ratio  $\beta$ , so it would be more than interesting to study electromagnetic plasma behavior. The main difference to the previous set-up is a constant heat source of 1.2MW equally distributed among ions and electrons at the core boundary. For higher fidelity, we also replace the fixed particle source by interaction with fluid neutrals using the most recent implemented model[72]. However, this simulation setup is not entirely realistic, as at such high power, substantial external heating is applied to the edge plasma, and we cannot assume that all of it originates from the unsimulated core. Moreover, thresholding issues with the neutral model lead to an excessive particle source in the core, distorting density profiles. For this study we only consider the full model with magnetic induction, electron inertia and flutter.

### 7.2.1. Parallel heat conduction

Akin the simple magnetic inductive scenario the low-power scenario, the system reaches rapidly a quasi-steady state after 3ms. However, there is no uncontrolled collapse of the density and temperature in the core, at the contrary, steep gradients build up in the edge and just behind the separatrix. In the SOL, gradients are very small up to the first wall, leaving convenient low values throughout the region. This can be observed in the outer-mid plane profiles for ion density and temperature, taken at increasing simulation times in Fig. 7.4.

The temperature profile could indicate the formation of a pedestal, characteristic of the transport barrier in H-mode plasmas with an improved confinement quality. To properly assess such a condition, the simulation must however reach a full steady state, especially on the density, whose confinement time is much higher and far beyond the end of this simulation.

## 7. Diverted Geometry – 7.2. Flutter in higher power

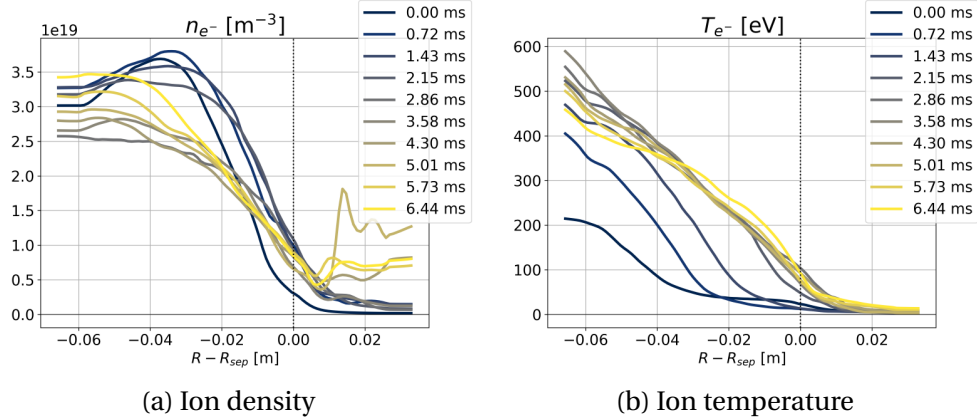


Figure 7.4.: Averaged profiles at the outer mid plane taken at different simulation times for the TCV scenario with a 1.2MW heat source.

We can still investigate heat fluxes to understand the behavior of the temperature. Let us examine the components to the total heat flux at the separatrix, as they will ultimately define the confinement of the core plasma. For that, we have a closer look to the different contributions to the radial heat flux in the energy conservation equation. The main terms are advection of thermal and kinetic plasma energy by electric and curvature drifts as well as the radial redirection of parallel fluxes due to flutter. The parallel heat conduction  $q_{\parallel}$  now also contains a radial component. The contribution of the viscous fluxes vanishes for electrons and is negligible for the ion heat flux, so we do not consider it in our analysis. We can express the total radial power transfer from core to SOL as:

$$P_{\psi}^{sep} = \underbrace{\int_{sep} \mathbf{e}_{\psi} \cdot \epsilon n \mathbf{u}^{ExB} dA_{sep}}_{\text{ExB}} + \underbrace{\int_{sep} \mathbf{e}_{\psi} \cdot \epsilon n \mathbf{u}^{\nabla B} dA_{sep}}_{\text{gradB}} + \underbrace{\int_{sep} \mathbf{e}_{\psi} \cdot \epsilon n v_{\parallel} \mathbf{b} dA_{sep}}_{\text{EM}} + \underbrace{\int_{sep} \mathbf{e}_{\psi} \cdot [-\kappa_{SH} \nabla_{\parallel} T \mathbf{b}] dA_{sep}}_{\text{qpara}} \quad (7.1)$$

In Fig. 7.5, we compare the evolution of each individual term to the total power over the simulation time, integrated over the entire separatrix flux surface. The simulation outputs were also scaled by a factor four to express the power on the full torus (and not only the simulated quarter).

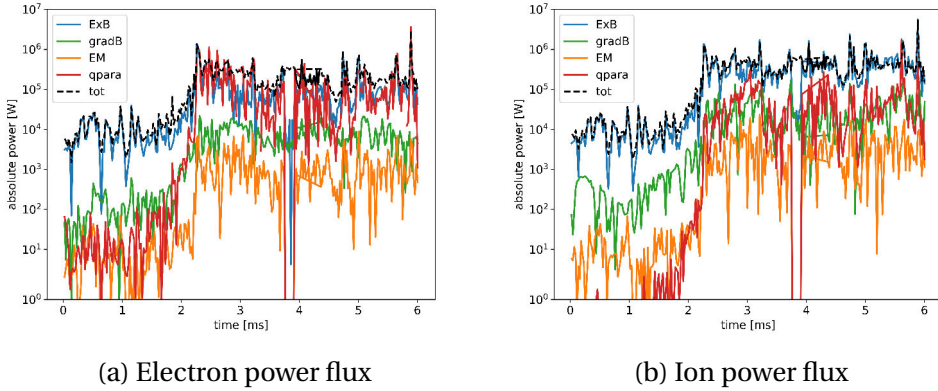


Figure 7.5.: Contribution of the different terms in the energy conservation equation to the power transfer from the core to the SOL.

## 7.2.2. Characteristics of the fluctuating field

As electromagnetic transport in the tokamak edge starts to play a role, the time has come to investigate electromagnetic flutter a bit more in detail.

### 7.2.2.1. View of the flutter field

Let us trace the perturbed field lines driven by flutter on the first poloidal plane at the end of the simulation. Fig. 7.6 shows the field lines starting at 2500 points seeded randomly across the entire domain. As the integration length for each line has been fixed beforehand, longer lines correlate with higher magnitudes of  $\tilde{\mathbf{B}}$ . This is not a true Poincaré plot however, as flutter also contains a toroidal component, that is much smaller than the other two components, but was neglected for this analysis. If it was included, field lines would immediately leave the plane of interest and only return sporadically, leaving not much more than the seed points on the Poincaré plot. It could also have been possible to create this plot for the full magnetic field, including the equilibrium component, but then it would have been utterly hard to distinguish unique features of flutter.

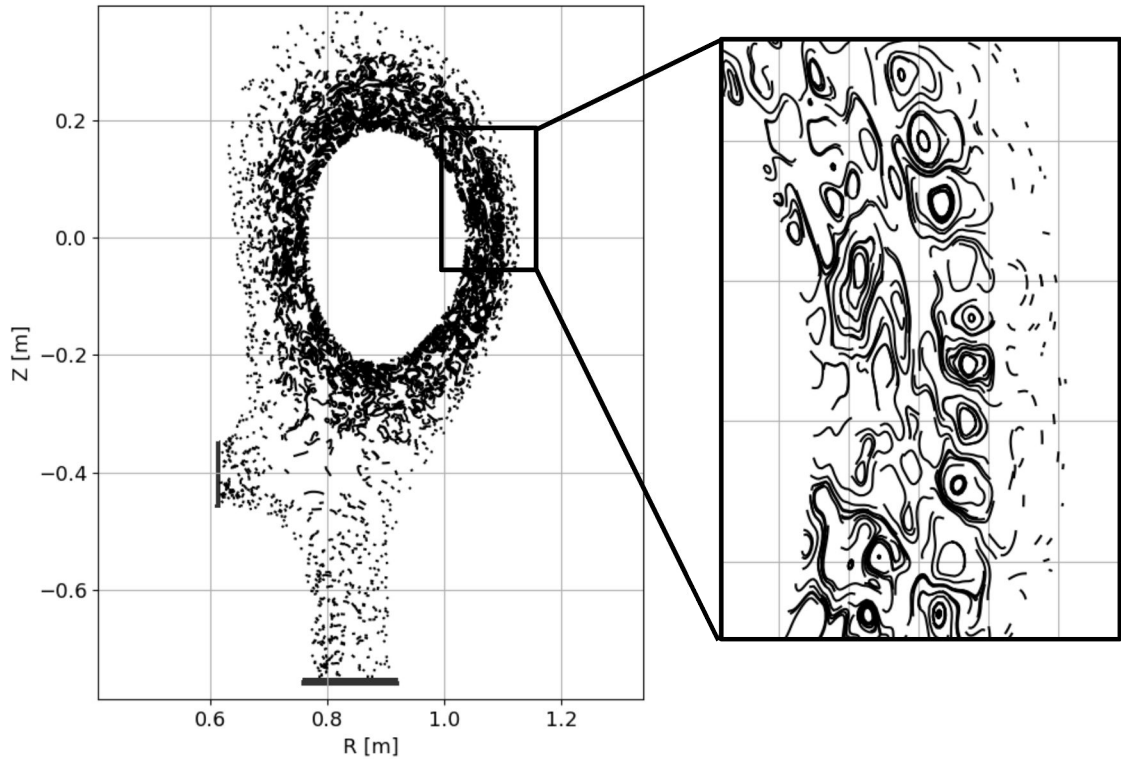


Figure 7.6.: Poincaré plot of the fluctuating magnetic field in the TCV high-power case for a random seed of 2500 points in a TCV poloidal plane.

We observe the formation of islands whose centers are aligned with the separatrix. Their size corresponds approximately to typical turbulent filaments and their radial extent correlates to the region with steep temperature gradients. Some islands form also in vicinity to the core boundary, but this region is prone to artificial turbulence from the close heat source and fluid models only have a limited validity there. A similar plot for the X21 flutter case, in App. C.3, does not exhibit any coherent structures, reinforcing the idea that the magnetic fluctuations play an important role for the transport barrier at high power. The exact physical mechanisms behind this observation still need to be investigated thoroughly.

### 7.2.2.2. Grad-Shafranov shift

In Sec. 3.3.3, we discussed the necessity of removing the equilibrium component from  $A_{\parallel}$  before calculating the flutter field components. The concern was that  $A_{\parallel}$  contains contributions from the Pfirsch-Schlüter current, which have already been accounted for in the poloidal flux function  $\Psi$  that defines the equilibrium field  $B_{pol}$ . For the time being, we remove the toroidal average of  $A_{\parallel}$  at each timestep, yielding stable simulations. The effects of this procedure are shown in Fig. 7.7, where we compare the flutter field to  $B_{pol}$  with and without removing the average. When the full  $A_{\parallel}$  is used, large structures appear, particularly on the low-field side, reaching 13% of the

## 7. Diverted Geometry – 7.2. Flutter in higher power

amplitude of  $B_{pol}$ . However, when we use only the toroidal fluctuations of  $A_{\parallel}$  for the flutter, these structures disappear, leaving fine filaments at a much lower amplitude against a  $\tilde{\mathbf{B}} = 0$  background. Thus, this pre-processing step for  $A_{\parallel}$  appears necessary and effective. It also suggests that for the current applications of SOLEDGE3X, there is no need to apply an additional time-averaging process, as proposed by [108], since we do not observe transient structures.

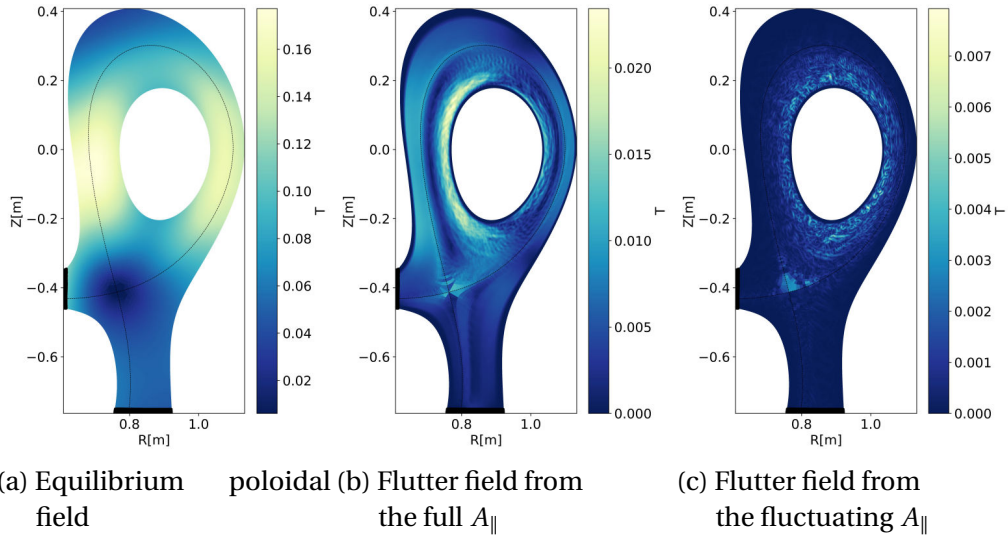


Figure 7.7.: Comparison of the magnitude of the flutter field to the poloidal magnetic field strength  $B_{pol}$ . Snapshot on the first poloidal plane at the end of the high-power scenario.

## 8. Perspectives for Studying Magnetic Ripple

### Chapter Summary

The SOLEDGE3X code was adapted to impose external non-axisymmetric perturbations of the magnetic equilibrium. In tokamaks such as WEST, the pronounced toroidal magnetic ripple significantly affects plasma confinement and power exhaust, modulating both the poloidal and toroidal components of the equilibrium field. Using the Biot-Savart law, the ripple field is calculated as a magnetic perturbation on the SOLEDGE3X mesh. It is calculated at every grid point from the current in discretized coil segments:

$$\mathbf{B}_{ripple} = \frac{\mu_0}{4\pi} I_c \sum_{i=1}^{N_c} \sum_{j=1}^{N_{seg}} \frac{\mathbf{d}_{i,j} \times (\mathbf{s}_{i,j+1} - \mathbf{s}_{i,j})}{\|\mathbf{d}_{i,j}\|^3}$$

Preliminary simulations of a WEST scenario reveal a "snake-skin" heat deposition pattern in the divertor region, consistent with experimental observations from infrared cameras.

Developments performed in the scope of this thesis can be useful for applications other than electromagnetic effects on plasmas. In transport mode with large perpendicular diffusion coefficients, a regime where drifts and turbulent scales are not solved, modulations of the magnetic field can have an external source. Because of the toroidal locality of toroidal field coils, the equilibrium magnetic field itself is not axisymmetric, a phenomenon usually referred to as "magnetic ripple". This chapter describes how the implementation of fluctuating magnetic fields in the framework of flutter can be used to simulate perturbations of the equilibrium magnetic field. Sec. 8.1 motivates the study of magnetic ripple, Sec. 8.2 describes its calculation from an existing axi-symmetric equilibrium and Sec. 8.3 demonstrates its application on the divertor heat exhaust in WEST. The chapter is slightly adapted from the paper "Implementation of a non-axisymmetric magnetic configuration in SOLEDGE3X to simulate 3D toroidal magnetic ripple effects: Application to WEST", submitted to Nuclear Materials and Energy in the special issue for the PSI-26 conference held in May 2024, Marseille.

## 8.1. Motivation for simulating magnetic ripple

Power exhaust is a major concern in magnetic fusion research. Accurately predicting the heat load on the divertor plates is essential for the design and operation of current and future tokamaks. Estimates for the International Thermonuclear Experimental Reactor (ITER), the most powerful device currently under construction, indicate maximum local heat loads close to material limits[39]. For this reason it is important to study transport of heat and particle fluxes in present experiments, coupling the experimental analysis with a modelling effort with dedicated numerical tools.

Experiments conducted on the tungsten environment steady-state tokamak (WEST) at CEA in Cadarache, France[8], have demonstrated that the heat deposition on the divertor targets is not uniform in the toroidal direction. A "snake skin" pattern (see Fig. 8.1), with alternating local maxima, appears on the inner and outer divertor targets. Reconstructions from infrared camera images exhibit a considerable difference between peaks and lows along a target line. These variations correlate with the disposition of the toroidal magnetic field coils, which locally modify the field lines and amplitude. This effect is known as magnetic ripple[98], and it is particularly pronounced on WEST, where the 18 coils cause strong variations in the amplitude of the magnetic field  $\mathbf{B}$ . For example, fast ions trapped in the toroidal magnetic field ripple have been found to be responsible for significant power losses[66]. Moreover, it is important to determine the impact of this toroidal modulation on impurity transport, in particular on tungstene contamination of the core[21].

For heat exhaust studies, SOLEDGE3X is used in "transport" mode, where cross-field transport is approximated with effective diffusion coefficients. It allows simulations to run until convergence on large machines like ITER[78] or JT-60SA[20]. Applications of

## 8. Perspectives for Studying Magnetic Ripple – 8.2. Generation of a non-axisymmetric magnetic configuration

this code include studies on impurity transport[14], heat exhaust[77], and detachment regimes in the divertor[105].

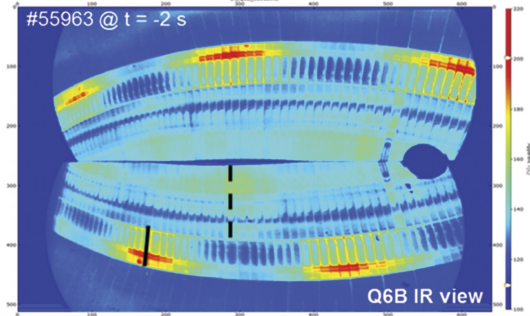


Figure 8.1.: Infrared camera view of the divertor target, taken from [8]. Red zones correspond to hot regions with high heat deposition. One can see the "snake skin" pattern, where the maximal intensity alternates between the inner and outer strike points.

In its current form, SOLEDGE3X can address 2D and 3D axisymmetric configurations as well as 3D non axisymmetric wall geometries[22], but still requires a 3D axisymmetric magnetic field. Therefore, toroidal variations of the magnetic field due to ripple could not be taken into account. Moreover, matching simulation results to experimental data is made difficult by the toroidal locality of Langmuir probes and their consequent susceptibility to ripple effects. Recent developments in the turbulence model have introduced electromagnetic effects[28], where magnetic field lines are perturbed by fluctuations of the magnetic vector potential. In this paper, we demonstrate that the new implementations can be used not only for plasma-induced perturbations but also for external perturbations of the axisymmetric magnetic field. This paves the way for ripple simulations in SOLEDGE3X and will be applied to a WEST scenario in this paper.

## 8.2. Generation of a non-axisymmetric magnetic configuration

The SOLEDGE3X framework is capable of addressing magnetic configurations with singularities at one or more X-points. Constructed by a combination of a toroidal field,  $\mathbf{B}_t$ , and a poloidal field,  $\mathbf{B}_{pol}$ , the expression for the magnetic field is:

$$\mathbf{B}_{axi} = \mathbf{B}_t + \mathbf{B}_{pol} = F \nabla \varphi + \nabla \Psi \times \nabla \varphi \quad (8.1)$$

where  $\varphi$  represents the toroidal angle. The toroidal field  $\mathbf{B}_t$  is derived from a toroidal flux  $F$  and  $\mathbf{B}_{pol}$  from a poloidal flux function  $\Psi$ . For high numerical accuracy, the meshing in SOLEGE3X is aligned to magnetic flux surfaces, treating singularities with

a multi-domain decomposition shown in Fig. 8.2

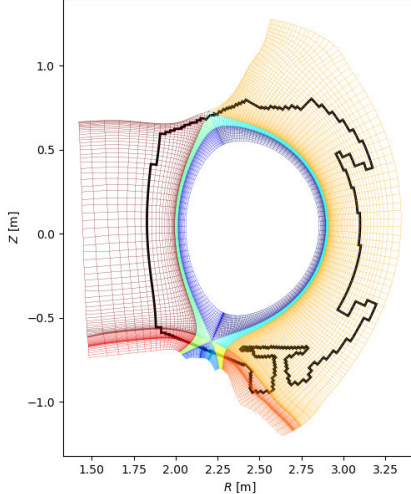


Figure 8.2.: Exemplary SOLEDGE3X mesh for a WEST single-null geometry

On top of this axisymmetric basis, we calculate the ripple perturbation of the magnetic field induced by the toroidal distribution of the toroidal field coils. For that, we simplify each coil to a single, circular wire. We first discretize each of the  $N_c$  coils into  $N_{seg}$  segments. For every cell in the SOLEDGE3X grid, we then calculate the magnetic field associated with the coils using the Biot-Savart law:

$$\mathbf{B}_{ripple} = \frac{\mu_0}{4\pi} I_c \sum_{i=1}^{N_c} \sum_{j=1}^{N_{seg}} \frac{\mathbf{d}_{i,j} \times (\mathbf{s}_{i,j+1} - \mathbf{s}_{i,j})}{\|\mathbf{d}_{i,j}\|^3} \quad (8.2)$$

where the coil current  $I_c$  corresponds to the nominal coil current times the number of wire turns in a coil,  $\mathbf{s}_{i,j}$  represents the start and end locations of each coil segment, and  $\mathbf{d}_{i,j}$  is the vector from each mesh point to the segment center. To avoid accounting for the axisymmetric component of the magnetic field twice, we define the perturbation field as the toroidal fluctuations of the ripple field:

$$\mathbf{B}_{pert} = \mathbf{B}_{ripple} - \langle \mathbf{B}_{ripple} \rangle_\varphi \quad (8.3)$$

Together with the axisymmetric part from Eq. 8.1, the equilibrium magnetic field as applied to the simulation is given by:

$$\mathbf{B} = \mathbf{B}_{axi} + \mathbf{B}_{pert} \quad (8.4)$$

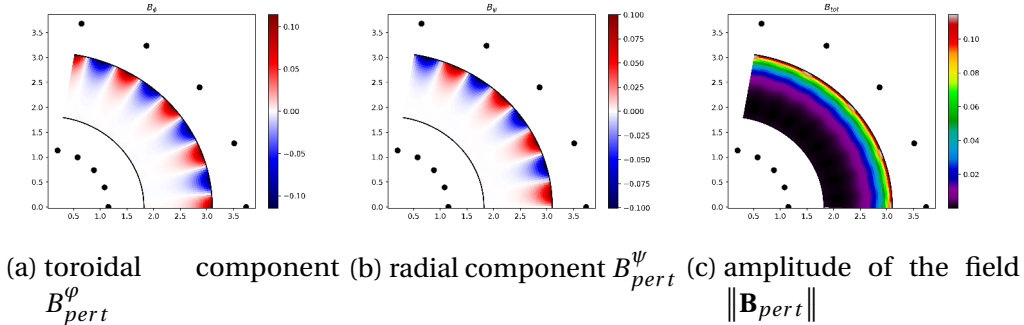


Figure 8.3.: Top views of the perturbed field  $\mathbf{B}_{\text{pert}}$  on the WEST tokamak at the mid plane. The black dots indicate the position of the toroidal field coils. The amplitude of the perturbed field remains much smaller than the axisymmetric component, whose amplitude ranges around 1T.

This strategy is now applied to compute the magnetic field ripple for the WEST tokamak, with the coil parameters described in Tab. 8.1. The ripple has a twofold impact on the magnetic equilibrium. A toroidal perturbation field, as shown in Fig. 8.3a, modifies  $\mathbf{B}_t$  with local maxima located at the coils' positions and minima midway between two coils. Conversely, the radial perturbation in Fig. 8.3b vanishes at the coils and midway, and modifies the poloidal field  $\mathbf{B}_{\text{pol}}$ .

Number of coils	$N_c$	18
Major coil radius	$R_c$	2.443 m
Minor coil radius	$a_c$	1.292 m
Nominal coil current	$I_c$	1.2 kA
Number of wire turns	$N_{\text{turns}}$	2028

Table 8.1.: Technical parameters of the toroidal field coils used to generate the ripple field for the WEST tokamak

Even if the amplitude of the ripple field is small compared to the axisymmetric one, it strongly impacts the poloidal field  $\mathbf{B}_{\text{pol}}$  from one poloidal plane to another. As  $\mathbf{B}_{\text{pol}}$  approaches zero at X-points, the radial perturbation  $\mathbf{B}_{\rho}^{\psi}$  induced by the coils dominates over the axisymmetric component. In Fig. 8.4, we observe that the X-point based on  $B_{\text{pol}}$  shifts by about 4.1 cm towards the high-field side at the maximal radial perturbation and by 2.7 cm inwards at the minimum.

## 8. Perspectives for Studying Magnetic Ripple – 8.2. Generation of a non-axisymmetric magnetic configuration

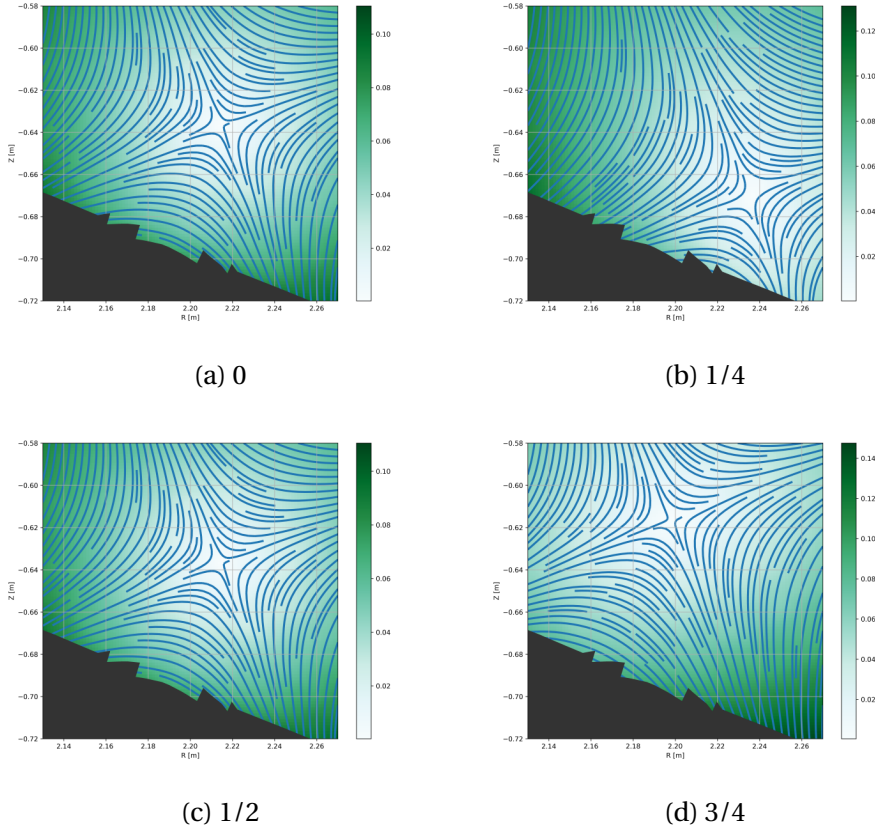


Figure 8.4.: Map of the poloidal field  $B_{pol}$  [T] at several poloidal planes within a ripple period around the lower X-point and the divertor targets. Streamlines are superposed to the fields to better visualize the position of the X-point and the separatrix at the divertor. The phase shifts 0 and 1/2 with respect to the coil positions are identical to the axisymmetric configuration as  $B_{pert}^\psi$  vanishes while the planes at 1/4 and 3/4 correspond to the respective maximum and minimum of  $B_{pert}^\psi$

However, this does not mean that the last closed flux surface (LCFS) experiences such a strong modulation. Indeed, the toroidal field  $\mathbf{B}_t$  imposes a strong self-similarity between poloidal planes. Tracing particles in the magnetic field, we observe in Fig. 8.5 that particles seeded at the same position in different poloidal planes are only modulated by a few millimeters, and key features of the configuration, such as strike points or the X-point, remain almost unaffected.

## 8. Perspectives for Studying Magnetic Ripple – 8.3. Application to a WEST scenario

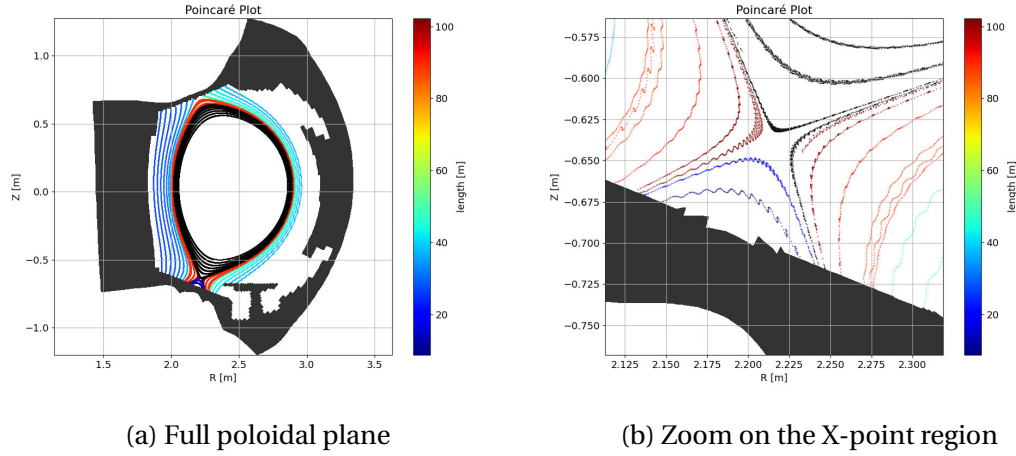


Figure 8.5.: Poincaré plot at coil-aligned poloidal planes. Seed points are uniformly distributed on the mid-plane along the radial and toroidal directions. Because of the periodicity of the perturbated field, each point corresponds to a field line crossing any of the  $N_c$  planes aligned with a coil. The total length of a field line from wall to wall translates in its color, black standing for an infinite closed field line.

### 8.3. Application to a WEST scenario

To demonstrate the newly implemented feature, we perform a SOLEDGE3X simulation on a WEST scenario with ripple. We consider a simple deuterium plasma with recycling fluid neutrals (recycling coefficient 98%). The core density fixed to  $2 \times 10^{19}$  particles/m<sup>3</sup>, and 1 MW Ohmic heating is equally applied to electrons and ions. Cross-field transport is emulated by a constant diffusion of 0.3 m<sup>2</sup>/s.

To reduce numerical costs, we only simulate one ripple period, or 1/18th of the full torus, and periodically expand the simulated plasma in the toroidal direction. The simulation contains 250,000 cells spread over 16 poloidal planes and was run on 384 processors of the MARCONI computing center[52] for 20 ms simulated plasma time. The plasma has not yet reached a converged state, but is sufficiently stable to observe ripple-induced phenomena.

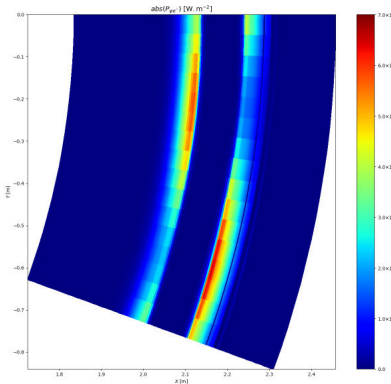


Figure 8.6.: Calculated electron wall heat flux in the divertor region from the SOLEDGE3X simulation. View on the target from the top for one ripple period.

In Fig. 8.6, the heat fluxes originating at the core source reach the divertor target with maximal heat loads that alternate between the inner and the outer strike point with the toroidal coordinate. It has a strong resemblance with the "snake skin" pattern in Fig. 8.1 observed on infrared imagery during the tokamak operation.

## 8.4. Conclusion

The incorporation of magnetic ripple perturbations into the SOLEDGE3X framework significantly enhances its capability to simulate complex magnetic configurations in tokamaks. Using the Biot-Savart law to calculate the ripple effects, this study exhibits the impact of the toroidal magnetic ripple on the magnetic equilibrium configuration in the WEST tokamak. These perturbations both affect the poloidal and the radial component of the axisymmetric magnetic equilibrium, with an important modulation of the poloidal field.

The perturbed magnetic field has been integrated into all parallel advection and gradient terms of the SOLEDGE3X transport model. The radial component of the poloidal perturbation field required major refactoring of the transport model because the mesh remains aligned to axisymmetric flux surfaces. Parallel fluxes now occur in all three directions in the curvilinear coordinates. Consequently, implicit solvers for the heat and viscosity problems are now applied to full-domain 3D systems instead of independent 2D systems on each flux surface, resulting in additional computational costs.

Simulations on a realistic WEST geometry demonstrate the new capability to perform simulations in a non-axisymmetric magnetic configuration. Key features of magnetic ripple, such as the modulation of heat loads on the divertor strike points along the toroidal coordinate, are successfully recovered.

## *8. Perspectives for Studying Magnetic Ripple – 8.4. Conclusion*

With this new implementation, it will be possible to explore new physics, such as ripple effects on tungsten core contamination or improved predictions of power exhaust in tokamaks. Additionally, this enhancement allows for better comparisons between simulation and experimental data due to the toroidal locality of several plasma diagnostics.

## **Part V.**

# **Conclusion**

In this thesis, an electromagnetic model was introduced to the SOLEDGE3X code for turbulent simulations in tokamak edge plasma. We are in the general framework of tokamaks for nuclear fusion, a constantly developing technology that aims to generate energy from the fusion of light atoms, as it occurs in stars. The physical processes that occur at the edge of the plasma, near the physical wall, are crucial to the quality of confinement and are still subject to active research today. In the present work, the physical model of the drift-reduced fluid code SOLEDGE3X was enhanced with an electromagnetic model, in which magnetic induction and magnetic perturbations affect the dynamics of drift-wave turbulence. This lays the foundations for turbulent simulations of larger machines and at higher temperatures, and, perhaps, contributes to a better understanding of edge theory and optimization of future reactor concepts.

In Chapter 1, the fundamental physics of particles in a magnetized plasma were introduced and applied to the specific configuration of a tokamak. Special attention was given to the magnetohydrodynamic equilibrium between thermodynamic and magnetic pressures, resistive and diffusive processes resulting from particle collisions, and the specific physics of the sheath at the boundary between the plasma and the reactor wall. In Chapter 2, we explained how the plasma can be described mathematically such that supercomputers can solve relevant physics. Starting from a direct particle description, including (gyro-)kinetic approaches, we derived the magnetohydrodynamic (MHD) description of plasmas that studies the evolution of mean fields similar to methods from computational fluid dynamics. This model can be further extended to drift-reduced fluid models, which are particularly well-suited to studying drift-wave turbulence in the plasma edge and the Scrape-Off Layer (SOL). We then discussed how electromagnetic effects in Ohm's law modify the non-adiabatic electron response to perturbations. They have a non-negligible impact on the turbulent dynamics in this region, even when the pressure ratio  $\beta$  has very low values.

This leads us to Chapter 3, where we presented the new electromagnetic model in SOLEDGE3X that constitutes the main contribution of this work. It can be broken down into three components. First, magnetic induction appears in the parallel electric field  $E_{\parallel}$  through the temporal change of the parallel magnetic vector potential  $\partial_t A_{\parallel}$ . The unknown  $A_{\parallel}$  is computed from the parallel current density  $j_{\parallel}$  using Ampère's law. These new fields drive fluctuations  $\tilde{B}$  in the magnetic field, commonly called flutter, which form the second component of the new model. The fluctuations are assumed to be small compared to the equilibrium field and are applied at first order. They reorient parallel transport channels and modify parallel gradients in Ohm's law or parallel heat conduction. Finally, taking a nonzero electron mass in Ohm's law adds electron inertia to the non-adiabatic response. This effect is necessary to constrain the Alfvén speed to physical values that might occur at steep perpendicular gradients and substitutes electric resistivity in hot plasmas. In Chapter 4, more technical details of the new model are explained. Two new fields had to be added: the parallel projection of the magnetic vector potential  $A_{\parallel}$  and the parallel current density  $j_{\parallel}$ , required to solve electron inertia effects. In the flux-surface aligned meshing of

SOLEDGE3X, they are defined on a poloidally and toroidally staggered grid to benefit from first-order parallel derivatives, requiring a whole set of new discrete operators. In the implicit-explicit time discretization, collisional processes are historically solved implicitly, which includes the vorticity equation on the electric potential  $\Phi$ . To avoid additional restrictions on the CFL condition, the new Alfvénic and electron inertial terms are solved implicitly in a large coupled 3D system with the vorticity equation. Due to the complex structure of the system, magnetic induction deteriorates the matrix condition; however, taking a finite electron mass reduces the anisotropy between the perpendicular and parallel Laplacians on  $\Phi$  and hence improves the condition. Flutter adds a severe layer of complexity to the entire model, as magnetic fluctuations introduce a radial component to the magnetic field. It required extensions of all parallel operators and had a particularly significant impact on the implicit viscosity and parallel heat conduction problems, as the coupling between magnetic flux surfaces imposes new 3D operators. The implementation was verified and validated in Chapter 5. Using the method of manufactured solutions, the new electromagnetic vorticity equation and the 3D heat diffusion with flutter were checked for correctness and second-order spatial convergence. Integration tests on slab geometries allowed recovery of frequencies from linear theory, especially the transition from shear Alfvén to thermal electron waves as the perpendicular wavenumber increases.

The final part is dedicated to applications in turbulent simulations. In Chapter 6, we explore electromagnetic effects on simple limited geometries. In a long toroidal slab with a pure toroidal magnetic field and a limiter at each end, we observed that magnetic induction enhances radial blob propagation at a certain distance from the sheath. With a sharp-edged heat and particle source, magnetic induction promotes the generation and expansion of turbulent structures, while flutter has a clear stabilizing effect on them. The next set of tests were performed on a circular geometry with a flat limiter on the low-field side. A scan on the electron mass  $m_e$  and the electromagnetic parameter  $\beta$  showed that both effects accelerate the initial growth of instabilities as one would expect from linear theory. Adding flutter to the system reduces the growth rate again, and this is also an expected effect. Complex diverted geometries with X-points are addressed in Chapter 7, with a comparison between electrostatic, electron inertia, inductive, and fully electromagnetic scenarios based on the TCV-X21 benchmark. In this L-mode plasma, it was found that magnetic induction alone significantly increases radial particle and heat transport across the separatrix, such that the temperature can barely build up and quickly reaches a quasi-steady state on energy. The stabilizing effect of flutter is quite present here, as the energy confinement returns, or even surpasses, electrostatic levels. Nonetheless, ExB drifts always dominates the cross-field transport and is much stronger than electromagnetic energy advection or redirection of the parallel heat flux. The last Chapter 8 shows applications of the new model beyond the realm of turbulent transport and electromagnetic effects. Perturbations to the magnetic equilibrium can also be imposed externally, allowing to run non-axisymmetric magnetic configurations, as long as the perturbations remain small compared to the axisymmetric average. This comes particularly handy to study mag-

netic ripple, small toroidal and poloidal perturbations of  $B$  due to the toroidal locality of poloidal field coils, that was observed to be particularly strong on WEST tokamak in Cadarache. Preliminary results of a simulation in transport mode could exhibit a snake skin pattern on the divertor plates with alternating peaks in heat deposition on the inner and outer targets, that were previously only observed on infrared imagery.

One key issue for self-consistent turbulent simulations is the very long execution time to reach convergence, and the electromagnetic model further worsens code performance. To obtain stable and significant mid-plane profiles, one must wait at least for a particle confinement time, which can reach up to 100ms for TCV and be much higher for larger machines. The simulations presented in this thesis were still far from convergence, even though the mesh used was still very coarse. While investigating drift-wave turbulence is important for understanding edge plasma behavior and cross-field transport, it is of limited use for global simulations. The current setup could benefit from improved initial conditions to reduce computational overhead. One option would be to start from experimental profiles that, while lacking fine-grained density and temperature distributions or toroidal fluctuations, could considerably accelerate the time to reach a quasi-steady state in an already converged environment. Our simulations showed that turbulent dynamics establish and respond quickly to changes in global profiles. This could allow for studying drift-wave turbulence in specific scenarios, such as L- or H-mode on a given tokamak or during an ELM event. The main drawback of using experimental profiles is that the model must perfectly match reality, otherwise slightly different profiles could establish, and the problem of waiting a full confinement time re-emerges. Alternatively, coupling turbulent and transport modes could be considered, where mean profiles evolve in a fast 2D simulation, with diffusion coefficients for cross-field transport regularly updated from 3D turbulent simulations restarted at specific intervals.

Regarding the electromagnetic model, the new terms have a considerable impact on turbulent dynamics and appear necessary for an accurate modeling of both interchange and drift-wave instabilities. Electron inertia is already beneficial for existing electrostatic scenarios, offering numerical advantages and regulating plasma dynamics in regions of low resistivity. However, it is not advisable to include magnetic induction without flutter or electron inertia; the full electromagnetic model should always be used. Preliminary results suggest that flutter stabilizes turbulent dynamics, but its precise role in forming or maintaining transport barriers, particularly in higher  $\beta$  scenarios, remains unclear. Further analysis of flutter in complex configurations with H-mode plasmas could open the door to exploring turbulence in future machines like ITER or DEMO. However, in the current implementation, simulations with flut-

ter come at a significant numerical cost, as it introduces a radial component to the magnetic field, leading to flux surface coupling in the aligned meshing. This affects all implicit solvers involving (now fluctuating) parallel gradients, including those for viscosity, parallel heat conduction, and vorticity. A potential solution could involve an explicit-implicit splitting between the equilibrium and fluctuating field components. Since flutter is added at first order and is required to be much smaller than the equilibrium field, it may not impose strong restrictions on the CFL condition in explicit time-stepping. The hybrid approach would preserve model accuracy while making it more suitable for longer simulated times, higher resolutions, or larger tokamaks.

Building on the electromagnetic framework, future developments of SOLEDGE3X could target simulations of edge localized modes (ELMs) and their suppression with resonant magnetic perturbations (RMPs). The main challenge in capturing these instabilities is the separation of large-scale dynamics over long timescales from the smaller-scale drift-wave turbulence, which may require calculating the flutter field without solving for drifts. Currently, the model does not solve for the necessary bootstrap current, which arises from radial pressure gradients in conjunction with trapped electrons. It is also unclear whether the perturbative approach  $\mathbf{B} = \mathbf{B}_{eq} + \tilde{\mathbf{B}}$  is sufficient to grow large magnetic islands that could trigger tearing modes. The ripple simulations presented in this work were a first step toward modeling non-axisymmetric magnetic fields and open the door to more ambitious configurations. For example, ergodic divertors are designed to break magnetic field lines into a chaotic state, spreading plasma heat fluxes over a wider area on the divertor plates.

# Bibliography

- [1] M. Abdou, M. Riva, A. Ying, et al. “Physics and technology considerations for the deuterium–tritium fuel cycle and conditions for tritium fuel self sufficiency”. In: *Nuclear Fusion* 61.1 (2020), p. 013001 (cit. on p. 22).
- [2] H. Abu-Shawareb, R. Acree, P. Adams, et al. “Achievement of target gain larger than unity in an inertial fusion experiment”. In: *Physical Review Letters* 132.6 (2024), p. 065102 (cit. on p. 21).
- [3] E. A. Azizov. “Tokamaks: from A D Sakharov to the present (the 60-year history of tokamaks)”. In: *Physics-Uspekhi* 55.2 (2012), p. 190 (cit. on p. 22).
- [4] S. Balay, S. Abhyankar, M. F. Adams, et al. *PETSc Web page*. <https://petsc.org/>. 2023 (cit. on p. 138).
- [5] C. K. Birdsall. “Particle-in-cell charged-particle simulations, plus Monte Carlo collisions with neutral atoms, PIC-MCC”. In: *IEEE Transactions on plasma science* 19.2 (1991), pp. 65–85 (cit. on p. 45).
- [6] S. I. Braginskii. “Transport processes in a plasma”. In: *Reviews of plasma physics* 1 (1965), p. 205 (cit. on pp. 50, 69).
- [7] A. Brandt, S. McCormick, and J. Ruge. “Algebraic multigrid (AMG) for sparse matrix equations”. In: *Sparsity and its Applications* 257 (1984) (cit. on p. 92).
- [8] J. Bucalossi, J. Achard, O. Agullo, et al. “Operating a full tungsten actively cooled tokamak: overview of WEST first phase of operation”. In: *Nuclear Fusion* 62.4 (Feb. 2022), p. 042007. DOI: [10.1088/1741-4326/ac2525](https://doi.org/10.1088/1741-4326/ac2525) (cit. on pp. 146, 147).
- [9] H. Bufferand, J. Bucalossi, G. Ciraolo, et al. “Progress in edge plasma turbulence modelling—hierarchy of models from 2D transport application to 3D fluid simulations in realistic tokamak geometry”. In: *Nuclear Fusion* 61.11 (2021), p. 116052 (cit. on pp. 80, 91, 138).
- [10] H. Bufferand, J. Bucalossi, G. Ciraolo, et al. “Progress in edge plasma turbulence modelling—hierarchy of models from 2D transport application to 3D fluid simulations in realistic tokamak geometry”. In: *Nuclear Fusion* 61.11 (2021), p. 116052 (cit. on pp. 23, 66).
- [11] H. Bufferand, G. Ciraolo, Y. Marandet, et al. “Numerical modeling for divertor design of the WEST device with a focus on plasma wall interactions”. In: *Nucl. Fus.* 55(5) (2015), p. 053025 (cit. on p. 66).
- [12] J. D. Callen. “Drift-Wave Turbulence Effects on Magnetic Structure and Plasma Transport in Tokamaks”. In: *Phys. Rev. Lett.* 39 (24 Dec. 1977), pp. 1540–1543. DOI: [10.1103/PhysRevLett.39.1540](https://doi.org/10.1103/PhysRevLett.39.1540) (cit. on p. 58).

## Bibliography

- [13] C. S. Chang, S. Ku, A. Loarte, et al. “Gyrokinetic projection of the divertor heat-flux width from present tokamaks to ITER”. In: *Nuclear Fusion* 57.11 (2017), p. 116023 (cit. on p. [46](#)).
- [14] G. Ciraolo, S. Di Genova, H. Yang, et al. “Interpretative modeling of impurity transport and tungsten sources in WEST boundary plasma”. In: *Nuclear Fusion* 61.12 (2021), p. 126015 (cit. on pp. [66](#), [147](#)).
- [15] L. Cohen. “Wave propagation with dispersion and damping”. In: *Proceedings of SPIE - The International Society for Optical Engineering* 5559 (Oct. 2004). DOI: [10.1117/12.564247](https://doi.org/10.1117/12.564247) (cit. on p. [112](#)).
- [16] M. D. Cole, R. Hager, T. Moritaka, et al. “Verification of the global gyrokinetic stellarator code XGC-S for linear ion temperature gradient driven modes”. In: *Physics of Plasmas* 26.8 (2019) (cit. on p. [46](#)).
- [17] G. D. Conway, A. I. Smolyakov, and T. Ido. “Geodesic acoustic modes in magnetic confinement devices”. In: *Nuclear Fusion* 62.1 (2021), p. 013001 (cit. on p. [57](#)).
- [18] J. W. S. Cook, R. Dendy, and S. C. Chapman. “Particle-in-cell simulations of the magnetoacoustic cyclotron instability of fusion-born alpha-particles in tokamak plasmas”. In: *Plasma Physics and Controlled Fusion* 55.6 (2013), p. 065003 (cit. on p. [45](#)).
- [19] W. D. D’haeseleer, W. N. G. Hitchon, J. D. S. Callen, et al. *Flux Coordinates and Magnetic Field Structure*. Springer Series in Computational Physics, 1991. ISBN: 978-3-642-75595-8 (cit. on p. [82](#)).
- [20] L. De Gianni, G. Ciraolo, G. Giruzzi, et al. “Core and edge modeling of JT-60SA H-mode highly radiative scenarios using SOLEDGE3X-EIRENE and METIS codes”. In: *Frontiers in Physics* 12 (2024), p. 1422286 (cit. on p. [146](#)).
- [21] S. Di Genova, A. Gallo, N. Fedorczak, et al. “Modelling of tungsten contamination and screening in WEST plasma discharges”. In: *Nuclear Fusion* 61.10 (2021), p. 106019 (cit. on p. [146](#)).
- [22] S. Di Genova. “Heavy ions migration in tokamak boundary plasmas : development of a numerical model to interpret WEST experiments”. PhD thesis. Aix-Marseille University, 2023 (cit. on p. [147](#)).
- [23] G. Dif-Pradalier, V. Grandgirard, Y. Sarazin, et al. “Interplay between Gyrokinetic Turbulence, Flows, and Collisions: Perspectives on Transport and Poloidal Rotation”. In: *Phys. Rev. Lett.* 103 (6 Aug. 2009), p. 065002. DOI: [10 . 1103 / PhysRevLett . 103 . 065002](https://doi.org/10.1103/PhysRevLett.103.065002) (cit. on p. [51](#)).
- [24] J. Drkošová, A. Greenbaum, M. Rozložník, et al. “Numerical stability of GMRES”. In: *BIT Numerical Mathematics* 35.3 (1995), pp. 309–330 (cit. on p. [93](#)).
- [25] B. D. Dudson, A. Allen, G. Breyiannis, et al. “BOUT : Recent and current developments”. In: *Journal of Plasma Physics* 81.1 (2015), p. 365810104. DOI: [10 . 1017 / S0022377814000816](https://doi.org/10.1017/S0022377814000816) (cit. on pp. [23](#), [58](#)).

## Bibliography

- [26] B. D. Dudson, S. L. Newton, J. T. Omotani, et al. “On Ohm’s law in reduced plasma fluid models”. In: *Plasma Physics and Controlled Fusion* 63.12 (Oct. 2021). ISSN: 0741-3335. DOI: [10.1088/1361-6587/ac2af9](https://doi.org/10.1088/1361-6587/ac2af9) (cit. on pp. 59, 116).
- [27] B. Dudson, M. Umansky, X. Xu, et al. “BOUT++: A framework for parallel plasma fluid simulations”. In: *Computer Physics Communications* 180.9 (2009), pp. 1467–1480. ISSN: 0010-4655. DOI: <https://doi.org/10.1016/j.cpc.2009.03.008> (cit. on pp. 23, 51, 58).
- [28] R. Düll, H. Bufferand, E. Serre, et al. “Introducing electromagnetic effects in Soledge3X”. In: *Contributions to Plasma Physics* (2024), e202300147 (cit. on p. 147).
- [29] T. Eich, A. Leonard, R. Pitts, et al. “Scaling of the tokamak near the scrape-off layer H-mode power width and implications for ITER”. In: *Nuclear fusion* 53.9 (2013), p. 093031 (cit. on p. 42).
- [30] R. Fitzpatrick. “A simple model of the resistive wall mode in tokamaks”. In: *Physics of Plasmas* 9.8 (2002), pp. 3459–3469 (cit. on p. 31).
- [31] H. Furth, P. Rutherford, and H. Selberg. “Tearing mode in the cylindrical tokamak”. In: *The Physics of Fluids* 16.7 (1973), pp. 1054–1063 (cit. on p. 31).
- [32] J. Gallier et al. “The Schur complement and symmetric positive semidefinite (and definite) matrices”. In: *Penn Engineering* (2010), pp. 1–12 (cit. on p. 95).
- [33] M. Giacomin, P. Ricci, A. Corrado, et al. “The GBS code for the self-consistent simulation of plasma turbulence and kinetic neutral dynamics in the tokamak boundary”. In: *Journal of Computational Physics* 463 (2022), p. 111294. ISSN: 0021-9991. DOI: [10.1016/j.jcp.2022.111294](https://doi.org/10.1016/j.jcp.2022.111294) (cit. on pp. 23, 51, 58, 76).
- [34] T. Goerler, X. Lapillonne, S. Brunner, et al. “The global version of the gyrokinetic turbulence code GENE”. In: *Journal of Computational Physics* 230.18 (2011), pp. 7053–7071 (cit. on p. 46).
- [35] H. Grad and H. Rubin. *Hydromagnetic Equilibria and Force-Free Fields*. INIS-XU-021. United Nations (UN), 1958, pp. 190–197 (cit. on p. 32).
- [36] V. Grandgirard, J. Abiteboul, J. Bigot, et al. “A 5D gyrokinetic full-f global semi-Lagrangian code for flux-driven ion turbulence simulations”. In: *Computer physics communications* 207 (2016), pp. 35–68 (cit. on p. 46).
- [37] V. Grandgirard, Y. Sarazin, P. Angelino, et al. “Global full-f gyrokinetic simulations of plasma turbulence”. In: *Plasma Physics and Controlled Fusion* 49.12B (2007), B173 (cit. on p. 46).
- [38] A. Greenbaum, M. Rozložník, and Z. Strakoš. “Numerical behaviour of the modified Gram-Schmidt GMRES implementation”. In: *BIT Numerical Mathematics* 37.3 (1997), pp. 706–719 (cit. on p. 93).
- [39] J. P. Gunn, S. Carpentier-Chouchana, F. Escourbiac, et al. “Surface heat loads on the ITER divertor vertical targets”. In: *Nuclear Fusion* 57.4 (2017), p. 046025 (cit. on pp. 42, 146).

## Bibliography

- [40] S. Günter, Q. Yu, J. Krüger, et al. “Modelling of heat transport in magnetised plasmas using non-aligned coordinates”. In: *Journal of Computational Physics* 209.1 (2005), pp. 354–370. ISSN: 0021-9991. DOI: <https://doi.org/10.1016/j.jcp.2005.03.021> (cit. on pp. 86, 98, 99).
- [41] R. Hager, S. Ku, A. Y. Sharma, et al. “Electromagnetic total-f algorithm for gyrokinetic particle-in-cell simulations of boundary plasma in XGC”. In: *Phys. Plasmas* 29.11 (2022), p. 112308. DOI: [10.1063/5.0097855](https://doi.org/10.1063/5.0097855) (cit. on pp. 46, 76).
- [42] A. Hasegawa and M. Wakatani. “Plasma edge turbulence”. In: *Physical Review Letters* 50.9 (1983), p. 682 (cit. on p. 55).
- [43] K. Hasegawa and T. Shimada. “Staggered Grid with Collocated Grid Points of Velocities for Modeling Propagation of Elastic Waves in Anisotropic Solids by Finite-Difference Time Domain Method”. In: *Japanese Journal of Applied Physics* 51.7S (2012), 07GB04 (cit. on p. 86).
- [44] R. Hastie, J. J. Ramos, and F. Porcelli. “Drift ballooning instabilities in tokamak edge plasmas”. In: *Physics of Plasmas* 10.11 (2003), pp. 4405–4412 (cit. on p. 57).
- [45] R. Hazeltine, M. Kotschenreuther, and P. Morrison. “A four-field model for tokamak plasma dynamics”. In: *Physics of Fluids* 28.8 (1985), p. 2466 (cit. on p. 52).
- [46] P. Helander and D. J. Sigmar. *Collisional transport in magnetized plasmas*. Vol. 4. Cambridge university press, 2005 (cit. on p. 69).
- [47] P. Hennequin, R. Sabot, C. Honoré, et al. “Scaling laws of density fluctuations at high-k on Tore Supra”. In: *Plasma Physics and Controlled Fusion* 46.12B (Nov. 2004), B121. DOI: [10.1088/0741-3335/46/12B/011](https://doi.org/10.1088/0741-3335/46/12B/011) (cit. on p. 44).
- [48] M. Hoelzl, G. T. Huijsmans, S. Pamela, et al. “The JOREK non-linear extended MHD code and applications to large-scale instabilities and their control in magnetically confined fusion plasmas”. In: *Nuclear Fusion* 61.6 (2021), p. 065001 (cit. on pp. 50, 61).
- [49] N. Horsten, G. Samaey, and M. Baelmans. “Development and assessment of 2D fluid neutral models that include atomic databases and a microscopic reflection model”. In: *Nuclear Fusion* 57.11 (Aug. 2017), p. 116043. DOI: [10.1088/1741-4326/aa8009](https://doi.org/10.1088/1741-4326/aa8009) (cit. on p. 135).
- [50] I. Hutchinson, J. Freidberg, et al. “Introduction to plasma physics”. In: *Electronic book available from: http://silas.psfc.mit.edu/introplasma/index.html* (2001) (cit. on p. 37).
- [51] G. Huysmans and O. Czarny. “MHD stability in X-point geometry: simulation of ELMs”. In: *Nuclear fusion* 47.7 (2007), p. 659 (cit. on p. 50).
- [52] F. Iannone, G. Bracco, C. Cavazzoni, et al. “MARCONI-FUSION: The new high-performance computing facility for European nuclear fusion modelling”. In: *Fusion Engineering and Design* 129 (2018), pp. 354–358. ISSN: 0920-3796. DOI: [10.1016/j.fusengdes.2017.11.004](https://doi.org/10.1016/j.fusengdes.2017.11.004) (cit. on pp. 138, 151).

## Bibliography

- [53] I. Keramidas Charidakos, J. R. Myra, S. Parker, et al. “Analysis of equilibrium and turbulent fluxes across the separatrix in a gyrokinetic simulation”. In: *Physics of Plasmas* 25.7 (July 2018), p. 072306. ISSN: 1070-664X. DOI: [10.1063/1.5037723](https://doi.org/10.1063/1.5037723). eprint: [https://pubs.aip.org/aip/pop/article-pdf/doi/10.1063/1.5037723/14763677/072306\\_1\\_online.pdf](https://pubs.aip.org/aip/pop/article-pdf/doi/10.1063/1.5037723/14763677/072306_1_online.pdf) (cit. on p. 51).
- [54] R. Khaziev and D. Curreli. “hPIC: A scalable electrostatic particle-in-cell for plasma–material interactions”. In: *Computer Physics Communications* 229 (2018), pp. 87–98 (cit. on p. 45).
- [55] M. Kruskal and J. Tuck. “The instability of a pinched fluid with a longitudinal magnetic field”. In: *Proceedings of the Royal Society of London. Series A. Mathematical and Physical Sciences* 245.1241 (1958), pp. 222–237 (cit. on p. 31).
- [56] J. D. Lawson. “Some Criteria for a Power Producing Thermonuclear Reactor”. In: *Proceedings of the Physical Society. Section B* 70.1 (Jan. 1957), p. 6. DOI: [10.1088/0370-1301/70/1/303](https://doi.org/10.1088/0370-1301/70/1/303) (cit. on p. 20).
- [57] J. Leddy, B. Dudson, M. Romanelli, et al. “On the validity of drift-reduced fluid models for tokamak plasma simulation”. In: *Plasma Physics and Controlled Fusion* 57.12 (2015), p. 125016 (cit. on p. 57).
- [58] W. Lee, J. Angus, M. V. Umansky, et al. “Electromagnetic effects on plasma blob-filament transport”. In: *Journal of Nuclear Materials* 463 (2015), pp. 765–768. ISSN: 0022-3115. DOI: [10.1016/j.jnucmat.2014.09.083](https://doi.org/10.1016/j.jnucmat.2014.09.083) (cit. on pp. 58, 124).
- [59] W. Lee, M. V. Umansky, J. Angus, et al. “Electromagnetic effects on dynamics of high-beta filamentary structures”. In: *Physics of Plasmas* 22.1 (2015) (cit. on p. 124).
- [60] A. Lessig, C. C. Queiros, E. Franck, et al. “Fluid models for Tokamak Plasmas: Magneto-Hydrodynamic”. In: (2016) (cit. on p. 49).
- [61] A. Loarte, B. Lipschultz, A. Kukushkin, et al. “Chapter 4: Power and particle control”. In: *Nuclear Fusion* 47.6 (June 2007), S203. DOI: [10.1088/0029-5515/47/6/S04](https://doi.org/10.1088/0029-5515/47/6/S04) (cit. on p. 23).
- [62] H. Meier, J. Alves, and M. Mori. “Comparison between staggered and collocated grids in the finite-volume method performance for single and multi-phase flows”. In: *Computers & chemical engineering* 23.3 (1999), pp. 247–262 (cit. on p. 83).
- [63] D. Michels, A. Stegmeir, P. Ulbl, et al. “GENE-X: A full-f gyrokinetic turbulence code based on the flux-coordinate independent approach”. In: *Computer Physics Communications* 264 (2021), p. 107986 (cit. on p. 46).
- [64] A. Mikhailovskii and L. Rudakov. “The stability of a spatially inhomogeneous plasma in a magnetic field”. In: *Soviet Physics JETP* 44 (1963), pp. 912–918 (cit. on p. 59).

- [65] A. Mikhailovskii and V. Tsypin. “Transport equations and gradient instabilities in a high pressure collisional plasma”. In: *Plasma Physics* 13.9 (1971), p. 785 (cit. on p. 52).
- [66] D. Moiraf, J. Morales, L. Colas, et al. “Optimization of the operational domain for ICRH scenarios in WEST from statistical analysis”. In: *Nuclear Fusion* 63.8 (2023), p. 086010 (cit. on p. 146).
- [67] E. Nardon, A. Fil, M. Hoelzl, et al. “Progress in understanding disruptions triggered by massive gas injection via 3D non-linear MHD modelling with JOREK”. In: *Plasma physics and controlled fusion* 59.1 (2016), p. 014006 (cit. on p. 61).
- [68] D. Oliveira, T. Body, D. Galassi, et al. “Validation of edge turbulence codes against the TCV-X21 diverted L-mode reference case”. In: *Nuclear Fusion* 62.9 (July 2022), p. 096001. DOI: [10.1088/1741-4326/ac4cde](https://doi.org/10.1088/1741-4326/ac4cde) (cit. on p. 135).
- [69] S. Pamela, G. T. Huijsmans, T. Eich, et al. “Recent progress in the quantitative validation of JOREK simulations of ELMs in JET”. In: *Nuclear Fusion* 57.7 (2017), p. 076006 (cit. on p. 61).
- [70] B. N. Parlett and C. Reinsch. “Balancing a matrix for calculation of eigenvalues and eigenvectors”. In: *Numerische Mathematik* 13 (1969), pp. 293–304 (cit. on p. 91).
- [71] A. Pyzara, B. Bylina, and J. Bylina. “The influence of a matrix condition number on iterative methods’ convergence”. In: *2011 Federated Conference on Computer Science and Information Systems (FedCSIS)*. IEEE. 2011, pp. 459–464 (cit. on p. 93).
- [72] V. Quadri, P. Tamain, Y. Marandet, et al. “Self-organization of plasma edge turbulence in interaction with recycling neutrals”. In: *Contributions to Plasma Physics* n/a.n/a (), e202300146. DOI: <https://doi.org/10.1002/ctpp.202300146>. eprint: <https://onlinelibrary.wiley.com/doi/pdf/10.1002/ctpp.202300146> (cit. on pp. 135, 140).
- [73] T. Rafiq, C. C. Hegna, J. D. Callen, et al. “Unified theory of resistive and inertial ballooning modes in three-dimensional configurations”. In: *Physics of Plasmas* 16.10 (2009) (cit. on p. 59).
- [74] P. Ricci, F. D. Halpern, S. Jolliet, et al. “Simulation of plasma turbulence in scrape-off layer conditions: the GBS code, simulation results and code validation”. In: *Plasma Physics and Controlled Fusion* 54.12 (Nov. 2012), p. 124047. DOI: [10.1088/0741-3335/54/12/124047](https://doi.org/10.1088/0741-3335/54/12/124047) (cit. on pp. 23, 58).
- [75] K.-U. Riemann. “The Bohm criterion and sheath formation”. In: *Journal of Physics D: Applied Physics* 24.4 (1991), p. 493 (cit. on p. 41).
- [76] N. Rivals, P. Tamain, Y. Marandet, et al. “SOLEDGE3X full vessel plasma simulations for computation of ITER first-wall fluxes”. In: *Contributions to Plasma Physics* 262.5–6 (2022), e202100182 (cit. on p. 66).

- [77] N. Rivals, P. Tamain, Y. Marandet, et al. “Impact of enhanced far-SOL transport on first wall fluxes in ITER from full vessel edge-plasma simulations”. In: *Nuclear Materials and Energy* 33 (2022), p. 101293 (cit. on p. 147).
- [78] N. Rivals, P. Tamain, Y. Marandet, et al. “SOLEDGE3X full vessel plasma simulations for computation of ITER first-wall fluxes”. In: *Contributions to Plasma Physics* 62.5-6 (2022), e202100182 (cit. on p. 146).
- [79] P. J. Roache. “Code Verification by the Method of Manufactured Solutions ”. In: *Journal of Fluids Engineering* 124.1 (Nov. 2001), pp. 4–10. ISSN: 0098-2202. DOI: [10.1115/1.1436090](https://doi.org/10.1115/1.1436090) (cit. on p. 102).
- [80] F. Rubio, M. Hanzich, A. Farrés, et al. “Finite-difference staggered grids in GPUs for anisotropic elastic wave propagation simulation”. In: *Computers & geosciences* 70 (2014), pp. 181–189 (cit. on p. 86).
- [81] D. Ryutov, R. Cohen, T. Rognlien, et al. “The magnetic field structure of a snowflake divertor”. In: *Physics of Plasmas* 15.9 (2008) (cit. on p. 36).
- [82] F. Schwander, E. Serre, H. Bufferand, et al. “Global fluid simulations of edge plasma turbulence in tokamaks: a review”. In: *Computers & Fluids* 270 (2024), p. 106141. ISSN: 0045-7930. DOI: <https://doi.org/10.1016/j.compfluid.2023.106141> (cit. on pp. 51, 75).
- [83] B. Scott. “Three-dimensional computation of collisional drift wave turbulence and transport in tokamak geometry”. In: *Plasma physics and controlled fusion* 39.3 (1997), p. 471 (cit. on p. 59).
- [84] B. D. Scott. “Three-dimensional computation of drift Alfvén turbulence”. In: *Plasma Phys. Control. Fusion* 39 (1997), p. 1635 (cit. on pp. 58, 59).
- [85] B. D. Scott. “Computation of electromagnetic turbulence and anomalous transport mechanisms in tokamak plasmas”. In: *Plasma Phys. Control. Fusion* 45 (2003), A385 (cit. on p. 59).
- [86] V. Shafranov. “Stability of plasmas confined by magnetic fields”. In: *Soviet Journal of Atomic Energy* 5 (1956), p. 38 (cit. on p. 31).
- [87] V. Shafranov. “On equilibrium magnetohydrodynamic configurations”. In: *Zh. Eksp. Teor. Fiz.* 33.3 (1957), pp. 710–722 (cit. on p. 32).
- [88] V. D. Shafranov. “Trends in magnetic helical systems for CNF”. In: *Physics-Uspekhi* 42.7 (1999), p. 720 (cit. on p. 22).
- [89] A. Simakov and P. Catto. “Drift-ordered fluid equations for field-aligned modes in low- beta collisional plasma with equilibrium pressure pedestals”. In: *Phys. of Plasma* 10.1 (2003), pp. 4744–57 (cit. on pp. 52, 54).
- [90] R. Sinkhorn and P. Knopp. “Concerning nonnegative matrices and doubly stochastic matrices”. In: *Pacific Journal of Mathematics* 21.2 (1967), pp. 343–348 (cit. on p. 91).

- [91] L. Spitzer and R. Härm. “Transport Phenomena in a Completely Ionized Gas”. In: *Phys. Rev.* 89 (5 Mar. 1953), pp. 977–981. DOI: [10.1103/PhysRev.89.977](https://doi.org/10.1103/PhysRev.89.977) (cit. on p. 40).
- [92] P. C. Stangeby. *The Plasma Boundary of Magnetic Fusion Devices (1st ed.)* Boca Raton: CRC Press, 2000 (cit. on pp. 42, 78).
- [93] A. Stegmeir, A. Ross, T. Body, et al. “Global turbulence simulations of the tokamak edge region with GRILLIX”. In: *Phys. Plasmas* 26.5 (2019), p. 052517. DOI: [10.1063/1.5089864](https://doi.org/10.1063/1.5089864) (cit. on pp. 23, 51, 58, 116).
- [94] A. Stegmeir, D. Coster, A. Ross, et al. “GRILLIX: a 3D turbulence code based on the flux-coordinate independent approach”. In: *Plasma Physics and Controlled Fusion* 60.3 (2018), p. 035005 (cit. on p. 23).
- [95] A. A. Stepanenko. “Impact of electromagnetic effects on macroscopic dynamics of blobs in hot low- $\beta$  edge plasma of fusion devices”. In: *Physics of Plasmas* 27.9 (Sept. 2020), p. 092301. DOI: [10.1063/5.0013435](https://doi.org/10.1063/5.0013435) (cit. on pp. 58, 124).
- [96] Z. Strakoš. “On the real convergence rate of the conjugate gradient method”. In: *Linear algebra and its applications* 154 (1991), pp. 535–549 (cit. on p. 93).
- [97] P. Tamain, H. Bufferand, G. Ciraolo, et al. “The TOKAM3X code for edge turbulence fluid simulations of tokamak plasmas in versatile magnetic geometries”. In: *Journal of Computational Physics* 321 (2016), pp. 606–623. ISSN: 0021-9991. DOI: [10.1016/j.jcp.2016.05.038](https://doi.org/10.1016/j.jcp.2016.05.038) (cit. on pp. 23, 66, 80, 81, 138).
- [98] K. Tani, M. Azumi, H. Kishimoto, et al. “Effect of toroidal field ripple on fast ion behavior in a tokamak”. In: *Journal of the Physical Society of Japan* 50.5 (1981), pp. 1726–1737 (cit. on p. 146).
- [99] A. Team et al. “The H-mode of ASDEX”. In: *Nuclear Fusion* 29.11 (1989), p. 1959 (cit. on p. 34).
- [100] D. Tskhakaya, K. Matyash, R. Schneider, et al. “The Particle-In-Cell Method”. In: *Contributions to Plasma Physics* 47.8-9 (2007), pp. 563–594 (cit. on p. 45).
- [101] A. Van der Sluis. “Condition numbers and equilibration of matrices”. In: *Numerische Mathematik* 14.1 (1969), pp. 14–23 (cit. on p. 92).
- [102] H. A. van der Vorst. “Bi-CGSTAB: A Fast and Smoothly Converging Variant of Bi-CG for the Solution of Nonsymmetric Linear Systems”. In: *SIAM J. Sci. Stat. Comput.* 13.2 (1992), pp. 631–644. DOI: [10.1137/0913035](https://doi.org/10.1137/0913035) (cit. on p. 138).
- [103] D. Wang and S. J. Ruuth. “Variable step-size implicit-explicit linear multistep methods for time-dependent partial differential equations”. In: *Journal of Computational Mathematics* (2008), pp. 838–855 (cit. on p. 80).
- [104] S. E. Wurzel and S. C. Hsu. “Progress toward fusion energy breakeven and gain as measured against the Lawson criterion”. In: *Physics of Plasmas* 29.6 (2022) (cit. on p. 21).

## Bibliography

- [105] H. Yang. “Control of detachment in the divertor region of tokamaks: impact of wall geometry, particle, and energy sources”. PhD thesis. Aix-Marseille University, 2023 (cit. on p. [147](#)).
- [106] K. Yee. “Numerical solution of initial boundary value problems involving Maxwell’s equations in isotropic media”. In: *IEEE Transactions on antennas and propagation* 14.3 (1966), pp. 302–307 (cit. on p. [86](#)).
- [107] A. Zeiler, J. Drake, and B. Rogers. “Nonlinear reduced Braginskii equations with ion thermal dynamics in toroidal plasma”. In: *Physics of Plasmas* 4.6 (1997), pp. 2134–2138 (cit. on p. [69](#)).
- [108] K. Zhang, W. Zholobenko, A. Stegmeir, et al. “Magnetic flutter effect on validated edge turbulence simulations”. In: *Nuclear Fusion* 64.3 (2024), p. 036016 (cit. on pp. [58](#), [76](#), [144](#)).
- [109] V. M. Zhdanov. *Transport processes in multicomponent plasma*. CRC Press, 2002 (cit. on p. [51](#)).
- [110] W. Zholobenko, K. Zhang, A. Stegmeir, et al. “Tokamak edge-SOL turbulence in H-mode conditions simulated with a global, electromagnetic, transcollisional drift-fluid model”. In: *Nuclear Fusion* (2024) (cit. on p. [58](#)).
- [111] B. Zhu, X.-Q. Xu, and X.-Z. Tang. “Electromagnetic turbulence simulation of tokamak edge plasma dynamics and divertor heat load during thermal quench”. In: *Nuclear Fusion* 63.8 (July 11, 2023). Not subject to copyright in the USA. Contribution of U.S. Department of Energy, p. 086027. DOI: [10.1088/1741-4326/acdf4e](https://doi.org/10.1088/1741-4326/acdf4e) (cit. on p. [58](#)).

# **APPENDICES**

# A. New software modules

In the course of the PhD, several software modules were extended or created. This appendix gives an overview of the major novelties and might be of interest for SOLEDGE3X users.

## A.1. New options in SOLEDGE3X

The `param_raptorX.txt` file is a text formatted file which sets main SOLEDGE3X simulation parameters. The files contains a set of namelist that will be read by the code at initialisation. The new or modified entries related to the electromagnetic model and other necessary developments in the thesis are summarized here.

Parameter	Value	Properties
<code>solveAPara</code>	logical	If set to <code>.TRUE.</code> , the parallel projection of the magnetic vector potential $A_{\parallel}$ is computed along with potential $\Phi$ , introducing electromagnetic induction. At higher power, inductive effects may have a decisive impact on turbulent structures. The implicit vorticity system doubles in size and the solve time is affected accordingly.
<code>solveJPara</code>	logical	If set to <code>.TRUE.</code> , we take a finite electron mass to compute the parallel current density $j_{\parallel}$ in Ohm's law. This adds an inertial term to the vorticity equation and is deemed crucial for electromagnetic simulations. As a positive side effect, it reduces the anisotropy of the vorticity equation, facilitating thereby its iterative solving.

### A. New software modules – A.1. New options in SOLEDGE3X

Parameter	Value	Properties
EnableEMflutter	logical	If set to .TRUE., electromagnetic flutter is calculated. A perturbation of the magnetic field is calculated from the local value of the parallel magnetic vector potential $A_{\parallel}$ . The magnetic configuration loses its axi-symmetry and particularly, a (small) radial component $b_{\psi}$ appears. Parallel gradients and transport are affected by flutter in first place. It affects the solve time of the parallel diffusion operators (if NuParal = .TRUE.) as $N$ independent 2D system are combined to one 3D system.
BpertScale	$F \in ]-\infty, \infty[$	This float parameter can be used to rescale the external perturbation to the magnetic field. To suppress the perturbated field, set BpertScale=0. Useful for non-axisymmetric configurations as for ripple.
LphiDiv	$I \in [[1, \infty[$	Sets the angular length in the toroidal direction. The angular length of the domain in degrees is given by $360^\circ / LphiDiv$ . E.g., set to 1 for full torus simulation, 2 for half-torus... In simulations with mesh loaded from external files (PrecodedMesh=0), the toroidal extent of the mesh in the input mesh file is scaled by $1/LphiDiv$ . In analytic meshes, a negative LphiDiv will multiply the toroidal extent by its absolute value (e.g. -2 for 4pi, -3 for 6pi ...). This last option shall be used with care, it allows to artificially increase the connection length in a toroidal configuration while keeping a high curvature.
nu0	f-list	List of comma separated floats. Cross-field viscosity (parallel momentum balance) for every element including electrons expressed in $m^2 s^{-1}$ . The size of the list is $N_{elt} + 1$ . The first element, for electrons, is only used for the parallel current density $j_{\parallel}$ and is only effective in combination with solvejPara=.TRUE.. When loadDiffusionMap is set to .TRUE., the value is used as a lower bound for viscosity.
xi0	float	Cross-field diffusivity for the parallel vector potential $A_{\parallel}$ expressed in $m^2 s^{-1}$ .

A. New software modules – A.1. New options in SOLEDGE3X

Parameter	Value	Properties
ElectronMassMultiplier	$f \in [0, \infty[$	Artificially modify the electron mass for electron inertia effects. Set ElectronMassMultiplier=1 for the physical mass and ElectronMassMultiplier=0 to remove electron inertia.
BetaMultiplier	$f \in [0, \infty[$	Artificially modify the reference pressure ratio $\beta_0$ . Set BetaMultiplier=1 for the physical value.
filteringAPara	logical	If .TRUE., a diffusive filtering is applied on the magnetic vector potential before computing flutter. The smoothed potential is stored in the variable AParaSmooth.
LsmoothAPara	$f \in [0, \infty[$	Radius of the diffusive filtering set in meter. The parameter is ignored if filteringAPara=.FALSE..
NgroundedPoints	$i \in [0, \infty[$	If greater than 0, the electric potential at a set of points in the grid will be forced to zero. Grounding points can be useful to simulate a domain without wall where no reference potential exists. Setting a point to zero then makes the vorticity equation invertible.
groundedDiagonal	logical	If .TRUE., an array of points diagonal to the domain is grounded. This option is reasonable in slab cases with an identical number of discretization points in all directions. In 2D, the diagonal is line from the $[\psi^-, \theta^+]$ to the $[\psi^+, \theta^-]$ corners. In 3D, the diagonal is the plane orthogonal to the $[\psi^-, \theta^-, \varphi^-] - [\psi^+, \theta^+, \varphi^+]$ line at the center of the domain (ignored if NgroundedPoints=0)
groundedZone	i-list	List of zone indices of the grounded points. If 0, it is applied to all zones (ignored if NgroundedPoints=0 or groundedDiagonal=.TRUE.)
groundedipsi	i-list	List of radial indices of the grounded points. If 0, it is applied to all radial indices (ignored if NgroundedPoints=0 or groundedDiagonal=.TRUE.)
groundeditheta	i-list	List of poloidal indices of the grounded points. If 0, it is applied to all poloidal indices (ignored if NgroundedPoints=0 or groundedDiagonal=.TRUE.)

### A. New software modules – A.1. New options in SOLEDGE3X

Parameter	Value	Properties
groundeddiphi	i-list	List of toroidal indices of the grounded points. If 0, it is applied to all toroidal indices (ignored if NgroundedPoints=0 or groundedDiagonal=.TRUE.)
excitationFrequency	f-list	If non-zero, a list of frequencies at which the respective grounded points shall be excited [unit: $1/(\tau_0 s)$ ]. If groundedDiagonal=.TRUE., the first array value is used(ignored if NgroundedPoints=0)
excitationAmplitude	f-list	If non-zero, a list of amplitudes to which the respective grounded points shall be excited [in $1/(\Phi_0 V)$ ]. If groundedDiagonal=.TRUE., the first array value is used (ignored if NgroundedPoints=0)
forceSingleMatrix2DSolver	logical	Generate a single matrix with independent block matrices for 2D solvers? Unless one has a good reason to do so (like solving with GPU), it is advised to keep this parameter to .FALSE. for better performances.

Table A.1.: New or modified parameters for the SOLEDGE3X parameter file  
param\_raptorX.txt

The param\_geom.txt file is a text formatted file to generate analytic meshes in circular or slab configuration.

Parameter	Value	Properties
blob_r	$F \in [r_{min}, r_{max}]$	The radial position of the center blob. It is expressed in relative units to the separatrix. In poloidal direction, it is always set at the outer midplane or at the center of the box in slab simulations.
blob_radius	$F \in [0, \infty[$	The radius of the blob, in units relative to the separatrix. It defines the variance of the Gaussian profile for the blob. The blob will then get a 2D Gaussian profile on the cartesian R-Z grid.
blob_amp	$F \in ]-\infty, \infty[$	Amplitude of the blob w.r.t the background plasma.

Table A.2.: New parameters for analytic meshes in the file param\_geom.txt

## A.2. Grad-Shafranov solver

A short script was developed to calculate the poloidal flux function  $\Psi$  for given minor and major radii  $a$  and  $R_0$  and a given pressure profile  $p(r)$  as a function of the minor radius. Dirichlet boundary conditions 0 are imposed outside the domain defined by  $a$ . It solves the Grad-Shafranov equation:

$$\Delta^* \Psi = R \partial_R \left( \frac{1}{R} \partial_R \Psi \right) + \partial_Z^2 \Psi \quad (\text{A.1})$$

iteratively using the Newton-Krylov solver of the Python package `scipy.optimize`.

## A.3. Poincaré plots

A new script was created to generate the Poincaré of a given magnetic configuration. The code follows a particle along its magnetic field line and plot a dot at every intersection with a poloidal plane. Several particles can be plotted in parallel. The script automatically detects the presence of a perturbated field (e.g. ripple) in the provided `mesh_raptorX.h5` file. If electromagnetic flutters modifies the equilibrium, a plasma save file is additionally required. It is also possible to only plot the flutter field.

The user must specify the plane (or planes) on which you want to visualize the intersection with the particle trajectory. If none are provided, it plots the poloidal position at every integrated point (not a true Poincare plot anymore). This script requires to define seed points from which the integrator starts in both directions until it hits the core, a wall or reaches the integration length. There are three ways to define seed points on a list of poloidal planes (usually one or all), that can be combined:

- define a line with equally spaced seed points along its length
- define a box with N seed points
- randomly distribute N seed points in the domain (preferred method)

The code first extracts all mesh points in the  $[R, Z, \varphi]$  coordinate system and the total magnetic field components  $B_R$ ,  $B_Z$  and  $B_\varphi$  and store them in 1D arrays. A Delaunay triangulation is then performed of the poloidal geometry, such that the magnetic field at any point in the domain can be easily interpolated. The integration of the field lines, starting in both directions from the seeding points using the initial value problem solver of `scipy.integrate`.

## A.4. Time plots

A script was developed to track global metrics over the simulation time and compare different scenarios.  $V$  describes the total volume of the domain  $\Omega$  and  $A_{sep}$  the surface of the separatrix.

A. New software modules – A.4. Time plots

Name	Expression	Unit
Root mean square of density	$\frac{1}{V} \int_V \sqrt{\frac{(n - \langle n \rangle_\varphi)^2}{\langle n \rangle_\varphi^2}} d\Omega$	-
Root mean square of temperature	$\frac{1}{V} \int_V \sqrt{\frac{(T - \langle T \rangle_\varphi)^2}{\langle T \rangle_\varphi^2}} d\Omega$	-
Kinetic energy of ExB drifts for a species $\alpha$	$\frac{1}{2} m_\alpha \int_V n \ \mathbf{u}\ ^2 d\Omega$	J
Total thermal energy	$\sum_\alpha \frac{3}{2} \int_V e n T d\Omega$	J
ExB flux across the separatrix	$\int_{sep}  n \mathbf{e}_\psi \cdot \mathbf{u}^{E \times B}  dA_{sep}$	$m^{-2} s^{-1}$
Flutter flux across the separatrix	$\int_{sep}  n v_\parallel \mathbf{e}_\psi \cdot \mathbf{b}  dA_{sep}$	$m^{-2} s^{-1}$
Turbulent kinetic energy at the separatrix	$\frac{1}{A_{sep}} \int_{sep} \frac{n \mathbf{e}_\psi \cdot \mathbf{u} - \langle n \mathbf{e}_\psi \cdot \mathbf{u} \rangle_\varphi}{\langle n \rangle_\varphi}  n v_\parallel \mathbf{e}_\psi \cdot \mathbf{b}  dA_{sep}$	$m^2 s^{-2}$
Components to the total heat flux across the separatrix	$\underbrace{\int_{sep} \mathbf{e}_\psi \cdot \varepsilon n \mathbf{u}^{ExB} dA_{sep}}_{ExB} + \underbrace{\int_{sep} \mathbf{e}_\psi \cdot \varepsilon n \mathbf{u}^{\nabla B} dA_{sep}}_{gradB} + \underbrace{\int_{sep} \mathbf{e}_\psi \cdot \varepsilon n v_\parallel \mathbf{b} dA_{sep}}_{EM} + \underbrace{\int_{sep} \mathbf{e}_\psi \cdot [-\kappa_{SH} \nabla_\parallel T \mathbf{b}] dA_{sep}}_{qpara}$	W
Total entering and leaving heat fluxes	$\sum_\alpha P_{in,\alpha} , \quad \sum_\alpha P_{out,\alpha}$	W
Number of iterative steps to solve the vorticity system	-	-

A. New software modules – A.4. Time plots

Name	Expression	Unit
Norm of the vorticity matrix	-	-
Norm of the vorticity RHS vector	-	-
Norm of the vorticity solution vector	-	-
Time to solve the vorticity system	-	s
Ideal CFL timestep size and actual timestep size	-	s

Table A.3.: Global metrics available to plot the time evolution

# B. Operators on the curvilinear metric

## B.1. Linear algebra

The metric coefficients together with the co-/contravariant vectors are useful tools to perform several operations on the curvilinear grid. First of all, the squared Jacobian of the transformation from the cartesian to the curvilinear coordinate systems is equal to the determinant of  $g_{ij}$ .

$$J = \frac{\partial(x, y, z)}{\partial(u^\psi, u^\theta, u^\varphi)} = \sqrt{\det[g_{ij}]} \quad (\text{B.1})$$

The dot product between two vectors  $\vec{v}$  and  $\vec{w}$  is calculated with the co-/contravariant vectors.

$$\vec{v} \cdot \vec{w} = g_{ij} v^i w^j = g^{ij} v_i w_j \quad (\text{B.2})$$

The co-/contravariant components of the cross product can also be calculated:

$$\begin{cases} (\vec{v} \times \vec{w})_k = J \epsilon_{ijk} v^i w^j \\ (\vec{v} \times \vec{w})^k = \frac{1}{J} \epsilon_{ijk} v_i w_j \end{cases} \quad (\text{B.3})$$

This operations involves the Levi-Civita symbol  $\epsilon_{ijk}$  which takes the value +1 for all even permutations  $\{\psi, \theta, \varphi\}, \{\theta, \varphi, \psi\}$  and  $\{\varphi, \psi, \theta\}$ , the value -1 for all odd permutations  $\{\varphi, \theta, \psi\}, \{\theta, \psi, \varphi\}$  and  $\{\psi, \varphi, \theta\}$ , and is 0 for all other cases.

In the drift-reduced framework, we need to split a vector into its parallel and perpendicular component with respect to the magnetic field  $\vec{B}$ .

$$\vec{v}_\parallel = \vec{v} \cdot \vec{b} \quad \vec{v}_\perp = -\vec{b} \times (\vec{b} \times \vec{v}) \quad (\text{B.4})$$

The vector  $\vec{b}$  contains the normalized magnetic field and hence represents a unit vector in parallel direction at each point. In the code only its co- and contravariants are calculated and stored for the entire mesh:

$$b_\psi = \vec{b} \cdot \vec{e}_\psi \quad b_\theta = \vec{b} \cdot \vec{e}_\theta \quad b_\varphi = \vec{b} \cdot \vec{e}_\varphi \quad (\text{B.5})$$

$$b^\psi = \vec{b} \cdot \vec{e}^\psi \quad b^\theta = \vec{b} \cdot \vec{e}^\theta \quad b^\varphi = \vec{b} \cdot \vec{e}^\varphi \quad (\text{B.6})$$

## B.2. Centered differentiation stencils

The gradient of a scalar field  $S(u^\psi, u^\theta, u^\varphi)$  is calculated in terms of the reciprocal basis:

$$(\nabla S)_i = \frac{\partial S}{\partial u^i} \vec{e}^i \quad (\text{B.7})$$

In the transport equations, we need to calculate gradients in parallel direction of the field which allows us to express  $\vec{\nabla}_\parallel$  in terms of the contravariant vector of the unit magnetic field from [Equation B.6](#).

$$\nabla_\parallel S = \frac{\partial S}{\partial u^i} \vec{b} \cdot \vec{e}^i = \frac{\partial S}{\partial u^\theta} b^\theta + \frac{\partial S}{\partial u^\varphi} b^\varphi \quad (\text{B.8})$$

The terms in  $\psi$  are omitted in the above formula since the equilibrium magnetic flux surfaces are located on the  $\theta$ - $\varphi$  coordinate surface and the vector  $\vec{b}$  has therefore a zero value in its radial component. Note that this gradient is a scalar as it always points in  $\vec{b}$  direction.

Similarly, a perpendicular gradient can be defined as:

$$\vec{\nabla}_\perp S = \vec{\nabla} S - (\nabla_\parallel S) \vec{b}$$

In terms of metric coefficients, it translates to:

$$\begin{aligned} (\vec{\nabla}_\perp S)^i &= g^{ij} (\nabla S)_j - (\nabla_\parallel S) b^i \\ &= g^{ij} \frac{\partial S}{\partial u^j} - \left( \frac{\partial S}{\partial u^\theta} b^\theta + \frac{\partial S}{\partial u^\varphi} b^\varphi \right) b^i \end{aligned} \quad (\text{B.9})$$

We have to keep in mind that the above expression leads to the contravariant components of the perpendicular gradient whereas the general expression for the gradient in [Equation B.7](#) gives its covariant components.

Next, the divergence of a vector  $\vec{v}$  is calculated by:

$$\vec{\nabla} \cdot \vec{v} = \frac{1}{J} \frac{\partial (JA^i)}{\partial u^i} \quad (\text{B.10})$$

and further the divergence of parallel vector fields  $S_\parallel \vec{b}$  comes in handy:

$$\vec{\nabla} \cdot (S_\parallel \vec{b}) = \frac{1}{J} \left[ \frac{\partial (JS_\parallel b^\theta)}{\partial u^\theta} + \frac{\partial (JS_\parallel b^\varphi)}{\partial u^\varphi} \right] \quad (\text{B.11})$$

The gradient and divergence operators can be combined to define a diffusion operator. The parallel Laplacian with some diffusion coefficients  $D$  reads in metric

terms:

$$\vec{\nabla} \cdot [D(\nabla_{\parallel} S) \vec{b}] = \frac{1}{J} \left[ \frac{\partial \left( JD \left( \frac{\partial S}{\partial u^{\theta}} b^{\theta} + \frac{\partial S}{\partial u^{\varphi}} b^{\varphi} \right) b^{\theta} \right)}{\partial u^{\theta}} + \frac{\partial \left( JD \left( \frac{\partial S}{\partial u^{\theta}} b^{\theta} + \frac{\partial S}{\partial u^{\varphi}} b^{\varphi} \right) b^{\varphi} \right)}{\partial u^{\varphi}} \right] \quad (\text{B.12})$$

Similarly, a perpendicular diffusion operator can be defined:

$$\begin{aligned} \vec{\nabla} \cdot [D \vec{\nabla}_{\perp} S] &= \vec{\nabla} \cdot \left[ D \left( \vec{\nabla} S - (\nabla_{\parallel} S) \vec{b} \right) \right] \\ &= \frac{1}{J} \frac{\partial}{\partial u^i} \left[ JD \left( g^{ij} \frac{\partial S}{\partial u^j} - \left( \frac{\partial S}{\partial u^{\theta}} b^{\theta} + \frac{\partial S}{\partial u^{\varphi}} b^{\varphi} \right) b^i \right) \right] \\ &= \frac{1}{J} \left( \frac{\partial}{\partial u^{\psi}} \left[ JD \left( g^{\psi\psi} \frac{\partial S}{\partial u^{\psi}} + g^{\psi\varphi} \frac{\partial S}{\partial u^{\theta}} + g^{\psi\theta} \frac{\partial S}{\partial u^{\varphi}} \right) \right] \right. \\ &\quad + \frac{\partial}{\partial u^{\theta}} \left[ JD \left( g^{\theta\psi} \frac{\partial S}{\partial u^{\psi}} + (g^{\theta\theta} - b^{\theta} b^{\theta}) \frac{\partial S}{\partial u^{\theta}} + (g^{\theta\varphi} - b^{\varphi} b^{\theta}) \frac{\partial S}{\partial u^{\varphi}} \right) \right] \\ &\quad \left. + \frac{\partial}{\partial u^{\varphi}} \left[ JD \left( g^{\varphi\psi} \frac{\partial S}{\partial u^{\psi}} + (g^{\varphi\varphi} - b^{\theta} b^{\varphi}) \frac{\partial S}{\partial u^{\theta}} + (g^{\varphi\theta} - b^{\varphi} b^{\theta}) \frac{\partial S}{\partial u^{\varphi}} \right) \right] \right) \end{aligned} \quad (\text{B.13})$$

## B.3. Staggered operators

### B.3.1. Parallel gradient

In the electromagnetic vorticity equation, a discrete operator is needed to represent the gradient of  $A_{\parallel} \mathbf{b}$  on the staggered grid.

$$[\nabla_{\parallel} X^{col}]_{[i_{\psi}, i_{\theta}, i_{\varphi}]}^{stg}$$

According to [Equation B.8](#), its numerical evaluation is quite straight-forward:

$$\begin{aligned} [\nabla_{\parallel} X^{col}]_{[i_{\psi}, i_{\theta}, i_{\varphi}]}^{stg} &= \frac{1}{2} \left( X_{[i_{\psi}, i_{\theta}, i_{\varphi}]} - X_{[i_{\psi}, i_{\theta}-1, i_{\varphi}]} \right) b_{[i_{\psi}, i_{\theta}-\frac{1}{2}, i_{\varphi}-\frac{1}{2}]}^{\theta} \\ &\quad + \frac{1}{2} \left( X_{[i_{\psi}, i_{\theta}, i_{\varphi}]} - X_{[i_{\psi}, i_{\theta}, i_{\varphi}-1]} \right) b_{[i_{\psi}, i_{\theta}-\frac{1}{2}, i_{\varphi}-\frac{1}{2}]}^{\varphi} \end{aligned} \quad (\text{B.14})$$

If any of the used  $X$  happens to lie inside the boundary, it is eliminated from the stencil.

The staggered divergence and parallel gradient stencils already existed in a hidden form in the original SOLEDGE3X implementation as part of the parallel Laplacian operator on collocated fields, which first computes the parallel gradient leading to intermediate staggered results and then applies the divergence operator on these staggered intermediate results.

### B.3.2. Perpendicular Laplacian

The perpendicular Laplacian can be succinctly written in term of the fluxes in and out of a staggered cell:

$$[\Delta_{\perp} X^{stg}]_{[i_{\psi}, i_{\theta}, i_{\varphi}]}^{stg} = \frac{1}{J_{[i_{\psi}, i_{\theta} - \frac{1}{2}, i_{\varphi} - \frac{1}{2}]}} \left( F_{[i_{\psi} + \frac{1}{2}, i_{\theta} - \frac{1}{2}, i_{\varphi} - \frac{1}{2}]}^{Y, \psi} - F_{[i_{\psi} - \frac{1}{2}, i_{\theta} - \frac{1}{2}, i_{\varphi} - \frac{1}{2}]}^{Y, \psi} \right. \\ \left. + F_{[i_{\psi}, i_{\theta}, i_{\varphi} - \frac{1}{2}]}^{Y, \theta} - F_{[i_{\psi}, i_{\theta} - 1, i_{\varphi} - \frac{1}{2}]}^{Y, \theta} + F_{[i_{\psi}, i_{\theta} - \frac{1}{2}, i_{\varphi}]}^{Y, \varphi} - F_{[i_{\psi}, i_{\theta} - \frac{1}{2}, i_{\varphi} - 1]}^{Y, \varphi} \right) \quad (\text{B.15})$$

If any of the staggered cell faces touches the domain boundary in any form, the corresponding flux is excluded from the divergence operator. It only remains to calculate the fluxes  $F^{Y,i}$ . The metric and diffusion coefficients at all faces have already been described and are represented by the term  $\xi^{ij} = JD(g^{ij} - b^i b^j)$ . We then can express the fluxes as:

$$F^{Y,i} = \xi^{ij} \frac{\partial X}{\partial u^j}$$

The remaining gradient must use  $X^{stg}$  at staggered points in the domain. If  $[ijk]$  stands for any permutation of the staggered indices  $[i_{\psi}, i_{\theta} - \frac{1}{2}, i_{\varphi} - \frac{1}{2}]$  we always have a flux of the kind:

$$F_{i - \frac{1}{2}, jk}^{Y, i} = \xi^{ii} \left( X_{ijk}^{stg} - X_{i-1,jk}^{stg} \right) \\ + \frac{1}{4} \xi^{ij} \left( X_{i,j+1,k}^{stg} - X_{i,j-1,k}^{stg} + X_{i-1,j+1,k}^{stg} - X_{i-1,j-1,k}^{stg} \right) \\ + \frac{1}{4} \xi^{ik} \left( X_{i,j,k+1}^{stg} - X_{i,j,k-1}^{stg} + X_{i-1,j,k+1}^{stg} - X_{i-1,j,k-1}^{stg} \right)$$

If any of the field points  $X$  lie in or on the domain boundary, it is not considered in the stencil and the factor  $\frac{1}{4}$  is changed to  $\frac{1}{3}$ .

## C. Turbulent profiles

This section contains some complementary graphs for turbulent simulations that have not been shown in the main text, but can be interesting to extend the discussion.

### C.1. Mid-plane plots for density

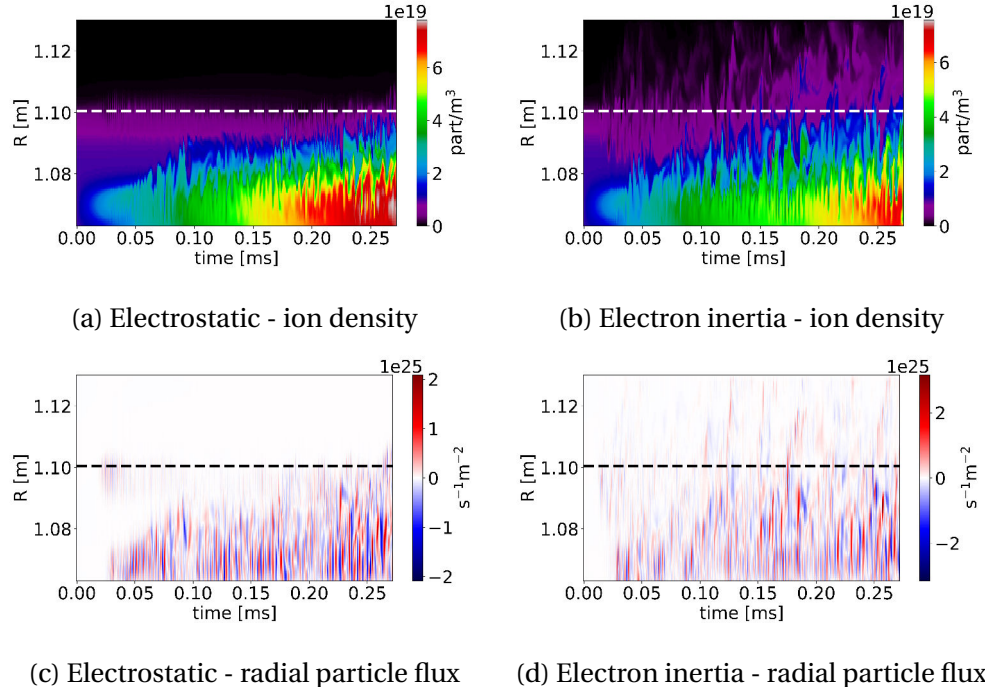


Figure C.1.: Evolution of the radial ion density profiles and particle fluxes at the outer mid-plane for the electrostatic scenarios. The dashed line indicates the position of the separatrix and the plasma in the first poloidal plane is taken

*C. Turbulent profiles – C.1. Mid-plane plots for density*

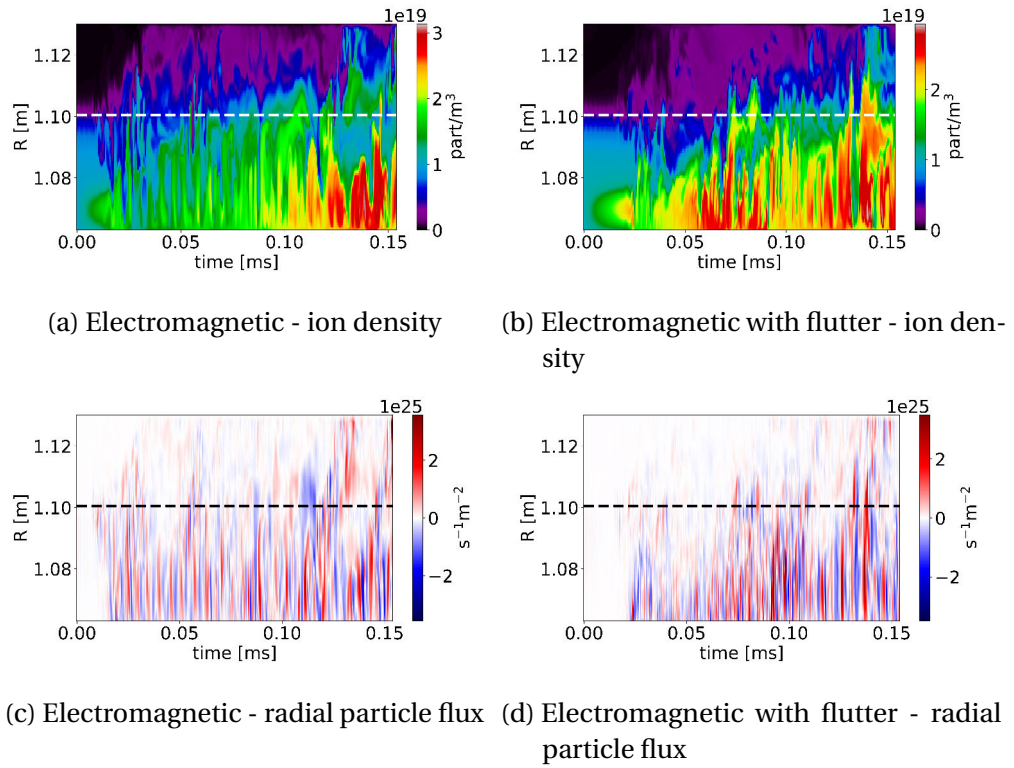


Figure C.2.: Evolution of the radial ion density profiles and particle fluxes at the outer mid-plane for the electromagnetic scenarios. The dashed line indicates the position of the separatrix and the plasma in the first poloidal plane is taken

## C.2. Perpendicular modes on for electron inertia and magnetic induction on the circular scenario

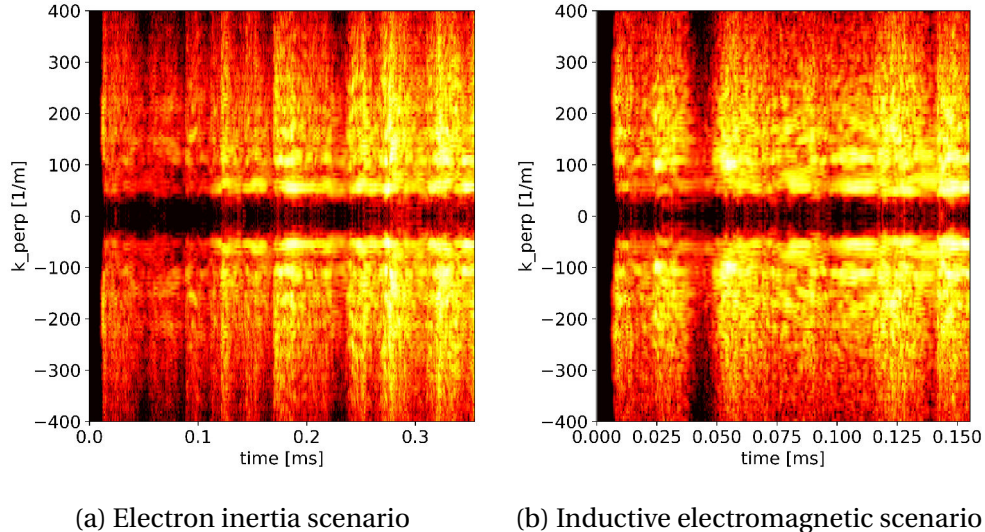


Figure C.3.: Evolution of the power spectrum associated to the perpendicular modes  $k_{\perp}$  over the simulation time. Complement to Fig. 6.12

### **C.3. Flutter field in the low-power TCV scenario**

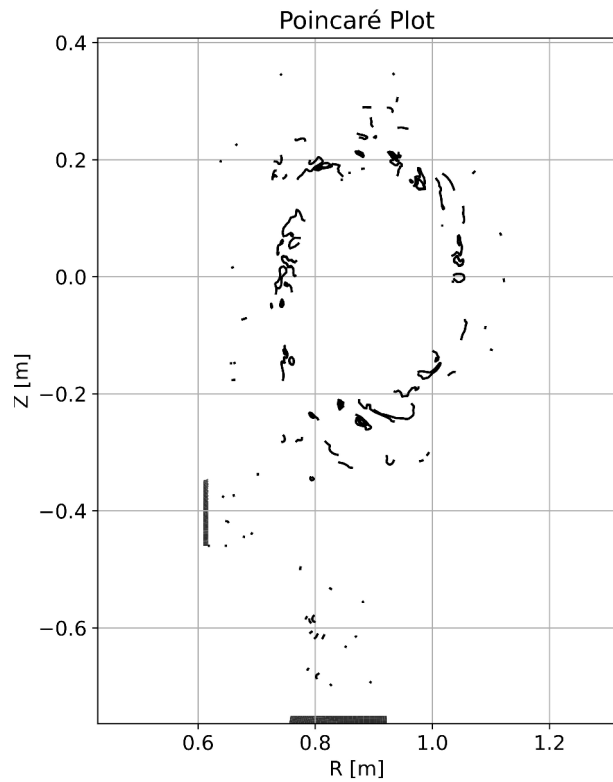


Figure C.4.: Poincaré plot of the fluctuating magnetic field in the TCV low-power case for a random seed of 500 points in a TCV poloidal plane.